BERGISCHE
UNIVERSITÄT
WUPPERTAL

Laser-Based Synthesis and Sintering of Binary, Ternary, and Compositionally Complex Alloy Nanoparticles for Magnetocaloric Cooling

Dissertation
to obtain the doctoral degree Dr.-Ing. (Doktor-Ingenieur)

in the
School of Mechanical Engineering and Safety Engineering

University of Wuppertal

Submitted by:
Shabbir Tahir
from Karachi

Wuppertal 2026

Abstract

Refrigeration is essential for modern society, ranging from food preservation to medical transport. However, most established cooling technologies still rely on vapor-compression systems that depend on refrigerants and are associated with environmental and energy-related challenges. Magnetic refrigeration, based on the magnetocaloric effect, offers a promising solid-state alternative with the potential for improved efficiency, compact device integration, and reduced environmental impact. In this context, this thesis investigates the development of rare-earth-free magnetocaloric materials using pulsed laser ablation in liquids (PLAL) and laser sintering for the synthesis and structuring of compositionally complex alloys (CCAs) at the nanoscale. By addressing challenges related to composition control, phase stability, and miniaturization, this work contributes to the development of sustainable solid-state cooling technologies.

A central focus of this thesis is the investigation of PLAL-derived nanoparticles beyond binary systems, with particular emphasis on ternary and compositionally complex alloy systems and on the influence of composition on phase stability and magnetic transitions. In contrast to bulk materials, which typically exhibit ferromagnetic-to-paramagnetic transitions, the synthesized nanoparticles show superparamagnetic behavior, highlighting the strong size dependence of magnetic properties in magnetocaloric systems. The choice of target preparation strategy was found to strongly influence nanoparticle productivity, composition, and phase stability. In particular, pressed and sintered targets prepared from elemental or alloy powders proved to be a versatile and cost-effective approach. This is especially evident for Al-based compositionally complex alloys, where self-mixed and pressed targets provide a scalable synthesis route that enables the replacement of scarce Ge without significantly compromising functional performance. At the same time, this strategy allows precise compositional tuning, as demonstrated for NiMnSn nanoparticles, where Mn losses during ablation could be compensated by modifying the initial target composition, thereby improving the magnetic and magnetocaloric response. The synthesized NiMnSn Heusler nanoparticles, Ge-based compositionally complex alloy nanoparticles, and Al-based compositionally complex alloy nanoparticles exhibit magnetic transition temperatures in the low- to near-room-temperature range (300 K, 179 K, and 263 K, respectively), making them promising rare-earth-free candidates for magnetocaloric applications.

A further focus of this thesis is the formulation of nanoparticle inks and the laser-based fabrication of magnetocaloric microstructures with micrometer-scale resolution. The results demonstrate that continuous-wave laser sintering enables the direct patterning and phase control of FeRh- and NiMnSn-based microstructures. In addition to improving resolution and phase transformation efficiency, laser sintering also enhances magnetic performance. For FeRh nanoparticle inks, laser sintering increases the antiferromagnetic-to-ferromagnetic magnetization change by a factor of four compared with conventional annealing, while for NiMnSn microparticles it increases the magnetization after processing, thereby improving suitability for functional magnetocaloric devices. These findings establish laser-based 2D printing as a scalable and precise fabrication approach for integrating magnetocaloric materials into applications such as microelectronic cooling and MEMS.

By combining nanoparticle synthesis with laser structuring, this thesis establishes PLAL and laser processing as complementary tools for the development of next-generation magnetocaloric materials and opens new opportunities for compact, sustainable, and efficient thermal management technologies.

Abstract (German)

Kühltechnologien sind für das moderne Leben unverzichtbar, etwa für die Lebensmittelkonservierung und den medizinischen Transport. Der Großteil heutiger Kühlsysteme basiert jedoch weiterhin auf Dampfkompressionsverfahren, deren Einsatz von Kältemitteln mit ökologischen und energetischen Herausforderungen verbunden ist. Die magnetische Kühlung auf Grundlage des magnetokalorischen Effekts stellt hierzu eine vielversprechende Festkörperalternative dar, da sie das Potenzial für höhere Energieeffizienz, kompakte Bauweisen und eine geringere Umweltbelastung bietet. Vor diesem Hintergrund untersucht diese Arbeit die Entwicklung seltenerdfreier magnetokalorischer Materialien mittels gepulster Laserablation in Flüssigkeiten (PLAL) und Lasersintern zur Synthese und Strukturierung zusammensetzungskomplexer Legierungen (CCAs) auf der Nanoskala. Durch die Bearbeitung zentraler Fragestellungen der Zusammensetzungskontrolle, Phasenstabilität und Miniaturisierung leistet diese Arbeit einen Beitrag zur Entwicklung nachhaltiger Festkörper-Kühltechnologien.

Ein Schwerpunkt dieser Arbeit liegt auf der Untersuchung von mittels PLAL hergestellten Nanopartikeln jenseits binärer Systeme, insbesondere ternären und zusammensetzungskomplexen Legierungen, sowie auf dem Einfluss der Zusammensetzung auf Phasenstabilität und magnetische Übergänge. Im Gegensatz zu Bulk-Materialien, die typischerweise ferromagnetisch-paramagnetische Übergänge zeigen, weisen die synthetisierten Nanopartikel ein superparamagnetisches Verhalten auf. Dies verdeutlicht den starken Einfluss der Partikelgröße auf die magnetischen Eigenschaften magnetokalorischer Systeme. Zudem wurde gezeigt, dass die Wahl der Target-Herstellungsstrategie einen entscheidenden Einfluss auf Produktivität, Zusammensetzung und Phasenstabilität der Nanopartikel hat. Als besonders vielseitig und kosteneffizient erwiesen sich gepresste und gesinterte Targets auf Basis elementarer oder legierter Pulver. Dies zeigte sich insbesondere bei Al-basierten zusammensetzungskomplexen Legierungen, bei denen selbstgemischte und gepresste Targets eine skalierbare Syntheseroute ermöglichen und gleichzeitig den Ersatz des knappen Elements Ge erlauben, ohne die funktionellen Eigenschaften wesentlich zu beeinträchtigen. Gleichzeitig erlaubt dieser Ansatz eine präzise Zusammensetzungssteuerung, wie am Beispiel von NiMnSn-Nanopartikeln gezeigt wurde, bei denen Mn-Verluste während der Ablation durch eine gezielte Anpassung der Ausgangszusammensetzung kompensiert werden konnten. Die synthetisierten NiMnSn-Heusler-Nanopartikel, Ge-basierten zusammensetzungskomplexen Legierungsnanopartikel und Al-basierten zusammensetzungskomplexen Legierungsnanopartikel zeigen magnetische Übergangstemperaturen im niedrigen bis nahe Raumtemperaturbereich (300 K, 179 K bzw.

263 K) und stellen damit vielversprechende seltenerdfreie Kandidaten für magnetokalorische Anwendungen dar.

Ein weiterer Schwerpunkt dieser Arbeit ist die Formulierung nanopartikelbasierter Tinten sowie die laserbasierte Herstellung magnetokalorischer Mikrostrukturen mit Auflösungen im Mikrometerbereich. Die Ergebnisse zeigen, dass kontinuierliches Lasersintern die direkte Strukturierung und Phasenkontrolle von FeRh- und NiMnSn-basierten Mikrostrukturen ermöglicht. Neben einer verbesserten Auflösung und effizienteren Phasenumwandlung führt das Lasersintern auch zu einer Verbesserung der magnetischen Eigenschaften. Bei FeRh-Nanopartikeltinten erhöht das Lasersintern die antiferromagnetisch-ferromagnetische Magnetisierungsänderung im Vergleich zur konventionellen Wärmebehandlung um den Faktor vier. Bei NiMnSn-Mikropartikeln steigt die Magnetisierung nach dem Lasersintern ebenfalls an, wodurch sich ihre Eignung für funktionale magnetokalorische Bauelemente weiter verbessert. Diese Ergebnisse etablieren das laserbasierte 2D-Drucken als skalierbaren und präzisen Fertigungsansatz für die Integration magnetokalorischer Materialien in Anwendungen wie die Mikroelektronikkühlung und MEMS.

Durch die Kombination von Nanopartikelsynthese und Laserstrukturierung etabliert diese Arbeit PLAL und Laserprozesse als komplementäre Werkzeuge für die Entwicklung magnetokalorischer Materialien der nächsten Generation und eröffnet neue Möglichkeiten für kompakte, nachhaltige und effiziente Wärmemanagementlösungen.

Acknowledgments

First and foremost, I am deeply grateful to almighty God, the Most Admirable and Gracious, who granted me the opportunity to pursue and complete my Ph.D. thesis. It is through His blessings that I have been able to think, explore, and contribute at this level, and I remain forever thankful for His guidance, wisdom, and strength throughout this journey.

My deepest gratitude goes to my parents, whose unwavering love, sacrifices, and foresight laid the foundation for all my achievements. In particular, I dedicate this milestone to my beloved mother, who sadly left me last year but whose encouragement and vision motivated me to pursue the title of Doctor. Every ounce of effort I have put into this work is deeply rooted in their teachings, their resilience, their prayers, and their support at every stage of my life. Their hardships and dedication have shaped the person I am today, and I owe this success to them.

I am immensely thankful to my big brother, my wife, and my daughter, who have always stood by me, whether through discipline, emotional support, or their unwavering positivity. Their encouragement at every phase of this journey kept me going, and their presence has been an anchor through the challenges of research and life.

In my academic journey, my sincerest appreciation goes to Prof. Gökce and Dr. Doñate-Buendía, whose belief in me, mentorship, and constant support have played a crucial role in my development. Their patience in guiding me through scientific writing, publications, and even personal hurdles has been invaluable. I am deeply grateful for the countless fruitful discussions, their trust in my ideas, and the many opportunities they have provided me with. At the end of each of our discussions, I walked away with new insights, and for that, I am always thankful. Their approachability and flexibility allowed me to express my ideas freely, and I truly appreciate their mentorship.

I would also like to extend my heartfelt thanks to Prof. Wiggers for serving as my second reviewer and for his valuable contributions to shaping my thesis. His technical insights and support, particularly in the final months of my PhD, have been incredibly helpful, and I sincerely appreciate his patience and flexibility with his time.

Special thanks to the MAM group, especially my colleagues Inna and Farbod, who have been with me since the very beginning, even before the formation of MAM. I am also grateful to Dr. Fu, whose contributions in the final months of my Ph.D. had a profound impact, particularly in shaping the NiMnSn manuscript, which significantly strengthened this thesis. Additionally, I appreciate Ingo for his help with SEM imaging, along with Tobias Bochmann from the University of Duisburg-Essen.

My gratitude also extends to the entire CRC 270 community, whose support and collaborative environment have contributed immensely to my learning and growth. A special mention goes to Prof. Farle from the University of Duisburg-Essen, who helped me understand the fundamentals of magnetism.

Lastly, I extend a heartfelt thank you to all the HIWIs and students who assisted me in my experiments, helped achieve meaningful results, and brought innovative ideas to the table. Their contributions, enthusiasm, and teamwork have been essential in making this research possible.

This journey has been both challenging and rewarding, and I am truly grateful to each and every person who has been part of it. Thank you all for your guidance, support, and belief in me.

List of Figures

List of Tables

List of abbreviations

AFM	Antiferromagnetic
APT	Atom Probe Tomography
CCA	Compositionally Complex Alloy
CFC	Chlorofluorocarbon
CW	Continuous Wave
DOE	Diffractive Optical Element
EDX	Elemental Dispersive X-Ray Spectroscopy
FM	Ferromagnetic
FMR	Ferromagnetic Resonance
H_C	Coercivity
HEA	High-Entropy Alloy
HEBM	High Energy Ball Milling
HFC	Hydrofluorocarbon
IEA	International Energy Agency
MCC	Magnetocaloric Cooling
MCE	Magnetocaloric Effect
MEMs	Microelectromechanical systems
MS	Mass Spectrometer
MP	Microparticle
NP	Nanoparticle
PDI	Poly Dispersity Index
PLAL	Pulsed Laser Ablation in Liquid
PM	Paramagnetic
PPMS	Physical Property Measurement System
SEM	Scanning Electron Microscopy
SPM	Superparamagnetic
SPS	Spark Plasma Sintering
TEM	Transmission Electron Microscopy
TOF-SIMS	Time-Of-Flight Secondary Ion Mass Spectrometry
VSM	Vibrating Sample Magnetometry
XRD	X-Ray Diffraction

Glossary

Adiabatic Temperature Change (ΔT_{ad})	A temperature variation occurring in a material due to a magnetic field change under adiabatic conditions.
Antiferromagnetism	A type of magnetic ordering where adjacent atomic spins are aligned oppositely, resulting in no net magnetization.
Coercivity (H_c)	The intensity of the applied magnetic field required to reduce the magnetization of a material to zero after it has been magnetized. It indicates a material's resistance to becoming demagnetized.
Curie Temperature (T_c)	The temperature at which a ferromagnetic material transitions to a paramagnetic state.
Exchange Interaction	A quantum mechanical effect responsible for the alignment of magnetic moments in a material.
Ferromagnetism	A magnetic ordering where atomic spins align parallel to each other, creating a strong net magnetization.
Heusler Alloys	A class of intermetallic compounds known for their multifunctional properties, including magnetism and shape memory effects.
Hysteresis	The lag between changes in magnetization and the applied magnetic field, forming a loop in the magnetization vs. field curve
Isothermal Entropy Change (ΔS_M)	The change in entropy in a material when exposed to an external magnetic field under constant temperature conditions
Magnetic Entropy Change	A measure of the disorder in a magnetic system, typically occurring during a phase transition.
Magnetocaloric Effect (MCE)	The phenomenon where a material exhibits a temperature change upon application or removal of a magnetic field.
Magneto-Structural Transition	A coupled change in both the crystal structure and magnetic properties of a material.
Metamagnetic Transition	A transition between different magnetic states, such as from AFM to FM, induced by an external field.
Nanoparticle (NP)	A particle with at least one dimension in the nanometer range (1-100 nm)

Pulsed Laser Ablation in Liquid (PLAL)	A technique used to synthesize NPs by ablating a solid target submerged in liquid using pulsed laser irradiation.
Saturation Magnetization (M_s)	The maximum magnetization a material can achieve under an applied magnetic field when all magnetic moments are fully aligned.
Superparamagnetism (SPM)	A phenomenon in which magnetic NPs behave like paramagnets due to thermal fluctuations, preventing permanent magnetization.

List of Symbols

A	Exchange constant
C	Heat capacity
d	Laser spot diameter
d_c	Critical diameter
F	Laser fluence
H_c	Coercivity
H	Magnetic field
K_{eff}	Anisotropy constant
k_B	Boltzmann constant
M	Magnetization
M_s	Saturation Magnetization
S	Mass specific Entropy
S_{EL}	Mass specific electronic entropy
S_L	Mass specific lattice entropy
S_M	Mass specific magnetic entropy
ΔS_{total}	Mass specific total entropy
T_0	Initial temperature
T_{ad}	Temperature at adiabatic conditions
T_B	Blocking temperature
T_c	Curie temperature
T_N	Neels temperature
P	Laser powder
Q	Heat energy
μ_0	vacuum permeability
v_s	Scanning speed
γ	Gamma phase

Preface

This thesis is structured into five main sections, beginning with an introduction, followed by summaries of four research studies: (1) laser structuring of FeRh nanoparticle inks, (2) synthesis of high-entropy alloy nanoparticles via pulsed laser ablation in liquids (PLAL), with emphasis on the influence of target preparation methods, (3) investigation of magnetic phase transitions in compositionally complex alloys at both bulk and nanoscale, and (4) compositionally controlled synthesis of NiMnSn nanoparticles and their comparison with corresponding microparticles. Three of these studies have been published in peer-reviewed international journals, while one is currently in preparation. The thesis concludes with a general discussion, followed by references and an appendix containing the full versions of all studies. The introduction provides a comprehensive overview of the current research landscape, highlighting the significance of transitioning from unary and binary materials to compositionally complex alloy (CCA) systems. It then delves into the fundamentals of magnetism and the magnetocaloric effect (MCE), as well as the evolution of material systems from binary to CCAs for magnetic and magnetocaloric applications. Additionally, it explores how these advanced alloy systems can be synthesized and structured using laser-based processing techniques, contextualizing their relevance within the scope of the four studies presented in this thesis. The second part of the introduction reviews the initial works, including the ones where I am co-author, contributing to the fundamentals of the thesis. The subsequent Section 2 presents structured summaries of these four studies, detailing their objectives, methodologies, and key findings. The general discussion expands on these results, positioning them within the existing body of research. Additionally, it examines the contributions of this thesis, its limitations, and potential directions for future research. The thesis concludes with a summary of key findings and an outlook on the potential impact of this research. The reference list and an appendix containing the full versions of the four studies are provided at the end.

The four core studies which are the basis of the thesis, are the following:

- **Study 1 (Tahir et al., 2023)**

  Tahir, S., Landers, J., Salamon, S., Koch, D., Doñate-Buendía, C., Ziefuß, A. R., . . . Gökce, B. (2023). Development of Magnetocaloric Microstructures from Equiatomic Iron–Rhodium Nanoparticles through Laser Sintering. Advanced Engineering Materials, 25(20), 2300245. DOI: https://doi.org/10.1002/adem.202300245

- **Study 2 (Tahir et al., 2024)**

Tahir, S., Shkodich, N., Eggert, B., Lill, J., Gatsa, O., Flimelová, M., . . . Gökce, B. (2024). Synthesis of High-Entropy Alloy Nanoparticles by Pulsed Laser Ablation in Liquids: Influence of Target Preparation on Stoichiometry and Productivity. ChemNanoMat, 10(5), e202400064. DOI: https://doi.org/10.1002/cnma.202400064

- **Study 3 (Tahir et al., 2024)**

Tahir, S., Smoliarova, T., Doñate-Buendía, C., Farle, M., Shkodich, M., and Gökce,B. (2025). Synthesis and magnetic transitions of rare-earth-free Fe–Mn–Ni–Si-based compositionally complex alloys at bulk and nanoscale. Beilstein J. Nanotechnol, 16, 823–836. DOI: https://doi.org/10.3762/bjnano.16.62

- **Study 4**

Tahir, S., Scheibel, F., Doñate-Buendía, C Fu, Z., Koch, D., Heidelmann, M., Donner, W., Gutfleisch, O., Gökce, B. "Compositionally Controlled Synthesis and Magnetic Properties of NiMnSn Heusler Alloy Nanoparticles" (To be submitted).

The initial studies by Nadarajah (Nadarajah et al., 2020), (Nadarajah et al., 2021) A and B, along with the parallel study by Gatsa (Gatsa et al., 2024), where I contributed as a co-author, are also outlined in the work.

Contents

1. Introduction

This introduction first provides an overview of the current state of research in subsection 1.1, beginning with the growing global demand for cooling and the potential of magnetocaloric cooling (MCC) as a sustainable alternative, particularly for cooling at nanoscale. It then discusses the transition from unary materials to compositionally complex systems, highlighting the need for novel materials in advanced cooling technologies. The fundamental principles of magnetism, MCE, and the unique magnetic properties of NPs are explored in the subsequent sections, followed by emphasizing recent advancements in materials within the scope of this thesis. Additionally, the synthesis of NPs via pulsed laser ablation in liquids (PLAL) and their integration into functional structures through laser-based printing are explained in detail. Following this literature review, the introduction also outlines initial research contributions by and concludes with a subsection detailing the 'Research Questions and Scope of the Thesis', which defines the key research objectives and direction of this work.

1.1. Background

The demand for cooling systems has grown significantly over the past few decades, driven by global warming, rising populations, and urbanization. According to the IEA, space cooling could account for over 37% of total electricity demand by 2050, driven primarily by increasing temperatures and the need for improved living standards, particularly in developing regions like India and Africa (Fig. 1a).(IEA, 2018) Already, there are over 2 billion air conditioning units in use, and this number is expected to more than double by mid-century (Fig. 1b). This trend presents not only energy challenges but also significant environmental concerns due to the widespread use of refrigerants like CFCs and HFCs, which contribute to both ozone depletion and global warming.(Kroeze & Reijnders, 1992) In addition to increasing energy consumption, the surge in cooling places pressure on electricity grids, often relying on fossil fuels, further exacerbating carbon emissions. The World Bank has warned that growing cooling demand may widen social inequality, as many low-income households struggle to afford efficient technologies, leaving them vulnerable to extreme heat.(Bangalore et al., 2014) As the global climate continues to warm, finding sustainable solutions for cooling is becoming increasingly critical, with the potential to influence energy policies and infrastructure across the globe.

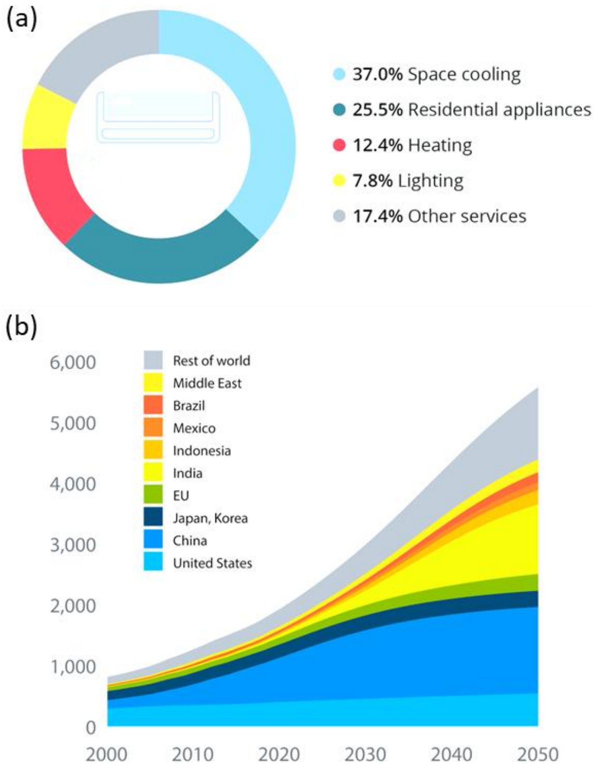

Figure 1. (a) Global electricity demand growth from 2018 to 2015 by energy use category. (b) Projected number of air conditioning units in use worldwide (in millions). (Source: IEA)

In this context, MCC represents a groundbreaking solution to the environmental challenges posed by conventional cooling systems. Unlike vapor-compression refrigeration, which relies on refrigerants like CFCs and HFCs that contribute to global warming and ozone depletion, MCC operates using the MCE, where certain materials heat up or cool down when subjected to changing magnetic fields.(Ram et al., 2018). MCC systems also offer advantages such as fewer moving parts, reduced noise and maintenance requirements, and enhanced system reliability compared to conventional vapor-compression technologies.(Brück, 2005; Y. Zhang et al., 2022) One of the key materials used in MCC systems is gadolinium (Gd), which has demonstrated great promise in near-room-temperature cooling applications due to its significant MCE at its Curie temperature (T_c).(Lyubina, 2017) These changes stem from the high magnetic moments of rare-earth materials, driven by their unpaired 4f electrons, which align or disorder with the application or removal of a magnetic field. However, due to the high cost, unavailability, environmental risk together with mining difficulties and supply chain risk of rare earth materials; replacing them with other materials for MCC is crucial.(Cui et al., 2018; Gutfleisch et al., 2011) Intensive research is dedicated to developing rare-earth-free alternatives, with focus areas including Ni-Mn based Heusler alloys (Ahn, 2024; Passamani et al., 2009), Fe_2P alloys (Cedervall et al., 2019; Ghorai et al., 2025), LaFeSi based alloys (Del

Rose, Chouhan, Doyle, Pathak, & Mudryk, 2024; Paul-Boncour & Bessais, 2021), and HEAs/CCAs (Y. Guo et al., 2022; Law & Franco, 2023). In particular, HEA/CCAs have been investigated due to their unique multi-element compositions, exhibit high configurational entropy and improved thermal stability. These properties allow for fine-tuning of magnetic behavior and T_c to meet specific application needs.

To enable the use of MCC in microelectronics and semiconductor devices, magnetocaloric materials need to be miniaturized to the nanoscale.(Belo, Pires, Araújo, & Pereira, 2019; Dudek, Dudek, Wolak, Wojciechowski, & Grima, 2019) MCC materials at nanoscale can provide localized cooling in sensitive areas, improving device performance and longevity by addressing the heat dissipation challenges associated with increasing function-to-area ratios. Furthermore, reducing these materials to the nanoscale brings several benefits, including increased surface area-to-volume ratios, modified magnetic properties, and enhanced control over phase transitions and magnetization behavior.(Chen et al., 2019) Together, these features make nanoscale magnetocaloric materials more adaptable and efficient for a variety of applications.

To synthesize nanoscale magnetocaloric materials, pulsed laser ablation in liquid (PLAL) appears as an effective and versatile method due to its simplicity and environmental friendliness.(Johny et al., 2022; Tahir et al., 2024; Waag et al., 2019) The process involves directing laser pulses onto a solid target submerged in a liquid medium, where the laser's high energy initiates ablation, creating a plasma that rapidly cools and produces NPs within the liquid. This approach allows to produce NPs of varying compositions depending on the composition of targets either from single or multiple elements. This approach is not only scalable but also safe and capable of generating ligand-free NPs, which are advantageous for applications requiring high purity and clean surfaces.(Fazio et al., 2020; Gökce, Amendola, & Barcikowski, 2017; Dongshi Zhang, Gökce, & Barcikowski, 2017).

Now to harness the benefits of magnetocaloric NPs, one promising approach is the use of advanced printing technologies to fabricate devices directly from these NPs. Among printing technologies, laser printing offers several advantages over traditional methods, such as precise spatial resolution (Geng, Xu, Yan, Shi, & Qiu, 2023), in-situ annealing (Tu, Seah, Li, Wang, & Tan, 2022), substrate flexibility (Brown et al., 2023), fast processing (Geng et al., 2023) and enables the creation of complex geometries tailored for specific applications (Young, Xu, Sarker, & Sochol, 2024). This would allow for the direct writing of magnetocaloric materials onto substrates, facilitating the integration of these materials into microelectronic systems paving the way for efficient, small-scale cooling solutions that traditional bulk materials cannot provide. Apart from MCC applications, the miniaturized laser printing of magnetocaloric materials can be explored for the development of thermal switches, magnetocaloric micropumps, heat sensors and actuators.

In alignment with this context, this thesis comprises four primary studies aimed at advancing the synthesis and application of magnetocaloric NPs. The first study demonstrates a pathway to transform laser-synthesized FeRh NPs from an equimolar bulk alloy into customized microstructures through laser-based direct writing of NP inks. Building on the synthesis of binary alloy NPs, the second study investigates the PLAL synthesis of multicomponent HEA NPs, assessing how different target preparation techniques influence their characteristics. This foundation supports the third study, which focuses on the synthesis of rare-earth-free magnetocaloric CCA NPs via PLAL and their comparison with bulk target properties. Lastly, the fourth study explores compositionally controlled synthesis strategies for NiMnSn Heusler alloy NPs, analyzing the magnetic property variations between NPs, MPs of similar composition, and their sintered structures.

To provide a comprehensive foundation for this research, the thesis will first present a state-of-the-art review, covering the transition from unary to HEA alloys, fundamental principles and classifications of magnetism, the MCE, and magnetism at the nanoscale. This will be followed by an overview of recent advancements in magnetocaloric materials, particularly focusing on rare-earth-free alternatives. The discussion will then progress to the synthesis of NPs using PLAL and conclude with the laser printing of NP inks, paving the way for novel applications in microelectronics and small-scale cooling solutions.

1.1.1. Transition from Single-Element to Multicomponent alloy

The development of alloys has been a crucial advancement in human civilization, dating back to the Bronze Age when early metallurgists discovered that combining copper with tin produced a material with enhanced strength and durability. This process of alloying was driven by the need to improve mechanical properties, corrosion resistance, and thermal stability beyond what pure metals could offer. Over time, more complex alloys emerged, such as brass, an alloy of copper and zinc, which provided improved workability and resistance to tarnishing. As metallurgy evolved, the understanding of phase diagrams and thermodynamic principles allowed for the development of more sophisticated alloy systems, particularly in the 19th and 20th centuries, when steels and superalloys revolutionized industrial applications. Traditional alloy design has typically relied on one principal element, with minor additions of other elements to achieve specific properties. However, this approach has limitations in terms of performance optimization, as it is largely constrained by the dominant characteristics of the base metal.

The concept of HEAs represents a fundamental shift from this conventional alloying strategy. Unlike traditional alloys, which are based on one or two principal elements, HEAs consist of five or more elements mixed in near-equiatomic or equimolar ratios.(George, Raabe, & Ritchie, 2019) This departure from conventional alloying principles introduces unique material behaviors that cannot be predicted based on the properties of individual constituents. In HEAs, high configurational entropy stabilizes solid-solution phases by suppressing intermetallic formation (Ye, Wang, Lu, Liu, & Yang, 2016), while atomic size mismatch among constituent elements induces lattice distortion that enhances strength and hardness.(Tandoc, Hu, Qi, & Liaw, 2023) Another distinguishing feature is the sluggish diffusion effect, which slows atomic movement and improves thermal stability, making HEAs highly resistant to phase transformations at elevated temperatures.(Samolyuk, Osetsky, Stocks, & Morris, 2021). Depending on composition and processing conditions, the interplay of these effects can lead to exceptional mechanical properties, superior wear and corrosion resistance, and tunable electrical and magnetic behaviors, making HEAs promising candidates for applications ranging from aerospace engineering (Popoola, Dada, Adeosun, & Mathe, 2019) to biomedical implants (de Oliveira, Fagundes, Capellato, Sachs, & da Silva, 2022). A broader category of materials known as compositionally complex alloys (CCAs) follow a similar multi-element approach but without strict equimolarity, allowing greater flexibility in tailoring material properties.(Pervan et al., 2023)

HEA NPs have emerged as a groundbreaking advancement in nanomaterials, leveraging the unique functional properties of both their multicomponent composition and nanoscale effects, such as a high surface-to-volume ratio and quantum confinement. Similar to their bulk counterparts, HEA NPs exhibit exceptional mechanical strength, thermal stability, and resistance to fatigue, fracture, and corrosion. These attributes make them highly promising for a wide range of applications, including catalysis (Yu et al., 2022; Q. Zhang et al., 2023), optics (Kim et al., 2024; Liao et al., 2022), energy storage (A. Sarkar et al., 2018; Wei et al., 2023), chemical sensors (Mondal et al., 2023), drug-delivery agents (Banizi, Khakbiz, Shakibania, Amiri, & Naserian, 2024; Chang, Jing, Liu, Qiu, & Ling, 2024) and magnetic applications (Han et al., 2021; D. Jiang, Yuan, Zhu, & Yao, 2024). For instance, Gao et al (Gao et al., 2020) synthesized FeCoPdIrPt NPs using fast-moving bed pyrolysis, which exhibited stable catalytic performance over 150 hours of continuous operation and a mass activity 26 times higher than commercial Pt/C for the hydrogen evolution reaction at an overpotential of 100 mV. Such advancements highlight the transformative potential of HEA NPs in next-generation materials science.

The incorporation of multiple elements in alloy design has significantly expanded the range of achievable properties at both bulk and nanoscale levels. For magnetic and magnetocaloric applications, a fundamental understanding of magnetism and the MCE is essential. The next section will delve into these principles, providing the theoretical foundation necessary to comprehend the behavior of these advanced materials.

1.1.2. Magnetism: Fundamental Principles

Magnetism, one of the fundamental forces of nature, has played a crucial role in the development of modern technology and scientific understanding. The earliest recorded observations of magnetism date back to ancient civilizations, where natural magnets, known as lodestones, were discovered to attract iron. However, the modern theoretical framework for magnetism began in the 19th and 20th centuries with the development of Maxwell's equations and quantum mechanics, which provided insight into the microscopic origins of magnetic phenomena. At the atomic level, magnetism arises from the intrinsic properties of electrons, namely, their spin and orbital angular momentum.(Coey, 2020) The interaction of these microscopic magnetic moments through exchange interactions leads to different macroscopic magnetic behaviors observed in materials, forming the basis for the classification of magnetic materials.

Magnetic materials are generally classified into four main categories based on their response to external magnetic fields. Diamagnetic materials, such as copper and bismuth, exhibit a weak repulsion to magnetic fields because the applied magnetic field induces orbital currents in the electron clouds, which produce a magnetic moment opposing the applied field. Paramagnetic (PM) materials, including aluminum and platinum, possess unpaired electrons, which align weakly with an external magnetic field but lose their alignment when the field is removed. Ferromagnetic (FM) materials, such as iron, cobalt, and nickel, exhibit spontaneous magnetization due to strong exchange interactions that align neighboring atomic moments in the same direction, resulting in a net magnetization even in the absence of an external field. Even though electronic exchange forces in ferromagnets are very large, thermal energy eventually overcomes the exchange and produces a randomizing effect. This occurs at a particular temperature called the Curie temperature (T_c).(Teja & Koh, 2009) Below the T_c, the ferromagnet is ordered while above T_c thermal fluctuations destroy long-range magnetic order. As a result, the saturation magnetization (M_s), defined as the maximum magnetization achievable under an applied field, goes to zero at the T_c. In contrast, Antiferromagnetic (AFM) materials, like manganese oxide (MnO), have alternating magnetic moments that cancel each other out, leading to no macroscopic magnetization. This type of magnetic ordering is called antiferromagnetic ordering.

The directional dependence of magnetic properties, known as magnetic anisotropy, plays a crucial role in defining the coercivity (H_C) and remanence of materials.(Skomski, Manchanda,

& Kashyap, 2021) Magnetic anisotropy can originate from multiple factors, including the crystal lattice structure, which determines magnetocrystalline anisotropy, the shape of a particle, which induces shape anisotropy, and the presence of internal or external stress, which leads to stress anisotropy. These anisotropic effects influence the energy barrier required for magnetization reversal, which is a critical parameter in data storage, spintronics, and permanent magnet applications. The effect of anisotropy is also reflected in the shape of hysteresis loops, impacting the efficiency and stability of magnetization processes.

Magnetic domains provide further insight into the behavior of ferromagnetic materials.(Schäfer, 2021) A magnetic domain is a microscopic region where atomic moments are aligned in the same direction due to exchange interactions. Although the magnitude of spontaneous magnetization remains uniform within a material, its direction varies across different regions, typically on a micron-to-millimeter scale. Uniform magnetization occurs only when a strong external field forces all domains to align or when the particle size is small enough to prevent domain formation altogether. Depending on grain size, the magnetic behavior of a material falls into different regimes. In sufficiently small magnetic particles, thermal energy becomes comparable to the magnetic anisotropy energy, leading to spontaneous fluctuations of the magnetization and the onset of superparamagnetic (SPM) behavior. When the particle size falls within the single-domain regime, the magnetization remains spatially uniform, as domain-wall formation is energetically unfavorable, resulting in a maximum coercive field (H_C). With increasing particle size, a pseudo–single-domain state develops, in which the magnetic configuration gradually evolves toward a multidomain structure. In larger particles, the formation of multiple domains lowers the magnetostatic energy, leading to a reduction in H_C. Consequently, the coercive field reaches a maximum within the single-domain size range and decreases for both larger particles, due to domain subdivision, and smaller particles, where thermal fluctuations destabilize the magnetization.(Sung Lee, Myung Cha, Young Yoon, Lee, & Keun Kim, 2015)

The understanding of magnetism, from atomic interactions to macroscopic domain behavior, enables further advancements in controlling and manipulating magnetic states. The interplay between exchange interactions, thermal effects, anisotropy, and external fields governs the stability and reversibility of magnetization. As research progresses, the ability to tailor magnetic properties through material design and external stimuli continues to refine both theoretical models and technological applications, pushing the boundaries of how magnetism is utilized in fundamental science and engineered systems.

1.1.3. Magnetocaloric Effect (MCE)

The MCE is a phenomenon where certain materials experience a reversible temperature change upon application or removal of an external magnetic field. his effect originates from changes in magnetic entropy caused by the field-induced alignment and disordering of magnetic moments, which can be exploited for solid-state cooling.(Aprea, Greco, Maiorino, & Masselli, 2020; Y. Lin et al., 2024)

The magnetocaloric effect operates through a thermodynamic cycle analogous to a Carnot cycle, in which magnetic entropy (ΔS_M) and adiabatic temperature change (ΔT_{ad}) play roles similar to entropy and temperature variations in conventional heat engines. The cycle comprises four idealized steps: isothermal magnetization, isothermal heat rejection, adiabatic demagnetization, and isothermal heat absorption.(Meddeb & Razak, 2015)

1. **Isothermal Magnetization**: When a magnetic field is applied, the material's magnetic moments align with the field direction, leading to a decrease in magnetic entropy. The alignment results in a compensatory increase in lattice entropy, which causes a rise in temperature under adiabatic conditions.
2. **Isothermal Heat Release**: The heat generated during magnetization is transferred to an external sink, allowing the material to return to thermal equilibrium at a higher magnetic field.
3. **Adiabatic Demagnetization**: Removing the magnetic field causes the magnetic moments to become disordered. This transition increases magnetic entropy and reduces lattice entropy, resulting in a temperature decrease under adiabatic conditions.
4. **Isothermal Heat Absorption**: The cooled material absorbs heat from the environment, completing the cooling cycle. The cycle then repeats, maintaining a continuous cooling effect under cyclic magnetic field changes.

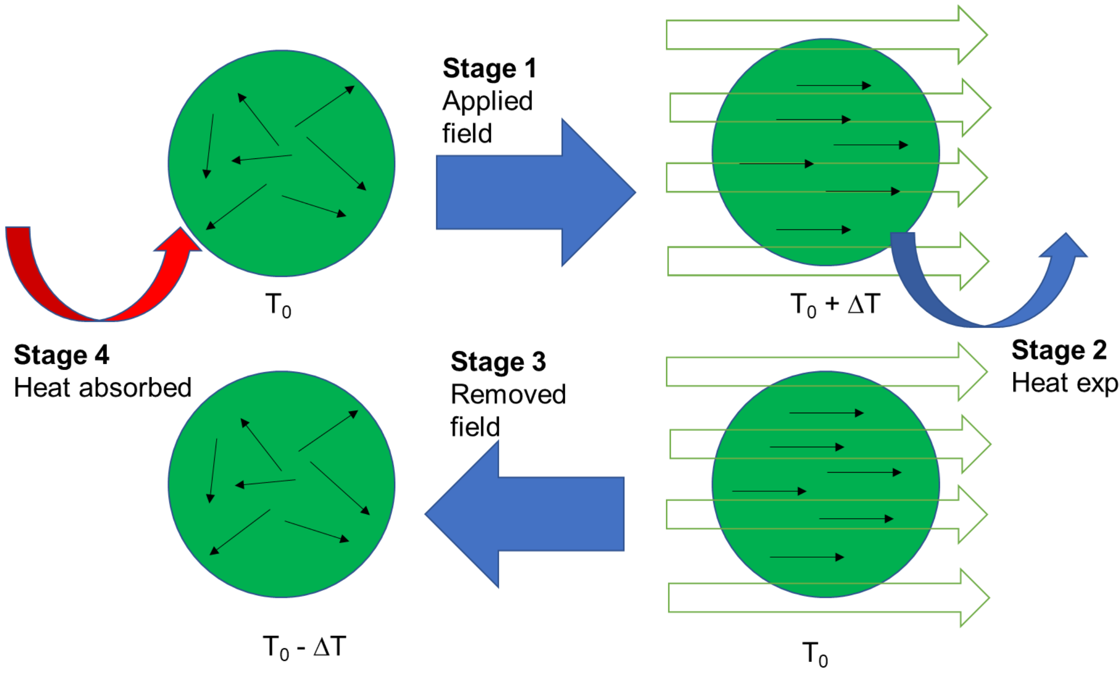

Figure 2. Magnetocaloric refrigeration cycle shows heating and cooling after magnetization and demagnetization processes, where T_0 is initial temperature and ΔT is change in temperature.

The MCE can be quantified through specific thermodynamic relations that connect entropy, temperature, and magnetic field variations. Key parameters of interest include ΔS_M and ΔT_{ad}

The total entropy in a magnetocaloric material can be represented as the sum of various entropy components (Equation 1) (Maraytta et al., 2019)

$$S_{total} = S_L + S_M + S_{EL} \tag{1}$$

where S_L is the lattice entropy (related to atomic vibrations), S_M is the magnetic entropy (related to magnetic moment alignment), and S_{EL} is the electronic entropy (related to electron occupancy across energy states). The S_M is the primary component influenced by magnetic field changes, impacting the MCE.

The magnetic entropy change (ΔS_M) induced by a change in the applied magnetic field is obtained from the temperature dependence of magnetization at fixed magnetic fields via the Maxwell relation (Gschneidner & Pecharsky, 2000) (Equation 2):

$$\left(\frac{\partial S}{\partial H}\right)_T = \left(\frac{\partial M}{\partial T}\right)_H \tag{2}$$

Where, S is the entropy, H is the magnetic field, M is the magnetization, and T is the temperature. Integrating the above equation from an initial magnetic field H_1 to a final magnetic field H_2 gives the isothermal entropy change:

$$\Delta S_M(T, \Delta H) = \int_{H1}^{H2} \frac{\partial M(T,H)}{\partial T} dH \tag{3}$$

This expression shows that the magnetic entropy change is determined by the temperature dependence of the magnetization evaluated at fixed magnetic fields, which is typically most pronounced in the vicinity of the T_c .

Under adiabatic conditions ($dS = 0$), the entropy differential of a magnetic system can be written as

$$dS = \left(\frac{\partial S}{\partial T}\right)_H dT + \left(\frac{\partial S}{\partial H}\right)_T dH \tag{4}$$

Here, the heat capacity at constant magnetic field $C_H(T, H)$ is introduced through the thermodynamic definition

$$C_H(T, H) = T \left(\frac{\partial S}{\partial T}\right)_H \tag{5}$$

Substituting this relation together with the Maxwell relation from Eq. (2) into Eq. (4) and imposing the adiabatic condition ($dS = 0$), yields the differential adiabatic temperature change:

$$dT = -\left(\frac{T}{C(T,H)}\right)_M \left(\frac{\partial M(T,H)}{\partial T}\right)_H dH \tag{6}$$

Integration of Eq (6) from $H1$ to $H2$ result in results in the adiabatic temperature change:

$$\Delta T_{ad}(T, \Delta H) = -\int_{H1}^{H2} \left(\frac{T}{C(T,H)}\right)_M \left(\frac{\partial M(T,H)}{\partial T}\right)_H dH \tag{7}$$

Equations (3) and (7) demonstrate that both the isothermal magnetic entropy change and the adiabatic temperature change originate from the same temperature derivative of the magnetization evaluated at fixed magnetic fields. However, in the adiabatic case, the magnitude of the temperature change is additionally governed by the heat capacity, which moderates the conversion of entropy change into a temperature change.

When the magnetic field is applied the entropy change $\Delta S_M(T, \Delta H)$. Under adiabatic conditions, this entropy reduction is compensated by an increase in temperature change in temperature $\Delta T_{ad}(T, \Delta H)$ is positive leading to the heating of the material. When the magnetic field is removed, $\Delta S_M(T, \Delta H)$ is positive and $\Delta T_{ad}(T, \Delta H)$ is negative leading to the cooling of material.

1.1.4. Magnetism in nanomaterials

Magnetic NPs display distinctive magnetic properties that set them apart from their bulk counterparts due to factors such as finite-size effects, surface anisotropy, and quantum confinement. When the size of a magnetic material is sufficiently reduced, the energy required to create domain walls within the particle volume exceeds the magnetostatic energy saved by domain formation, making a single-domain magnetic state energetically favorable. As a result, the overall magnetization of the NP can be considered as a single giant magnetic moment, derived from the sum of the individual magnetic moments of each atom. In this state, the material exhibits SPM behaviour. This threshold size, known as the critical diameter (D_c), is material-dependent and can range from a few nanometres to tens of nanometres.(Sergei, Yurii, Khomutov, & Gleb Yu, 2005; Singamaneni, Bliznyuk, Binek, & Tsymbal, 2011). The transition to a single-domain state leads to unique magnetic behaviours that are distinct from bulk materials.

In the strong anisotropy limit the critical diameter can be estimated according to (Bedanta & Kleemann, 2009)

$$d_c \approx 18\frac{\sqrt{AK_{eff}}}{\mu_0 M_S^2} \tag{8}$$

Where, A is the magnetic exchange stiffness constant describing the strength of exchange interactions between neighbouring spins, K_{eff} is the anisotropy constant M_s is the saturation magnetization and μ_0 is the vacuum permeability. However, since these material-specific parameters are not available for complex material system, the critical diameter can be estimated using the data of a urinary or binary system with similar crystal structure and comparable magnetization.

For sufficiently small NPs, the energy barriers that oppose magnetization reversal, are relatively low compared to thermal energy. If the particle size is sufficiently small and thermal energy is high enough, magnetization can spontaneously flip directions within short time intervals. The average time between two such flips is referred to as the Néel relaxation time. When the measurement duration is much shorter than the Néel relaxation time, the system is said to be in a blocked state, where the observed magnetization corresponds to the instantaneous value at the beginning of the measurement since there is no time for directional flipping. In this state, NPs behave similarly to a paramagnet but with a significantly enhanced magnetic susceptibility. On the other hand, when the measurement duration greatly exceeds the Néel relaxation time, the material enters a SPM state, where continuous fluctuations in magnetization result in an overall net moment of zero over time. The blocking temperature

(T_B), is the temperature between the blocked and SPM states. Above T_B, both ferromagnetic and ferrimagnetic NPs exhibit SPM behaviour with rapid and random magnetization reversals leading to an average magnetic moment of zero. The value of T_B, associated with the energy barrier, depends on the characteristic measuring time, which can vary from 100 to 10^{-8} s. Experimentally, the value of T_B is typically identified as the temperature at which the zero-field-cooled (ZFC) and field-cooled (FC) magnetization curves merge. In a ZFC measurement, the sample is initially cooled to a low temperature without an external magnetic field. A weak external field is then applied, and the magnetization is measured while gradually increasing the temperature. In contrast, in an FC measurement, the sample is cooled in the presence of an external field, which remains applied as the temperature rises, and magnetization is measured throughout the process. The blocking temperature can also be estimated using the following equation, assuming the particles maintain a single-domain structure.(Kolhatkar, Jamison, Litvinov, Willson, & Lee, 2013)

$$T_B = \frac{K_{eff}V}{25\ k_B} \tag{9}$$

where, k_B is the Boltzmann constant and V is the volume of a particle. This equation indicates that as particle size increases, blocking temperature rises accordingly. However, for larger particles, where uniform magnetization is interrupted by domain boundaries formed during the nucleation and growth process, this equation may not accurately predict T_B. By maintaining the NP size below a critical threshold during synthesis, NPs tend to develop as single-domain structures. At sufficiently small sizes, they display SPM properties under standard conditions.

Magnetic NPs have broad applications, particularly in magnetocaloric refrigeration, where the absence of hysteresis and easier alignment of magnetic moment enhances cooling efficiency.(de Paula et al., 2016; K. Sarkar et al., 2022) They are also widely used in biomedicine, where SPM iron oxide NPs (SPIONs) serve as contrast agents for magnetic resonance imaging (MRI) (Kanithi et al., 2024; Pucci, Degl'Innocenti, Belenli Gümüş, & Ciofani, 2022; Schleich, Danhier, & Préat, 2015) and as heat generators in cancer hyperthermia treatments (Pucci et al., 2022). The ability to fine-tune particle size, anisotropy, and interparticle interactions allows for precise control over their magnetic properties, making them essential for next-generation magnetic materials.

According to McMichael et al. calculations, the NPs may exhibit an effective magnetic moment that is greater than magnetic moment of its constituent atoms so maximally enhances MCE.(X. G. Liu et al., 2008) Biswas et al.(Biswas, Chandra, Phan, & Srikanth, 2012) has shown improvement in magnetocaloric properties of $LaMnO_3$ by reducing particle size and improved relative cooling power upto 65% in the nanocrystalline sample compared to bulk. However, in some cases such as for $HoCrO_3$ (Yin, Sauyet, Seehra, & Jain, 2017), both the refrigerant capacity and ΔS decrease with decreasing particle size from 425 nm to 60 nm. In some cases, such as $Pr_{0.6}Sr_{0.4}MnO_3$ the particle size decrease from 120 nm to 30 nm, the entropy decreases but the relative cooling power improves due to large larger temperature span.(Souza, Vagadia, & Daivajna, 2021) For magnetocaloric applications, the optimal particle size is governed by the intrinsic material properties and the trade-off between magnetic performance and thermal transport. Accordingly, different particle size regimes can provide specific advantages, depending on whether magnetic entropy change, thermal conductivity, or dynamic response is prioritized. The bulk and large particles possess high magnetization due to well-ordered magnetic domain but can have slower thermal response due to poor heat exchange. The NPs have enhanced surface area for rapid heat exchange, has potential for tunable T_c and ΔS_M and reduce hysteresis losses due to single domain behavior. However, surface spin disorder and thermal fluctuations may reduce magnetization and broaden phase transition.

1.1.5. Advancements in magnetic materials

The concept of magnetocaloric materials dates back to the late 19th century when Emil Warburg first observed the MCE in iron in 1881. Subsequent work by Weiss and Piccard in 1917 quantified the temperature changes in nickel under an applied magnetic field, laying the foundation for the field of magnetocaloric materials.(Mellari, 2023) These studies demonstrated the potential for using magnetic entropy changes to create temperature gradients, sparking interest in the development of materials with enhanced magnetocaloric properties. A significant breakthrough occurred in the late 20th century with the discovery of giant magnetocaloric materials, such as $Gd_5(Si_2Ge_2)$ which exhibited large ΔS_M and ΔT_{ad} under moderate magnetic fields.(Pecharsky & Gschneidner, 1997) These materials offered a path forward for the realization of MCC technologies, particularly for applications near room temperature.

1.1.5.1 FeRh alloy

FeRh was selected in this thesis as a benchmark magnetocaloric material due to its pronounced first-order antiferromagnetic-to-ferromagnetic phase transition near room temperature, which results in one of the largest reported magnetocaloric effects. Its well-studied magnetic behavior and strong magnetoelastic coupling make FeRh an ideal model system for investigating size effects, synthesis challenges, and processing strategies relevant to magnetocaloric materials. FeRh alloys have been extensively studied since the 1930s, following the pioneering work of Fallot. Near to equiatomic FeRh exhibits a unique magnetic phase transition near room temperature, shifting from an AFM state to a FM state upon heating past a critical temperature (300–350 K).(McKinnon, Melville, & Lee, 1970) This transition is isostructural, occurring within the ordered CsCl-type B2 structure, and is accompanied by a ~1% lattice expansion.(Shirane, Chen, Flinn, & Nathans, 1963b)

The AFM-to-FM transition in near to equiatomic FeRh is classified as a first-order phase transition, characterized by abrupt changes in entropy and magnetization. This transition is driven by complex magnetic and structural interactions, including exchange coupling between Fe and Rh atoms. Notably, Fe atoms exhibit a magnetic moment of ~3 μB in the AFM state, while Rh remains nearly nonmagnetic.(McKinnon et al., 1970; Shirane, Chen, Flinn, & Nathans, 1963a) In the FM phase, Rh develops a moment (~1 μB), further stabilizing the ferromagnetic order. This magnetoelastic transition is of particular interest for magnetocaloric applications, as it yields a significant entropy change (ΔS_M ≈ 16 J/kg·K) and adiabatic temperature changes(ΔT_{ad} ≈ 12.9 K) under a 2 T magnetic field.(Annaorazov et al., 1992) i.e. largest MCE that undergo first order phase transition. Under conditions of strong mechanical deformation or epitaxial strain imposed during thin-film growth, FeRh can adopt metastable crystallographic phases, such as the face-centered cubic (FCC) structure (γ-FeRh), which are not stable in the bulk equilibrium phase diagram.(Aschauer, Braddell, Brechbühl, Derlet, & Spaldin, 2016) This FCC phase exhibits distinct magnetic properties, including spin-glass behavior at low temperatures, and can revert to the B2 structure (i.e. sum of AFM and FM phase) upon annealing.

FeRh's AFM-to-FM transition near room temperature positions it as a benchmark material for solid-state cooling technologies. Its relatively high ΔS_M and reversibility under cyclic magnetic fields make it a promising candidate for refrigeration systems. Beyond cooling, FeRh's unique magnetic behavior is being explored in spintronics (Kang et al., 2023; Popescu, Rodriguez-Lopez, Haney, & Woods, 2018), heat-assisted magnetic recording (Huang & Victora, 2014; Vogler, Abert, Bruckner, & Suess, 2017), biomedical applications such as hyperthermia (Jordan et al., 1993; Pimentel et al., 2018) and targeted drug delivery (Amirov et al., 2025; Komlev, Gimaev, & Zverev, 2021).

Despite its exceptional magnetocaloric properties, the widespread use of FeRh is limited by the high cost and scarcity of rhodium.(L. Guo et al., 2023) Research efforts are focused on enhancing the performance of FeRh-based alloys, such as doping with other elements to reduce rhodium content (Rumiantsev et al., 2024) or stabilize desirable magnetic phases (J.-H. Park et al., 2024). Additionally, thin-film and NP forms of FeRh are being developed to harness its properties in micro-scale devices and applications requiring precise thermal management.

While bulk FeRh exhibits outstanding magnetocaloric properties, its integration into miniaturized, shape-defined, or locally addressable cooling elements requires the material to be processed in reduced dimensions. In particular, nanoparticle-based and printed architectures are of interest for applications involving localized thermal management and microscale devices. However, reducing FeRh to the nanoscale introduces additional challenges, including size-dependent phase stability, compositional control, and susceptibility to oxidation, which strongly depend on the employed synthesis route. Several studies have explored the synthesis of FeRh NPs using wet chemical methods, primarily focusing on achieving compositional control and desirable magnetic properties.(Cao et al., 2020; Diana Ciuculescu et al., 2007; D. Ciuculescu et al., 2007; Jia, Harrell, & Misra, 2008) These methods typically involve the co-reduction of Fe and Rh precursors in a solvent medium, often stabilized by surfactants such as oleic acid, oleylamine, or hexadecylamine, which help regulate particle size and dispersion. However, wet-chemical approaches often yield nanoparticles smaller than approximately 20 nm, where the large surface-to-volume ratio leads to a high fraction of surface atoms and, consequently, an increased susceptibility to surface oxidation. In FeRh nanoparticles, such oxidation and surface disorder can significantly suppress the antiferromagnetic-to-ferromagnetic phase transition and degrade the magnetocaloric response.

1.1.5.2 $Ni_{50}Mn_{50-x}Sn_x$ (Heusler alloy)

NiMnSn belongs to the class of Ni-Mn-based Heusler alloys, which have been widely investigated for their multifunctional properties, including MCEs (Dan et al., 2015), shape memory behavior (Scheibel et al., 2023), and magnetoresistance (Koyama et al., 2006). NiMnSn exhibits a first or second order martensitic transition, where the high-temperature austenitic phase transforms into a low-temperature martensitic phase.(Aydogdu et al., 2016; Datta & Kar, 2022; Tao et al., 2012) This transition is strongly coupled to magnetic ordering, enabling an inverse MCE. The material undergoes a metamagnetic transition, where an applied magnetic field can induce a phase change from a weakly magnetic or AFM martensitic phase to a FM austenitic phase. This results in a significant change in entropy, making NiMnSn a promising candidate for magnetic refrigeration applications. Reports indicate that NiMnSn can achieve ΔS_M up to 18 J/kg·K under a 5 T field, with ΔT_{ad} reaching 2.5 K, depending on the composition and processing conditions.(Krenke et al., 2005b) The ability to tune its transformation temperature by adjusting the Mn/Sn ratio further enhances its versatility for room-temperature cooling applications.(Xuan et al., 2015). Among the Ni-Mn-Sn compositions, Heusler-type alloys with the stoichiometry of $Ni_{50}Mn_{50-x}Sn_x$ (at. %; for 13 at. % < x < 15 at. %) have been identified as having particularly favorable magnetocaloric properties producing an inverse MCE nearly three times larger than that of Ni-Mn-Ga-based alloys (Krenke et al., 2005a). Additionally, increasing Mn content has shown to improve the magnetization and a large magnetization change of 44 Am^2/kg across the martensitic transformation was observed in $Ni_{37}Mn_{54}Sn_9$.(Tao et al., 2012) This tunability makes NiMnSn alloys highly versatile for room-temperature cooling applications. Compared to conventional rare-earth-based magnetocaloric materials such as Gd or LaFeSi alloys, NiMnSn offers the advantage of being rare-earth-free, reducing cost and supply chain dependency. Additionally, its strong magnetoelastic coupling allows for a high degree of tunability, enabling tailored transition temperatures for specific applications. However, like many first-order transition materials, NiMnSn alloys exhibit hysteresis effects, which can reduce cooling efficiency over repeated cycles.(Aydogdu et al., 2016) Additionally, Heusler alloy has severe grain boundary brittleness that hinders their application.(Meng, Xie, Yu, Wang, & Jiang, 2024) Recent efforts have focused on mitigating these effects through composition optimization (Xuan et al., 2015), thermal treatments (Kunzler, Schreiner, Bristoti, & BrandÃo, 1977), and advanced processing techniques (Sun et al., 2023). The use of additive manufacturing and rapid solidification techniques has been explored to refine microstructures and improve mechanical stability.(Rittinghaus et al., 2023).

At the nanoscale, NiMnSn has attracted interest due to the possibility of modifying its magnetic behavior through size and surface-related effects that are not accessible in bulk or microparticle form. Reducing the particle size introduces changes in surface-to-volume ratio, internal strain, and magnetic exchange interactions, which can significantly influence magnetic ordering, phase stability, and hysteresis behavior. NiMnSn nanoparticles have already been employed as magnetic precipitates in copper alloys, where their nanoscale dimensions contribute to enhanced mechanical strength and electromagnetic shielding. In related Heusler systems, such as Co_2FeAl, size reduction has been shown to influence key magnetic parameters, including M_s and T_c.(Ahmad, Mitra, Srivastava, & Das, 2019) This highlights the importance of studying the size-dependent magnetic properties of NiMnSn. For magnetocaloric applications in particular, nanoscaling is of interest as it may enable a reduction of thermal and magnetic hysteresis, improved reversibility of the martensitic transition, and enhanced heat transfer due to increased surface area. However, in NiMnSn, the strong coupling between composition and magnetic properties makes such effects difficult to assess without strict compositional control. Therefore, the synthesis of compositionally well-defined NiMnSn nanoparticles is essential to isolate genuine size effects from compositional variations. This motivates a systematic investigation of NiMnSn nanoparticles, focusing on how particle size reduction influences magnetic phase transitions and magnetocaloric behavior in comparison to composition-matched microparticles.

1.1.5.3 MnTX-based Compositionally Complex Alloys

MnTX-based CCAs have emerged as promising candidates for magnetocaloric applications due to their unique multi-element design, which enhances configurational entropy, stabilizes novel crystal structures, and enables tunable magnetic transitions. These alloys typically consist of Mn combined with various transition metals such as Fe, Ni, Co, and Cr, along with main group elements (X) such as Ge, Si, or Al, forming multi-principal element systems with exceptional magnetocaloric properties properties.(E. Liu et al., 2012; E. K. Liu et al., 2010; C. L. Zhang et al., 2009) Their potential stems from their ability to undergo magneto-structural phase transitions, which significantly influence their magnetocaloric performance. Compared to traditional rare-earth-based magnetocaloric materials, MnTX-based CCAs offer cost-effectiveness, high tunability, and better mechanical stability. The presence of Mn in these alloys provides the basis for strong magnetic interactions, while the additional elements contribute to fine-tuning the T_c, ΔS_M, and thermal hysteresis.

Among MnTX alloys, MnFeNiGeSi (Ge-based CCA) (Law et al., 2021) have attracted considerable interest due to their ability to undergo first-order magneto-structural transitions, exhibiting a large isothermal ΔS_M of approximately 7.3 J/kg.K under a moderate magnetic field of 2.5 T, making them among the best-performing rare-earth-free CCAs. Also, MnFeNiSiAl (Al-based CCAs) (Biswas et al., 2019) alloys demonstrate ΔS_M of up to 23 J/kg K under a field change of 2 T. These alloys undergo a structural transition between a PM hexagonal Ni_2In-type phase and a ferromagnetic orthorhombic TiNiSi-type phase, which can be tuned near room temperature by adjusting the Al concentration. This transition is highly sensitive to external hydrostatic pressure, offering a large barocaloric effect in addition to the MCE. The ability to fine-tune transition temperatures and magnetic properties by compositional control makes both Ge-based and Al-based CCAs highly attractive for solid-state magnetic refrigeration applications. Furthermore, their composition relies on earth-abundant and non-toxic elements, avoiding the supply risks associated with rare-earth-based magnetocaloric materials.

The central objective of this part of the thesis is to investigate whether the characteristic magneto-structural phase transitions observed in bulk MnTX-based CCAs can be preserved upon size reduction to the nanoscale. To this end, Ge- and Al-based CCA nanoparticles are synthesized with controlled compositions and their magnetic and magnetocaloric properties are systematically compared with those of their bulk counterparts. This comparative approach is designed to isolate size effects from compositional effects and to elucidate how nanoscaling influences phase stability, transition temperatures, and entropy changes. Additionally, this study will explore whether Al-based CCAs can serve as a viable alternative to Ge-based CCAs at the nanoscale, given that germanium is nearly a thousand times more expensive than aluminum, making this substitution highly economically advantageous.(Ramasamy & Hurd, 2021) To achieve this, a time- and cost-efficient production method will be employed to fabricate Al-based CCA targets, aiming to develop sustainable magnetic material at nanoscale. By addressing the economic challenges associated with costly elements and rare-earth materials, this research provides a pathway for developing functional magnetic materials at both bulk and nanoscale dimensions, contributing to the advancement of modern technological applications.

Among the various methods available for synthesizing CCA NPs, PLAL can be utilized to produce binary, ternary, and CCA NPs. The details of this method, including its mechanism, advantages, and its suitability for compositionally controlled NP synthesis, will be discussed in the next section

1.1.6. Pulsed laser ablation in liquid

Laser ablation in general has been widely used in material processing, micromachining, and thin-film deposition since the advent of pulsed lasers in the 1960s.(Maiman, 1960) Initially, nanosecond lasers were the primary tool for ablation processes, where long pulse durations allowed for gradual thermal diffusion into the material.(D. Zhang & Guan, 2014) With advancements in laser technology, ultrafast lasers, particularly femtosecond and picosecond lasers, became more favorable due to their ability to localize energy within extremely short timescales, reducing collateral damage and improving precision.(A. Liu et al., 2025) The ability to control material ejection at ultrafast timescales made laser ablation highly attractive for applications ranging from surface patterning to NP synthesis.

PLAL is a powerful and versatile technique for synthesizing NPs in a controlled and environmentally friendly manner.(Johny et al., 2022; Tahir et al., 2024; Waag et al., 2019) Unlike conventional chemical synthesis methods that require reducing agents, surfactants, and stabilizers, PLAL enables the production of ligand-free NPs, making them highly suitable for biomedical, catalytic, magnetic and electronic applications. (Fazio et al., 2020; Gökce et al., 2017; Dongshi Zhang, Gökce, et al., 2017) This method involves focusing high-energy laser pulses onto a solid target submerged in a liquid medium, where the intense energy input induces material removal, plasma formation, cavitation bubble dynamics, and NP condensation.

The mechanism of PLAL begins with the absorption of laser energy by the target, leading to rapid heating, vaporization, and plasma formation at the solid-liquid interface.(Dell'Aglio, Gaudiuso, De Pascale, & De Giacomo, 2015; Naddeo & Bubb, 2014) This plasma consists of highly energetic ions, electrons, and neutral atoms, which expand into the surrounding liquid. The intense thermal energy transfer to the liquid medium generates a cavitation bubble, which encapsulates the ablated material and plays a crucial role in NP formation. As the plasma cools, the vaporized material undergoes nucleation and growth, leading to NP formation within the bubble. This dynamic interaction between laser energy, plasma expansion, and bubble dynamics dictates the final NP characteristics.

The selection of pulse duration is a key factor in determining the efficiency and quality of NP synthesis in PLAL. Femtosecond and picosecond lasers differ in their interaction with materials and subsequent NP formation. In femtosecond and picosecond (less than 10 ps) ablation, the laser pulse duration is shorter than the electron-phonon relaxation time, leading to a non-thermal ablation mechanism where the energy is confined to the electrons before the lattice absorbs it.(L. Jiang, Wang, Li, Cui, & Lu, 2018) This results in explosive material ejection with minimal heat diffusion into the bulk. Compared to femtosecond pulses, picosecond laser pulses offer a practical advantage for large-scale NP production due to their higher ablation rate and increased mass removal per pulse in liquid environments, while still preserving non-thermal ablation characteristics. This higher ablation efficiency directly translates into larger NP yields per unit time, making picosecond lasers more suitable for synthesis routes where gram-scale quantities or continuous production are required.(Shaheen, Gagnon, & Fryer, 2013) The two-temperature model (2T model) is commonly used to describe ultrafast laser interactions with materials. In this model, the laser pulse initially excites the free electrons in the material, causing a rapid rise in electron temperature while the lattice remains relatively cool. Over time, the energy is transferred from the electrons to the lattice through electron-phonon interactions, leading to a delayed material response. The ablation threshold is the minimum fluence required to initiate material removal and as laser fluence increases beyond the threshold. The ablation rate initially rises due to more efficient material removal and ablation process shows maximum efficiency at an optimum fluence of e^2 times the corresponding ablation threshold fluence and at much higher fluence the ablation rate is gradually saturated.(Žemaitis et al., 2018; Dongshi Zhang & Wada, 2021)

The ablation of target leads to the production of NPs with varying particle sizes consisting of small and large particles (depending on the laser and scanning parameters, target properties and its interaction with the liquid). The formation of large and small NPs during PLAL is governed by two distinct mechanisms. The study by Shih et al., (Shih et al., 2018) explores these mechanisms in detail, revealing the underlying physical processes responsible for generating NPs of different sizes.The first mechanism involves the rapid nucleation and growth of small NPs within the metal-liquid mixing region formed during the ablation process. As the laser pulse strikes the solid target submerged in liquid, material is ejected, forming a dense, highly energetic plasma. This ablation plume expands and interacts with the surrounding liquid, leading to supercooling and condensation of vapor-phase species. The resulting metal atoms and small clusters rapidly nucleate within the expanding cavitation bubble, forming NPs typically in the size range of a few nanometers. This process is enhanced at shorter pulse durations (picoseconds to femtoseconds), where rapid cooling and condensation favor the formation of ultrasmall nanoparticles, often with a narrower particle size distribution. The second mechanism responsible for the formation of larger NPs is governed by hydrodynamic instabilities at the interface between the expanding plasma plume and the surrounding liquid. During the ablation process, molten droplets and fragments of the target material can be ejected due to hydrodynamic effects such as the Rayleigh-Taylor and Richtmyer-Meshkov instabilities. These instabilities cause the formation of nanojets from the molten layer, which subsequently break up into larger droplets, typically tens to hundreds of nanometers in size. These larger NPs are carried away from the ablation site by cavitation bubble collapse and interactions with the liquid environment.

One of the major advantages of PLAL is its ability to synthesize compositionally complex NPs, including binary, ternary, and HEA (as shown in Fig. 3), depending on the composition of the target material. Unlike chemical synthesis routes that require precise precursor ratios and reaction conditions, PLAL directly transfers the target composition to the NPs, making it an effective method for producing multicomponent alloys with controlled stoichiometry. This is particularly useful for HEAs, which consist of multiple principal elements and exhibit unique structural and functional properties. Furthermore, the rapid quenching inherent in PLAL can stabilize metastable phases that may not be achievable through conventional synthesis routes, further expanding the potential applications of laser-synthesized NPs.

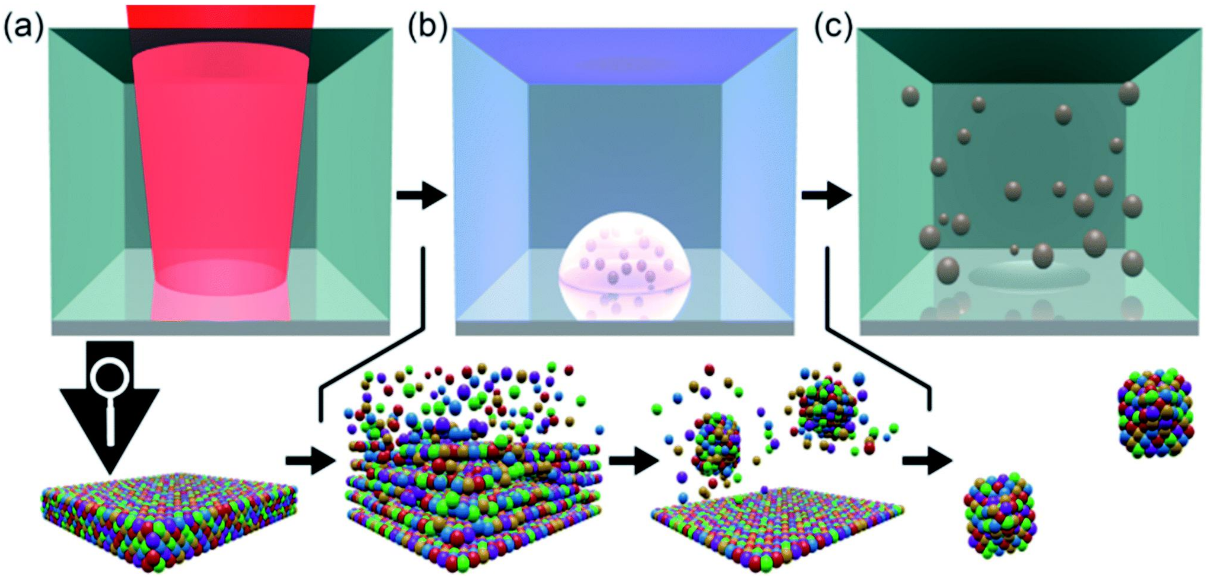

Figure 3. Qualitative representation of the PLAL of HEA target producing HEA NPs. The synthesis method consists of the following stages: (a) ultrashort-pulsed laser irradiation of the bulk HEA. (b) the atomization/ionization of the bulk causing the formation of a plume, and subsequent nucleation and condensation of the ablated matter in the vapor phase of the liquid. (c) and the colloidal HEA alloy NPs electrostatically stabilized in liquid. (Waag et al., 2019)

The produced NPs can be further processed to formulate nanoparticle inks that can be converted into structured microarchitectures using advanced printing technologies, enabling the fabrication of microcoolers, thermal switches, actuators, and sensors which will be further explored in the next section.

1.1.7. Nanoparticle ink printing

NP-based printing technologies have revolutionized the fabrication of functional microstructures, offering efficient and scalable methods for integrating NPs into a variety of applications, including solar cells (Dullweber et al., 2012; Hilali, Gee, & Hacke, 2007; Nguyen & Ito, 2013), biomedical devices (Wang et al., 2021; Xu et al., 2022; Zhou & Grayson), and energy storage systems (Montanino et al., 2021; Nazri et al., 2021; Yang, Li, Lee, & Fan, 2022). Inkjet and screen printing are widely used due to their simplicity and accessibility, enabling the direct deposition of NP inks onto substrates. However, these conventional techniques are often limited in terms of resolution, ink stability, and material compatibility. (Jones, Büttner, Chudasama, Wimpenny, & Krüger, 2012; Niittynen & Mäntysalo, 2014; S. Park, Kim, Kim, & Yeo, 2020) (Jones et al., 2012; Niittynen & Mäntysalo, 2014). Laser-based printing methods have emerged as a powerful alternative, providing micrometric spatial resolution (Hurtado et al., 2018; Kathuria, 1997; J. H. Park et al., 2022; Yuan, Liu, Zhang, Han, & Chen, 2018), and a fast processing speed (Nazir & Jeng, 2019; Roy, Behera, Dibua, Foong, & Cullinan, 2019). Additionally, the short processing time reduces the risk of oxidation for the metallic inks (Niittynen & Mäntysalo, 2014), negating the need for an inert gas atmosphere or vacuum setup during the process (Tumkin, Khairullina, Panov, Yoshidomi, & Mizoshiri, 2021).

The laser printing technique can be combined with ink deposition methods such as spin coating or inkjet printing to selectively sinter specific regions of a nanoparticle-coated substrate and thereby form continuous structures. A major challenge in nanoparticle ink printing is maintaining ink stability, since nanoparticles tend to agglomerate due to interparticle attractive forces. Therefore, careful ink formulation with suitable solvents and stabilizing agents is required to preserve a well-dispersed suspension. This is especially important in laser-based printing, where an inhomogeneous nanoparticle distribution can generate local variations in film thickness, particle packing density, and light absorption. These variations result in non-uniform heat generation during laser irradiation, which may lead to incomplete sintering or local overheating and, consequently, to structural defects in the printed features.

Laser irradiation results in localized heating of NPs which can lead to sintering improving the integrity of printed patterns that consolidate NPs into a solid microstructure, inducing densification and enhancing material adhesion. This process allows the formation of continuous conductive films, magnetic structures, and thermally stable layers, making it an essential step in the production of functional devices. The driving force behind sintering is the reduction of surface energy, which facilitates atomic diffusion and particle coalescence.(Dillon et al., 2023) The sintering kinetics are governed by several mass transport mechanisms, including surface diffusion, grain boundary diffusion, and lattice diffusion. However, these mechanisms do not affect the microstructure in the same way. Surface diffusion primarily promotes neck growth between adjacent particles without significant densification, whereas grain boundary diffusion and lattice diffusion can contribute to pore shrinkage and densification of the printed material.(Bruchon, Pino-Muñoz, Valdivieso, & Drapier, 2012) Thermodynamically, the process is driven by the curvature of particle surfaces, creating a potential gradient that promote material transport.(Al-Qudsi, Kammler, Bouguecha, Bonk, & Behrens, 2015) Depending on the material system and processing conditions, sintering can occur via solid-state or liquid-phase mechanisms. In solid-state sintering, particle bonding is achieved through atomic migration without the presence of a liquid phase, while in liquid-phase sintering, a transient liquid assists in particle rearrangement and densification. The transition between these sintering modes depends on factors such as temperature, material composition, and the presence of secondary phases. In laser sintering, the balance between sintering and ablation thresholds is crucial, as excessive energy input can lead to material removal rather than densification. The sintering threshold defines the minimum energy required to induce particle fusion, while the ablation threshold represents the point at which material vaporization occurs. Controlling these parameters ensures that the laser process enhances densification without causing unwanted structural damage.

In laser sintering, the effective energy input delivered to the nanoparticle layer is determined by the laser power, scanning speed, and beam diameter. For a moving laser beam, the applied fluence can be estimated as follows (Ermak et al., 2016)

$$F = \frac{4 \cdot P}{v_S \cdot d \cdot \pi} \tag{10}$$

where $F =$ laser fluence, $P =$ laser power, $v_s =$ scanning speed, and $d =$ laser spot diameter. This expression illustrates how the deposited energy per unit area increases with increasing laser power and decreases with increasing scanning speed or beam diameter. Accordingly, these parameters must be carefully adjusted to achieve sufficient nanoparticle sintering and densification while avoiding ablation, substrate damage, excessive thermal stress, or microcrack formation.

In the case of magnetocaloric materials, laser sintering is particularly attractive because it enables the consolidation of nanoparticle deposits into defined microstructures and can, depending on the material system, also influence phase evolution. This makes the process highly relevant for the fabrication of patterned functional structures for compact cooling devices, thermal management components, and sensor-related applications.

1.2. Initial work and developments

The research activities that preceded the main work of this thesis started with FeRh nanoparticles, motivated by the exceptional magnetocaloric potential of near-equiatomic FeRh and its first-order antiferromagnetic-to-ferromagnetic phase transition close to room temperature. In this early phase, I contributed as a coauthor to investigations on the synthesis, stabilization, and magnetic characterization of FeRh nanoparticles produced by pulsed laser ablation in liquid. These initial studies were particularly important because FeRh is highly sensitive to oxidation, stoichiometric deviations, and processing conditions, all of which strongly influence its structural and magnetic behavior and therefore its magnetocaloric performance.(Nadarajah et al., 2021; Nadarajah et al., 2020)

The earlier work focused first on establishing a suitable synthesis route for FeRh nanoparticles while minimizing oxidation and preserving a near-equiatomic FeRh composition. In this context, the influence of solvent environment, oxygen content, and ablation conditions on particle composition and phase stability was investigated. The results showed that monodisperse nanoparticles with mean particle sizes of about 14–15 nm could be obtained, while EDX and APT analyses indicated near-equimolar FeRh composition. In addition, oxidation could be significantly reduced by using oxygen-reduced solvents and inert processing conditions, which was further supported by Mössbauer spectroscopy and ferromagnetic resonance measurements.(Nadarajah et al., 2020)

Building on this, subsequent work examined the magnetic and magnetocaloric behavior of the FeRh nanoparticles and their suitability for further processing into structured materials. It was shown that annealing promoted the transformation of the metastable γ-FeRh phase into the ordered B2-FeRh phase, with XRD and magnetic measurements confirming a substantial increase in the B2 fraction and corresponding changes in magnetization. The magnetocaloric response was evaluated indirectly, revealing a broadened and reduced entropy change compared with bulk FeRh, which reflects the strong effect of nanoscaling on the phase transition. In addition, preliminary laser processing demonstrated the potential of integrating FeRh nanoparticles into structured magnetocaloric microfeatures.(Nadarajah et al., 2021)

Although these FeRh investigations are not part of the main original studies presented in this thesis, they provided important scientific and methodological groundwork. In particular, they established experience in nanoparticle synthesis by PLAL, oxidation-sensitive alloy processing, phase transformation analysis, and magnetic characterization, which helped shape the later research direction toward more complex magnetocaloric nanoparticle systems.

1.3. Research Questions and Scope of the Thesis

Initial studies have demonstrated that near-equiatomic FeRh can be achieved with minimal oxidation when synthesized using pulsed laser ablation in organic solvents. While this synthesis route resulted in the formation of the PM γ-FeRh phase, an annealing step is required to induce the B2 phase, which is crucial for magnetocaloric applications. In parallel, preliminary investigations into laser sintering have shown that magnetocaloric structures can be fabricated, although the achievable feature size remains limited to the millimeter range. Since practical miniaturized thermal-management applications require much finer structures, an important objective is to determine whether these features can be reduced to the micrometer scale while preserving the relevant magnetic and functional properties. These findings point to several open questions regarding phase formation, material complexity, and the miniaturization of functional magnetocaloric structures, which define the scope of this thesis.

RQ 1: Is it possible to extend PLAL beyond binary systems to successfully synthesize ternary and HEA/CCA NPs?

Moving beyond simple alloy systems to multicomponent HEA/CCAs can enhance tunability in magnetic and structural properties. Understanding whether PLAL can precisely control the formation of CCAs will determine its feasibility as a scalable technique.

RQ 2: Can rare-earth-free magnetocaloric CCAs NPs be synthesized that exhibit low-to-room temperature magnetic transitions?

The search for rare-earth-free magnetocaloric materials is crucial for sustainable refrigeration technologies. Developing CCAs with tunable phase transitions can provide viable alternatives to conventional rare-earth-based materials.

RQ 3: How do the structural and magnetic properties of nanoparticles differ from those of their bulk and microparticle counterparts, and how do these differences influence their functional behavior?

The effect of increasing surface to volume ratio and quantum confinement effect influences their structural, magnetic, and functional properties compared to bulk and MP counterparts and can unlock new applications making NPs more versatile and efficient for next-generation technologies.

RQ 4: Can laser sintering be used to control phase transformations and tailor the magnetic functionality of magnetocaloric materials while enabling their miniaturized fabrication?

Laser sintering offers not only a route for fabricating magnetocaloric structures at the micron scale, but also a means to influence phase constitution, microstructure, and magnetic behavior. Understanding how laser processing parameters affect phase transformation, functional properties, and printing resolution is essential for bridging the gap between lab-scale demonstration and application-oriented miniaturized devices.

In the scope of these 4 research questions, the following questions can be derived

How can the γ-FeRh to B2 phase transition be controlled and optimized through laser sintering? Achieving a controlled γ → B2 transformation is vital for tuning magnetocaloric properties. Determining the optimal laser parameters to induce this transition without compromising structural integrity is a key challenge.

Can laser sintering enhance the AFM-FM transition in FeRh NPs, and how does it compare to bulk materials? The AFM-FM transition is fundamental for the MCE. Exploring whether laser sintering can surpass traditional annealing methods in enhancing this transformation could unlock superior material performance.

How do different target preparation methods influence the composition and phase stability of CCAs? The fabrication of CCA targets plays a crucial role in achieving homogeneity in the final NPs. Identifying the effects of powder pressing and heat treatment, mechanical alloying via high energy ball milling, and bulk homogenization via arc melting for polycrystalline target or Bridgeman method for single crystal target will help optimize material synthesis.

What underlying mechanisms contribute to compositional inhomogeneity in CCAs, and how can they be mitigated? Elemental segregation and vaporization loss during PLAL can lead to undesired variations in composition. Investigating diffusion dynamics and ablation mechanisms will be crucial in maintaining phase stability.

How can PLAL productivity of HEA/CCA NPs be enhanced while maintaining composition control? Identifying strategies such as varying repetition rate, multi-beam ablation, and optimized target design will be essential for large-scale NP production.

Can rare-earth-free magnetocaloric CCAs that exhibit low-to-room temperature phase transitions be synthesized? The search for rare-earth-free magnetocaloric materials is crucial for sustainable refrigeration technologies. Developing CCAs with tunable magnetic transitions can provide viable alternatives to conventional rare-earth-based materials.

How do key magnetic and magnetocaloric parameters such as transition temperature, saturation magnetization, coercivity, and hysteresis of NPs compare with those of their bulk and MP counterparts? Nanostructuring significantly impacts magnetic and thermodynamic behavior. Investigating how NPs properties deviate from bulk/MP characteristics will provide insights into nanoscale effects on magnetocaloric performance.

What strategies can be employed to achieve compositionally controlled synthesis of NPs, given the disparity in melting and vaporization temperatures of its constituent elements? The difference in the volatility and ionization potential poses significant challenges in maintaining the target stoichiometry during ablation. Optimizing laser parameters, target design and composition could offer solutions for stabilizing and controlling the composition during synthesis.

How do variations in composition affect the NPs magnetocaloric properties? Small deviations in stoichiometry can significantly alter T_c, magnetic transition, and phase stability. Evaluating the trade-offs between compositional precision and functional performance will refine synthesis protocols.

How does particle size (nanoparticles vs microparticles) affect laser sintering behavior, achievable feature resolution, phase constitution, and magnetic response? Sintering kinetics vary with particle size, affecting grain growth, defect formation, and interfacial bonding. Identifying the optimal sintering conditions for particle size in nanometer and micrometer range will enhance the fabrication of functional microstructures.

By addressing these critical research questions, this thesis seeks to push the boundaries of laser-based NP synthesis and processing, paving the way for novel applications in magnetocaloric refrigeration, microelectronics cooling, and advanced functional materials.

1.3.1. Studies

The research gaps identified in this thesis have been investigated and addressed in four key studies:

1. **Shabbir Tahir**, Joachim Landers, Soma Salamon, David Koch, Carlos Donate-Buendía, Anna R. Ziefuß, Heiko Wende, and Bilal Gökce "Development of Magnetocaloric Microstructures from Equiatomic FeRh Nanoparticles through Laser Sintering" Advanced Engineering Materials (2023). DOI: 10.1002/adem.202300245

This study focuses on fabricating FeRh magnetocaloric structures using laser sintering and investigates phase transformations at microscale resolution.

2. **Shabbir Tahir**, Natalia Shkodich, Benedikt Eggert, Johanna Lill, Oleksandr Gatsa, Miroslava Flimelová, Esmaeil Adabifiroozjaei, Nadezhda M. Bulgakova, Leopoldo Molina-Luna, Heiko Wende, Michael Farle, Alexander V. Bulgakov, Carlos Doñate-Buendía, and Bilal Gökce "Synthesis of High-Entropy Alloy Nanoparticles by Pulsed Laser Ablation in Liquids: Influence of Target Composition and Ablation Parameters" ChemNanoMat (2024). DOI: doi.org/10.1002/cnma.202400064

   This study explores the synthesis of HEA NPs via PLAL and examines the effects of target composition and laser parameters on NP properties.

3. **Shabbir Tahir**, Tatiana Smoliarova, Carlos Doñate-Buendía, Michael Farle, Natalia Shkodich and Bilal Gökce. " Synthesis and magnetic transitions of rare-earth-free Fe–Mn–Ni–Si-based compositionally complex alloys at bulk and nanoscale''. (2025). Beilstein J. Nanotechnol, 16, 823–836. DOI: https://doi.org/10.3762/bjnano.16.62
   This research investigates the synthesis and magnetocaloric properties of CCA NPs, aiming to develop a rare-earth-free alternative for cooling applications.
4. **Shabbir Tahir**, Franziska Scheibel, Carlos Doñate-Buendía, Zongwen Fu, David Koch, Markus Heidelmann, Wolfgang Donner, Oliver Gutfleish, and Bilal Gökce. "Compositionally Controlled Synthesis and Magnetic Properties of NiMnSn Heusler Alloy Nanoparticles " (To be submitted to a high-impact journal in the field of materials science).

   This study addresses the challenge of achieving compositional control in NiMnSn Heusler alloy NPs and evaluates their magnetic and magnetocaloric properties.

1.3.2. Journal Details

- The first study is published in the Journal of Advanced Engineering Materials, which is an internationally recognized journal that publishes cutting-edge research on novel materials and their engineering applications, with a focus on structural, functional, and smart materials. According to SCImago Journal Rank (SJR), it is classified as a Q1 journal in Condensed Matter Physics and Q2 in Materials Science (miscellaneous), with an SJR of 0.76 and an impact factor of 3.76 as of 2024.

- The second study is published in the Journal of ChemNanoMat, which is a leading journal in the field of nanomaterials and chemical synthesis, covering fundamental and applied research in chemical nanotechnology. As per SJR, it falls under Q2 in Biomaterials, Energy Engineering and Power Technology, Materials Chemistry, and

Renewable Energy, Sustainability and the Environment, with an SJR of 0.645 and an impact factor of 2.6 as of 2024

- The third study is publshed in the Beilstein Journal of Nanotechnology, which is a high-quality, open-access journal that publishes research on nanoscale materials and their applications in nanoscience and nanotechnology. According to SJR, it is categorized as Q2 in Electrical and Electronic Engineering, Materials Science (miscellaneous), Nanoscience and Nanotechnology, and Physics and Astronomy (miscellaneous), with an SJR of 0.435 and an impact factor of 2.6 as of 2023
- A high-impact materials science journal will be selected for the submission of the fourth study, ensuring maximum visibility and academic impact

By systematically addressing these research gaps across four studies, this thesis contributes to advancing knowledge in magnetocaloric materials, HEA alloys, and laser-based NP synthesis, with direct applications in next-generation cooling and energy-efficient technologies.

2. Summary of Studies

This section provides a concise summary of each study which includes an overview of the research, the aim of the study, the experimental or analytical approach used, and the main results obtained.

2.1. Summary of Study 1: Laser structuring of FeRh nanoparticle inks

2.1.1. Study Overview

The first study focuses on the fabrication of FeRh-based magnetocaloric microstructures via laser sintering of NPs. While PLAL has previously been used to synthesize FeRh NPs with near-equiatomic composition, a key challenge remained: achieving a phase transition from the metastable γ-FeRh to the magnetically ordered B2 phase while maintaining structural integrity at microscales. This study aimed to bridge this gap by exploring CW laser sintering as a means to fabricate functional microstructures while tuning the magnetic phase of FeRh NPs.

2.1.2. Aim of the Study

The primary aim of this study was to investigate the feasibility of laser sintering for direct-write fabrication of FeRh magnetocaloric microstructures and to determine whether laser-induced thermal processing could effectively transform FeRh NPs from the PM γ-phase to the desired B2 phase while preserving their magnetocaloric functionality. Specific objectives included:

- Develop a method to employ PLAL synthesized FeRh NPs to achieve high concentration ink and achieve uniform dispersion
- Improving the resolution limits of CW laser printing in fabricating FeRh-based microstructures i.e., from millimetric to micrometric scale
- Evaluating whether the γ-FeRh to B2 transformation can be controlled through localized laser heating
- Comparing the phase transition and magnetic response of FeRh sintered structures and annealed FeRh NPs
- Comparing the magnetocaloric phase transition of FeRh sintered structure with annealed FeRh NPs

- Assessing the effects of laser-induced phase transformation on structural integrity and functional performance
- Establishing the viability of laser-printed FeRh microstructures for potential applications in micro-cooling devices

2.1.3. Methods

The study employed a multi-step experimental approach, combining NP synthesis, laser printing, structural characterization, and magnetic measurements.

2.1.3.1. FeRh NP synthesis and formulation of FeRh NP Ink

The synthesis was carried out using a $Fe_{50}Rh_{50}$ bulk target in ethanol. A near-infrared picosecond-pulsed Nd:YAG solid-state laser (Ekspla, Atlantic Series) was employed for ablation, operating at a wavelength of 1064 nm, with a pulse duration of 10 ps, a repetition rate of 100 kHz, and a pulse energy of 80 µJ. The laser beam was focused on the target's surface using an f = 100 mm lens, while the surface was scanned at a speed of 2 m/s to ensure uniform ablation.

The synthesized FeRh NPs were suspended in ethanol to form a colloidal solution, which was then concentrated by partial evaporation of ethanol at room temperature using a 64 W axial fan with a flow rate of 925 m^3/h. To prepare the substrate for deposition, glass slides were treated in a UV cleaner for 5 minutes to remove organic contaminants. A polymer coating was applied by adding 200 µL of 10 wt% polyvinylpyrrolidone (PVP, MW = 40k) in ethanol onto a 25 × 75 mm glass substrate. To prevent NP agglomeration, the FeRh ink was ultrasonicated for 10 minutes before dispersion. Finally, 100 µL of the ink was deposited onto a ~25 × 15 mm polymer-coated glass substrate for further applications.

The size distribution of the FeRh NPs was analyzed using SEM in STEM mode.

2.1.3.2. Sintering of FeRh NP ink

For FeRh furnance sintering, the FeRh NP ink was heat-treated in a programmable furnace under argon flow (Fig. 1d, Appendix: Study 1). The glass substrates containing the deposited ink were heated at a controlled rate of 10 K/min until reaching a maximum temperature of 873 K, where they were held for 1 hour. After the heating cycle, the furnace was switched off, allowing the substrates to cool gradually to room temperature within the chamber.

For laser sintering a CW laser (Laser Quantum, 532 nm) was used in combination with a programmable two-axis linear stage (Thorlabs DDSM100/M). The laser beam was focused using a 10× Mitutoyo microscope objective, and the substrate was scanned along a single axis to produce a sintered line. To characterize larger sintered areas, successive parallel lines were processed using the X-Y programmable stage, ensuring uniform laser irradiation over the entire ink-deposited region. Custom sintering patterns were achieved by controlling movement along both the X and Y axes.

After laser sintering, the substrate was immersed in an ethanol bath and ultrasonicated for 5 minutes, removing non-sintered ink and polymer residues.

The laser fluence was adjusted to explore the optimal sintering window and was calculated using equation 10 (mentioned in section 1.7, Appendix: Study 1).

For all experiments, the scanning speed was fixed at 10 mm/s, while the laser fluence was varied between 16 and 246 J/cm² to study its impact on sintering behavior. The sintered microstructures were analyzed using optical microscopy (Leica DM2700 M) and SEM (Apreo S LoVac, Thermo Fisher Scientific). The line width of the sintered structures was measured at ten different positions using ImageJ software.

At high fluences, laser processing led to simultaneous ablation and sintering, increasing the porosity of the magnetocaloric structures. The effect of laser-induced ablation on FeRh NP ink was monitored using reflectance spectroscopy. (Fig.S3, Appendix: Study 1)

2.1.3.3. Structural and Magnetic Characterization

To compare the effects of laser and furnace sintering on the FeRh crystal structure, XRD was performed in θ–2θ geometry using a Philips PW1730 X-ray diffractometer with Cu-Kα radiation and a graphite monochromator. Rietveld refinement (Fullprof suite) was used to quantify the phase composition, particularly the formation of the B2-ordered FeRh phase.

To assess the sintering conditions that yielded the highest B2-phase fraction, magnetometry measurements were conducted. M-H curves were obtained using a vibrating-sample magnetometer (VSM) option of a PPMS DynaCool (Quantum Design), measuring in the temperature range 5–400 K and extending up to 500 K using a VSM oven option. M-T measurements were performed between 150 and 700 K under an applied field of 0.1 T, with corrections applied to account for the diamagnetic and PM contributions from the glass substrate background signal.

2.1.4. Results

2.1.4.1. Sintering Behavior of FeRh NP Ink

The sintering process of FeRh NP ink was investigated under different laser fluence conditions (Fig. 2, Appendix: Study 1). At lower fluences, partial sintering resulted in a discontinuous pattern with both sintered and non-sintered regions. As the fluence increased above 16 J/cm², the NPs began forming necks and percolation networks. At 41 J/cm², the NPs fully sintered into a continuous and dense magnetocaloric structure. A further increase in fluence to 57 J/cm² led to the formation of compact agglomerates indicating pronounced particle coalescence and grain growth.

At high fluences, ablation occurred alongside sintering, particularly in the central region of the laser spot, where laser intensity was highest. This resulted in networked structures rather than continuous NP films. Further increasing the laser fluence led to more pronounced ablation and a reduction in overall NP density, creating porous structures. These porous features have potential advantages in improving convective heat transfer for magnetocaloric applications.

A comparison with furnace sintering at 873 K for 1 hour revealed that furnace-sintered NPs formed more compact structures due to slow heating and uniform temperature distribution (Fig 3, Study 1). The gradual heating promoted more homogeneous densification and uniform sintering, but also increased the risk of surface oxidation, which could negatively affect the mechanical and magnetic properties.

2.1.4.2. Crystallographic and Magnetic Features of FeRh sintered ink

Annealing FeRh NPs induces a transformation from the γ-phase to the B2-phase, which is critical for enhancing magnetic and magnetocaloric properties. Furnace annealing in air at 873 K led to full oxidation into Fe_2O_3 (hematite), while annealing in an argon atmosphere resulted in a mix of B2- and γ-phases with minor Fe_3O_4 (magnetite) contributions. (Fig. 5, Table 1, Appendix: Study 1)

Higher laser fluences during laser printing promotes an increase in B2-phase fraction while reducing the γ-phase and no visible oxide formation, demonstrating that laser sintering not only enhances γ-to-B2 transformation but also offers better oxidation resistance than furnace sintering. This is particularly significant since laser sintering occurs in air, eliminating the need for expensive inert gas environments. Additionally, the high fluences led to NP ablation and micropore formation, which could facilitate heat transfer in magnetocaloric regenerators.

Magnetometry measurements further validated the structural analysis (Fig. 6, Appendix: Study 1). Field-dependent magnetization curves at 500 K showed an increase in M_S with rising fluence, indicating a partial transformation from PM γ-FeRh to FM B2-FeRh. At fluences below 131 J/cm², a different magnetic alignment behavior was observed in the low-field region, likely due to partial oxidation leading to a magnetite/maghemite phase. A strong correlation between the B2-phase fraction and magnetization at 500 K was observed, with deviations in oxidized samples due to the presence of magnetite.

A comparison with furnace-annealed FeRh ink (Fig. 7, Appendix: Study 1) revealed that oxidation in air led to hematite formation, reducing magnetization. Annealing in argon preserved the magnetic structure, showing a steady increase in magnetization with temperature due to γ-to-B2 conversion. Laser sintering resulted in higher mass magnetization than furnace sintering while enabling direct patterning of FeRh structures. Despite achieving high B2-phase fractions, some FeRh material remained pinned in a FM state, similar to previous studies on furnace-annealed FeRh NPs.

2.1.4.3. Magnetocaloric Response of FeRh sintered ink

Laser-sintered FeRh ink at 246 J/cm² exhibited notable magnetization even below the AFM phase transition at 150 K, indicating a fraction of pinned FM order (Fig.8, Appendix: Study 1). This could result from slight stoichiometric variations during NP synthesis, as small changes in Fe content can shift the AFM-FM transition temperature or even stabilize FM behavior. Additionally, structural defects induced by laser ablation may contribute to FM ordering.

Temperature-dependent magnetization measurements indicated a broad AFM-FM transition starting around 150-200 K, with a peak transition temperature at approximately 460 K (Fig S4, Appendix: Study 1). At 400 K, a M_S of about 98 Am²/kg was reached at high fields, with a field-driven magnetization increase of approximately 35 Am²/kg, significantly higher than values observed for furnace-annealed FeRh. The laser sintering route, therefore, provides superior field-driven magnetization changes, highlighting its potential for magnetocaloric applications.

2.1.4.4. Custom Microstructures via Laser Sintering of FeRh ink

Laser sintering at 246 J/cm² led to higher conversion to magnetic phases while minimizing FeRh oxidation compared to furnace sintering. The rapid heating and cooling characteristic of laser sintering helped preserve FeRh composition and structure. Furthermore, the high spatial resolution and flexibility of laser processing enabled the fabrication of custom magnetocaloric microstructures (Fig. 9, Appendix: Study 1).

Following the laser processing, unsintered ink was easily removed using ethanol, leaving behind well-defined sintered structures. The ability to directly pattern FeRh thin films with precise control over microstructure and magnetic properties makes laser sintering a promising technique for miniaturized cooling applications in electronic devices. Compared to conventional furnace sintering, laser sintering allows for rapid, localized heating and patterning, reducing processing time while maintaining high-performance magnetocaloric properties.

2.2. Summary of Study 2: Effect of Target preparation on High Entropy Alloy nanoparticle synthesis via Pulsed laser Ablation in Liquids

2.2.1. Study Overview

This study investigates the synthesis of HEA NPs using PLAL and evaluates how different target preparation methods affect NP composition and productivity. HEAs, known for their unique mechanical, magnetic, and catalytic properties, have diverse applications, yet their NP synthesis remains challenging due to elemental immiscibility and phase segregation.

The research explores three distinct HEA target preparation methods:

1. Elemental Powder-Pressed Heat-Treated Target (HEA-PP) - A cost-effective approach where elemental powders are mixed, pressed, and heat-treated to form a bulk target

2. Ball-Milled Hot-Pressed Powder Target (HEA-BP) - A method where elemental powders are first alloyed via high-energy ball milling before being consolidated by hot pressing

3. Single-Crystal Alloy Target (HEA-SX) - A method involving the melting and controlled crystallization of high-purity elements to produce a single-crystal HEA structure

NPs were synthesized by ablating these targets in ethanol using a near-infrared picosecond pulsed Nd:YAG laser. The study examines the influence of target crystallinity, elemental homogeneity, and preparation method on NP yield, stoichiometry, and phase stability. The composition, structure, and oxidation of the produced HEA NPs were analyzed using TEM-EDX, XRD, Mössbauer spectroscopy, and MS.

2.2.2. Aim of the Study

The primary goal of this study is to determine how the preparation method of HEA targets affects the composition, productivity, and structural properties of HEA NPs synthesized via PLAL. The key objectives include:

- Evaluating the effect of target crystallinity and elemental homogeneity on NP generation
- Investigating the stoichiometric variations and phase formation in NPs produced from different targets
- Comparing the productivity and efficiency of PLAL when using HEA-PP, HEA-BP, and HEA-SX targets
- Assessing the oxidation behavior of HEA NPs and their structural characteristics
- Establishing PLAL as a scalable and cost-effective approach for producing compositionally controlled HEA NPs

By addressing these aspects, the study aims to provide insights into optimizing HEA NP synthesis, improving stoichiometric control, and enhancing the efficiency of PLAL for scalable production.

2.2.3. Methods

2.2.3.1. Fabrication of CoCrFeMnNi HEA Targets

The CoCrFeMnNi HEA targets were prepared using three different fabrication methods (Fig 1, Appendix: Study 2) and each method aimed to produce targets with equiatomic composition while varying the degree of elemental homogeneity and crystallinity.

For the HEA-PP targets, elemental Co (99.8%, 1.6 μm), Cr (99.2%, <10 μm), Fe (99.5%, 6-10 μm), Mn (99.6%, <10 μm), and Ni (99.9%, 3-7 μm) powders were accurately weighed to achieve an equiatomic ratio. The powders were manually mixed using a mortar and pestle for 20 minutes to ensure uniform distribution. The homogenized powder was then compressed under 100 MPa to form cylindrical pellets with a thickness of 2 mm and a diameter of 10 mm. The pellets were subsequently heat-treated in a vacuum atmosphere at 1000°C for 20 hours to promote diffusion and alloying, leading to the formation of a face-centered cubic (FCC) HEA structure.

The HEA-BP targets were synthesized using a two-step process. First, the elemental powders of Co (99.7%, mean particle size 3 μm), Cr (99.35%, >71 μm), Fe (99.96%, 10-20 μm), Ni (99.5%, 45-60 μm), and Mn (99.2%, 3 μm) were subjected to high-energy ball milling (HEBM) in an argon environment for 60 minutes. This resulted in nanocrystalline FCC HEA micropowders with increased homogeneity. The milling was conducted at a ball-to-powder weight ratio of 20:1, with sun disk and jar rotation speeds of 700 rpm and 1400 rpm, respectively. In the second step, the processed HEA powder was consolidated via hot pressing at 800°C for 60 minutes under an argon atmosphere. The powder was placed in a cylindrical graphite die with a diameter of 50 mm and subjected to uniaxial compression at 50 MPa to form dense targets with a final thickness of approximately 3 mm.

For the HEA-SX targets, single-crystal CoCrFeMnNi alloys were prepared through arc melting of high-purity bulk elements (>99.9%) under an argon atmosphere at a pressure of 5×10^{-4} Pa. The melted material was then cast into a single crystal using the Bridgman investment casting method. This involved melting multiple arc-melted buttons at approximately 1600°C in a shell-molded material, followed by controlled solidification under a thermal gradient of 6 K/mm at a withdrawal rate of 3 mm/min. The resulting single-crystal rods had a diameter of 15 mm and a length of 130 mm. These rods were subsequently cut into 2 mm thick pellets using wire-electrical discharge machining. Post-processing included etching the samples to confirm the absence of grain boundaries and ensure the single-crystalline nature of the material.

To assess target morphology, composition, and homogeneity, SEM with EDX analysis were performed on both ablated and non-ablated regions (Fig.3, Appendix: Study 2). The non-ablated regions provided insight into the initial elemental distribution, while the ablated areas were examined to understand laser-induced modifications.

2.2.3.2. Laser-Based Synthesis of Colloidal CoCrFeMnNi High-Entropy Alloy Nanoparticles

CoCrFeMnNi NPs were synthesized using PLAL, employing a near-infrared picosecond-pulsed Nd:YAG laser (Coherent, HyperRapid NX) with a pulse duration of 10 ps and a wavelength of 1064 nm (Fig. 2, Appendix: Study 2). The laser beam was focused using an f-theta lens (f = 167 mm) and controlled by a galvanometric scanner, which generated a 6 mm-diameter hollow spiral pattern on the target surface at a scan speed of 10 m/s. Ethanol was used as the liquid medium to promote NP formation and stabilize the generated colloids.

To prevent excessive laser shielding effects due to particle accumulation, a gear pump was utilized to maintain continuous liquid flow at a rate of 100 ml/min. This ensured uniform ablation conditions, improved NP dispersion, and minimized re-deposition onto the target surface. The laser fluence and repetition rate were optimized to maximize NP productivity while maintaining stoichiometric balance.

2.2.3.3. Characterization of CoCrFeMnNi Nanoparticles

The NPs synthesized from each target were subjected to detailed characterization to evaluate their production rate, size distribution, morphology, elemental composition, crystallinity, and oxidation state.

The production rate was measured (by varying the repetition rate) gravimetrically by determining the mass loss from the target before and after ablation and normalizing it to the ablation time. To analyze NP morphology and size, TEM was performed using a JEOL JEM-2200FS microscope equipped with a ZrO_2/W emitter and a JEOL JEM-2100 microscope with a LaB_6 gun. For TEM sample preparation, the colloidal NPs were drop-cast onto copper grids and dried under ambient conditions.

The crystal structure of the NPs was examined using XRD performed on a Huber G670-360 Gunier-Camera with Mo-Kα1 radiation. The oxidation state and magnetic properties of the NPs were investigated via ^{57}Fe-Mössbauer spectroscopy, conducted on dried powder samples in zero-field conditions. Mössbauer spectra were recorded in transmission geometry using a constant acceleration mode at 4.3 K within a closed-cycle helium cryostat (SHI-850-5, Lake

Shore Cryotronics). The elemental composition of the NPs was determined by TEM-EDX, which provided detailed elemental distribution maps.

2.2.3.4. Investigation of Ablation Dynamics in CoCrFeMnNi HEAs via Time-of-Flight Mass Spectrometry

To gain deeper insights into the ablation dynamics and material ejection mechanisms TOF-MS was performed in a vacuum environment. The three HEA targets (HEA-PP, HEA-BP, and HEA-SX) were simultaneously placed in a vacuum chamber with a base pressure of 10^{-6} mbar. Laser ablation was carried out at a 45° incidence angle using a Yb:KGW PHAROS laser (1030 nm, 2 kHz, 7 ps pulse duration). The laser beam was focused using a glass lens (f = 400 mm) onto a circular spot with an effective radius of 150 µm ($1/e^2$ criterion), and the fluence was varied from 0.2 to 3 J/cm². The beam was scanned over the target surface in a zig-zag pattern, covering an area of 10 × 8 mm².

The TOF-MS analysis was conducted using a customized mass spectrometer (Kore Technology, UK) to measure the abundance and velocity distributions of laser-produced particles. At a distance of 46 cm from the target, the positive ions of the ablation plume were extracted using a 760-V repeller pulse and directed into the mass spectrometer drift tube. The ions, covering a mass-to-charge range of 6 – 600 u/e, were detected in analog mode using a dual microchannel-plate detector connected to a digital oscilloscope (DSOS054A, Keysight, USA). The time delay between the repeller and laser pulse was varied to analyze the velocity distributions of the emitted particles. Mass spectra were averaged over 200 laser pulses to ensure statistical reliability.

The TOF-MS analysis provided critical insights into the compositional deviations in the ablation plume, revealing differences in the vaporization behavior of individual elements. The results were used to interpret the stoichiometric variations observed in the synthesized NPs and to evaluate the effects of target preparation on ablation dynamics.

2.2.4. Results

2.2.4.1. Elemental Composition of CoCrFeMnNi Targets

The elemental distribution in the HEA-PP target was non-uniform, with Mn and Cr concentrations reaching 28 ± 9 at.% and 32 ± 12 at.%, respectively (of desired 20 at.%), indicating significant segregation. In contrast, HEA-BP and HEA-SX showed a more homogeneous composition, with Cr deviations of 22 ± 2 at.% and 20 ± 2 at.%, respectively. The ablation process resulted in a notable reduction in Mn content, with Mn concentrations in the ablated regions measured at 12 ± 4 at.% for HEA-PP, whereas HEA-BP and HEA-SX exhibited more consistent Mn content at 22 ± 1 at.% and 23 ± 1 at.%. These variations suggest that the initial target structure plays a key role in the ablation dynamics, influencing the elemental loss during PLAL.

2.2.4.2. CoCrFeMnNi Nanoparticle Productivity via Pulsed Laser Ablation in Liquid

The NP production rate peaked at 311 mg/h when using an optimized laser fluence of 2.8 J/cm² and a repetition rate of 2000 kHz (Fig. 4, Appendix: Study 2). The ablation threshold fluence for HEA-PP was determined to be 0.38 J/cm², which is higher than the reported 0.24 J/cm² for crystalline HEA. Notably, HEA-PP exhibited the highest NP productivity, surpassing HEA-BP by 6.8% and HEA-SX by 15.1%. The increased productivity of HEA-PP can be attributed to the differences in material mixing, diffusion, and sintering, which affect the ablation efficiency. HEA-SX, being a single-crystal material, had the lowest productivity, likely due to its higher structural integrity and resistance to laser-induced fragmentation.

2.2.4.3. CoCrFeMnNi Nanoparticle Size Distribution

The laser ablation of HEA targets generated NPs with a broad size distribution between (2 – 120 nm) (Fig.5, Appendix: Study 2). The mean NP sizes were 8.6 nm for HEA-PP, 6.8 nm for HEA-BP, and 6.2 nm for HEA-SX. The polydispersity index exceeded 0.3 in all cases, indicating a significant spread in particle sizes. The larger average particle size in HEA-PP-derived NPs could be linked to the non-uniform elemental distribution in the target, which likely affects the laser-induced melting and condensation process. HEA-BP and HEA-SX, with more homogeneous elemental distributions, resulted in smaller NPs with relatively uniform sizes. This suggests that the target microstructure influences the energy absorption and vaporization dynamics, ultimately shaping the size distribution of the NPs.

2.2.4.4. Elemental Composition of CoCrFeMnNi Nanoparticles

NPs synthesized via PLAL retained a near-equiatomic composition but exhibited compositional fluctuations among individual particles (Fig. 6, Appendix: Study 2). Large NPs (>20 nm) derived from HEA-PP existed primarily in a solid solution state, whereas those from HEA-BP and HEA-SX also developed a core-shell structures with Mn-rich shells (Fig. S4, Appendix: Study 2). The shell thickness varied, measuring 5.7 ± 1.3 nm for HEA-BP and 6.7 ± 3.6 nm for HEA-SX. This core-shell formation in HEA-BP and HEA-SX NPs likely resulted from the preferential vaporization of Mn during ablation, followed by its recondensation on the particle surface. In contrast, the lower Mn content in HEA-PP bulk target reduced the extent of shell formation in NPs, leading to a more uniform solid solution.

2.2.4.5. Mössbauer Spectroscopy Analysis

Mössbauer spectroscopy identified three distinct spectral contributions in all samples (Fig. 7, Appendix: Study 2). The dominant contribution (~50% of the spectral area) corresponded to

FCC-structured HEA in a low-spin state, confirming that the primary phase remained unchanged in the synthesized NPs. A secondary magnetically ordered component (~30% of the spectral area) was characterized by a broad hyperfine field distribution ranging from 15 to 35 T and an average isomer shift of 0.34 mm/s. This component is consistent with Fe-rich or Mn-rich phases, possibly resulting from localized segregation. Additionally, an oxide phase (~20%) was observed in all samples, indicating partial oxidation of the NPs. The oxide contribution remained consistent across all target types, suggesting that oxidation occurred post-synthesis rather than during the ablation process. The presence of these phases aligns with the elemental mapping results, supporting the notion that Mn-rich shell formation in HEA-BP and HEA-SX could be linked to differential oxidation behavior.

2.2.4.6. Time-of-Flight Mass Spectrometric Analysis of Laser-Ablated CoCrFeMnNi Plumes

Mass spectrometric analysis of the plasma plumes revealed that the dominant species consisted of singly charged Cr, Fe, Co, Ni, and Mn ions, with doubly charged ions appearing at fluences above 1 J/cm² (Fig. 8 and Fig. 9, Appendix: Study 2). The relative ion abundances in the HEA-PP plasma plume were Mn (1.0), Cr (1.1), Fe (0.35), Ni (0.30), and Co (0.26), suggesting preferential ejection of Mn and Cr. The mean kinetic energies of the emitted species were determined as 50 eV for Mn, 42 eV for Cr, 64 eV for Fe, 76 eV for Ni, and 75 eV for Co. The mean velocities were measured at 13.2 km/s for Mn, 12.5 km/s for Cr, 14.9 km/s for Fe, 15.9 km/s for Ni, and 15.7 km/s for Co.

For HEA-BP and HEA-SX, Mn was the most abundant species in the plasma plume, correlating with the observed Mn-rich shells in the resulting NPs. The delayed vaporization of Mn and Cr was more pronounced in HEA-BP and HEA-SX, which contributed to the formation of core-shell structures in their respective NPs.

These findings highlight the critical role of target preparation in defining the productivity, elemental distribution, and phase structure of HEA NPs synthesized via PLAL. The observed variations in ablation behavior and NP characteristics demonstrate that the method used to prepare HEA targets significantly influences the efficiency and compositional control of the produced NPs.

2.3. Summary of Study 3: Magnetic transition in Compositionally Complex Alloys at Bulk and Nanoscale

2.3.1. Study Overview

This study investigates the synthesis and magnetic transitions of rare-earth-free Fe-Mn-Ni-Si-based CCAs at both bulk and nanoscale levels. The research was motivated by the need for sustainable and cost-effective magnetic materials with tunable phase transitions, particularly for applications in magnetocaloric refrigeration, sensors, and energy-efficient magnetic technologies. The study focuses on two CCAs: $Mn_{22.3}Fe_{22.2}Ni_{22.2}Ge_{16.65}Si_{16.65}$ (Ge-based CCA) and $Mn_{0.5}Fe_{0.5}NiSi_{0.93}Al_{0.07}$ (Al-based CCA). These materials were selected based on their potential to exhibit tunable magnetic properties while replacing expensive and scarce rare-earth elements with more abundant and economical alternatives such as Al and Si.

The bulk CCAs were synthesized using distinct processing routes: the Ge-based CCA was prepared via high-energy ball milling followed by spark plasma sintering (Fig. 1, Appendix: Study 3), while the Al-based CCA was produced through powder pressing and sintering in a vacuum environment. To evaluate how the transition from bulk to nanoscale affects magnetic properties, NPs of both CCAs were synthesized using PLAL, a surfactant-free and scalable method. The structural, compositional, and magnetic characteristics of both bulk and nanoscale CCAs were analyzed using a range of techniques, including SEM/TEM with EDX, XRD and magnetometry.

The study explores the relationship between material composition, synthesis method, and magnetic phase transitions to provide insights into how CCAs behave in different states. By systematically comparing bulk and nanoscale properties, the research aims to identify key factors governing the magnetic behavior of these alloys and assess their viability for applications that require tunable magnetic phase transitions.

2.3.2. Aim of the Study

The primary objective of this study is to develop and evaluate rare-earth-free CCAs with tunable magnetic phase transitions at both bulk and nanoscale dimensions. The research aims to:

- Synthesize CCAs: Fabricate Ge-based and Al-based CCAs using scalable and cost-effective techniques, ensuring homogeneity and phase stability
- Generate NPs via PLAL: Produce colloidal CCA NPs directly from bulk targets to investigate their structural integrity and magnetic properties at reduced dimensions
- Characterize Magnetic Transitions: Determine the T_c for bulk CCAs T_B for NPs, assessing their suitability for magnetocaloric and sensing applications
- Compare Bulk and Nanoscale Properties: Identify differences in magnetic behavior between bulk and nanoscale materials, particularly focusing on H_C and M_s
- Evaluate Cost-Effectiveness and Scalability: Examine the feasibility of substituting Ge with Al in CCAs, addressing both economic and material availability concerns while maintaining functional magnetic properties

By systematically investigating these objectives, the study provides a comprehensive understanding of the synthesis-microstructure-property relationships in Fe-Mn-Ni-Si-based CCAs. The findings offer valuable insights for the development of sustainable, rare-earth-free magnetic materials for applications in refrigeration, sensors, and low-energy-loss magnetic devices.

2.3.3. Methods

2.3.3.1. Fabrication of Bulk Ge-Based Compositionally Complex alloys

The Ge-based CCA was synthesized using a two-stage process. First, high-purity elemental powders of Mn (99.2%, 3 µm), Fe (99.96%, 10-20 µm), Ni (99.5%, 45-60 µm), Si (99.999%, 45-60 µm), and Ge (99.99%, <250 µm) were combined in the required stoichiometric ratios. The mixture underwent HEBM in a planetary mill under an argon atmosphere for 90 minutes, with a ball-to-powder weight ratio of 20:1 and rotation speeds of 700 rpm for the sun disk and 1400 rpm for the jars.

Following the milling process, the resulting powder was compacted using SPS in a vacuum chamber. The powder was placed into a cylindrical graphite die (inner diameter Ø = 10 mm) and uniaxially pressed at 50 MPa. The sintering was performed at 1073 K with a dwell time of 10 minutes and a heating rate of 100 K/min. A K-type thermocouple inserted into a radial hole in the die monitored the temperature during sintering. The final sintered disks had a thickness of approximately 3-4 mm and a diameter of 10 mm.

2.3.3.2. Fabrication of Bulk Al-Based Compositionally Complex alloys

The Al-based CCA was prepared from high-purity elemental powders of Mn (99.6%, <10 µm), Fe (99.5%, 6-10 µm), Ni (99.9%, 3-7 µm), Al (99.5%, 44 µm), and Si (99%, 44 µm). To achieve the desired alloy composition, precise amounts of each powder were thoroughly mixed using a mortar and pestle for 20 minutes.

Once homogenized, the powder mixture was compressed under 100 MPa into cylindrical pellets measuring 10 mm in diameter and 2 mm in thickness. The pressed samples were then subjected to heat treatment in a vacuum environment (pressure reduced to 10 mbar) at 600°C for 7 days, followed by rapid quenching in water to enhance alloy homogeneity. This method serves as an efficient and cost-effective alternative to conventional preparation techniques, such as arc melting or HEBM followed by SPS, making it particularly suitable for generating CCA NPs through PLAL.

The synthesized bulk CCAs were ground and polished before structural and compositional characterization. SEM was performed using a JEOL JSM-7600 F (Japan) to examine the microstructure. EDX analysis was conducted using an Oxford Inca spectrometer to determine the elemental composition.

The crystalline phases of the bulk CCAs were characterized using XRD with a DRON-4-07 diffractometer employing Co-Kα radiation, scanning over a 2θ range of 20–110°. Magnetic measurements were performed using a Quantum Design DynaCool PPMS across a temperature range of 5-390 K under an applied magnetic field of up to 9 Tesla.

2.3.3.3. Synthesis of Compositionally Complex alloy Nanoparticles via Pulsed Laser Ablation in Liquid

Colloidal NPs of the Ge-based and Al-based CCAs were produced using PLAL. The bulk alloy targets were immersed in ethanol and irradiated using a near-infrared picosecond pulsed Nd:YAG laser (Coherent, HyperRapid NX, Kaiserslautern, Germany) with a pulse duration of 10 ps at a wavelength of 1064 nm. A laser fluence of 2.8 J/cm² was applied to facilitate NP formation. To optimize NP concentration and minimize solvent consumption, a closed-loop liquid flow system was employed.

The synthesized NPs were analyzed for size distribution, morphology, elemental composition, and crystallinity using TEM and EDX. TEM imaging was carried out using a JEOL 2200FS microscope (Japan) equipped with an Oxford X-MaxN TLE 80 EDX detector (UK). The microscope operated at an acceleration voltage of 200 kV and was coupled with a 2k × 2k GATAN UltraScan 1000XP CCD camera for high-resolution imaging.

For TEM sample preparation, the colloidal NPs were dispersed onto a carbon-supported copper TEM grid and dried at ambient conditions. The particle size distribution was determined by analyzing TEM images and measuring the Feret diameter of individual NPs using ImageJ software. The crystalline structure of the NPs was assessed by generating digital diffractograms using CrysTBox software. EDX data were processed and quantified using AZtec software to determine elemental distributions.

2.3.4. Results and Discussion

2.3.4.1. Microstructural and Phase Characterization of Bulk Compositionally Complex alloys

SEM and EDX analysis confirmed a homogeneous microstructure in the Ge-based CCA, with minimal elemental segregation (Fig. 2a, Appendix: Study 3). The composition analysis showed that most elements were near their expected stoichiometric values, with Ge displaying the highest variance (14.1%). XRD analysis revealed a combination of BCC and FCC phases (Fig.2b, Appendix: Study 3), differing from previous reports of a single-phase structure in arc-melted samples.

The Al-based CCA showed a porous microstructure with noticeable elemental segregation (Fig. 2c, Appendix: Study 3). The elemental composition varied significantly, particularly for Al, which exhibited a deviation of 121.7%. XRD analysis identified multiple phases, including hexagonal and cubic structures, indicating incomplete alloying (Fig.2d, Appendix: Study 3).

2.3.4.2. Particle size distribution of Compositionally Complex alloys Nanoparticles

NPs produced by PLAL exhibited a broad size distribution ranging from 2 to 130 nm, following a lognormal trend (Fig. 3, Appendix: Study 3). The Ge-based CCA NPs had an average size of 13.4 ± 9.1 nm, while the Al-based CCA NPs were slightly larger at 18.4 ± 15.5 nm. The difference in NP size between the two CCAs can be attributed to variations in the material properties, including thermal conductivity, melting point, and volatility of the elements, which influence the ablation and condensation dynamics during laser processing.

2.3.4.3. Elemental and structural characterization of Compositionally Complex alloys Nanoparticles

EDX mapping confirmed the presence of all target elements in the NPs (Fig. 4 and table 2, Appendix: Study 3), though deviations from the bulk composition were observed. In the Ge-based CCA NPs, Mn exhibited the largest deviation, with a 31.5% reduction, whereas Ge was relatively stable. The Al-based CCA NPs showed a significant reduction in Al content (43.5%), likely due to its high volatility. The Ge-based NPs exhibited a core-shell structure with Mn enrichment at the surface, whereas the Al-based NPs displayed a more uniform elemental distribution with minimal oxidation.

High-resolution TEM images of both Ge- and Al-based CCA NPs revealed well-defined crystalline structures with variations in contrast, indicating compositional heterogeneity and possible phase separation (Fig. 5, Appendix: Study 3). The diffraction patterns of Ge-based NPs confirmed an orthorhombic NiSiTi-type crystal structure, which is different from the bulk counterpart, where a mix of FCC and BCC phases was observed. This suggests that the rapid cooling rates in PLAL stabilized a different crystal structure compared to the slower cooling during SPS. For the Al-based CCA NPs, the diffraction pattern showed peaks corresponding to an orthorhombic NiSi-type crystal structure, consistent with previous reports on similar alloys. Interestingly, the bulk Al-based CCA exhibited multiple phases, whereas the NPs formed a more uniform structure.

2.3.4.4. Magnetic Behavior of Bulk and Nanoscale Compositionally Complex Alloys

The Ge-based bulk CCA showed a clear FM-to-PM transition at 179 K, with a M_s of 68.2 Am²/kg at 5 K and a H_C of 8.4 kA/m. At 300 K, M_s decreased to 18 Am²/kg, and H_C dropped to

1.2 kA/m. The Al-based bulk CCA had a higher transition temperature of 263 K. At 5 K, M_S was 32.7 Am²/kg, with a H_C of 11 kA/m. At 300 K, M_S dropped to 9.5 Am²/kg, and H_C decreased to 1 kA/m. (Fig 6 and Table 3, Appendix: Study 3)

The Ge-based CCA NPs exhibited a SPM blocking temperature at 100 K, with a M_S of 25.1 Am²/kg at 5 K and a H_C of 26.2 kA/m. At 300 K, M_S was reduced to 6.6 Am²/kg, with a H_C of 0.7 kA/m. The Al-based CCA NPs displayed similar SPM behavior, with a T_B of ~100 K. The M_S at 5 K was 25.9 Am²/kg, with a H_C of 16.6 kA/m. At 300 K, M_S was 6.8 Am²/kg, and H_C decreased to 1.1 kA/m. The main differences between the two NP systems can be attributed to oxidation effects and elemental segregation. The Ge-based NPs exhibited a core-shell structure with Mn enrichment at the surface, leading to higher H_C and reduced M_S. The Al-based NPs, in contrast, showed a more homogeneous composition and lower oxidation, resulting in a lower H_C while maintaining comparable magnetization values. (Fig. 7 and Table. 4, Appendix: Study 3)

2.4. Summary of Study 4: Compositionally controlled Synthesis and Printing of NiMnSn nanoparticles

2.4.1. Study overview

This study investigates the synthesis of compositionally controlled NiMnSn NPs and their application in 2D laser printing of magnetocaloric materials. NiMnSn MPs were used as feedstock, and PLAL was employed to generate NPs. Different target fabrication strategies were explored to determine the best approach for obtaining NPs with compositions close to the desired $Ni_{50}Mn_{50-x}Sn_x$ (at. %; for 13 at. % < x < 15 at. %),. The composition, structure, and magnetic properties of the synthesized NPs were analyzed and compared to the original MPs. Additionally, both MPs and NPs were formulated into inks for laser sintering, and their printability and sintering behavior after printing were examined. The effects of laser fluence on the final material properties were also studied.

2.4.2. Aim of the study

The primary aim of this study was to synthesize rare-earth free compositionally controlled ternary alloy NPs via PLAL and compare its properties with the MPs. The research aims at

- Development of a Compositionally Controlled Approach for Synthesizing $Ni_{50}Mn_{50-x}Sn_x$ (at. %; for 13 at. % < x < 15 at. %) NPs
- Investigating Magnetic Properties of NiMnSn MPs and NPs of similar composition
- Exploring High-Resolution 2D Laser Printing of NiMnSn Materials by employing laser printing strategy to print its MP and NP ink

- Investigating the sintering behavior of both MP and NP-based inks under different laser fluences to determine their suitability for structured magnetocaloric applications.
- Assessing the Influence of Laser Processing on Magnetic Transitions

By investigating these objectives, the findings can contribute to the advancement of solid-state cooling technologies, offering new insights into the scalability and structuring of NiMnSn-based materials for next-generation microdevices.

2.4.3. Methods

2.4.3.1. Synthesis of NiMnSn Fine Microparticles

NiMnSn MPs were produced through gas atomization and analyzed to determine their elemental composition using X-ray fluorescence. Their structural and elemental distribution was further examined through EDX in combination with SEM. The study involved a series of steps, including target preparation, NP synthesis through PLAL, formulation of inks, and subsequent laser sintering.

2.4.3.2. Fabrication of NiMnSn Targets

To achieve compositionally controlled synthesis of NiMnSn NPs, different target preparation approaches were employed. (Fig. 1a and b, Appendix: Study 4) The first method (Type 1 target) involved the fabrication of polycrystalline alloy targets through arc melting under an inert argon atmosphere, followed by an annealing at an elevated temperature to ensure homogeneity. The solidified material was then sectioned into thin slices and immersed in water for subsequent laser processing.

Another approach utilized powder-based targets (Type 2 Targets), where elemental MPs of Ni, Mn, and Sn were combined in various proportions and mixed with polyvinylpyrrolidone as a binder. The blended powders were compacted into pellet form to serve as targets for NP synthesis.

Type 3 targets were prepared using pre-alloyed MPs, which were blended with additional Mn MPs to adjust composition. The mixture was manually ground to ensure uniformity, pressed into cylindrical pellets under controlled pressure, and subjected to heat treatment in a nitrogen environment.

2.4.3.3. Pulsed laser ablation of NiMnSn targets

NPs were generated by performing PLAL using different target materials. (Fig. 1c, Appendix: Study 4) The ablation process was carried out in ethanol using a near-infrared picosecond pulsed laser. The laser beam was precisely controlled through a scanning system to create a defined ablation pattern, ensuring uniform material removal. The resulting NPs were collected in a continuously circulated liquid environment to improve yield and minimize solvent usage.

The synthesized NPs were characterized for their size distribution, morphology, and elemental composition. Their structural analysis was conducted using TEM, while crystal structure determination was performed through XRD. The magnetic properties of the NPs were assessed using vibrating sample magnetometry, with temperature-dependent magnetization measurements recorded under different applied magnetic fields.

2.4.3.4. Formulation and Laser Processing of NiMnSn Nanoparticle Inks

To formulate inks, the NPs were dispersed in ethanol, and their concentration was adjusted through partial solvent evaporation. A polymer stabilizer was introduced to enhance dispersion stability. In separate preparation, MP-based inks were formulated by dispersing commercial NiMnSn MPs with a polymer additive in ethanol, followed by ultrasonication to ensure uniform mixing. (Fig. 1d, Appendix: Study 4)

The inks were deposited onto glass substrates in controlled volumes to form thin layers. Laser sintering was performed using a continuous-wave laser in conjunction with a programmable linear stage. The laser parameters were adjusted to achieve optimal sintering conditions while minimizing material ablation.

The sintered structures were examined using SEM to evaluate their morphology, while TEM was used to analyze their structural characteristics at a higher resolution. Magnetic measurements were performed to determine the effects of laser sintering on the magnetic properties of the printed structures.

2.4.4. Results

2.4.4.1. Composition Control and Particle Size Characterization of NiMnSn Microparticles and Nanoparticles

Elemental composition of NiMnSn MPs and NPs produced via different approaches were investigated (Fig. 2, Appendix: Study 4). Elemental analysis of NiMnSn MPs and NPs synthesized through PLAL shows that the composition of the MPs closely matches the intended $Ni_{50}Mn_{50-x}Sn_x$ (at.%; for 13 at.% < x < 15 at.%), with $Ni_{47.2}Mn_{39.2}Sn_{13.0}$ (at.%). A slight increase in Mn content was used to offset potential evaporation losses during laser processing.

NPs obtained from the arc-melted $Ni_{50}Mn_{36}Sn_{14}$ (at.%) bulk target exhibit a significant reduction in Mn content, with Mn measured at 15.3 ± 4.6 at.%, i.e., 31.5% lower than the target composition. This selective Mn loss is attributed to its lower boiling point (2095°C) compared to Ni (2913°C) and Sn (2602°C), making it more susceptible to vaporization during laser ablation.

NPs synthesized from powder-pressed elemental targets with an adjusted ratio of Ni (37 at.%), Mn (53 at.%), and Sn (10 at.%) aimed to compensate for Mn loss. However, substantial deviations were still observed, with Ni content fluctuating up to ±30 at.%. The uneven distribution of elements is likely due to differences in latent heat of fusion and vaporization, leading to compositionally inconsistent NPs.

A more controlled composition is achieved when NPs are synthesized using pre-alloyed MPs mixed with an additional 20 at.% Mn, resulting in NPs with Mn content of 12.0 ± 1.8 at.%, Ni at 35.3 ± 4.1 at.%, and Sn at 1.30 ± 0.4 at.%. These values closely align with the desired stoichiometry, with deviations reduced to ~7 at.% for Mn. Despite some minor fluctuations, the NPs exhibit a significantly improved compositional homogeneity compared to other methods.

Particle size analysis (Fig. 2c, Appendix: Study 4) reveals that MPs have an average diameter of approximately 10.0 µm, while NPs produced via PLAL show a much smaller average size of 12.4 ± 6 nm. The NP size distribution is monomodal and narrow, indicating a more uniform particle population compared to the broader size range of MPs. Both MPs and NPs maintain a spherical morphology, making them suitable for comparative analysis in subsequent processing steps.

2.4.4.2. Magnetic Properties of Microparticles and Nanoparticles

Temperature-dependent magnetization measurements of MPs reveal two distinct magnetic transitions at approximately 300 K and 200 K (Fig. 3a, Appendix: Study 4). These transitions correspond to the transformation from the high-temperature austenite phase to the martensite phase. The T_c ≈ 315 K, and the martensitic phase, T_c ≈ 230 K, indicate a mixed-phase system. Under a higher field of 1 T, the first transition shifts downward by ≈ 5 K to 295 K, while the second transition becomes indistinguishable due to similar magnetization values between the austenite and martensite phases, leading to dM/dT ≈ 0.

In contrast, NiMnSn NPs (from Type 3 target), the M-T curve shows a gradual decrease in magnetization with increasing temperature under both 10 mT and 1 T fields (Fig. 3b, Appendix: Study 4). Unlike the MPs, which exhibit two clear magnetic transitions, the NPs display broad and weak features around 200 K and 300 K. These transitions appear diffuse and are less pronounced. The M-T curves of NPs synthesized via PLAL of Type 1 target (Fig. S5 Appendix: Study 4) do not exhibit these broad transitions, indicating the importance of compositionally controlled synthesis in achieving a distinct austenite-martensite transformation near room temperature. At 1 T, the transitions are further suppressed due to the reduced magnetic contrast between the phases, similar to the behavior observed in MPs.

2.4.4.3. Laser processing of Microparticles and Nanoparticles

Laser irradiation successfully sinters both MP and NP inks (Fig. 4, Appendix: Study 4). For MPs, sintering begins at a fluence of 0.76 J/cm², with complete fusion achieved at 0.89 J/cm². The average sintered line width is 254 ± 17 μm, but at fluences above this range, partial ablation occurs. The Gaussian intensity profile of the laser beam leads to higher intensity at the center, causing non-uniform sintering in some areas.

For NPs, sintering initiates at a lower fluence of 0.66 J/cm² and is fully achieved at 0.87 J/cm², with an average sintered line width of 65 ± 4 μm. The resolution was characterized by the standard deviation of the line thickness which was 4 times higher than MP sintering. Compared to MPs, NP sintering produces structures with four times better uniformity, due to the smaller particle size allowing for more precise structuring. The lower sintered line width of NPs is attributed to their finer resolution and higher energy absorption efficiency.

The ratio of ablation to sintering is higher for NPs than MPs, likely due to their larger surface area, which increases sensitivity to laser heating. Microscopic analysis confirms that NPs form tightly fused clusters, whereas MPs exhibit partial fusion at contact points. This suggests that NPs offer superior resolution and homogeneity for miniaturized device applications. The ratio of ablation to sintering is higher for NPs than for MPs, which could be due to their larger surface area and different thermal absorption characteristics. Microscopic analysis confirms that NPs form tightly fused clusters upon sintering, while MPs display partial fusion at contact points.

2.4.4.4. Magnetic Properties of Laser-Sintered Structures

Sintered MPs maintain distinct magnetic phase transitions similar to their unsintered counterparts, with ~ 2 times increase in magnetization (Fig. 5a, Appendix: Study 4). The enhancement is likely due to improved particle connectivity and stronger magnetic interactions after sintering. At higher laser fluences, however, some material loss occurs, leading to a reduction in overall magnetization (Fig. 5b, Appendix: Study 4).

NP sintered structures exhibit a gradual decline in magnetization with temperature, similar to unsintered NPs (Fig.5c, Appendix: Study 4). The absence of sharp transitions suggests that sintering does not significantly alter the magnetic properties of the NPs. Higher laser fluences further suppress transition features (Fig.5d, Appendix: Study 4), possibly due to increased structural disorders or minor compositional changes caused by heating effects during sintering.

Overall, laser printing and sintering enable the fabrication of structured NiMnSn materials while preserving their key magnetic properties. The differences in sintering behavior between MPs and NPs highlight the advantages of NPs for high-resolution structuring and controlled material processing.

2.5. Summary overview: Linking the Four Studies

This thesis explores the synthesis and characterization of rare-earth-free magnetocaloric materials across a compositional and dimensional gradient, from binary alloys to high-entropy and compositionally complex systems, and from bulk to nanoscale. The overarching goal was to develop scalable, compositionally controlled fabrication routes for magnetocaloric materials tailored for miniaturized applications, including microcooling, MEMS, and flexible electronics. Four distinct studies collectively underpin this aim, each addressing key challenges in composition tuning, nanoparticle synthesis, magnetic phase transition control, and laser structuring for device integration.

The first study established a direct-write approach for producing functional magnetocaloric microstructures using laser-sintered FeRh nanoparticles. Through precise control of laser parameters, a transition from the paramagnetic γ-FeRh phase to the magnetically ordered B2 phase was achieved while preserving the material's integrity and magnetocaloric functionality. The study demonstrated that laser sintering offers superior oxidation resistance and spatial control compared to conventional furnace annealing, enabling high-resolution 2D structuring of magnetocaloric materials for localized cooling.

The second study extended the scope from binary FeRh to multi-element CoCrFeMnNi HEAs, emphasizing the role of target preparation in nanoparticle synthesis PLAL. By comparing powder-pressed, ball-milled, and single-crystal alloy targets, it revealed how differences in target homogeneity and crystallinity influence nanoparticle yield, size distribution, composition, and magnetic behavior. Time-of-flight mass spectrometry clarified the ablation dynamics and vaporization sequence of individual elements, highlighting the potential of PLAL to produce compositionally stable HEA nanoparticles when target design is optimized.

The success of producing multicomponent NPs has been translated to the third study in which magnetically tunable CCAs-namely MnFeNiGeSi and MnFeNiSiAl-were synthesized both in bulk and nanoparticle form. The bulk CCAs were prepared via scalable sintering routes, while nanoparticles were generated via PLAL. A comparative study of their magnetic transitions revealed key size-dependent effects: while bulk samples exhibited clear ferromagnetic–paramagnetic transitions, the nanoparticles displayed superparamagnetic behavior with blocking temperatures shifted due to surface effects and compositional inhomogeneities. The replacement of Ge with Al demonstrated a cost-effective pathway to engineer magnetocaloric materials without sacrificing performance.

The fourth study focused on achieving precise composition control in ternary NiMnSn nanoparticles, known for their room-temperature inverse magnetocaloric effect using various PLAL target strategies. Among these, the use of pre-alloyed micropowders mixed with Mn yielded nanoparticles closest to the desired stoichiometry. These compositionally optimized nanoparticles were formulated into printable inks and successfully laser-sintered into microstructures. A comparative analysis of microparticle and nanoparticle inks highlighted that nanoparticle inks provided superior spatial resolution and homogeneity, though magnetic transitions were broader due to surface and size effects.

Collectively, these studies demonstrate a progressive advancement from composition tuning and phase stabilization in simple binary systems toward scalable nanoparticle synthesis and device integration in complex multicomponent alloys. The work bridges fundamental understanding of laser–material interaction at micro and nanoscale with the practical need for customizable, energy-efficient magnetocaloric materials, offering new opportunities for on-chip thermal management and solid-state refrigeration.

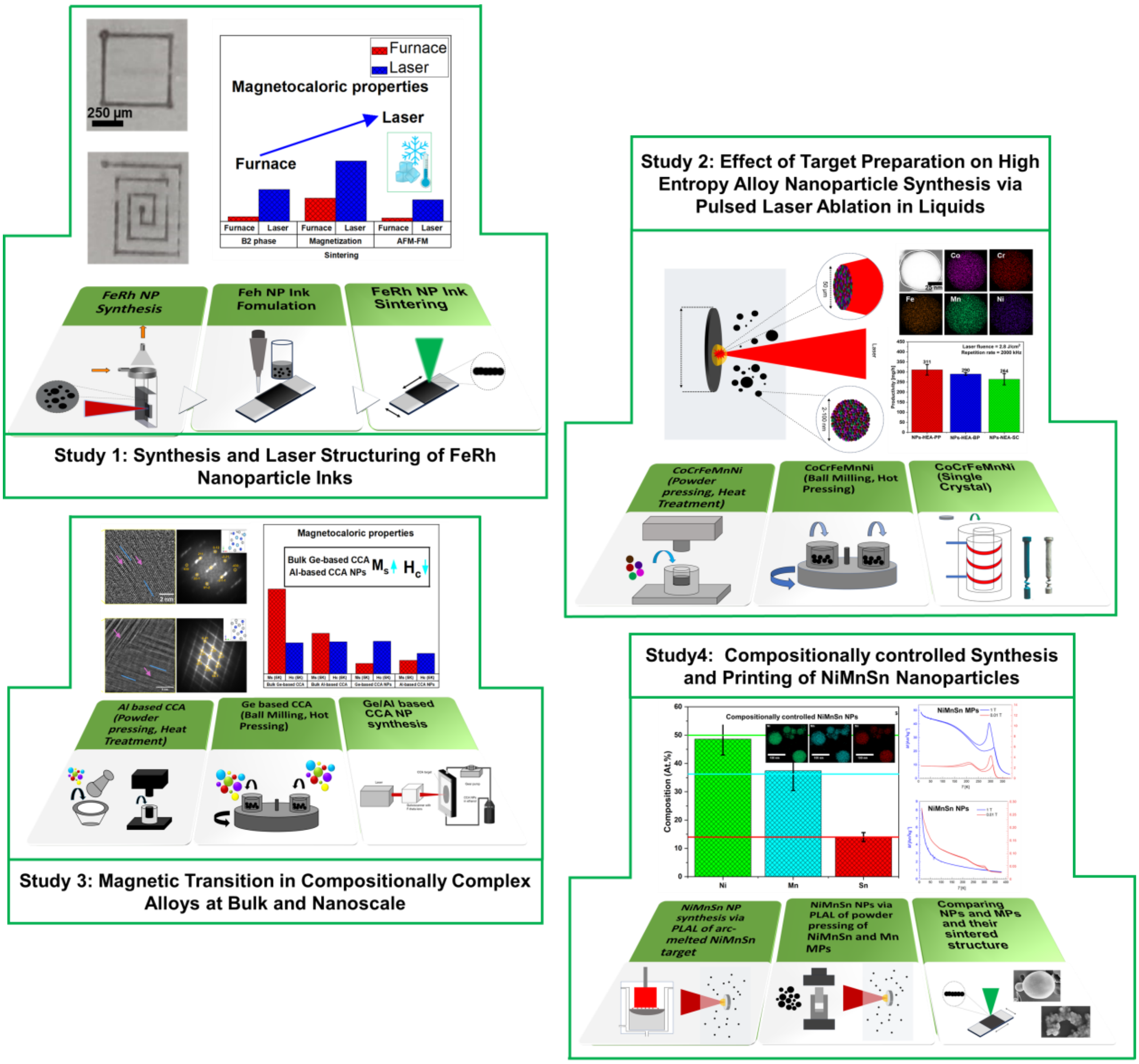

Figure 4: Graphical overview of the four studies presented in this thesis. **Top left (Study 1):** Synthesis, ink formulation, and laser sintering of FeRh nanoparticles for fabricating magnetocaloric microstructures, with comparison to furnace sintering. **Top right (Study 2):** Influence of target preparation (pressed powders, ball-milled powders, and single crystals) on the synthesis of CoCrFeMnNi high-entropy alloy nanoparticles via pulsed laser ablation in liquids (PLAL). **Bottom left (Study 3):** Synthesis and magnetic characterization of FeMnNiGeSi and FeMnNiSiAl compositionally complex alloys at both bulk and nanoscale, revealing distinct magnetocaloric behavior. **Bottom right (Study 4):** Compositionally controlled synthesis of NiMnSn nanoparticles via PLAL using various target strategies, followed by 2D laser printing and magnetic evaluation of both nanoparticle and microparticle inks.

2.6. Specific Contributions in Each Study

2.6.1. Contribution in Study 1: Laser structuring of FeRh Nanoparticle inks

In this study, I played a central role in developing a streamlined, scalable route to fabricate magnetocaloric microstructures from FeRh nanoparticles. My contributions began with the PLAL of bulk FeRh targets to synthesize nanoparticles. I then formulated functional inks from these nanoparticles, optimizing dispersibility and sinterability by incorporating appropriate polymers. A major technical focus was to understand the influence of polymer additives on ink homogeneity, interparticle contact, and the sintering behavior necessary for achieving high-quality microstructures.

I conducted detailed particle size distribution analysis of the synthesized FeRh nanoparticles visualized using TEM, and examined the morphology of sintered structures via SEM. Both furnace-sintered and laser-sintered samples were studied across a range of laser fluences. I evaluated the magnetic properties through temperature- and field-dependent magnetization measurements and correlated the results with X-ray diffraction (XRD) data to determine the relative content of the desired B2 phase versus the disordered gamma-FeRh phase. These correlations were critical in establishing that laser sintering can induce the AFM-to-FM transition by stabilizing the B2 phase, whereas furnace sintering was associated with a stronger tendency toward oxidation.

One of the key challenges addressed was the development of a rapid and reproducible process for creating magnetocaloric structures with enhanced B2 phase content and improved magnetic transitions. Another important task was the fabrication of custom 2D structures using direct laser writing. I actively optimized laser processing parameters to achieve spatially resolved functional structures. Finally, I led the preparation of the manuscript, including writing and revising the first draft.

2.6.2. Contribution in Study 2: Effect of Target Preparation on High entropy Nanoparticles via Pulsed Laser Ablation in Liquids

My work in this study focused on understanding how different target preparation methods influence the yield, composition, and magnetic properties of CoCrFeMnNi HEA nanoparticles synthesized via PLAL. I prepared HEA targets using powder pressing followed by heat treatment—a simpler and more scalable alternative to ball milling or single crystal growth. These targets were compared with those prepared by coauthors using alternative routes.

A central challenge was to optimize the laser and scanner parameters for each type of target to ensure high ablation efficiency and nanoparticle productivity. I carried out microstructural analysis of both targets and nanoparticles using SEM and TEM, respectively, to investigate morphology, size distribution, and crystallinity. Furthermore, I linked the microstructure of the targets to the characteristics of the resulting nanoparticles to identify processing–property relationships.

I also participated in the interpretation of advanced characterization techniques such as Mössbauer spectroscopy and ToF-SIMS. These analyses were critical in understanding element-specific ablation behaviors and possible fractionation effects. I worked closely on the integration of these results with physical observations to explain differences in magnetic performance and compositional uniformity. Additionally, I contributed extensively to drafting the manuscript and compiling figures.

2.6.3. Contribution in Study 3: Magnetic Transitions in Compositionally Complex Alloys at Bulk and Nanoscale

In this study, I contributed to the fabrication of compositionally complex alloys (CCAs) based on MnFeNiSiAl and MnFeNiGeSi systems and studied their magnetic behavior at both bulk and nanoparticle scales. My major task was to fabricate the Al-based CCA via powder-pressing followed by heat treatment. This method provided a low-cost and scalable route to produce alloy targets for PLAL.

I was actively involved in the microstructural analysis of both the bulk targets and the nanoparticles derived from them. Using SEM and TEM, I evaluated particle morphologies and size distributions. I also used CrystBox software to perform crystal structure indexing from high-resolution TEM images. Elemental compositions were determined using EDX analysis, and I conducted a comparative analysis of compositional deviations between bulk and nanoscale forms.

I also analyzed the initial magnetization measurements and helped identify the differences in magnetic behavior between the Al- and Ge-based CCAs. A key challenge in this work was to demonstrate that rare-earth-free nanoparticles with magnetocaloric properties could be synthesized using five-element alloy systems, and to assess whether Al could serve as a cost-effective replacement for Ge.

2.6.4. Contribution in Study 4: Composition-Controlled Synthesis and Printing of NiMnSn Nanoparticles

This study focused on the synthesis of NiMnSn nanoparticles with a composition close to $Ni_{50}Mn_{36}Sn_{14}$, which exhibits an inverse magnetocaloric effect near room temperature. I was responsible for designing and testing various target preparation strategies to minimize compositional deviation in the resulting nanoparticles. These included PLAL of arc-melted bulk targets, pressed elemental powders, and micropowder blends.

The optimal composition was achieved using pressed micropowder blends of NiMnSn and additional Mn, which yielded nanoparticles closely matching the desired stoichiometry. A major challenge was to formulate printable inks from these microparticles. Due to their higher magnetization and faster sedimentation, stabilizing microparticles in suspension required extensive optimization. I developed ink formulations that balanced stability, printability, and functional performance.

I also optimized laser sintering parameters for both microparticle and nanoparticle inks, and evaluated the resulting structures using SEM and EDX mapping. I interpreted magnetic and XRD analyses to understand how processing conditions influenced phase purity and transition behavior. This comprehensive approach enabled a direct comparison of sintered structures from both particle types. I was responsible for writing and revising the first draft of the manuscript and will be responsible for further revisions.

Through all four studies, I contributed to the full research workflow, from experimental planning and synthesis to characterization, optimization, and scientific writing, while addressing key challenges in composition control, scale-up, and magnetocaloric performance enhancement.

3. General discussion

3.1. Discussion of results

In this section we will discuss together the results from PLAL synthesized binary, ternary and CCAs NPs comparing their composition, particle size distribution, productivity and magnetic responses and the challenges associated with each material system

3.1.1. Nanoparticle Composition and Phase Control: Target preparation techniques

FeRh alloy NPs synthesized via PLAL demonstrated that when using an equimolar FeRh arc melted target in ethanol and acetone, the resulting NPs retained an equimolar composition. (Nadarajah et al., 2020) The oxidation level was significantly lower in these solvents compared to water. Further improvements in oxidation resistance were achieved using molecular-sieve-treated solvents and inert or reducing gases, reducing oxidation to as low as 4 at.%. These findings highlight the importance of solvent choice and inert or reducing gas atmosphere in controlling composition and phase purity in laser-ablated NPs.

The synthesis of multicomponent alloy NPs, particularly those composed of Heusler alloys, HEAs, and other complex compositions, presents significant challenges in achieving homogeneous elemental distribution. Unlike bulk materials, where thermodynamic equilibrium allows for atomic diffusion and homogenization over time, NP formation occurs in highly dynamic and non-equilibrium conditions. This complexity is further amplified in PLAL synthesis, where rapid vaporization and condensation determine the final NP composition and structure. The timeline of NP formation in PLAL is extremely rapid. Immediately after laser irradiation, the material undergoes intense heating, reaching several thousand Kelvin within a few picoseconds. The ejected atoms and ions form a hot plasma plume that expands into the liquid medium. Within nanoseconds, the plasma begins cooling, allowing nucleation of NPs. Over the following microseconds to milliseconds, particle growth, aggregation, and secondary reactions take place, further influencing composition. This rapid heating and cooling process along with differences in intrinsic material properties such as melting points, boiling points, ionization potentials, atomic diffusion rates, and other material properties such as thermal conductivity, specific heat capacities and so on, could result in preferential evaporation, altering the final composition of condensed NP and can lead to elemental segregation and core-shell structures.

The target preparation method plays a crucial role in determining the composition and phase distribution of the synthesized NPs. In Study 2, CoCrFeMnNi HEA targets prepared using different approaches for HEA-PP, HEA-BP, HEA-SX. PLAL of HEA-BP and HEA-SX resulted in the formation of an Mn-rich oxide shell around the NPs (for particles > 20 nm), as confirmed by TEM-EDX mapping. However, no such oxide shell was observed in NPs synthesized from HEA-PP targets. The mass spectrometric analysis of the ablation plume provides insights into this selective Mn surface enrichment. Mn has a significantly lower boiling point (2095°C) and latent heat of vaporization (226 kJ/mol) compared to other elements in the HEA system (Ni: 2913°C, 379 kJ/mol; Fe: 2862°C, 340 kJ/mol; Co: 2927°C, 376 kJ/mol; Cr: 2671°C, 347 kJ/mol). This high volatility causes Mn to evaporate preferentially during laser ablation, increasing its concentration in the plasma plume compared to less volatile elements. Additionally, Mn has a lower ionization potential (7.43 eV) than Co (7.86 eV), Fe (7.90 eV), Ni (7.64 eV), and Cr (6.77 eV), making it more prone to ionization and reactive interactions with residual oxygen in the ablation environment. These factors contribute to Mn being preferentially segregated in the expanding plasma plume and more likely to condense at the NP surface upon cooling. In the HEA-BP and HEA-SX targets, where the elements were more homogeneously alloyed, the ablation process resulted in a compositionally uniform plasma, allowing Mn to preferentially migrate to the NP surface and form Mn-rich oxides due to its high reactivity with oxygen. The presence of Mn oxides was confirmed by EDX mapping, indicating that Mn oxidation occurred as the NPs formed and cooled. In contrast, the HEA-PP target was prepared by pressing elemental powders followed by heat treatment. This process might have led to Mn surface segregation within the target itself, resulting in an Mn-deficient bulk composition. Consequently, PLAL of the HEA-PP target generated a plasma plume with an overall lower Mn content, preventing the formation of a distinct Mn-rich oxide shell around the NPs. However, the average Mn content between the NPs was near to 20 at.%. Additionally, because HEA-PP targets retained some elemental characteristics from their precursor powders rather than forming a fully homogeneous alloy, the ablation process could have promoted direct recombination of elements in the plasma phase, leading to more homogeneous NP formation without Mn segregation. These findings highlight that the extent of pre-alloying in the target directly influences element redistribution during PLAL, affecting both NP composition and oxidation behavior. The results also emphasize how elemental volatility, ionization energy, and plasma dynamics contribute to compositional variations, which must be carefully controlled to achieve the desired HEA NP properties.

Additionally, when synthesizing magnetocaloric CCA NPs (Study 3) compositional deviations were observed in Ge-based and Al-based CCA NPs synthesized using PLAL. In Ge-based CCA NPs, Mn exhibited a 31.5% reduction compared to the expected composition, again likely due to its higher volatility and lower ionization potential. In Al-based CCA NPs, Al content was reduced by 43.5%, attributed to its low melting point and increased likelihood of preferential evaporation. These deviations emphasize the critical influence of elemental properties on NP composition during PLAL and further demonstrate that target preparation strategies must be carefully optimized to mitigate these effects.

In study 4, the target preparation method was studied to achieve composition-controlled synthesis of NPs, i.e., close to the desired composition $Ni_{50}Mn_{50-x}Sn_x$ (at. %; for 13 at. % < x < 15 at. %). PLAL of an arc-melted NiMnSn bulk target ($Ni_{50}Mn_{36}Sn_{14}$) Mn depletion was significant, leading to a Ni-rich composition that lacked the desired magnetocaloric phase transitions. Similarly, when using a target formed by pressing elemental Ni, Mn, and Sn Mps, compositional deviations between NPs were excessively high, likely due to differential evaporation rates and incomplete atomic recombination during condensation. However, by preparing the target using powder pressing and heat treatment of prealloyed NiMnSn MPs mixed with additional Mn MPs, compositionally close to the desired composition with minimum deviation between the NPs was successfully achieved. This could be due to the small difference in the volatility of alloy MPs and Mn MPs compared to volatility of other elements (Ni, Sn) as individual. This method compensated for Mn losses during ablation, ensuring that the resulting NPs closely matched the intended stoichiometry. This highlights the crucial role of target preparation in achieving precise elemental control in PLAL-synthesized NPs.

Table 1. Effect of target preparation method on the composition of target and PLAL synthesized NPs.

Alloy system	**Target preparation**	**Variation in target composition**	**NP composition after PLAL**
FeRh	$Fe_{50}Rh_{50}$ target prepared via arc melting	$Fe_{50}Rh_{50}$	Near to equiatomic FeRh NP
CoCrFeMnNi HEA	HEA-PP target prepared via equiatomic elemental powder pressing and Heat treatment	Lower Mn in ablated region	Average composition near to equiatomic with large deviations between NPs, solid solution alloy
	HEA-BP target prepared via equiatomic elemental powder HEBM and	Near to equiatomic composition	Average composition near to equiatomic with large deviations between NPs, Core-

	hot pressing of equiatomic powder		Mn rich shell fromation
	HEA-SX target prepared via Bridgeman method	Near to equiatomic composition	Average composition near to equiatomic with large deviations between NPs, Core-Mn rich shell formation
CCAs	Ge-based CCA	Lower Ge content on the surface	Deficient in Mn with large deviation between particles
	Al-based CCA	Higher Al content on the surface	Deficient in Mn and Al, with large deviation between particles
NiMnSn	NiMnSn prepared via arc melting	$Ni_{50}Mn_{36}Sn_4$ after casting	14 at. % lower Mn than
desired composition $Ni_{50}Mn_{50-x}Sn_x$ (at.%; for 13 at.% $<$ x $<$ 15 at.%)	NiMnSn target prepared via elemental powder pressing and heat treatment	Varying Ni, Mn and Sn elemental ratios. 37 at.% Ni, 53 at.% Mn, and 10 at.% Sn were the closest composition to achieve the average desired ratio $Ni_{50}Mn_{50-x}Sn_x$ (at.%; for 13 at.% $<$ x $<$ 15 at.%) after PLAL	substantial deviations (maximum 30 at.% in Ni)
	NiMnSn target prepared via pressing of NiMnSn alloy MPs with Mn MPs	Prealloyed MPs $Ni_{47.2}Mn_{39.2}Sn_{13.0}$ (at.%) with 20 at.% Mn NP were the closest composition to achieve the average desired ratio $Ni_{50}Mn_{50-x}Sn_x$ (at.%; for 13 at.%	Small deviations between NPs, desired composition achieved

		< x < 15 at.%) after PLAL	

3.1.2. Nanoparticle Size Distributions

Particle size plays a crucial role in determining the magnetic properties of materials, influencing magnetization, H_C, and phase transitions. These size-dependent effects also impact magnetocaloric performance, as smaller particles can exhibit tunable T_c and reduced hysteresis losses, which are beneficial for energy-efficient magnetic refrigeration. Additionally, NPs enhance heat exchange efficiency due to their high surface area, making them suitable for fluid-based MCC applications. However, extremely small sizes may lead to excessive thermal fluctuations, weakening the MCE, necessitating an optimal size range for practical applications.

The particle size distribution of FeRh alloy NPs synthesized via PLAL in acetone and acetonitrile were analysed. The NPs had a mean size of 16.4 ± 6.7 nm in acetone and 15.8 ± 5.9 nm in acetonitrile, with a PDI below 0.3, indicating a relatively narrow size distribution. (Nadarajah et al., 2020) In study 1, FeRh NPs synthesized in ethanol under similar laser and scanning parameters exhibited a significantly smaller mean size of 6.9 ± 3.0 nm (Fig. S1, Appendix: Study 1). For all synthesis, the typical size range from 2 nm to 120 nm was observed.

To improve oxidation control, additional solvents were tested. NPs synthesized in propylene carbonate had a mean size of 6.6 ± 1.9 nm, while those in methylcyclohexane measured 15.9 ± 10.7 nm. However, these solvents were not used in further investigations due to either low NP production rates or non-uniform particle morphology and were not part of any of the studies.

Table 2. Effect of varying solvent on the NP size distribution produced via PLAL with similar laser and scanning parameters.

Solvent	Mean Particle Size (nm) ± Std Dev
Acetone	16.4 ± 6.7
Acetonitrile	15.8 ± 5.9
Ethanol	6.9 ± 3.0
Propylene Carbonate	6.6 ± 1.9
Methylcyclohexane	15.9 ± 10.7
Iron Pentacarbonyl	38.1 ± 25.5

To refine the NP size distribution, post-processing techniques such as centrifugation were employed. Centrifugation in ethanol at 5000 rpm for 30 minutes effectively separated particles by size: the supernatant contained NPs below ~10 nm, while the pellet retained larger particles averaging 20–50 nm. This method preserves NP properties since laser parameters and solvent conditions remain unchanged. However, the lower mass of smaller particles necessitates high NP production for further characterization and comparative studies.

NiMnSn, HEA NPs (HEA-PP, HEA-BP, HEA-SX), Ge-based CCA, and Al-based CCA NPs were synthesized under identical PLAL conditions at a laser fluence of 2.8 J/cm² and a repetition rate of 2000 kHz. These parameters were initially optimized for HEA-PP, where maximum productivity was achieved, and were then applied to all other materials. Despite using the same conditions, variations in particle size distributions were observed Table 3. highlighting the influence of composition, alloy fabrication method, and material properties on NP formation.

Table 3. Effect of varying target material or target preparation method on the NP size distribution synthesized via PLAL with similar laser and scanning parameters.

NP System	**Mean Particle Size (nm) ± Std Dev**
NiMnSn	12.4 ± 6.0
HEA-PP	8.6 ± 5.5
HEA-BP	6.8 ± 2.8
HEA-SX	6.2 ± 3.3
Ge-based CCA	13.4 ± 9.1
Al-based CCA	18.4 ± 15.5

Across all studied systems, particle size distributions exhibit a characteristic lognormal shape, with an abundance of smaller particles and fewer larger ones and particle size range from 2 to 130 nm. The generation of big and small NPs in PLAL follows distinct mechanisms that explain the observed size distributions. As described earlier recent study by Shih et al.(Shih et al., 2018) have identified two primary mechanisms that govern NP formation in picosecond laser ablation: (1) rapid nucleation and growth of small NPs within an expanding metal-liquid mixing region and (2) hydrodynamic instabilities that launch large liquid droplets into the surrounding medium, leading to bimodal size distributions. The first mechanism, driven by the rapid cooling and recondensation of vaporized material, results in the formation of small NPs with narrow size distributions. These NPs rapidly solidify upon interaction with the cooler liquid, creating a population of sub-10 nm particles. The second mechanism, in contrast, occurs when molten droplets are ejected due to Richtmyer-Meshkov and Rayleigh-Taylor instabilities at the liquid-metal interface. The Richtmyer-Meshkov instability occurs at the interface of two fluids with different densities when a shockwave or sudden pressure disturbance passes through. In the case of laser ablation, this happens when the laser-generated plasma expands rapidly into the surrounding liquid.(Samulyak & Prykarpatskyy, 2004) The molten material at the target surface is suddenly pushed against the denser liquid environment, leading to the development of interfacial perturbations. These perturbations grow and cause fragments of molten material to be ejected as liquid droplets, which later cool and solidify into NPs. The instability is enhanced by the high-energy impact of the expanding plasma, leading to irregularly shaped and polydisperse particles in the tens to hundreds of nanometers range. The Rayleigh-Taylor instability, on the other hand, arises when a denser fluid (such as molten metal) is accelerated into a lighter fluid (such as the surrounding liquid) due to an external force, such as the recoil pressure generated by the laser pulse.(Petrov, Khokhlov, Zhakhovsky, & Inogamov, 2019) This leads to the formation of finger-like protrusions at the liquid-metal interface, which further destabilize and break apart, producing droplets of varying sizes. These droplets then undergo rapid cooling and solidification in the surrounding liquid. These instabilities drive the formation of larger NPs, often in the tens to hundreds of nanometers range, explaining the presence of broader size distributions observed experimentally.

Additionally, the cavitation bubble generated by the expanding ablation plume serves as a critical region where NPs grow and solidify.(Ibrahimkutty, Wagener, Menzel, Plech, & Barcikowski, 2012) The duration and collapse dynamics of this bubble influence the final size distribution.(DongShi Zhang, Liu, & Liang, 2017). However, the study related to cavitation bubble dynamics is not the scope of this thesis.

3.1.3. Nanoparticle Productivity

For the ablation of all the target in liquids, picosecond pulsed lasers were utilized in this study. According to Neuenschawnder et al.(Neuenschwander, Jaeggi, Schmid, & Hennig, 2014), the ablation rate increases with decreasing pulse durations. The rapid energy deposition from the picosecond laser pulses can be understood through the two-temperature model (2TM), where the laser energy is initially absorbed by the electron system before being transferred to the lattice.(Leitz, Redlingshöfer, Reg, Otto, & Schmidt, 2011) Since the electron-lattice coupling time occurs within a few picoseconds, the laser pulses are able to remove material efficiently before significant heat diffusion takes place While femtosecond lasers have demonstrated higher production rates in air, their efficiency in liquids is reduced due to nonlinear energy losses, such as self-focusing, filamentation, and non-linear optical absorption. Consequently, picosecond lasers are preferred for PLAL due to their optimal balance between energy efficiency and NP yield.(Khairani, Mínguez-Vega, Doñate-Buendía, & Gökce, 2023; Nastulyavichus, Smirnov, & Kudryashov, 2022)

For FeRh NP synthesis picosecond pulsed Nd-YAG laser irradiation (Ekspla, Atlantic Series, Vilnius, Lithuania, 10 ps, 100 kHz, 80 μJ, 1064 nm) was utilized and the the effect of solvent on the productivity was determined. FeRh NP productivity was found to be highly dependent on the solvent used during PLAL. At a laser fluence of 3.5 J/cm² and a scanning speed of 6 m/s, the maximum productivity was 43.6 mg/h in acetone and 41.2 mg/h in acetonitrile. However, using ethanol as the solvent resulted in a slightly lower productivity of 37 mg/h. Other solvents, including iron pentacarbonyl, methylcyclohexane, and iron pentacarbonyl, showed significantly lower NP yields and therefore were not included in the studies. Specifically, productivity in iron pentacarbonyl was four times lower than in acetone, while methylcyclohexane and iron pentacarbonyl resulted in two times and 1.5 times lower productivity, respectively. Despite the higher productivity in acetone, ethanol was chosen as the solvent for all future experiments due to its ability to facilitate the formation of stable high-concentration inks with better dispersion properties. Acetonitrile, although offering comparable productivity to acetone, was discarded due to its hazardous nature.

The optimization of NP productivity was achieved using a different laser system that allowed for tunable laser power and repetition rate, combined with an increased scanning speed. This was particularly investigated for the synthesis of HEA NPs, where the repetition rate was varied while keeping the laser power at its maximum value (110 W) to maximize productivity. Unlike the FeRh NP synthesis, which utilized the Ekspla Atlantic Series Nd:YAG laser (10 ps, 100 kHz, 1064 nm), we transitioned to a more advanced system for HEAs, CCAs and NiMnSn. These were synthesized via PLAL using a near-infrared picosecond pulsed Nd:YAG laser (Coherent, HyperRapid NX, Kaiserslautern, Germany, 10 ps, 1064 nm) at laser power of 110 W. The HEA targets were ablated by focusing the laser beam with an f = 167 mm f-theta lens, coupled to a galvanometric scanner (Raylase, SS-IV-15 [1070], Wessling, Germany), generating a 6 mm-diameter hollow spiral pattern on the target surface at a scanning speed of 10 m/s. The higher scanning speed, adjustable repetition rate and higher laser power provided a more efficient and scalable approach compared to the conditions used for FeRh synthesis.

The effect of repetition rate on productivity was systematically analyzed by ablating HEA-PP targets in ethanol at different repetition rates while keeping the laser power at 110 W. The highest ablation efficiency was achieved at a repetition rate of 2000 kHz and a laser fluence of 2.8 J/cm², yielding an average NP productivity of 311 mg/h. However, increasing the laser fluence beyond 2.8 J/cm² did not further enhance productivity; instead, it resulted in a decline (Fig. 4a, Appendix: Study 2). The decrease in ablation rate at higher fluences can be attributed to the formation of laser-induced periodic surface structures (LIPSS) which was evident on the ablated target (Fig. S2, Appendix: Study 2).(Bonse, Höhm, Kirner, Rosenfeld, & Krüger, 2017; S. Lin, Shuo, Haiyan, & Jingquan, 2022) The presence of LIPSS modifies the absorption properties of the target, leading to variations in energy deposition and redistribution of the incoming laser energy. This formation of LIPSS is a well-known phenomenon in laser ablation and is influenced by the laser wavelength, pulse duration, and fluence. Studies have shown that LIPSS formation can negatively impact ablation efficiency by altering the optical properties of the surface, leading to non-uniform energy absorption and increased scattering of the laser beam.

Additionally, the fluence dependence of productivity follows a trend where ablation rates increase initially before reaching a peak and subsequently declining at higher fluences. This behavior is consistent with theoretical models, including those developed by Kanitz et al.(Kanitz et al., 2017) who studied fluence-dependent ablation in liquids. Their model describes how productivity initially rises due to increased energy input but eventually decreases due to plasma shielding, cavitation, and target surface modifications. However, our experimental data did not fully align with the Kanitz et al. model, as their framework primarily applies to femtosecond laser ablation, where material removal occurs primarily through non-thermal mechanisms. In contrast, the 10 ps laser used in our study is at the boundary between ultrashort and short-pulse regimes, where thermal effects begin to play a more significant role. This means that in addition to non-thermal ablation, hot ablation mechanisms such as surface melting and vaporization contribute to material removal, leading to deviations from purely ultrashort pulse ablation predictions.

The ablation threshold fluence of the HEA-PP was calculated using the equation $F_{th} = F_{op} / e^2$, where F_{op} is the optimum fluence, yielding a threshold of 0.38 J/cm². This value is higher than the 0.24 J/cm² threshold previously reported for CoCrFeMnNi laser ablation in air. However, those experiments were performed on a crystalline HEA target in air, which exhibited a significantly lower ablation threshold than the HEA-PP target in liquid.

Variations in productivity were also observed depending on the target preparation method. The HEA-PP target exhibited the highest productivity, measuring 6.5% and 15.1% higher than the HEA-BP and HEA-SX targets, respectively. Upon further investigation using mass spectrometer study also suggest that the threshold fluence for HEA-PP was found to be 0.36

J/cm^2 (i.e close to 0.38 J/cm^2) and 0.22 J/cm^2 for HEA-BP and HEA-SX (i.e closer to 0.24 J/cm^2). The observed difference in the ablation thresholds for alloyed HEA-BP and HEA-SX targets and the mixed elemental HEA-PP sample is likely due to different optical and thermophysical properties of the targets.

In another work we explored a different approach to improving NP productivity of multi-beam pulsed laser ablation in liquids (MB-PLAL).(Gatsa et al., 2024) This method utilizes DOEs to split the laser beam into multiple sub-beams, enabling both temporal and spatial bypassing of the cavitation bubble, which is one of the main limiting factors in PLAL efficiency. By redistributing laser energy more effectively and reducing shielding effects from cavitation bubbles, the MB-PLAL technique significantly increased NP yields without compromising particle quality. Their study demonstrated that NP production in the gram-per-hour range is achievable using this approach, making it a promising strategy for scaling up laser-based NP synthesis.

3.1.4. Magnetic and magnetocaloric nanoparticles properties

The initial study lead by Nadarajah highlights the impact of phase stability and structural transformation on the magnetic behavior of FeRh NPs synthesized via PLAL.(Nadarajah et al., 2021) The primary observation is that rapid quenching during laser ablation stabilizes the metastable γ-phase, which is predominantly PM at room temperature. This phase is not typically observed in bulk FeRh, demonstrating how the nanoscale environment and synthesis method influence phase formation. Upon annealing, the γ-phase gradually transitions into the ordered B2-phase, which is known for its AFM to FM transition near room temperature. The progressive formation of the B2-phase is reflected by the XRD, Mössbauer and Magnetometry results. While the field driven magnetic transition shows AFM-FM transition. The ΔS_M extracted from the magnetocaloric analysis confirms that the transition temperature shifts with the applied magnetic field, reinforcing the idea that external stimuli can fine-tune the phase transformation.

Overall, the findings underscore that annealing significantly enhances the magnetocaloric response of FeRh NPs by stabilizing the B2-phase and optimizing the AFM-FM transition. However, residual FM fractions and transition broadening due to disorder must be carefully considered for future applications, particularly in MCC technologies.

3.1.4.1. Magnetic response of CCAs - Bulk vs Nanoparticles

In Study 2, highlights the contrasting magnetic behavior of bulk and NP forms of Ge-based and Al-based CCAs, emphasizing the role of size effects and phase transition mechanisms. In bulk form, these CCAs undergo a FM-to-PM transition, where long-range magnetic interactions define their T_c. However, for NPs, the transition is fundamentally different, as it is governed by SPM-to-PM behavior, influenced by finite-size effects and thermal fluctuations overcoming magnetic anisotropy.

The bulk CCAs exhibit distinct magnetic phase transitions, with the Ge-based CCA transitioning at a lower temperature than the Al-based CCA, which indicates differences in exchange interactions and microstructural stability. A sharper transition in the Ge-based CCA suggests a well-defined phase boundary, whereas the broader transition in the Al-based CCA implies a gradual transformation, possibly influenced by multiple coexisting phases or microstructural defects. Magnetic hysteresis loops further confirm that the bulk Ge-based CCA retains strong FM characteristics at low temperatures, whereas the Al-based CCA exhibits weaker magnetic ordering.

In contrast, the Ge-based and Al-based CCA NPs exhibit a SPM-to-PM transition instead of a FM-to-PM transition. The M-T curves for NPs show a distinct blocking temperature at 120 K, below which thermal energy is insufficient to overcome magnetic anisotropy, leading to a divergence between ZFC and FC magnetization curves. This behavior differs from the bulk materials, where the transition is driven by long-range FM ordering. The Ge-based CCA NPs exhibit a significantly lower magnetization at low temperatures compared to their bulk counterpart due to size effects, thermal fluctuations, and oxide shell formation, which reduces the magnetically active volume. Additionally, the H_C of the Ge-based CCA NPs at 5 K is much higher than in the bulk sample due to enhanced surface anisotropy and core-shell NP structure. Similarly, the Al-based CCA NPs exhibit a blocking temperature at 100 K and also display higher H_C compared to their bulk counterpart, which is again attributed to enhanced anisotropy in small particles. However, their lower H_C at 300 K compared to Ge-based NPs suggests differences in oxide shell formation and the proportion of larger ferromagnetic particles.

Since the magnetic phase transitions in bulk and NP CCAs are fundamentally different, direct comparisons of magnetic moment values between the two are not appropriate. In bulk materials, the transition is associated with FM to PM ordering, while in NPs, the transition occurs due to thermal activation overcoming the magnetic anisotropy barrier, leading to SPM behavior. The higher H_C in NPs at low temperatures could be due to enhanced surface anisotropy, while their lower magnetization results from oxide shell formation and size-dependent magnetic dilution effects. The differences in T_B, H_C, and magnetization highlight the size-dependent nature of magnetic properties in CCAs and demonstrate how nanoscale effects modify the fundamental phase transition mechanisms compared to bulk materials.

3.1.4.2. Magnetic response of NiMnSn – Nanoparticles vs Microparticles

To compare the magnetic properties of NPs and MPs, NiMnSn Heusler alloys was investigated. In this work, compositionally controlled synthesis of NPs was strategically achieved via PLAL of powder-pressed and sintered NiMnSn micropowder targets with additional Mn MPs to compensate for Mn loss during laser-induced evaporation. This approach ensured that the resulting NPs maintained a composition similar to the starting bulk material.

The M-T measurements of NiMnSn MPs revealed two distinct magnetic transitions under a low applied field of 10 mT. The first transition occurred at approximately 300 K, followed by a second transition around 200 K, both associated with the austenite-to-martensite transformation. The presence of two transitions suggests compositional inhomogeneity within the powder, likely due to segregation effects during gas atomization, which cause different regions to transform at slightly different temperatures. The T_c of the austenite phase was estimated at ~315 K, while the martensitic phase exhibited a lower T_c of ~230 K, indicating a mixed-phase system. These results are consistent with NiMn-based Heusler alloys, where atomic ordering and phase coexistence play a critical role in magnetic behavior. Under a higher applied field of 1 T, the first transition temperature shifted downward by ~5 K to 295 K, highlighting the effect of the external field in stabilizing one of the phases. Meanwhile, the second transition became indistinguishable due to the comparable magnetization values of the austenite and martensite phases, resulting in a flattened dM/dT signal.

In contrast, the M-T curves of NiMnSn NPs exhibited a more gradual decrease in magnetization with increasing temperature, lacking the distinct two-step phase transition observed in MPs. The broadening and weakening of the magnetic transitions in NPs can be attributed to multiple factors, including oxidation effects, which are common in nanosized materials, as well as SPM behavior in smaller particles and the presence of AFM interactions from surface oxides. The reduced fraction of austenite-martensite phase conversion in NPs suggests a compositional inhomogeneity at the nanoscale. Interestingly, these diffuse transitions were absent in off stoichiometric NPs synthesized by PLAL of bulk NiMnSn target produced via arc melting, indicating that compositionally controlled synthesis plays a crucial role in preserving a distinct austenite-martensite transition near room temperature. Similar to MPs, at 1 T, the transition was further suppressed, as the magnetization contrast between the austenite and martensite phases was reduced, making the transformation less distinguishable.

3.1.5. Laser Printing of magnetocaloric structures

3.1.5.1. Printing of FeRh microstructures

Initial Study on laser-printed structures of FeRh NP ink demonstrated that a phase transition could be induced in millimeter-scale printed lines using laser sintering.(Nadarajah et al., 2021) The FeRh ink, composed of PLAL-synthesized FeRh NPs dispersed in a solvent, was deposited onto a polymer coated glass substrate and then subjected to laser sintering to form compact 2D structures. Upon laser sintering, the NPs were densely compacted, forming a continuous bulk-like structure with significantly reduced porosity. The effectiveness of sintering was further confirmed by sheet resistance measurements, which serve as an indicator of electrical connectivity and interparticle compactness. Structural characterization revealed the presence of both fcc and bcc phases, indicating that thermal effects during laser sintering influenced phase stability. The unsintered FeRh ink exhibited minimal magnetization and no coercive field, confirming that as-synthesized FeRh NPs predominantly exist in the PM γ-phase. However, after laser sintering, the sample displayed a noticeable increase in magnetization, along with the emergence of a magnetic hysteresis loop, indicating that a partial γ-to-B2 phase transformation had occurred.

Compared to initial developments by Nadarajah and co (Nadarajah et al., 2021) where millimetre-scale laser-sintered FeRh structures were demonstrated, Study 1 shows successful printing of FeRh at micron-scale and optimizing both structural and magnetic properties. The laser fluence played a crucial role in determining the printing morphology, affecting the degree of NP sintering, densification, and phase transformation. At low fluences, partial sintering was observed, where NPs fused together but retained significant porosity due to incomplete coalescence. As fluence increased, the NPs densified, forming a continuous structure with enhanced interparticle connectivity. At even higher fluences, partial ablation occurred, leading to material loss, while at very high fluences, substrate damage was observed due to excessive energy absorption. The reflectance spectroscopy measurements (Fig. S1, Appendix: Study 1) provided key insights into the sintering and ablation mechanisms during laser processing of FeRh NP inks. By analyzing the reflectance at different laser fluences, it was observed that the reflectance increased linearly with fluence, indicating a reduction in NP concentration due to ablation. This effect is attributed to the thinning of the NP film, allowing more reflection from the underlying glass-ceramic substrate. The reflectance spectra were measured across wavelengths ranging from 600 to 900 nm, where a consistent increase was noted with fluence. This trend correlates with the ablation-induced porosity increase, which also impacts on the overall morphology of the printed structures.

The evolution of surface morphology with increasing fluence was examined through optical and SEM imaging, revealing a transition from discontinuous and porous regions at low fluences to fully consolidated structures at intermediate fluences (Fig. 2, Appendix: Study 1).

At 41 J/cm², continuous sintered lines were formed, but individual particles were still visible, suggesting incomplete densification. At 57 J/cm², the microstructures became denser, with fewer distinguishable particles and reduced porosity. Beyond 131 J/cm², partial ablation effects introduced defects such as voids and irregular surface textures, while at 246 J/cm², excessive laser energy led to a combination of material vaporization and substrate modification. These results demonstrate that optimal sintering conditions exist within a specific fluence range, where consolidation is maximized without inducing ablation-related defects.

The structural transformations induced by laser sintering were analyzed using XRD (Fig. 5 Appendix: Study 1), which confirmed the progressive transition from γ-FeRh to B2-FeRh with increasing fluence. The fraction of the magnetically ordered B2 phase increased steadily, reaching a maximum of 52% at 246 J/cm², while lower fluences resulted in a mixed-phase composition with a dominant γ-phase. In contrast, conventional furnace annealing at 873 K in air led to complete oxidation, forming Fe_2O_3, while annealing under argon resulted in a mixture of γ-FeRh, B2-FeRh, and minor Fe_3O_4 contributions. The laser-sintered structures exhibited significantly less oxidation, demonstrating that rapid heating and cooling during laser sintering effectively suppresses oxide formation, maintaining the desired FeRh composition.

The magnetic properties of the sintered structures were strongly correlated with the phase transformation (Fig. 6, Appendix: Study 1). Magnetization measurements at 500 K showed that increasing fluence enhanced the M_S, consistent with the progressive formation of the FM B2 phase. At fluences below 131 J/cm², minor oxide contributions influenced the H_C and introduced a secondary magnetic phase, while at higher fluences, a more significant FM response was observed, confirming the dominance of the B2 phase. Compared to furnace-annealed FeRh NPs, laser sintering produced higher magnetization values, indicating its superior ability to induce phase transformation while minimizing unwanted oxidation.

M-T curves confirmed the presence of the AFM-FM phase transition, which occurred at approximately 460 K in the laser-sintered structures (Fig. S4, Appendix: Study 1). Unlike bulk FeRh, which exhibits a sharp transition, the sintered structures displayed a broader transition, likely due to stoichiometric variations, structural defects, and residual γ-phase. Field-dependent magnetization curves revealed a progressive increase in FM ordering with increasing fluence, further validating the role of laser sintering in tuning FeRh's phase and magnetic properties. The magnetocaloric response of the printed structures was assessed by extracting the ΔS_M from field-dependent magnetization measurements (Fig. S5, Appendix: Study 1). The approached ΔS_M of 3-3.5 J/kg·K at 9 T, showing a notable improvement over furnace-annealed FeRh NPs, which exhibited a lower field-induced magnetization change.

The enhanced MCE in laser-sintered structures can be attributed to the higher B2-phase fraction and reduced oxidation, which minimize competing PM and AFM contributions.

3.1.5.2. Printing of NiMnSn microstructures

In final work (Study 4) the printing of NiMnSn was compared for both MP and NP inks, demonstrating significant resolution improvements when using NiMnSn NPs. The MP ink, composed of gas-atomized NiMnSn MPs dispersed in ethanol, was successfully printed into structured magnetocaloric materials, but the resulting features exhibited 4 times lower resolution and increased roughness due to the larger particle size (~10 μm) (Fig. 4, Appendix: Study 4). In contrast, the NP ink, formulated from PLAL-synthesized NiMnSn NPs (~12.4 nm average size), produced higher-resolution structures with greater uniformity, owing to the improved dispersion and finer particle distribution. The sintering threshold for both MP and NP inks was examined by varying laser fluence. For MP inks, sintering initiated at 0.76 J/cm², but complete and uniform sintering required 0.89 J/cm². Beyond this threshold, partial ablation occurred, leading to mass loss and localized defects. For NP inks, sintering began at a lower fluence of 0.66 J/cm², reaching complete densification at 0.87 J/cm², similar to MPs, showing laser sintering fluence is not affected by particle size.

The magnetic properties of the printed structures were analyzed in comparison to their unsintered counterparts (Fig. 5, Appendix: Study 4). The M-T curves for sintered MP structures at low fluence closely resembled those of raw MPs, exhibiting two distinct phase transitions at ~200 K and ~300 K, corresponding to the martensitic and austenitic transformation. However, the overall magnetization increased in the sintered MPs, likely due to improved interparticle connectivity and enhanced FM coupling during sintering. At high fluence, ablation-induced material loss caused a reduction in magnetization, and the 300 K transition became less pronounced, indicating that some of the material no longer underwent complete austenite-martensite transformation. These changes suggest that excessive heating and ablation may induce compositional inhomogeneity or oxidation, leading to a suppressed phase transition. For NP-printed structures, the M-T curves at low fluence showed a gradual decrease in magnetization with increasing temperature, with no sharp transitions at 200 K or 300 K. Instead, the transition appeared broad and weak, similar to unsintered NiMnSn NPs, suggesting that the martensitic transformation is significantly suppressed in NPs. This effect is attributed to oxidation, SPM behavior, and increased disorder introduced during laser sintering. At high fluence, the broad transition at 200–300 K was further suppressed, indicating that higher thermal energy and ablation effects further disrupted the structural transition. Similar trends were observed for sintered MPs at high fluence, reinforcing the idea that laser fluence optimization is crucial for preserving magnetic phase transitions.

Comparing NPs with laser printed NP structures, the phase transition features remained similar, but sintering at high fluence led to suppression of phase transition. In contrast, comparing printed MPs vs. laser printed MP structures, the magnetization of the sintered MPs increased at low fluence compared to MPs, whereas it decreased at high fluence due to ablation effects. The broadening and suppression of phase transitions in NiMnSn NPs were consistent with those observed for Ge-based and Al-based CCAs, confirming that nanoscale structuring and laser sintering introduce size-dependent and disorder-related modifications to magnetocaloric properties.

3.2. Discussion of the scope

This study extends the synthesis of magnetocaloric materials beyond binary systems, demonstrating that PLAL can produce ternary and CCA NPs. By carefully selecting target preparation methods, particularly the use of powder-pressed and sintered targets, it was possible to achieve desirable NP compositions. The successful synthesis of FeRh NPs, NiMnSn Heusler NPs, CoCrFeMnNi HEA NPs, and Ge-based and Al-based CCA NPs confirmed that PLAL can be used to fabricate multicomponent systems. Additionally, the laser printing of such NP inks on substrates lead to sintering of particles, achieving desirable phases and improved magnetic/magnetocaloric properties, forming high-resolution custom structures.

3.2.1. Application in the Real World

The findings of this study have significant implications for the development of next-generation magnetocaloric materials and their applications in energy-efficient cooling technologies, microelectronics, and functional coatings. The successful synthesis of ternary and CCA NPs via PLAL opens new avenues for creating rare-earth-free magnetocaloric materials, which are crucial for sustainable refrigeration. The ability to fabricate NiMnSn Heusler NPs, CoCrFeMnNi HEA NPs, and Ge-based and Al-based CCA NPs with controlled compositions by PLAL means that tunable magnetocaloric properties can be achieved, offering alternatives to conventional rare-earth-based systems.

Furthermore, the successful demonstration of laser-printed magnetocaloric microstructures at the micron scale provides new possibilities for miniaturized thermal management applications. In compact electronic devices, where precise temperature control is essential, the use of high-resolution magnetocaloric microstructures could significantly enhance heat dissipation, leading to more efficient performance and longevity. The insights gained from laser sintering of FeRh and NiMnSn structures show that material properties can be tailored through precise fluence adjustments, making it possible to integrate magnetocaloric materials into MEMS and microfluidic cooling systems.

Another potential application of the findings is in functional coatings for sensors and actuators. The ability to synthesize and structure magnetic NPs with controlled phase transitions can contribute to the development of responsive coatings, which exhibit tunable magnetic and thermal properties based on environmental conditions. These applications, coupled with the scalability of the synthesis and structuring methods explored in this study, underscore the potential of PLAL and laser printing in driving technological innovation in materials science.

3.2.2. Contribution to Literature

This research contributes to the growing body of literature on nanostructured magnetocaloric materials by systematically exploring composition control, phase stability, size-dependent magnetic transitions, and its printing via laser processing. One of the key contributions of this work is demonstrating how PLAL can be successfully extended to multicomponent alloys, including HEAs and CCAs, highlighting the role of target preparation and ablation mechanisms in determining final NP composition. Previous studies focused primarily on binary systems, whereas this study expands the synthesis methodology to more complex alloys, showing how elemental segregation and oxidation can be mitigated through optimized target fabrication.

Another significant contribution is the detailed comparison of magnetic properties across bulk, MP, and NP forms of with either NiMnSn and CCAs. The observation that NPs exhbit superparamagnetic behaviour refines our understanding of size-dependent magnetic properties. The application of blocking temperature calculations provides a new perspective on NP phase stability and magnetization behavior, building on previous works in the field.

In terms of laser structuring, this research advances the miniaturization of magnetocaloric materials, showing that NP-based inks provide significantly improved printing resolution compared to MP-based inks. This represents a major step forward in fabricating micron-scale functional materials for thermal management applications.

3.2.3. Strengths and Limitations

This study demonstrates several key strengths in both NP synthesis and structuring techniques. The use of PLAL for Heusler alloys, HEAs, and CCAs provided an efficient, solvent-controlled synthesis approach, enabling fine-tuned compositional control without the need for surfactants or additional reducing agents. The ability to synthesize compositionally controlled NiMnSn NPs by compensating for Mn loss was a novel approach, ensuring that phase transitions were preserved at the nanoscale.

A major strength of the study is the ability to directly compare bulk, MP, and NP forms of magnetocaloric materials. The findings provide insights into how size reduction alters magnetic phase transitions, H_C, and ΔS_M, which is critical for developing next-generation functional materials. Additionally, laser printing of NiMnSn and FeRh microstructures at micron resolution represents a significant advancement over previous millimeter-scale printing techniques, demonstrating the potential for miniaturized magnetocaloric devices.

However, several limitations remain. While PLAL successfully synthesized complex alloy NPs, elemental evaporation losses during ablation still led to minor compositional deviations, requiring further refinement of target compositions. Additionally, while laser sintering enabled controlled phase transitions, complete γ-FeRh to B2-FeRh conversion remains challenging, as residual γ-phase and oxidation effects persist. In NiMnSn-printed structures, high fluence led to phase suppression, indicating that precise control over energy deposition is necessary to maintain magnetic transitions. Another limitation is the low yield of PLAL compared to traditional solid-state synthesis methods. While increasing repetition rate and laser power enhanced productivity, further strategies such as optimization of multi-beam ablation and scanning approach to bypass cavitation bubbles could be explored to scale up production for practical applications.

3.3. Conclusion and Outlook

This thesis presents a comprehensive experimental framework for the synthesis, microstructural refinement, and can explore the functional integration of rare-earth-free magnetocaloric nanomaterials. The research combines pulsed laser ablation in liquids (PLAL) with continuous-wave laser sintering to systematically address long-standing challenges in the field, including precise composition control, magnetic phase retention, and microscale device integration. These issues are of particular importance when working with metallic alloys that exhibit magnetocaloric effects, as their performance is highly sensitive to composition, crystal structure, and thermal history. The experimental approach developed here is applied across four distinct alloy systems of increasing compositional complexity: the binary FeRh system, the equiatomic CoCrFeMnNi high-entropy alloy (HEA), the MnFeNiGeSi/Al compositionally complex alloys (CCAs), and the ternary NiMnSn Heusler compound. Collectively, these systems span the spectrum from model magnetocaloric compounds to materials with strong application potential. The laser-based techniques employed throughout the work enable not only rapid, surfactant-free nanoparticle (NP) synthesis with high compositional fidelity, but also precise structuring and phase activation of materials in thin-film or printed formats. The overall strategy offers a versatile, scalable, and compositionally tunable route to developing magnetocaloric materials that can meet the practical demands of solid-state cooling and thermomagnetic devices.

The investigation begins with the FeRh system, a prototypical magnetocaloric compound known for its sharp and reversible antiferromagnetic (AFM) to ferromagnetic (FM) phase transition, which occurs when the material adopts the ordered B2 structure. This transition is first-order in nature and is accompanied by a substantial entropy and magnetization change, making FeRh highly relevant for thermomagnetic and caloric applications. However, the practical application of FeRh is hindered by challenges in processing. Achieving the B2 phase typically requires extended high-temperature annealing, which often introduces oxidation, grain coarsening, and limited spatial control, rendering it unsuitable for miniaturized device fabrication. In this thesis, FeRh nanoparticles were synthesized via PLAL using arc-melted targets, yielding nearly equiatomic compositions and spherical particles with a mixed γ and B2 phase structure. The as-synthesized NPs exhibited weak magnetization and no clear transition behavior, indicating the need for post-synthesis phase activation. To address this, continuous-wave laser sintering was applied to printed FeRh NP layers, with fluence optimized at 246 J/cm². This treatment successfully induced the γ → B2 transformation, resulting in microstructures with increased phase purity, enhanced crystallinity, and low oxidation. Magnetization measurements confirmed a broad but robust AFM-FM transition spanning from 150 K to 460 K, with a field-induced magnetization jump (ΔM) of approximately 35 Am²/kg and a saturation magnetization of ~98 Am²/kg, values that represent a four- to six-fold enhancement over furnace-annealed counterparts.

One particularly notable outcome was the observation of ferromagnetic behavior at temperatures below the expected transition threshold. This phenomenon, attributed to pinned FM domains stabilized by rapid thermal gradients or strain during laser processing, underscores the potential of laser sintering not only as a densification method but also as a tool for inducing non-equilibrium magnetic states. This ability to locally modify magnetic phase behavior opens new pathways for tuning magnetocaloric performance by controlling laser parameters. Moreover, the successful printing and activation of micron-scale FeRh structures demonstrate the feasibility of integrating magnetocaloric materials into microelectromechanical systems (MEMS), thermal switches, and other miniaturized devices. The results from the FeRh system thus establish a strong precedent for combining PLAL and laser sintering to overcome the limitations of conventional thermal processing, while offering new degrees of freedom in spatially resolving magnetic function.

Building on these results, the research then moves into the CoCrFeMnNi HEA system to test the methodology on a compositionally more complex material. HEAs are of growing interest in the materials community due to their configurational entropy, which stabilizes single-phase solid solutions and provides remarkable thermal and mechanical stability. From a magnetocaloric perspective, HEAs offer tunable magnetic transitions, high corrosion resistance, and enhanced fatigue strength, making them promising for long-term cycling and multifunctional roles. However, their complex chemistry introduces significant challenges for nanoparticle synthesis, particularly in maintaining equiatomic composition and avoiding phase segregation. In this work, PLAL was applied to three HEA target types that are powder-pressed (HEA-PP), ball-milled and sintered (HEA-BP), and Bridgman-grown single-crystal (HEA-SX) ingots. Across all targets, PLAL in ethanol produced nanoparticles with FCC phase structure and sizes ranging from 2 to 100 nm. Among these, the HEA-PP targets were the most successful, producing spherical nanoparticles with minimal segregation and near-equiatomic distribution, as confirmed by energy-dispersive X-ray spectroscopy (EDX) and transmission electron microscopy (TEM). Importantly, HEA-PP targets also provided the highest productivity (~311 mg/h), reinforcing their suitability for scalable synthesis.

In contrast, HEA-BP and HEA-SX targets exhibited evidence of Mn enrichment at the nanoparticle surface and partial core–shell formation, likely due to differences in target microstructure and ablation dynamics. These findings emphasize the critical role of target preparation that not only in ensuring reproducibility and productivity, but also in dictating the final NP morphology and composition. These results also confirm that PLAL can be extended beyond binary or ternary systems to produce chemically complex alloy nanoparticles without requiring complex pre-alloying or arc-melting steps. The ability to tailor target design and laser parameters to produce NPs with specific structural and compositional features opens the door to high-throughput screening of novel HEA compositions for magnetic and thermofunctional applications.

The third material class studied in this thesis consists of CCAs based on the MnFeNiGeSi and MnFeNiSiAl systems. These alloys are of interest due to their first-order magnetostructural transitions, which are associated with large entropy changes and field-driven magnetization jumps. The Ge-based CCA exhibits a FM-PM transition at approximately 179 K with a saturation magnetization of 68.2 Am^2/kg at 5 K, while the Al-based analog transitions at 263 K with lower saturation but significant cost and resource advantages. In bulk form, these materials have been shown to exhibit reversible transitions and competitive magnetocaloric performance, but their processing is typically limited to high-temperature sintering or arc melting. In this thesis, the Ge-based alloy was synthesized via spark plasma sintering, while the Al-based version was prepared from powder-pressed targets. PLAL was applied to both, resulting in spherical nanoparticles with average sizes between 13 and 18 nm. Structural analysis indicated the retention of mixed BCC and FCC phases, with XRD peak broadening indicative of partial disorder and size-induced strain. Magnetically, both NP systems exhibited superparamagnetic behavior, with blocking temperatures near 120 K (Ge-based) and 100 K (Al-based), and significant reductions in saturation magnetization compared to the bulk. These observations are consistent with size effects, surface oxidation, and the suppression of long-range magnetic order in nanoscale particles.

Despite the expected reduction in magnetic response, the Al-based CCAs retained clear magnetic transition signatures and demonstrated an appealing balance between functional performance and elemental sustainability. The replacement of Ge with Al not only reduces material cost and environmental impact but also maintains critical magnetic properties at usable temperatures. This finding is significant because it supports the broader objective of developing magnetocaloric materials that are free from both rare-earth elements and other critical raw materials. Furthermore, the successful synthesis of CCA NPs via PLAL highlights the technique's applicability to metastable and structurally complex systems, providing a means to generate high-surface-area powders suitable for printing, sintering, or incorporation into composites. The behavior of these nanoparticles suggests they could be used in flexible or dispersed magnetocaloric architectures, especially when a distributed magnetic response or high surface-to-volume ratio is desirable. This work illustrates the potential of combining compositional tuning and laser-based synthesis to extend magnetocaloric material functionality beyond traditional systems, while aligning with goals for sustainable and scalable processing.

The final system investigated is NiMnSn, a Heusler-type alloy that undergoes a martensitic transition coupled with an FM-PM magnetic transition, resulting in a strong inverse magnetocaloric effect near room temperature. NiMnSn is particularly attractive due to its compositionally tunable transformation temperature and significant field-induced entropy change. However, its practical deployment is limited by its sensitivity to stoichiometry, especially with respect to Mn, which tends to evaporate or oxidize during processing. In this work, three target types were evaluated for PLAL: arc-melted ingots, powder-pressed elemental mixtures, and micropowder-based targets with excess Mn (Type 3). The Type 3 targets were the most successful, yielding nanoparticles with compositions close to $Ni_{50}Mn_{36}Sn_{14}$, average sizes of ~12 nm, and narrow size distributions. These NPs retained the desired Curie temperature (~300 K) and exhibited blocked superparamagnetic behavior. Arc-melted targets, by contrast, showed significant Mn loss and degraded magnetic response. The composition-stabilized NPs thus demonstrate the effectiveness of target engineering in preserving functional magnetic behavior during laser ablation.

Both NP and MP inks were prepared and sintered using laser processing. MP-based inks resulted in films with higher overall magnetization due to larger particle sizes and improved phase connectivity, but the NP-based inks allowed for finer patterning and smoother layers. Optimal fluence values enabled magnetic activation while avoiding thermal damage;

excessive fluence led to ablation or oxidation and loss of magnetocaloric properties. These observations reveal the processing sensitivities of NiMnSn and underscore the value of combining target design with carefully controlled sintering conditions. The NiMnSn results bridge the thesis from material development to application feasibility, demonstrating that laser-based processing routes can be used to fabricate functional magnetocaloric films with Curie temperatures near ambient conditions, suitable for room-temperature cooling or actuation.

In conclusion, this thesis presents a generalized, experimentally validated framework for synthesizing and microstructuring magnetocaloric materials using PLAL and laser sintering. Across four representative alloy systems, each presenting distinct challenges and advantages—the methods demonstrated here consistently enable the production of compositionally controlled, nanostructured materials with functional magnetic transitions. The FeRh study demonstrated phase transformation and enhancement via laser sintering. The CoCrFeMnNi HEA work showed that PLAL is feasible for multicomponent systems with high productivity and structural uniformity. The CCA research demonstrated compositional tuning toward sustainability, and the NiMnSn study emphasized the feasibility of tailoring sensitive materials through target design. Together, these results define a process-agnostic platform that is applicable to future research in magnetocaloric materials, whether for bulk powder production, thin-film deposition, or microscale patterning.

Looking ahead, the research opens numerous avenues. First, the integration of real-time composition monitoring during PLAL could enable closed-loop control over elemental losses and enhance reproducibility. Second, the functionalization of nanoparticle surfaces with protective or active layers could reduce oxidation and extend stability for storage or device integration. Third, advanced ink formulations incorporating binders, dispersants, or other functional additives could improve film homogeneity and enable multilayer or heterogeneous designs. Finally, further exploration of magnetocaloric composites with graded particle size or composition could enable broader thermal spans and more efficient cycling in practical cooling systems. The platform developed here is sufficiently flexible to accommodate these advances, and serves as a foundation for the next generation of environmentally responsible, thermomagnetic materials and devices.

4. References

Ahmad, A., Mitra, S., Srivastava, S. K., & Das, A. K. (2019). Size-dependent structural and magnetic properties of disordered Co2FeAl Heusler alloy nanoparticles. *Journal of Magnetism and Magnetic Materials, 474*, 599-604. doi:https://doi.org/10.1016/j.jmmm.2018.12.035

Ahn, K. (2024). Ni-Mn based conventional full Heusler alloys, all-d-metal full Heusler alloys, and their promising functional properties to solid state cooling by magnetocaloric effect. *Journal of Alloys and Compounds, 978*, 173378. doi:https://doi.org/10.1016/j.jallcom.2023.173378

Al-Qudsi, A., Kammler, M., Bouguecha, A., Bonk, C., & Behrens, B.-A. (2015). Comparison between different numerical models of densification during solid-state sintering of pure aluminium powder. *Production Engineering, 9*(1), 11-24. doi:https://doi.org/10.1007/s11740-014-0574-7

Amirov, A. A., Permyakova, E. S., Yusupov, D. M., Savintseva, I. V., Murliev, E. K., Rabadanov, K. S., . . . Aliev, A. M. (2025). Thermoresponsive PNIPAM/FeRh Smart Composite Activated by a Magnetic Field for Doxorubicin Release. *ACS Applied Engineering Materials, 3*(2), 410-418. doi:https://doi.org/10.1021/acsaenm.4c00730

Annaorazov, M. P., Asatryan, K. A., Myalikgulyev, G., Nikitin, S. A., Tishin, A. M., & Tyurin, A. L. (1992). Alloys of the FeRh system as a new class of working material for magnetic refrigerators. *Cryogenics, 32*(10), 867-872. doi:https://doi.org/10.1016/0011-2275(92)90352-B

Aprea, C., Greco, A., Maiorino, A., & Masselli, C. (2020). Magnetocaloric as Solid-State Cooling Technique for Energy Saving. In *Global Issues and Innovative Solutions in Healthcare, Culture, and the Environment* (pp. 226-252). doi:https://doi.org/10.4018/978-1-7998-3576-9.ch012

Aschauer, U., Braddell, R., Brechbühl, S. A., Derlet, P. M., & Spaldin, N. A. (2016). Strain-induced structural instability in FeRh. *Physical Review B, 94*(1), 014109. doi:https://10.1103/PhysRevB.94.014109

Aydogdu, Y., Turabi, A. S., Kok, M., Aydogdu, A., Yakinci, Z. D., Aksan, M. A., . . . Karaca, H. E. (2016). The effect of Sn content on mechanical, magnetization and shape memory behavior in NiMnSn alloys. *Journal of Alloys and Compounds, 683*, 339-345. doi:https://doi.org/10.1016/j.jallcom.2016.05.108

Bangalore, M., Hallegatte, S., Bonzanigo, L., Fay, M., Narloch, U., Rozenberg, J., & Vogt-Schilb, A. (2014). An Analytical Framework. Policy Research Working Paper;No. 7126. © World Bank Group. *World Bank Group, 7126*. doi:https://doi.org/10.1596/1813-9450-7126

Banizi, M. T., Khakbiz, M., Shakibania, S., Amiri, E., & Naserian, F. (2024). Functionalized high entropy alloys with ZIF-8 and LDH nanolayers for next-generation drug eluting medical implants. *Journal of Alloys and Compounds, 997*, 174883. doi:https://doi.org/10.1016/j.jallcom.2024.174883

Bedanta, S., & Kleemann, W. (2009). Supermagnetism. *Journal of Physics D: Applied Physics, 42*(1), 013001. doi:https://10.1088/0022-3727/42/1/013001

Belo, J. H., Pires, A. L., Araújo, J. P., & Pereira, A. M. (2019). Magnetocaloric materials: From micro- to nanoscale. *Journal of Materials Research, 34*(1), 134-157. doi:https://doi.org/10.1557/jmr.2018.352

Biswas, A., Chandra, S., Phan, M.-H., & Srikanth, H. (2012). Magnetocaloric properties of nanocrystalline LaMnO3: Enhancement of refrigerant capacity and relative cooling power. *Journal of Alloys and Compounds, 545*, 157-161. doi:https://doi.org/10.1016/j.jallcom.2012.08.001

Biswas, A., Pathak, A. K., Zarkevich, N. A., Liu, X., Mudryk, Y., Balema, V., . . . Pecharsky, V. K. (2019). Designed materials with the giant magnetocaloric effect near room temperature. *Acta Materialia, 180*, 341-348. doi:https://doi.org/10.1016/j.actamat.2019.09.023

Bonse, J., Höhm, S., Kirner, S. V., Rosenfeld, A., & Krüger, J. (2017). Laser-Induced Periodic Surface Structures— A Scientific Evergreen. *IEEE Journal of Selected Topics in Quantum Electronics, 23*(3), 1. doi:https://doi.org/10.1109/JSTQE.2016.2614183

Brown, M., Zappitelli, K., Singh, L., Yuan, R., Bemrose, M., Brogden, V., . . . Gardner, T. (2023). Direct laser writing of 3D electrodes on flexible substrates. *Nature Communications, 14*. doi:https://doi.org/10.1038/s41467-023-39152-7

Bruchon, J., Pino-Muñoz, D., Valdivieso, F., & Drapier, S. (2012). Finite Element Simulation of Mass Transport During Sintering of a Granular Packing. Part I. Surface and Lattice Diffusions. *Journal of the American Ceramic Society, 95*(8), 2398-2405. doi:https://doi.org/10.1111/j.1551-2916.2012.05073.x

Brück, E. (2005). Developments in magnetocaloric refrigeration. *Journal of Physics D: Applied Physics, 38*, R381. doi:https://doi.org/10.1088/0022-3727/38/23/R01

Cao, Y., Yuan, Y., Shang, Y., Zverev, V. I., Gimaev, R. R., Barua, R., . . . Fu, H. (2020). Phase transition and magnetocaloric effect in particulate Fe-Rh alloys. *Journal of Materials Science, 55*(27), 13363-13371. doi:https://doi.org/10.1007/s10853-020-04921-y

Cedervall, J., Andersson, M. S., Delczeg-Czirjak, E. K., Iuşan, D., Pereiro, M., Roy, P., . . . Deen, P. P. (2019). Magnetocaloric effect in Fe2P: Magnetic and phonon degrees of freedom. *Physical Review B, 99*(17), 174437. doi:https://doi.org/10.1103/PhysRevB.99.174437

Chang, L., Jing, H., Liu, C., Qiu, C., & Ling, X. (2024). High-Entropy Materials for Prospective Biomedical Applications: Challenges and Opportunities. *Advanced Science, 11*(42), 2406521. doi:https://doi.org/10.1002/advs.202406521

Chen, L., Liu, J., Jiang, C., Zhao, K., Chen, H., Shi, X., . . . Zhang, Z. (2019). Nanoscale Behavior and Manipulation of the Phase Transition in Single-Crystal Cu2Se. *Advanced Materials, 31*(4), 1804919. doi:https://doi.org/10.1002/adma.201804919

Ciuculescu, D., Amiens, C., Respaud, M., Falqui, A., Lecante, P., Benfield, R. E., . . . Chaudret, B. (2007). One-Pot Synthesis of Core−Shell FeRh Nanoparticles. *Chemistry of Materials, 19*(19), 4624-4626. doi:https://doi.org/10.1021/cm0715343

Ciuculescu, D., Amiens, C., Respaud, M., Lecante, P., Falqui, A., & Chaudret, B. (2007). Synthesis and characterization of FeRh nanoparticles. *Modern Physics Letters B, 21*(18), 1153-1159. doi:https://doi.org/10.1142/S0217984907013857

Coey, J. M. D. (2020). History of Magnetism and Basic Concepts. In M. Coey & S. Parkin (Eds.), *Handbook of Magnetism and Magnetic Materials* (pp. 1-49). Cham: Springer International Publishing. doi:https://doi.org/10.1007/978-3-030-63101-7_1-1

Cui, J., Kramer, M., Zhou, L., Liu, F., Gabay, A., Hadjipanayis, G., . . . Sellmyer, D. (2018). Current progress and future challenges in rare-earth-free permanent magnets. *Acta Materialia, 158*, 118-137. doi:https://doi.org/10.1016/j.actamat.2018.07.049

Dan, N. H., Duc, N. H., Yen, N. H., Thanh, P. T., Bau, L. V., An, N. M., . . . Yu, S. C. (2015). Magnetic properties and magnetocaloric effect in Ni–Mn–Sn alloys. *Journal of Magnetism and Magnetic Materials, 374*, 372-375. doi:https://doi.org/10.1016/j.jmmm.2014.08.061

Datta, S., & Kar, M. (2022). NiMnSn half Heusler alloy: Critical phenomena at the ferromagnetic to paramagnetic phase transition. *Materials Today: Proceedings, 57*, 431-435. doi:https://doi.org/10.1016/j.matpr.2021.12.540

de Oliveira, T. G., Fagundes, D. V., Capellato, P., Sachs, D., & da Silva, A. A. (2022). A Review of Biomaterials Based on High-Entropy Alloys. *Metals, 12*(11). doi:10.3390/met12111940

de Paula, V. G., da Silva, L. M., dos Santos, A. O., Lang, R., Otubo, L., Coelho, A. A., & Cardoso, L. P. (2016). Magnetocaloric effect and evidence of superparamagnetism in GdAl2 nanocrystallites: A magnetic-structural correlation. *Physical Review B, 93*(9), 094427. doi:https://doi.org/10.1103/PhysRevB.93.094427

Del Rose, T. J., Chouhan, R. K., Doyle, A., Pathak, A. K., & Mudryk, Y. (2024). LaFeSi–LaFe13−xSix composites: Modulating magnetic and magnetocaloric properties through inherent stress manipulation. *Journal of Applied Physics, 136*(3). doi:https://doi.org/10.1063/5.0212650

Dell'Aglio, M., Gaudiuso, R., De Pascale, O., & De Giacomo, A. (2015). Mechanisms and processes of pulsed laser ablation in liquids during nanoparticle production. *Applied Surface Science, 348*, 4-9. doi:https://doi.org/10.1016/j.apsusc.2015.01.082

Dillon, S. J., Ma, Y., Oyang, J.-h., Coffman, D. K., Hussein, O., Hattar, K., & Abdeljawad, F. (2023). Interface nucleation rate limited densification during sintering. *Acta Materialia, 242*, 118448. doi:https://doi.org/10.1016/j.actamat.2022.118448

Dudek, M., Dudek, K., Wolak, W., Wojciechowski, K., & Grima, J. (2019). Magnetocaloric materials with ultra-small magnetic nanoparticles working at room temperature. *Scientific Reports, 9*, 17607. doi:https://doi.org/10.1038/s41598-019-53617-0

Dullweber, T., Gatz, S., Hannebauer, H., Falcon, T., Hesse, R., Schmidt, J., & Brendel, R. (2012). Towards 20% efficient large-area screen-printed rear-passivated silicon solar cells. *PROGRESS IN PHOTOVOLTAICS, 20*(6), 630-638. doi:https://doi.org/10.1002/pip.1198

Ermak, O., Zenou, M., Toker, G. B., Ankri, J., Shacham-Diamand, Y., & Kotler, Z. (2016). Rapid laser sintering of metal nano-particles inks. *Nanotechnology, 27*(38), 385201. doi:https://doi.org/10.1088/0957-4484/27/38/385201

Fazio, E., Gökce, B., De Giacomo, A., Meneghetti, M., Compagnini, G., Tommasini, M., . . . Neri, F. (2020). Nanoparticles Engineering by Pulsed Laser Ablation in Liquids: Concepts and Applications. *Nanomaterials (Basel), 10*(11). doi:https://doi.org/10.3390/nano10112317

Gao, S., Hao, S., Huang, Z., Yuan, Y., Han, S., Lei, L., . . . Lu, J. (2020). Synthesis of high-entropy alloy nanoparticles on supports by the fast moving bed pyrolysis. *Nature Communications, 11*(1), 2016. doi:10.1038/s41467-020-15934-1

Gatsa, O., Tahir, S., Flimelová, M., Riahi, F., Doñate-Buendia, C., Gökce, B., & Bulgakov, A. V. (2024). Unveiling Fundamentals of Multi-Beam Pulsed Laser Ablation in Liquids toward Scaling up Nanoparticle Production. *Nanomaterials (Basel), 14*(4). doi:https://doi.org/10.3390/nano14040365

Geng, J., Xu, L., Yan, W., Shi, L., & Qiu, M. (2023). High-speed laser writing of structural colors for full-color inkless printing. *Nat Commun, 14*(1), 565. doi:https://doi.org/10.1038/s41467-023-36275-9

George, E. P., Raabe, D., & Ritchie, R. O. (2019). High-entropy alloys. *Nature Reviews Materials, 4*(8), 515-534. doi:https://doi.org/10.1038/s41578-019-0121-4

Ghorai, S., Clulow, R., Cedervall, J., Huang, S., Ericsson, T., Häggström, L., . . . Svedlindh, P. (2025). Design of thermal hysteresis in nonstoichiometric Fe2P-type alloys with giant magnetocaloric effect. *Physical Review B, 111*(22), 224401. doi:https://doi.org/10.1103/PhysRevB.111.224401

Gökce, B., Amendola, V., & Barcikowski, S. (2017). Opportunities and Challenges for Laser Synthesis of Colloids. *ChemPhysChem, 18*(9), 983-985. doi:https://doi.org/10.1002/cphc.201700310

Gschneidner, K., & Pecharsky, V. (2000). Magnetocaloric Materials. *Annual Review of Materials Science, 30*, 387-429. doi:https://doi.org/10.1146/annurev.matsci.30.1.387

Guo, L., Niu, Y., Hu, J., Ju, S., Gu, Y., & Tan, W. (2023). A New Process for Efficient Recovery of Rhodium from Spent Carbonyl Rhodium Catalyst by Microreactor. *Materials, 16*(18), 6271. doi:https://doi.org/10.3390/ma16186271

Guo, Y., Zhang, T., Zhang, Z., Chen, B., Guo, W., Pan, S., . . . Xu, F. (2022). Large reversible magnetocaloric effect in high-entropy MnFeCoNiGeSi system with low-hysteresis magnetostructural transformation. *APL Materials, 10*(9). doi:https://doi.org/10.1063/5.0108367

Gutfleisch, O., Willard, M. A., Brück, E., Chen, C. H., Sankar, S. G., & Liu, J. P. (2011). Magnetic Materials and Devices for the 21st Century: Stronger, Lighter, and More Energy Efficient. *Advanced Materials, 23*(7), 821-842. doi:https://doi.org/10.1002/adma.201002180

Han, L., Rao, Z., Souza Filho, I. R., Maccari, F., Wei, Y., Wu, G., . . . Li, Z. (2021). Ultrastrong and Ductile Soft Magnetic High-Entropy Alloys via Coherent Ordered Nanoprecipitates. *Advanced Materials, 33*(37), 2102139. doi:https://doi.org/10.1002/adma.202102139

Hilali, M. M., Gee, J. M., & Hacke, P. (2007). Bow in screen-printed back-contact industrial silicon solar cells. *Solar Energy Materials And Solar Cells 91*(13), 1228-1233. doi:https://doi.org/10.1016/j.solmat.2007.04.010

Huang, P. W., & Victora, R. H. (2014). Approaching the Grain-Size Limit for Jitter Using FeRh/FePt in Heat-Assisted Magnetic Recording. *IEEE Transactions on Magnetics, 50*(11), 1-4. doi:https://doi.org/10.1109/TMAG.2014.2318040

Hurtado, A., Jevtics, D., Guilhabert, B., Gao, Q., Tan, H. H., Jagadish, C., & Dawson, M. D. (2018). Transfer printing of semiconductor nanowire lasers. *IET Optoelectronics 12*(1), 30-35. doi:https://doi.org/10.1049/iet-opt.2017.0105

Ibrahimkutty, S., Wagener, P., Menzel, A., Plech, A., & Barcikowski, S. (2012). Nanoparticle formation in a cavitation bubble after pulsed laser ablation in liquid studied with high time resolution small angle x-ray scattering. *Applied Physics Letters, 101*(10). doi:https://doi.org/10.1063/1.4750250

IEA. (2018). IEA, The Future of Cooling. Retrieved from https://www.iea.org/reports/the-future-of-cooling

Jia, Z., Harrell, J. W., & Misra, R. D. K. (2008). Synthesis and magnetic properties of self-assembled FeRh nanoparticles. *Applied Physics Letters, 93*(2), 022504. doi:https://doi.org/10.1063/1.2952956

Jiang, D., Yuan, Z., Zhu, Z., & Yao, M. (2024). NiCoCrFeY High Entropy Alloy Nanopowders and Their Soft Magnetic Properties. *Materials, 17*(2), 534. doi:https://doi.org/10.3390/ma17020534

Jiang, L., Wang, A.-D., Li, B., Cui, T.-H., & Lu, Y.-F. (2018). Electrons dynamics control by shaping femtosecond laser pulses in micro/nanofabrication: modeling, method, measurement and application. *Light: Science & Applications, 7*(2), 17134-17134. doi:https://doi.org/10.1038/lsa.2017.134

Johny, J., Li, Y., Kamp, M., Prymak, O., Liang, S.-X., Krekeler, T., . . . Reichenberger, S. (2022). Laser-generated high entropy metallic glass nanoparticles as bifunctional electrocatalysts. *Nano Research, 15*(6), 4807-4819. doi:https://doi.org/10.1007/s12274-021-3804-2

Jones, J., Büttner, D., Chudasama, R., Wimpenny, D., & Krüger, K. (2012). Laser Printing Circuit Boards and Electronics. *Journal of Imaging Science and Technology, 56*, 1-11. doi:https://doi.org/10.2352/J.ImagingSci.Technol.2012.56.4.040503

Jordan, A., Wust, P., Fählin, H., John, W., Hinz, A., & Felix, R. (1993). Inductive heating of ferrimagnetic particles and magnetic fluids: Physical evaluation of their potential for hyperthermia. *International Journal of Hyperthermia, 9*(1), 51-68. doi:https://doi.org/10.3109/02656739309061478

Kang, K., Omura, H., Yesudas, D., Lee, O., Lee, K. J., Lee, H. W., . . . Choi, G. M. (2023). Spin current driven by ultrafast magnetization of FeRh. *Nat Commun, 14*(1), 3619. doi:https://doi.org/10.1038/s41467-023-39103-2

Kanithi, M., Kumari, L., Yalakaturi, K., Munjal, K., Jimitreddy, S., Kandamuri, M., . . . Junapudi, S. (2024). Nanoparticle Polymers Influence on Cardiac Health: Good or Bad for Cardiac Physiology? *Current Problems in Cardiology, 49*(1, Part C), 102145. doi:https://doi.org/10.1016/j.cpcardiol.2023.102145

Kanitz, A., Hoppius, J. S., Fiebrandt, M., Awakowicz, P., Esen, C., Ostendorf, A., & Gurevich, E. L. (2017). Impact of liquid environment on femtosecond laser ablation. *Applied Physics A, 123*(11), 674. doi:https://doi.org/10.1007/s00339-017-1280-z

Kathuria, Y. P. (1997, 5-8 Oct. 1997). *Selective laser sintering of metallic powder for microfabrication technology.* Paper presented at the 1997 International Symposium on Micromechanics and Human Science (Cat. No.97TH8311).doi:https://doi.org/10.1109/MHS.1997.768854

Khairani, I. Y., Mínguez-Vega, G., Doñate-Buendía, C., & Gökce, B. (2023). Green nanoparticle synthesis at scale: a perspective on overcoming the limits of pulsed laser ablation in liquids for high-throughput production. *Physical Chemistry Chemical Physics, 25*(29), 19380-19408. doi:https://doi.org/10.1039/D3CP01214J

Kim, K. S., Couillard, M., Tang, Z., Shin, H., Poitras, D., Cheng, C., . . . Zou, Y. (2024). Continuous synthesis of high-entropy alloy nanoparticles by in-flight alloying of elemental metals. *Nature Communications, 15*(1), 1450. doi:https://doi.org/10.1038/s41467-024-45731-z

Kolhatkar, A. G., Jamison, A. C., Litvinov, D., Willson, R. C., & Lee, T. R. (2013). Tuning the Magnetic Properties of Nanoparticles. *International Journal of Molecular Sciences, 14*(8), 15977-16009. doi:https://doi.org/10.3390/ijms140815977

Komlev, A. S., Gimaev, R. R., & Zverev, V. I. (2021). Smart magnetocaloric coatings for implants: Controlled drug release for targeted delivery. *Physics Open, 7*, 100063. doi:https://doi.org/10.1016/j.physo.2021.100063

Koyama, K., Okada, H., Watanabe, K., Kanomata, T., Kainuma, R., Ito, W., . . . Ishida, K. (2006). Observation of large magnetoresistance of magnetic Heusler alloy Ni50Mn36Sn14 in high magnetic fields. *Applied Physics Letters, 89*(18). doi:https://doi.org/10.1063/1.2374868

Krenke, T., Duman, E., Acet, M., Wassermann, E., Moya, X., Mañosa, L., & Planes, A. (2005a). Inverse magnetocaloric effect in ferromagnetic Ni-Mn-Sn alloys. *Nature Materials, 4*, 450-454. doi:https://doi.org/10.1038/nmat1395

Krenke, T., Duman, E., Acet, M., Wassermann, E. F., Moya, X., Mañosa, L., & Planes, A. (2005b). Inverse magnetocaloric effect in ferromagnetic Ni–Mn–Sn alloys. *Nature Materials, 4*(6), 450-454. doi:https://doi.org/10.1038/nmat1395

Kroeze, C., & Reijnders, L. (1992). Halocarbons and global warming. *Science of The Total Environment, 111*(1), 1-24. doi:https://doi.org/10.1016/0048-9697(92)90042-Q

Kunzler, J. V., Schreiner, W., Bristoti, A., & BrandÃo, D. E. (1977). Thermal and magnetization studies on Heusler alloys. *Journal of thermal analysis, 11*(1), 81-86. doi:https://doi.org/10.1007/BF02104086

Law, J. Y., & Franco, V. (2023). Review on magnetocaloric high-entropy alloys: Design and analysis methods. *Journal of Materials Research, 38*(1), 37-51. doi:https://doi.org/10.1557/s43578-022-00712-0

Law, J. Y., Moreno-Ramírez, L. M., Díaz-García, Á., Martín-Cid, A., Kobayashi, S., Kawaguchi, S., . . . Franco, V. (2021). MnFeNiGeSi high-entropy alloy with large magnetocaloric effect. *Journal of Alloys and Compounds, 855*, 157424. doi:https://doi.org/10.1016/j.jallcom.2020.157424

Leitz, K.-H., Redlingshöfer, B., Reg, Y., Otto, A., & Schmidt, M. (2011). Metal Ablation with Short and Ultrashort Laser Pulses. *Physics Procedia, 12*, 230-238. doi:https://doi.org/10.1016/j.phpro.2011.03.128

Liao, Y., Li, Y., Ji, L., Liu, X., Zhao, X., Rong, H., . . . Zhang, X. (2022). Confined high-entropy-alloy nanoparticles within graphitic shells for synergistically improved photothermal conversion. *Acta Materialia, 240*, 118338. doi:https://doi.org/10.1016/j.actamat.2022.118338

Lin, S., Shuo, W., Haiyan, T., & Jingquan, L. (2022). Effects of Ablation Regimes on the Formation and Evolution of Femtosecond Laser-Induced Periodic Structures on Titanium. *Frontiers in Physics, 10*. doi:https://doi.org/10.3389/fphy.2022.861098

Lin, Y., Wang, J., Dai, W., Qiao, K., Zhou, H., Zhao, T., . . . Shen, B. (2024). A full solid-state conceptual magnetocaloric refrigerator based on hybrid regeneration. *The Innovation, 5*(4), 100645. doi:https://doi.org/10.1016/j.xinn.2024.100645

Liu, A., Xia, T., Cao, S., Zhao, H., Hou, Y., Duan, X., . . . Yan, C. (2025). Comparative analysis of femtosecond, picosecond, and nanosecond laser techniques for transseptal puncture: An in vitro study with pathological correlation. *Journal of Photochemistry and Photobiology B: Biology, 266*, 113138. doi:https://doi.org/10.1016/j.jphotobiol.2025.113138

Liu, E., Wang, W., Feng, L., Zhu, W., Li, G., Chen, J., . . . de Boer, F. (2012). Stable magnetostructural coupling with tunable magnetoresponsive effects in hexagonal ferromagnets. *Nature Communications, 3*(1), 873. doi:https://doi.org/10.1038/ncomms1868

Liu, E. K., Zhu, W., Feng, L., Chen, J. L., Wang, W. H., Wu, G. H., . . . Li, Y. X. (2010). Vacancy-tuned paramagnetic/ferromagnetic martensitic transformation in Mn-poor Mn1-xCoGe alloys. *Europhysics Letters, 91*(1), 17003. doi:https://doi.org/10.1209/0295-5075/91/17003

Liu, X. G., Geng, D. Y., Du, J., Ma, S., Li, B., Shang, P. J., & Zhang, Z. D. (2008). The large cryogenic magnetocaloric effect of TbAl2 nanocapsules. *Scripta Materialia, 59*(3), 340-343. doi:https://doi.org/10.1016/j.scriptamat.2008.04.005

Lyubina, J. (2017). Magnetocaloric materials for energy efficient cooling. *Journal of Physics D: Applied Physics, 50*(5), 053002. doi:https://doi.org/10.1088/1361-6463/50/5/053002

Maiman, T. H. (1960). Stimulated Optical Radiation in Ruby. *Nature, 187*(4736), 493-494. doi:https://doi.org/10.1038/187493a0

Maraytta, N., Skourski, Y., Voigt, J., Friese, K., Herrmann, M. G., Perßon, J., . . . Brückel, T. (2019). Direct measurements of the magneto-caloric effect of MnFe4Si3 in pulsed magnetic fields. *Journal of Alloys and Compounds, 805*, 1161-1167. doi:https://doi.org/10.1016/j.jallcom.2019.07.113

McKinnon, J. B., Melville, D., & Lee, E. W. (1970). The antiferromagnetic-ferromagnetic transition in iron-rhodium alloys. *Journal of Physics C: Solid State Physics, 3*(1S), S46. doi:https://doi.org/10.1088/0022-3719/3/1S/306

Meddeb, Z., & Razak, J. (2015). Thermodynamic Study of the Active Magnetic Regenerative Refrigeration in Transitional Regime. *1*, 49-53. doi:https://doi.org/10.11648/j.ijfmts.20150103.12

Mellari, S. (2023). Introduction to magnetic refrigeration: magnetocaloric materials. *International Journal of Air-Conditioning and Refrigeration, 31*(1), 5. doi:https://doi.org/10.1007/s44189-023-00021-z

Meng, J., Xie, L., Yu, Q., Wang, J., & Jiang, C. (2024). Toughening the grain boundaries by introducing a small amount of the second phase: Ni-Cu-Mn-Ga shape memory alloys as an example. *Acta Materialia, 263*, 119469. doi:https://doi.org/10.1016/j.actamat.2023.119469

Mondal, B., Zhang, X., Kumar, S., Long, F., Katiyar, N. K., Kumar, M., . . . Biswas, K. (2023). A resistance-driven H2 gas sensor: high-entropy alloy nanoparticles decorated 2D MoS2. *Nanoscale, 15*(42), 17097-17104. doi:https://doi.org/10.1039/D3NR04810A

Montanino, M., Sico, G., Del Mauro, A. D., Asenbauer, J., Binder, J. R., Bresser, D., & Passerini, S. (2021). Gravure-Printed Conversion/Alloying Anodes for Lithium-Ion Batteries. *ENERGY TECHNOLOGY, 9*(9). doi:https://doi.org/10.1002/ente.202100315

Nadarajah, R., Landers, J., Salamon, S., Koch, D., Tahir, S., Doñate-Buendía, C., . . . Gökce, B. (2021). Towards laser printing of magnetocaloric structures by inducing a magnetic phase transition in iron-rhodium nanoparticles. *Sci Rep, 11*(1), 13719. doi:https://doi.org/10.1038/s41598-021-92760-5

Nadarajah, R., Tahir, S., Landers, J., Koch, D., Semisalova, A. S., Wiemeler, J., . . . Gökce, B. (2020). Controlling the Oxidation of Magnetic and Electrically Conductive Solid-Solution Iron-Rhodium Nanoparticles Synthesized by Laser Ablation in Liquids. *Nanomaterials, 10*(12). doi:https://doi.org/10.3390/nano10122362

Naddeo, J. J., & Bubb, D. M. (2014). Mechanisms of Nanoparticle Generation by Laser Ablation in Liquids. In B. Bhushan (Ed.), *Encyclopedia of Nanotechnology* (pp. 1-6). Dordrecht: Springer Netherlands. doi:https://doi.org/10.1007/978-94-007-6178-0_100912-1

Nastulyavichus, A., Smirnov, N., & Kudryashov, S. (2022). Quantitative evaluation of LAL productivity of colloidal nanomaterials: Which laser pulse width is more productive, ergonomic, and economic? *Chinese Physics B, 31*(7), 077803. doi:https://doi.org/10.1088/1674-1056/ac5602

Nazir, A., & Jeng, J.-Y. (2019). A high-speed additive manufacturing approach for achieving high printing speed and accuracy. *Proceedings of the Institution of Mechanical Engineers, Part C: Journal of Mechanical Engineering Science, 234*(14), 2741-2749. doi:https://doi.org/10.1177/0954406219861664

Nazri, M. A., Lim, L. M., Samsudin, Z., Ali, M. Y. T., Mansor, I., Suhaimi, M. I., . . . Nordin, A. N. (2021). Screen-Printed Nickel-Zinc Batteries: A Review of Additive Manufacturing and Evaluation Methods. *3D Printing and additive manufacturing* *8*(3), 176-192. doi:https://doi.org/10.1089/3dp.2020.0095

Neuenschwander, B., Jaeggi, B., Schmid, M., & Hennig, G. (2014). Surface Structuring with Ultra-short Laser Pulses: Basics, Limitations and Needs for High Throughput. *Physics Procedia, 56*, 1047-1058. doi:https://doi.org/10.1016/j.phpro.2014.08.017

Nguyen, D. C., & Ito, S. (2013). Cu2Te solar cells fabricated by printing. *International Journal of Nanotechnology 10*(3-4), 269-278. doi:https://doi.org/10.1504/IJNT.2013.053140

Niittynen, J., & Mäntysalo, M. (2014). Characterization of Laser Sintering of Copper Nanoparticle Ink by FEM and Experimental Testing. *IEEE Transactions on Components, Packaging and Manufacturing Technology,* *4*(12), 2018-2025. doi:https://doi.org/10.1109/TCPMT.2014.2363032

Park, J.-H., Park, M. T., Baek, G.-W., Kimura, S.-i., Jung, M.-H., & Kim, K.-J. (2024). Unraveling the origin of conductivity change in Co-doped FeRh phase transition. *Communications Materials, 5*(1), 250. doi:https://doi.org/10.1038/s43246-024-00694-y

Park, J. H., Lee, J. W., Ma, Y. W., Kang, B. S., Hong, S. M., & Shin, B. S. (2022). Direct Laser Interference Ink Printing Using Copper Metal-Organic Decomposition Ink for Nanofabrication. *Nanomaterials, 12*(3). doi:https://doi.org/10.3390/nano12030387

Park, S., Kim, H., Kim, J.-H., & Yeo, W.-H. (2020). Advanced Nanomaterials, Printing Processes, and Applications for Flexible Hybrid Electronics. *Materials, 13*(16), 3587. doi:https://doi.org/10.3390/ma13163587

Passamani, E. C., Xavier, F., Favre-Nicolin, E., Larica, C., Takeuchi, A. Y., Castro, I. L., & Proveti, J. R. (2009). Magnetic properties of NiMn-based Heusler alloys influenced by Fe atoms replacing Mn. *Journal of Applied Physics, 105*(3). doi:https://doi.org/10.1063/1.3075835

Paul-Boncour, V., & Bessais, L. (2021). Tuning the Magnetocaloric Properties of the La(Fe,Si)13 Compounds by Chemical Substitution and Light Element Insertion. *Magnetochemistry, 7*(1). doi:https://doi.org/10.3390/magnetochemistry7010013

Pecharsky, V. K., & Gschneidner, J. K. A. (1997). Giant Magnetocaloric Effect in Gd5Si2Ge2. *Physical Review Letters, 78*(23), 4494-4497. doi:https://doi.org/10.1103/PhysRevLett.78.4494

Pervan, P., Mikšić Trontl, V., Figueroa, I. A., Valla, T., Pletikosić, I., & Babić, E. (2023). Compositionally Complex Alloys: Some Insights from Photoemission Spectroscopy. *Materials, 16*(4). doi:https://doi.org/10.3390/ma16041486

Petrov, Y. V., Khokhlov, V. A., Zhakhovsky, V. V., & Inogamov, N. A. (2019). Hydrodynamic phenomena induced by laser ablation of metal into liquid. *Applied Surface Science, 492*, 285-297. doi:https://doi.org/10.1016/j.apsusc.2019.05.325

Pimentel, B., Caraballo-Vivas, R. J., Checca, N. R., Zverev, V. I., Salakhova, R. T., Makarova, L. A., . . . Reis, M. S. (2018). Threshold heating temperature for magnetic hyperthermia: Controlling the heat exchange with the blocking temperature of magnetic nanoparticles. *Journal of Solid State Chemistry, 260*, 34-38. doi:https://doi.org/10.1016/j.jssc.2018.01.001

Popescu, A., Rodriguez-Lopez, P., Haney, P. M., & Woods, L. M. (2018). Thermally driven anomalous Hall effect transitions in FeRh. *Physical Review B, 97*(14), 140407. doi:https://doi.org/10.1103/PhysRevB.97.140407

Popoola, P., Dada, M., Adeosun, S., & Mathe, N. (2019). High Entropy Alloys for Aerospace Applications. In M. Gorji-Bandpy & A.-M. Aly (Eds.), *Aerodynamics*. Rijeka: IntechOpen. doi:10.5772/intechopen.84982

Pucci, C., Degl'Innocenti, A., Belenli Gümüş, M., & Ciofani, G. (2022). Superparamagnetic iron oxide nanoparticles for magnetic hyperthermia: recent advancements, molecular effects, and future directions in the omics era. *Biomaterials Science, 10*(9), 2103-2121. doi:https://doi.org/10.1039/D1BM01963E

Ram, N. R., Prakash, M., Naresh, U., Kumar, N. S., Sarmash, T. S., Subbarao, T., . . . Naidu, K. C. B. (2018). Review on Magnetocaloric Effect and Materials. *Journal of Superconductivity and Novel Magnetism, 31*(7), 1971-1979. doi:https://doi.org/10.1007/s10948-018-4666-z

Ramasamy, R. P., & Hurd, A. J. (2021). Toward a least-effort principle for evaluating prices of elements as indicators of sustainability. *MRS Energy & Sustainability,* *8*(1), 16-32. doi:https://doi.org/10.1557/s43581-020-00001-5

Rittinghaus, S.-K., Shokri, H., Shkodich, N., Bruder, E., Farle, M., & Gökce, B. (2023). Comparative insights into microstructure and magnetism of Ni-Mn-Sn Heusler alloys manufactured by electron beam and laser beam powder bed fusion. *Additive Manufacturing Letters, 7*, 100159. doi:https://doi.org/10.1016/j.addlet.2023.100159

Roy, N. K., Behera, D., Dibua, O. G., Foong, C. S., & Cullinan, M. A. (2019). A novel microscale selective laser sintering (μ-SLS) process for the fabrication of microelectronic parts. *Microsystems & Nanoengineering, 5*(1), 64. doi:https://doi.org/10.1038/s41378-019-0116-8

Rumiantsev, E., Khrabrov, K., Tsypin, A., Peresypkin, N. D., Gimaev, R. R., Zverev, V., . . . Kadurin, A. (2024). Doping position estimation for FeRh-based alloys. *Scientific Reports, 14*(1), 20612. doi:https://doi.org/10.1038/s41598-024-71058-2

Samolyuk, G. D., Osetsky, Y. N., Stocks, G. M., & Morris, J. R. (2021). Role of Static Displacements in Stabilizing Body Centered Cubic High Entropy Alloys. *Physical Review Letters, 126*(2), 025501. doi:https://doi.org/10.1103/PhysRevLett.126.025501

Samulyak, R., & Prykarpatskyy, Y. (2004). Richtmyer–Meshkov instability in liquid metal flows: influence of cavitation and magnetic fields. *Mathematics and Computers in Simulation, 65*(4), 431-446. doi:https://doi.org/10.1016/j.matcom.2004.01.019

Sarkar, A., Velasco, L., Wang, D., Wang, Q., Talasila, G., de Biasi, L., . . . Breitung, B. (2018). High entropy oxides for reversible energy storage. *Nature Communications, 9*(1), 3400. doi:https://doi.org/10.1038/s41467-018-05774-5

Sarkar, K., Shaji, S., Sarin, S., Shield, J. E., Binek, C., & Kumar, D. (2022). Large refrigerant capacity in superparamagnetic iron nanoparticles embedded in a thin film matrix. *Journal of Applied Physics, 132*(19). doi:https://doi.org/10.1063/5.0120280

Schäfer, R. (2021). Magnetic Domains. In J. M. D. Coey & S. S. P. Parkin (Eds.), *Handbook of Magnetism and Magnetic Materials* (pp. 391-434). Cham: Springer International Publishing. doi:https://doi.org/10.1007/978-3-030-63210-6_8

Scheibel, F., Lauhoff, C., Krooß, P., Riegg, S., Sommer, N., Koch, D., . . . Gutfleisch, O. (2023). Additive manufacturing of Ni-Mn-Sn shape memory Heusler alloy – Microstructure and magnetic properties from powder to printed parts. *Materialia, 29*, 101783. doi:https://doi.org/10.1016/j.mtla.2023.101783

Schleich, N., Danhier, F., & Préat, V. (2015). Iron oxide-loaded nanotheranostics: Major obstacles to in vivo studies and clinical translation. *Journal of Controlled Release, 198*, 35-54. doi:https://doi.org/10.1016/j.jconrel.2014.11.024

Sergei, P. G., Yurii, A. K., Khomutov, G. B., & Gleb Yu, Y. (2005). Magnetic nanoparticles: preparation, structure and properties. *Russian Chemical Reviews, 74*(6), 489. doi:https://doi.org/10.1070/RC2005v074n06ABEH000897

Shaheen, M. E., Gagnon, J. E., & Fryer, B. J. (2013). Laser ablation of iron: A comparison between femtosecond and picosecond laser pulses. *Journal of Applied Physics, 114*(8). doi:https://doi.org/10.1063/1.4819804

Shih, C.-Y., Streubel, R., Heberle, J., Letzel, A., Shugaev, M. V., Wu, C., . . . Zhigilei, L. V. (2018). Two mechanisms of nanoparticle generation in picosecond laser ablation in liquids: the origin of the bimodal size distribution. *Nanoscale, 10*(15), 6900-6910. doi:https://doi.org/10.1039/C7NR08614H

Shirane, G., Chen, C. W., Flinn, P. A., & Nathans, R. (1963a). Hyperfine Fields and Magnetic Moments in the Fe–Rh System. *Journal of Applied Physics, 34*(4), 1044-1045. doi:https://doi.org/10.1063/1.1729362

Shirane, G., Chen, C. W., Flinn, P. A., & Nathans, R. (1963b). Mossbauer Study of Hyperfine Fields and Isomer Shifts in the Fe-Rh Alloys. *Physical Review, 131*(1), 183-190. doi:https://doi.org/10.1103/PhysRev.131.183

Singamaneni, S., Bliznyuk, V. N., Binek, C., & Tsymbal, E. Y. (2011). Magnetic nanoparticles: recent advances in synthesis, self-assembly and applications. *Journal of Materials Chemistry, 21*(42), 16819-16845. doi:https://doi.org/10.1039/C1JM11845E

Skomski, R., Manchanda, P., & Kashyap, A. (2021). Anisotropy and Crystal Field. In J. M. D. Coey & S. S. P. Parkin (Eds.), *Handbook of Magnetism and Magnetic Materials* (pp. 103-185). Cham: Springer International Publishing. doi:https://doi.org/10.1007/978-3-030-63210-6_3

Souza, A. D., Vagadia, M., & Daivajna, M. (2021). Tuning magnetic and magnetocaloric properties of Pr0.6Sr0.4MnO3 through size modifications. *Journal of Materials Science: Materials in Electronics, 32*(11), 14990-15002. doi:https://doi.org/10.1007/s10854-021-06052-9

Sun, K., Li, S., Mohamed, A. E.-M. A., Ma, K., Duan, R., Brooks, O. P., . . . Attallah, M. M. (2023). The effect of thermal post-processing treatment on laser powder bed fusion processed NiMnSn-based alloy for magnetic refrigeration. *Journal of Alloys and Compounds, 961*, 171063. doi:https://doi.org/10.1016/j.jallcom.2023.171063

Sung Lee, J., Myung Cha, J., Young Yoon, H., Lee, J.-K., & Keun Kim, Y. (2015). Magnetic multi-granule nanoclusters: A model system that exhibits universal size effect of magnetic coercivity. *Scientific Reports, 5*(1), 12135. doi:https://doi.org/10.1038/srep12135

Tahir, S., Landers, J., Salamon, S., Koch, D., Doñate-Buendía, C., Ziefuß, A. R., . . . Gökce, B. (2023). Development of Magnetocaloric Microstructures from Equiatomic Iron–Rhodium Nanoparticles through Laser Sintering. *Advanced Engineering Materials, 25*(20), 2300245. doi:https://doi.org/10.1002/adem.202300245

Tahir, S., Shkodich, N., Eggert, B., Lill, J., Gatsa, O., Flimelová, M., . . . Gökce, B. (2024). Synthesis of High Entropy Alloy Nanoparticles by Pulsed Laser Ablation in Liquids: Influence of Target Preparation on Stoichiometry and Productivity. *ChemNanoMat, 10*(5), e202400064. doi:https://doi.org/10.1002/cnma.202400064

Tandoc, C., Hu, Y.-J., Qi, L., & Liaw, P. K. (2023). Mining of lattice distortion, strength, and intrinsic ductility of refractory high entropy alloys. *npj Computational Materials, 9*(1), 53. doi:https://doi.org/10.1038/s41524-023-00993-x

Tao, Q., Han, Z. D., Wang, J. J., Qian, B., Zhang, P., Jiang, X. F., . . . Du, Y. W. (2012). Phase stability and magnetic-field-induced martensitic transformation in Mn-rich NiMnSn alloys. *AIP Advances, 2*(4). doi:https://doi.org/10.1063/1.4772626

Teja, A. S., & Koh, P.-Y. (2009). Synthesis, properties, and applications of magnetic iron oxide nanoparticles. *Progress in Crystal Growth and Characterization of Materials, 55*(1), 22-45. doi:https://doi.org/10.1016/j.pcrysgrow.2008.08.003

Tu, W. H., Seah, G. L., Li, Y., Wang, X., & Tan, K. W. (2022). Transient Laser-Annealing-Induced Mesophase Transitions of Block Copolymer–Resol Thin Films. *ACS Polymers Au, 2*(1), 42-49. doi:https://doi.org/10.1021/acspolymersau.1c00040

Tumkin, I. I., Khairullina, E. M., Panov, M. S., Yoshidomi, K., & Mizoshiri, M. (2021). Copper and Nickel Microsensors Produced by Selective Laser Reductive Sintering for Non-Enzymatic Glucose Detection. *Materials, 14*(10). doi:https://doi.org/10.3390/ma14102493

Vogler, C., Abert, C., Bruckner, F., & Suess, D. (2017). Noise Reduction Based on an Fe-Rh Interlayer in Exchange-Coupled Heat-Assisted Recording Media. *Physical Review Applied, 8*(5), 054021. doi:https://doi.org/10.1103/PhysRevApplied.8.054021

Waag, F., Li, Y., Ziefuß, A. R., Bertin, E., Kamp, M., Duppel, V., . . . Gökce, B. (2019). Kinetically-controlled laser-synthesis of colloidal high-entropy alloy nanoparticles. *RSC Advances, 9*(32), 18547-18558. doi:https://doi.org/10.1039/C9RA03254A

Wang, P. J., Sun, Y. Z., Shi, X. Q., Shen, H. X., Ning, H. H., & Liu, H. T. (2021). 3D printing of tissue engineering scaffolds: a focus on vascular regeneration. *BIO-DESIGN AND MANUFACTURING, 4*(2), 344-378. doi:10.1007/s42242-020-00109-0

Wei, Y., Liu, X., Yao, R., Qian, J., Yin, Y., Li, D., & Chen, Y. (2023). Embedding the high entropy alloy nanoparticles into carbon matrix toward high performance Li-ion batteries. *Journal of Alloys and Compounds, 938*, 168610. doi:https://doi.org/10.1016/j.jallcom.2022.168610

Xu, Y. H., Zhang, F. Y., Zhai, W. J., Cheng, S. J., Li, J. H., & Wang, Y. (2022). Unraveling of Advances in 3D-Printed Polymer-Based Bone Scaffolds. *POLYMERS, 14*(3). doi:https://doi.org/10.3390/polym14030566

Xuan, H. C., Zhang, Y. Q., Li, H., Han, P. D., Wang, D. H., & Du, Y. W. (2015). Effect of Ni/Sn ratio on martensitic transformation and magnetic properties in high-Mn content Mn2Ni1.64−Sn0.36+ ferromagnetic shape memory alloys. *physica status solidi (a), 212*(3), 680-685. doi:https://doi.org/10.1002/pssa.201431507

Yang, P. H., Li, J., Lee, S. W., & Fan, H. J. (2022). Printed Zinc Paper Batteries. *Advanced Science, 9*(2). doi:10.1002/advs.202103894

Ye, Y. F., Wang, Q., Lu, J., Liu, C. T., & Yang, Y. (2016). High-entropy alloy: challenges and prospects. *Materials Today, 19*(6), 349-362. doi:https://doi.org/10.1016/j.mattod.2015.11.026

Yin, S., Sauyet, T., Seehra, M. S., & Jain, M. (2017). Particle size dependence of the magnetic and magneto-caloric properties of HoCrO3. *Journal of Applied Physics, 121*(6). doi:https://doi.org/10.1063/1.4975405

Young, O. M., Xu, X., Sarker, S., & Sochol, R. D. (2024). Direct laser writing-enabled 3D printing strategies for microfluidic applications. *Lab Chip, 24*(9), 2371-2396. doi:https://doi.org/10.1039/d3lc00743j

Yu, Y., Xia, F., Wang, C., Wu, J., Fu, X., Ma, D., . . . Kang, Y. (2022). High-entropy alloy nanoparticles as a promising electrocatalyst to enhance activity and durability for oxygen reduction. *Nano Research, 15*(9), 7868-7876. doi:https://doi.org/10.1007/s12274-022-4432-1

Yuan, Y. P., Liu, Z., Zhang, K. H., Han, W. N., & Chen, J. M. (2018). Nanoscale welding of multi-walled carbon nanotubes by 1064 nm fiber laser. *OPTICS AND LASER TECHNOLOGY, 103*, 327-329. doi:https://doi.org/10.1016/j.optlastec.2018.01.049

Žemaitis, A., Gaidys, M., Brikas, M., Gečys, P., Račiukaitis, G., & Gedvilas, M. (2018). Advanced laser scanning for highly-efficient ablation and ultrafast surface structuring: experiment and model. *Scientific Reports, 8*(1), 17376. doi:https://doi.org/10.1038/s41598-018-35604-z

Zhang, C. L., Wang, D. H., Cao, Q. Q., Han, Z. D., Xuan, H. C., & Du, Y. W. (2009). Large magnetic entropy change and broad working temperature span in CoMnSi0.88Ge0.12 alloy. *Journal of Physics D: Applied Physics, 42*(1), 015007. doi:https://doi.org/10.1088/0022-3727/42/1/015007

Zhang, D., Gökce, B., & Barcikowski, S. (2017). Laser Synthesis and Processing of Colloids: Fundamentals and Applications. *Chemical Reviews, 117*(5), 3990-4103. doi:https://doi.org/10.1021/acs.chemrev.6b00468

Zhang, D., & Guan, L. (2014). 4.06 - Laser Ablation. In S. Hashmi, G. F. Batalha, C. J. Van Tyne, & B. Yilbas (Eds.), *Comprehensive Materials Processing* (pp. 125-169). Oxford: Elsevier. doi:https://doi.org/10.1016/B978-0-08-096532-1.00406-4

Zhang, D., Liu, J., & Liang, C. (2017). Perspective on how laser-ablated particles grow in liquids. *Science China Physics, Mechanics & Astronomy, 60*(7), 074201. doi:https://doi.org/10.1007/s11433-017-9035-8

Zhang, D., & Wada, H. (2021). Laser Ablation in Liquids for Nanomaterial Synthesis and Applications. In K. Sugioka (Ed.), *Handbook of Laser Micro- and Nano-Engineering* (pp. 1481-1515). Cham: Springer International Publishing. doi:https://doi.org/10.1007/978-3-030-63647-0_30

Zhang, Q., Lian, K., Liu, Q., Qi, G., Zhang, S., Luo, J., & Liu, X. (2023). High entropy alloy nanoparticles as efficient catalysts for alkaline overall seawater splitting and Zn-air batteries. *Journal of Colloid and Interface Science, 646*, 844-854. doi:https://doi.org/10.1016/j.jcis.2023.05.074

Zhang, Y., Han, K., Li, M., Gao, M., Wang, X., Wang, G., . . . Huo, J. (2022). Design of Co-based amorphous alloys with magnetocaloric effect near room temperature. *Journal of Non-Crystalline Solids, 592*, 121763. doi:https://doi.org/10.1016/j.jnoncrysol.2022.121763

Zhou, Y. X., & Grayson, W. Three-dimensional printing of scaffolds for facial reconstruction. *MRS Bulletin*. doi:https://doi.org/10.1557/s43577-021-00261-7

5. Appendix

5.1. Studies

5.1.1. Study 1

Tahir, S., Landers, J., Salamon, S., Koch, D., Doñate-Buendía, C., Ziefuß, A. R., . . . Gökce, B. (2023). Development of Magnetocaloric Microstructures from Equiatomic Iron–Rhodium Nanoparticles through Laser Sintering. Advanced Engineering Materials, 25(20), 2300245. DOI: https://doi.org/10.1002/adem.202300245

RESEARCH ARTICLE

ADVANCED ENGINEERING MATERIALS

www.aem-journal.com

Development of Magnetocaloric Microstructures from Equiatomic Iron–Rhodium Nanoparticles through Laser Sintering

*Shabbir Tahir, Joachim Landers, Soma Salamon, David Koch, Carlos Doñate-Buendía, Anna R. Ziefuß, Heiko Wende, and Bilal Gökce**

Pronounced magnetocaloric effects are typically observed in materials that often contain expensive and rare elements and are therefore costly to mass produce. However, they can rather be exploited on a small scale for miniaturized devices such as magnetic micro coolers, thermal sensors, and magnetic micropumps. Herein, a method is developed to generate magnetocaloric microstructures from an equiatomic iron–rhodium (FeRh) bulk target through a stepwise process. First, paramagnetic near-to-equiatomic solid-solution FeRh nanoparticles (NPs) are generated through picosecond (ps)-pulsed laser ablation in ethanol, which are then transformed into a printable ink and patterned using a continuous wave laser. Laser patterning not only leads to sintering of the NP ink but also triggers the phase transformation of the initial γ- to B2-FeRh. At a laser fluence of 246 J cm^{-2}, a partial (52%) phase transformation from γ- to B2-FeRh is obtained, resulting in a magnetization increase of 35 Am^2 kg^{-1} across the antiferromagnetic to ferromagnetic phase transition. This represents a ca. sixfold enhancement compared to previous furnace-annealed FeRh ink. Finally, herein, the ability is demonstrated to create FeRh 2D structures with different geometries using laser sintering of magnetocaloric inks, which offers advantages such as micrometric spatial resolution, in situ annealing, and structure design flexibility.

1. Introduction

Printing techniques using nanoparticle (NP) inks are utilized to generate thin films and structured materials with precise geometry. These methods are widely employed in the production of 2D structures, including solar cells,[1–3] light-emitting diodes (LEDs),[4–6] batteries,[7–9] sensors,[10–12] and biological scaffolds.[13–15] The performance and size of these devices rely on the capability to produce 2D miniaturized electronics–based and semiconductor-based devices.[16–20] Advancements in this field and the diversity of printing techniques have facilitated device miniaturization, thereby allowing size reduction of common electronics such as laptops, smart watches, pocket calculators, and the development of minuscule sensors.[21,22] Screen and nozzle printing techniques were employed to produce micron-size supercapacitors on paper, which can be used as a portable energy-storage device.[23] Although the printing technique is fast, low cost, and highly efficient, the screen cleaning process is difficult and time-consuming.[19] Photolithography was implemented to print micro-patterned electrode-based sensors on flexible substrates for glucose monitoring.[24] However, the technique consists of many processing steps and requires a predesigned photoresist layer, which can be difficult to produce. One of the most used techniques to deposit NP inks on the desired substrate is inkjet printing. Grubb et al.[20] have successfully achieved the inkjet printing of transistors with a channel size of 1 μm, enabling its integration into a smaller footprint on a chip. For individual printed material layers, oven curing is often employed making the fabrication technique time-consuming. Additionally, inkjet printers often have issues with head reliability, droplet formation

---

S. Tahir, C. Doñate-Buendía, B. Gökce
Chair of Materials Science and Additive Manufacturing
University of Wuppertal
Gaußstr. 20, 42119 Wuppertal, Germany
E-mail: goekce@uni-wuppertal.de

The ORCID identification number(s) for the author(s) of this article can be found under https://doi.org/10.1002/adem.202300245.

DOI: 10.1002/adem.202300245

J. Landers, S. Salamon, H. Wende
Faculty of Physics and Center for Nanointegration Duisburg-Essen (CENIDE)
University of Duisburg-Essen
Lotharstr. 1, 47057 Duisburg, Germany

D. Koch
Institute of Materials Science
Technical University of Darmstadt
Alarich-Weiss-Str. 2, 64287 Darmstadt, Germany

A. R. Ziefuß
Technical Chemistry I and Center for Nanointegration Duisburg-Essen (CENIDE)
University of Duisburg-Essen
Universitätsstr. 7, 45141 Essen, Germany

inconsistencies, and relatively low-material-deposition rates.[25,26] Among the different printing technologies developed, laser printing provides advantages such as a micrometric spatial resolution,[27–30] and a fast processing speed.[31,32] The technique is based on the irradiation of the deposited ink with a tightly focused laser beam.[33,34] It can be combined with different ink-deposition methodologies such as spin-coating or inkjet to sinter specific areas of the coated substrate and generate the desired continuous structures. The fast processing and localized energy delivery are advantages that allow thermally efficient heat transfer to the ink rather than the substrate, minimizing energy losses and permitting the use of inexpensive and/or low damage threshold substrates, which cannot bear high thermal loads during an extended time as required for oven sintering. Additionally, the short processing time reduces the risk of oxidation for the metallic inks,[25] negating the need for an inert gas atmosphere or vacuum setup during the process.[35] Laser printing has been used to fabricate printed electronics,[36,37] as well as for tissue engineering,[38,39] microfluidics,[40,41] magnetic sensors,[42,43] and holographic elements.[44,45] Material properties such as microstructure, crystallographic structure, and magnetic and electric conductivity can be manipulated by controlling the laser and scanning parameters, affecting the induced sintering process by modifying the temperature reached and the cooling rate.

Compact and efficient miniaturized electronics–based and semiconductor-based devices encounter challenges such as high power dissipation and uneven temperature distribution, resulting from their high function-to-area ratio. These problems can shorten the device's shelf life and impact its overall performance.[46] Various thermal management solutions have been investigated, such as design optimization of micro heat sinks,[47] varying working coolants[48,49] (such as nanofluids and dielectric coolants), and liquid flow system designs[50] (single-phase flow or multiphase flow). However, the applicability of these approaches is limited because of the electric short-circuiting possibility (due to the leakage of liquid-based coolants), the difficulty of heat extraction from local hotspots, and the complex design of miniaturized devices (which requires precise manufacturing of heat sinks), overall making it difficult to reduce the temperature effectively.[51]

Magnetocaloric materials have the potential to overcome the aforementioned limitations. These materials exhibit a temperature change when subjected to an external magnetic field, making them attractive for replacing compressed chlorofluorocarbon/fluorocarbon (CFC/FC) gas-based refrigeration systems.[52–55] Compared to conventional cooling systems, magnetocaloric refrigeration is more environmentally friendly, quieter, and potentially more efficient.[53,56] Furthermore, solid-state refrigeration is a viable option for miniaturized heat sinks, as it avoids leakage issues and efficiently extracts heat from hotspots. A number of materials have been investigated for magnetocaloric refrigeration across different temperature ranges.[57–59] For example, $La(FeSi)_{13}$[60] displays a temperature change of 6.9 K at an operating temperature of 190 K, while Mn_3GaC[61] exhibits a temperature variation of 4.5 K at 163 K, and $Gd_2Si_2Ge_2$[62] has a temperature change of 4.9 K at 262 K under an applied magnetic field of 2 T. These materials exhibit the most significant temperature change at the phase-transition temperature, and their operating range and cooling capacity depend on the width and characteristics of their magnetic phase transition.

Among the series of magnetocaloric materials investigated so far, the equiatomic iron-rhodium (FeRh) alloy achieves the largest adiabatic temperature change ($\Delta T = 12.9$ K at $\Delta H = 2$ T) with an entropy change up to 16 $\text{J kg}^{-1}\,\text{K}^{-1}$ at 308.2 K due to an antiferromagnetic to ferromagnetic (AFM–FM) first-order phase transition.[63] However, the phase-transition temperature of FeRh is greatly influenced by the alloy's composition and the existence of defects in the crystal structure. As a result, it can take place in a broad range from room temperature to 400 K.[64,65] This magnetoelastic transition does not lead to a change in crystallographic symmetry in the CsCl-type lattice structure (widely known as B2 structure), but is accompanied by significant magneto-structural volume expansion of about 1%.[66] The cause of this transition is attributed to a significant alteration in the exchange interaction and elastic energy resulting from a modification in the crystal lattice parameter. Bean and Rodbell's exchange–striction model[67] provides a viable method to simulate the underlying mechanism responsible for this transition. It has demonstrated strong consistency with theoretical and empirical data determining the magnetic characteristics of both the AFM and FM phases.[68] Despite the fact that the material displays a significant magnetocaloric effect, the high cost of the alloy limit its application in bulk. Rhodium (belonging to the platinum group of metals) is among the rarest elements in the periodic table, with a price twice as high as platinum and seven times higher than palladium.[69] Hence, its use in refrigeration systems requiring large amounts of bulk FeRh is limited by its availability and an associated price increase that a high industrial demand would imply. However, such alloys can be useful for the cooling of miniaturized devices, where a limited quantity is required.

Up to date, the synthesis of FeRh microparticles and NPs has been carried out mainly by wet chemical processes in the context of applications such as heat-assisted magnetic recordings, bio hyperthermia, and catalysis.[70–73] Microsized FeRh alloys have shown an appreciable magnetocaloric effect,[73] but their size limits the printing of structures with submicron or nanoscale resolution. Alternatively, FeRh NPs synthesized by a wet chemical process resulted in the inhomogeneous distribution of Fe and Rh in the NPs, which led to the coexistence of AFM and FM phases. In contrast, by using pulsed laser ablation in organic solvents, we created near-to-equiatomic γ-FeRh solid-solution NPs in a previous study.[74] This current study builds on that work and employs laser printing to create magnetocaloric custom structures with micrometric dimensions, improving the sintering characteristics and magnetic phase conversion of the printed structures. Additionally, the magnetic and magnetocaloric properties of the laser-sintered structures are compared to those produced through standard industrial furnace sintering to optimize the magnetocaloric response of the sintered structures. The direct writing of magnetocaloric materials in this manner presents the opportunity to design a range of devices, including magnetic actuator systems, thermal switches, magnetic micropumps, and magnetic microcoolers.[75,76]

2. Experimental Section

2.1. Synthesis of NPs and Ink Preparation and Deposition

Near-to-equimolar FeRh NPs were synthesized by laser ablation in liquids (LAL). LAL offers several benefits, including the ability to control the composition of the generated particles, and the potential to produce ligand-free NPs and tailored surface properties for a wide range of applications.[77–79] This NP synthesis method found numerous applications in fields such as biomedicine,[80,81] energy generation,[82,83] and additive manufacturing,[84,85] making it a versatile and promising technology. Here, the synthesis of the FeRh NPs was achieved by laser ablation of a $Fe_{50}Rh_{50}$ bulk target in ethanol employing a near-infrared picosecond (ps)-pulsed Nd:YAG solid-state laser source (Ekspla, Atlantic Series, Vilnius, Lithuania, 10 ps, 100 kHz, 80 μJ, 1064 nm). The ablation of the FeRh target was performed by focusing the laser beam with an $f = 100$ mm lens on the FeRh target's surface, with the surface being scanned at 2 m s^{-1} (**Figure 1**a).[74] The NP size distribution was analyzed by scanning electron microscopy (SEM) in the scanning transmission electron microscope (STEM) mode. The resulting NP size distribution is shown in (Figure S1, Supporting Information). The peak size obtained was 6.9 ± 3.0 nm with a polydispersity index of 0.4. The produced colloidal NPs (FeRh NPs in ethanol) were used to formulate a 1 wt% FeRh ink. This was done by partial evaporation of ethanol from the colloid at room temperature employing a 64 W axial fan with a flow rate of 925 m^3 h^{-1} (Figure 1b). Before the deposition of the ink, the glass substrates were processed in a UV cleaner for 5 min to remove any organic contaminations. The ink deposition on the substrate was performed by initially adding 200 μL of 10 wt% polyvinylpyrrolidone (PVP, MW = 40 k) in ethanol on the 25 × 75 mm glass substrate. To avoid agglomeration, the FeRh ink was ultrasonicated for 10 min before the dispersion, 100 μL of FeRh ink were then dispersed on the area of ≈25 × 15 mm polymer-coated glass substrate (Figure 1c).

2.2. FeRh NP Ink Sintering

The sintering of NPs was conducted using a programmable furnace with separate runs in air and argon flow (Figure 1d). The glass substrates with the deposited ink were subjected to a heating rate of 10 K min^{-1} and reached a maximum temperature of 873 K, where they were held for 1 h. Following this, the furnace was turned off, and the substrates were left in the furnace to cool down to room temperature.

The laser sintering (Figure 1e) was carried out using a continuous wave (CW)-laser (Laser Quantum, 532 nm) and a programmable two-axis linear stage (Thorlabs DDSM100/M) on the ink-deposited glass substrates. The laser beam was focused by a microscope objective (Mitutoyo, 10X). The substrate was placed on the stage and was scanned in a single axis to achieve a sintered line. For characterization techniques that required larger areas of study, the X–Y stage was programmed to produce successive parallel lines such that all the regions between the lines were irradiated, covering the whole ink-dispersed region. The laser-sintered custom patterns were obtained by programming the linear stage in both the X and Y axes, leading to the sintering of the desired areas of the deposited ink. The substrate was then dispersed in an ethanol bath and ultrasonicated for 5 min, removing all the non-sintered ink and polymer layers.

The laser fluence was varied to evaluate the material-sintering window, and was calculated using the following formula[86]

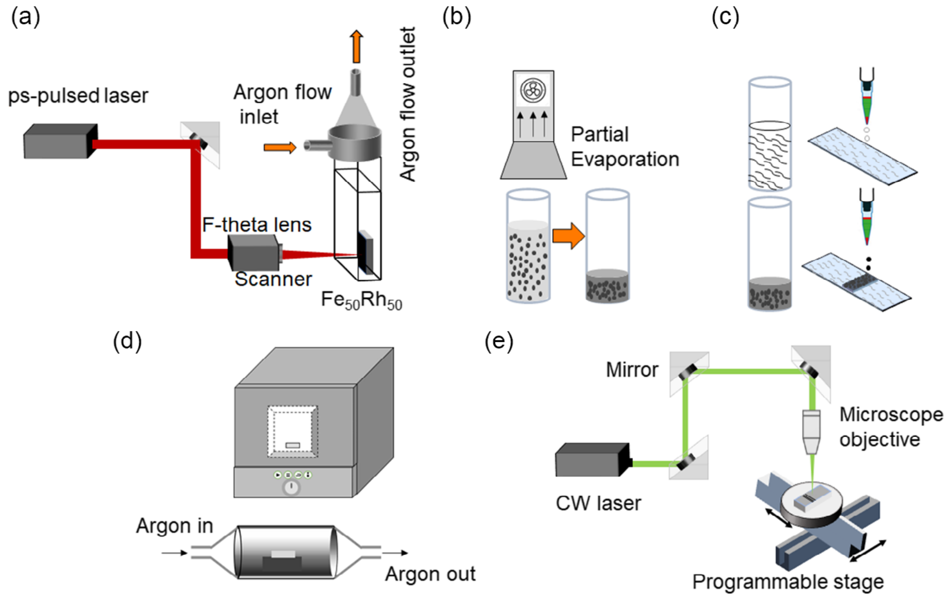

Figure 1. Schematic step-by-step process for sintering of near-to equimolar FeRh nanoparticles (NPs). a) Synthesis of NPs by picosecond (ps)-pulsed laser ablation in ethanol in a Schlenk chamber. b) Partial evaporation of ethanol from the FeRh NP colloid employing an axial fan at room temperature. c) Deposition of polyvinylpyrrolidone (PVP, MW = 40 000) and FeRh ink on a selected region of the glass substrate. d) FeRh nanoink sintering by programmable furnace in air and furnace with argon flow. e) Sintering by 532 nm continuous wave laser and a microscope objective (10×) providing the micrometric resolution required.

$$F = \frac{4 \cdot P}{v_s \cdot d \cdot \pi} \tag{1}$$

where F = laser fluence, P = laser power, v_s = scanning speed, and d = laser spot diameter. The scanning speed was kept constant at $10\,\text{mm s}^{-1}$ for all the experiments and the laser fluence was varied between 16 and $246\,\text{J cm}^{-2}$. The sintered micrometric lines were visualized by an optical microscope (Leica DM2700 M) and SEM (Apreo S LoVac, Thermo Fisher Scientific). The width was measured using ImageJ software at ten different positions on each line.

The laser processing at high fluences resulted in FeRh NP ablation along with the sintering (explained later in detail), enhancing the porosity of the magnetocaloric structures. The effect of laser fluence on the ablation of FeRh ink was monitored by reflectance spectroscopy (Supporting Information). The effect of laser-induced heating and furnace heating on the FeRh crystal structure was studied by X-ray diffraction (XRD) in θ–2θ geometry with Cu-Kα radiation using a Philips PW1730 X-ray diffractometer with a graphite monochromator, aiming to quantify the phase conversion achieved during the sintering processes. Rietveld refinement was carried out using the Fullprof suite.[87] The B2 fraction was also analyzed based on magnetometry data of the FeRh ink after laser and furnace sintering, to determine the sintering parameters yielding the highest B2-phase fraction. M(H) curves were measured using the vibrating-sample magnetometer (VSM) option of a PPMS DynaCool (Quantum Design) between 5 and 400 K and up to a maximum of 500 K using a VSM oven option in magnetic fields up to 9 T and were corrected for the distinct dia- and paramagnetic glass substrate background signal; M(T) measurements were performed between 150 and 700 K at an applied field of 0.1 T.

3. Results and Discussion

3.1. FeRh NP Ink Sintering

To examine the morphology of the sintered structures within different laser fluence regimes, optical microscopy and SEM were used, as shown in **Figure 2**. Initially, the ink is partially sintered leading to the formation of a discontinuous line pattern consisting of sintered and non-sintered regions (Figure 2a). The laser interaction leads to the NP densification and partial evaporation of the polymer. Increasing the laser fluence above $16\,\text{J cm}^{-2}$ results in the formation of necks and percolation networks start to grow. At a laser fluence of $41\,\text{J cm}^{-2}$, the NPs are sintered, forming a homogenous line with a dense magnetocaloric structure (Figure 2b). Increasing the fluence to $57\,\text{J cm}^{-2}$ results in the creation of compact agglomerates of NPs, attributed to fusion, grain growth, and lattice diffusion.[88] The increase in laser energy also leads to ablation along with sintering, mainly at the center of the line, where the intensity is the highest, resulting in distinct network structures rather than continuous NP films (Figure 2c). At higher fluences, NP ablation is more pronounced and the overall density of the dispersed NP layer is reduced (Figure 2d). The ablation causes an increase in the porosity of the magnetocaloric structure, which could potentially enhance the convective heat transfer to the working fluid in magnetocaloric regenerators.[89]

We also examined the morphology of FeRh ink furnace sintered at 873 K for 1 h. Compared to laser processing, the furnace-sintered NPs appeared more compact due to the slow heating rate and uniform temperature distribution (as shown in **Figure 3**). The gradual heating rate provided sufficient time for particle migration, promoting uniform sintering throughout the NP film, and to avoid the formation of individual networks of structures. The slow heating and cooling process may have resulted in surface oxidation due to residual oxygen, which could have a negative impact on the mechanical and magnetic properties of the sintered structures (as noted in Ref. [25]).

The optical microscopy and SEM results obtained from the laser-processed FeRh magnetocaloric ink can be explained by analyzing the intensity profile of the CW laser used in the process. The Gaussian intensity distribution of the laser defines various interaction regimes. At low fluence ($16\,\text{J cm}^{-2}$), only a small region at the center of the line is above the threshold intensity required for sintering (shown by the extrapolated dashed line (**Figure 4**a). Latter depicts the width of the line for each peak intensity. The line width increases upon increasing laser fluence (Figure 4b), which is also visualized by the black arrows in the optical microscopy images (Figure 2). For a sintered line ($41\,\text{J cm}^{-2}$), the peak intensity of the Gaussian beam lies below the ablation threshold with a significant area of the Gaussian

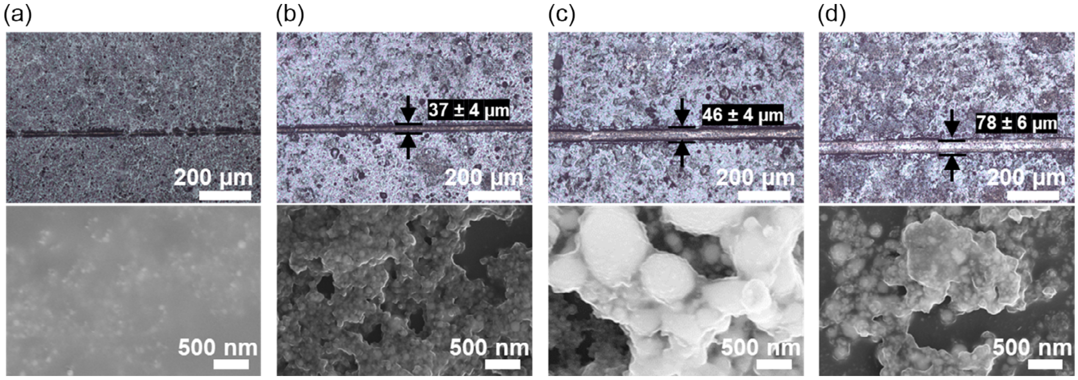

Figure 2. Surface morphology of laser-sintered structures of FeRh NPs after applying different laser fluences as visualized by optical microscopy and scanning electron microscopy: a) $16\,\text{J cm}^{-2}$, b) $41\,\text{J cm}^{-2}$, c) $57\,\text{J cm}^{-2}$, and d) $246\,\text{J cm}^{-2}$. The black arrows show the width of the sintered line.

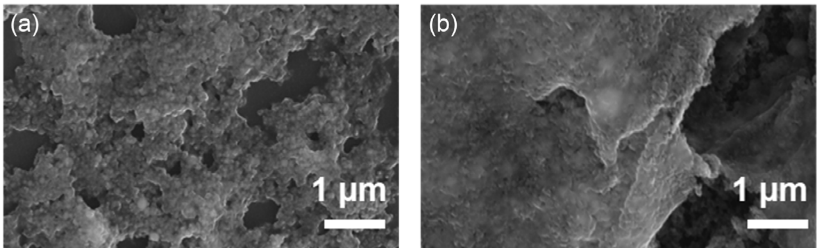

Figure 3. SEM images of the sintered FeRh NP ink surface morphology for a) laser sintering at a fluence of 41 J cm^{-2}, and b) a furnace-sintered structure at 873 K for 1 h.

distribution above the sintering threshold. At higher fluences, the ablation of NPs is observed along with sintering mainly in the central region of the lines where the intensity of the laser beam is the highest (Figure 2c,d). At higher fluences, the ablation of NPs is observed along with sintering mainly in the central region of the lines, where the intensity of the laser beam is the highest (Figure 2c,d). The ablation regimes can be analyzed by reflectance spectroscopy, as depicted in Figure S2, Supporting Information. The partial ablation of the ink resulted in the formation of porous structures confirmed by an increased optical transmission (Figure S3, Supporting Information). The maximum fluence that could be achieved without substrate damage was 246 J cm^{-2}. Although the line width increases with an increasing laser fluence, it saturates at 246 J cm^{-2}, limited by the Gaussian beam's shape and diameter.

3.2. Structural and Magnetic Characterization of the Magnetocaloric Microstructures

Annealing FeRh NPs induces a phase transition from the γ to the B2 phase, which is essential to enhance the material's magnetic and magnetocaloric properties.[74] To investigate the effect of laser-assisted heating and furnace heating on the crystal structure and phase formation of FeRh NP ink, we performed XRD experiments. **Figure** 5a shows the diffraction patterns indicating a phase change from the γ phase to a mixed B2-γ state as the laser fluence is increased. The B2-, γ-, and Fe_xO_y-molar-phase fractions were evaluated via Rietveld refinement (Figure 5c). The furnace-based annealing in air at 873 K leads to a complete transformation to the Fe_2O_3 (hematite) phase, while annealing in argon-flow results in a mixture of B2 and γ phase and a minor Fe_3O_4 (magnetite) contribution (Figure 5c). However, a lower degree of oxidation was observed for laser-processed inks and was mainly evident for laser fluences lower than 131 J cm^{-2} (Figure 5a marked with asterisk). The overall phase fraction shows that the B2 phase increases and the γ phase is reduced with increasing laser fluence, as summarized in **Table 1**. This shows that the laser-sintering technique not only leads to higher γ- to B2-phase conversion, but also represents a more oxidation-resistant process than a conventional one. This is a remarkable fact considering that laser sintering is performed in air, hence avoiding the time and resource–costly employment of inert gas atmospheres. Additionally, the high laser fluences lead to NP ablation, giving rise to the formation of micropores, which could be essential for heat transfer to the cooling media for magnetocaloric regenerators. For the laser-sintered sample, a small splitting of the reflections of the γ phase appears at some samples, indicating two γ-phases with different lattice parameters. This can be explained by hydrogen, which is incorporated into the structure during NP synthesis,[74] being released, resulting in a contraction of the lattice.[74]

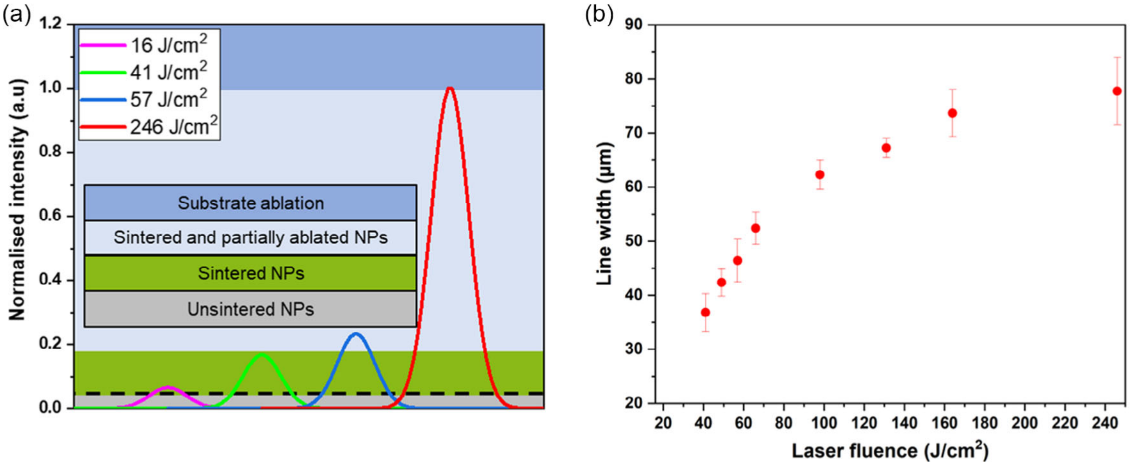

Figure 4. a) Gaussian intensity profile at laser fluences (ranging from 16 to 246 J cm^{-2}) showing the unsintered, sintered, and ablation regimes. The dashed line (black) indicates the width of the sintered line. b) Laser fluence effect (ranging from 41 to 246 J cm^{-2}) on the line width of the sintered magnetocaloric structures. The error bar shows the standard deviation of line widths measured at the 10 different positions of each sintered line.

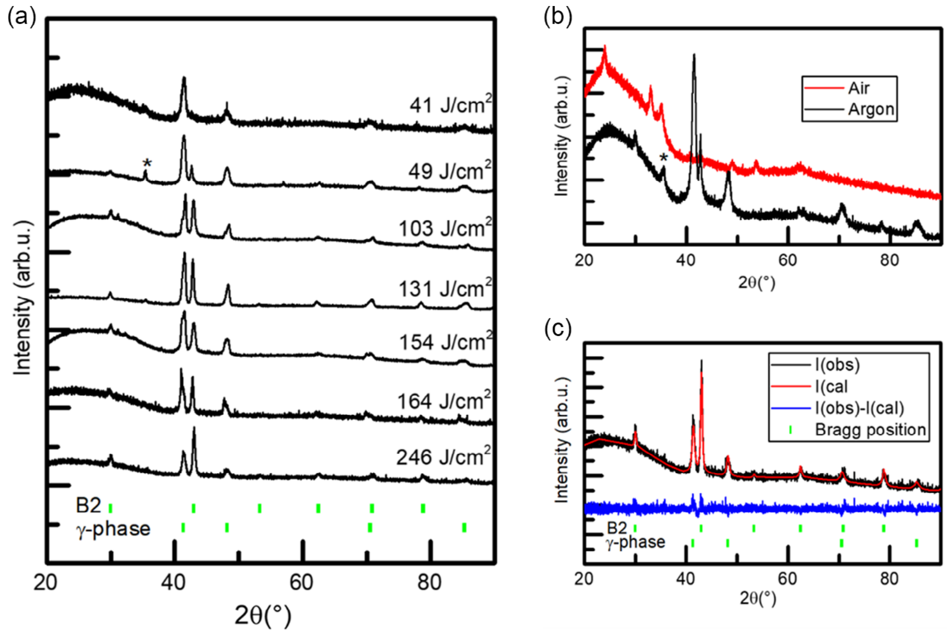

Figure 5. a) X-ray diffraction (XRD) data of laser-sintered samples with fluences from 41 to 246 J cm$-^2$. The tick marks indicate the possible position of reflections for the B2 phase and the γ phase. Reflections from oxide impurities are marked with an asterisk. b) Comparison of furnace-sintered samples on air and Ar atmosphere. c) Rietveld refinement of the laser-sintered sample with an fluence of 246 J cm^{-2}.

Table 1. Molar fraction of main crystalline phases of furnace-sintered and laser-sintered samples determined by XRD, estimated by Rietveld refinements.

Process	Parameters	B2-molar-phase fraction	γ-molar-phase fraction	Fe$_x$O$_y$-molar-phase fraction
Furnace sintering	873 K in air	–	–	1.00 (Fe$_2$O$_3$)
Furnace sintering	873 K in argon	0.08	0.65	0.27 (Fe$_3$O$_4$)
Laser sintering	41 J cm^{-2}	–	1.00	–
Laser sintering	49 J cm^2	0.08	0.74	0.18 (Fe$_3$O$_4$)
Laser sintering	103 J cm^2	0.38	0.62	–
Laser sintering	131 J cm^2	0.29	0.67	0.04 (Fe$_3$O$_4$)
Laser sintering	154 J cm^2	0.29	0.71	–
Laser sintering	164 J cm^2	0.30	0.70	–
Laser sintering	246 J cm^2	0.52	0.48	–

The magnetization response of the laser sintered as well as furnace-annealed FeRh NPs is studied via magnetometry regarding composition and the AFM–FM phase transition in direct comparison to XRD data analysis. Field-dependent magnetization curves of FeRh ink laser-irradiated at fluences of 41 up to 246 J cm^{-2} recorded at 500 K are shown in **Figure 6**a. Higher laser fluences result in an increase of the saturation magnetization M_S, which hints toward a partial phase transformation from paramagnetic γ-FeRh to FM B2-FeRh. For fluences lower than 131 J cm^{-2}, different magnetic alignment behavior is observed in the low-field region, together with slightly increased coercive fields. Both effects can be assigned to partial oxidation to a magnetite/maghemite phase, accompanied by an increase in total magnetization.

Magnetization $M_{(500\,\mathrm{K},2\,\mathrm{T})}$ values extracted from the measurements at 500 K and 2 T are compared to B2 fractions obtained in XRD analysis in Figure 6b. Since the FeRh-sintered structures are in the FM state above the phase transition at 500 K, the magnetization is expected to be representative for the B2-FeRh fraction of the sample (in case no oxides are present). In fact, a general agreement between XRD B2 fraction and $M_{(500\,\mathrm{K},2\,\mathrm{T})}$ can be observed, not including partially oxidized samples, where a magnetite fraction results in deviating magnetization values. Furthermore, it has to be considered that a direct determination of the remaining FeRh mass on the samples after laser treatment could not be performed, wherefore it was estimated based on the total amount of deposited FeRh material in relation to the area of the sample pieces studied in magnetometry, where minor inhomogeneities in NP coverage can increase the error margin. Disregarding samples with considerable oxide fraction, high-field magnetization $M_{(500\,\mathrm{K},2\,\mathrm{T})}$ and B2-phase fraction display a comparable trend in laser fluence assuming a saturation magnetization of ≈100 Am^2 kg^{-1}, matching the range of reported values for pure B2-FeRh at 500 K.[90]

The magnetization of laser-treated FeRh-deposited ink was compared to those from the conventional annealing processes. The FeRh inks deposited on glass substrate were subjected to elevated temperatures of 573–873 K under ambient air or argon atmosphere, respectively (**Figure 7**). After annealing in air, oxidation of the original γ-FeRh phase resulted in the formation of hematite (as also observed in XRD). This is clearly visible by the changes in the M(H) shape and by the decreasing high-field magnetization due to the canted AFM structure of hematite. In contrast, annealing of the FeRh NPs under argon atmosphere results

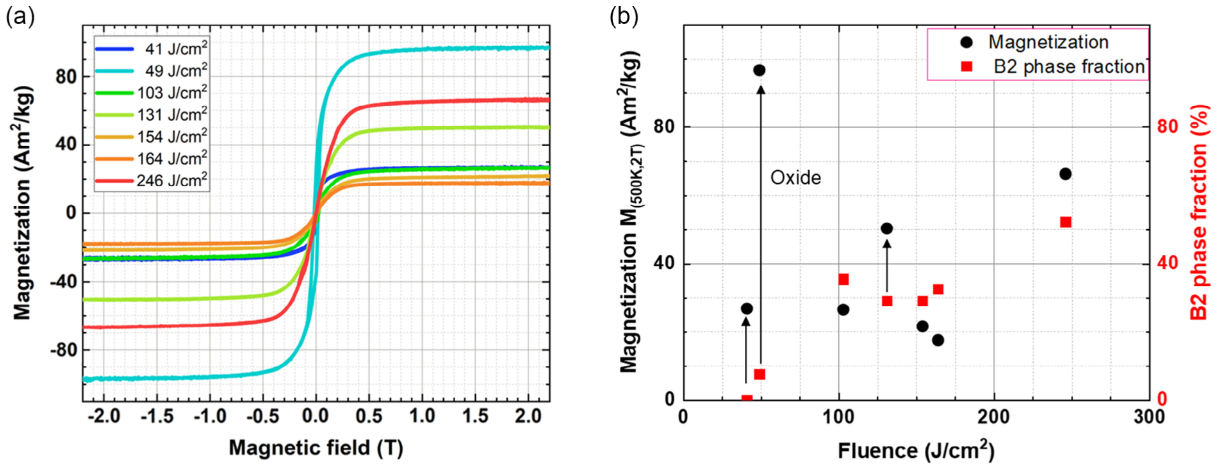

Figure 6. a) Field-dependent magnetization at 500 K of FeRh NPs deposited on glass substrate after laser sintering using fluences of 41 up to 246 J cm^{-2}. b) FeRh magnetization $M_{(500\,K,2\,T)}$ (black) was recorded at 500 K at 2 T (black dots) compared to B2-phase fractions (red) as determined from XRD analysis. The arrows indicate the samples whose magnetization was increased due to partial oxidation, that is, formation of magnetite, as indicated by XRD results.

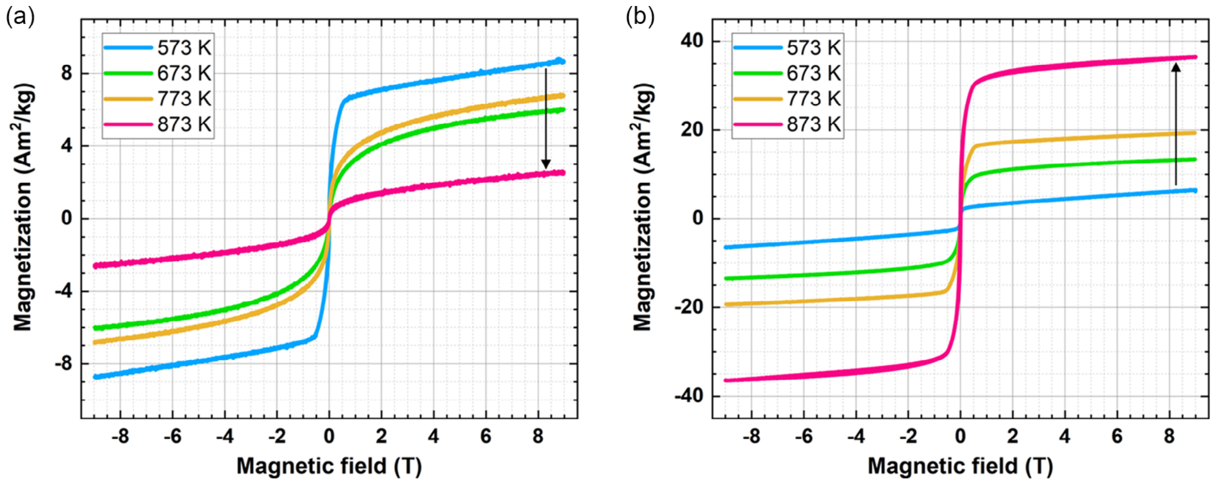

Figure 7. Field-dependent magnetization of FeRh NPs deposited on glass substrate at 300 K after annealing at $T_H = 573$ to 873 K in a) air or b) argon, respectively.

in the conservation of the M(H) shape, showing predominant magnetic alignment already at 0.5 T, combined with a continuous increase in magnetization upon increasing annealing temperature in reaction to γ- to B2-FeRh conversion, as seen in XRD data. The annealing under argon atmosphere results in much higher B2 fraction and, accordingly, higher magnetization, by preventing any oxidation of the FeRh material to hematite as observed under annealing in air. Comparing the conventional annealing processes in the furnace with laser sintering, highest mass magnetization values obtained via laser-sintering FeRh ink exceed that of furnace-sintered samples, while also allowing the simultaneous printing/writing of 2D structures.

Previous experiments on FeRh NP powder showed similar results to those of the argon-flow annealing discussed earlier, with almost complete conversion of the γ-FeRh phase to the B2 structure.[91] Still, while high B2 fractions were obtained, magnetization and Mössbauer spectroscopy experiments indicated only a moderate fraction of the FeRh material to participate in the AFM–FM phase transitions, being primarily pinned in a ferromagnetic state. To study the laser-based sintering route under this aspect, field-dependent magnetization behavior was analyzed across the phase-transition temperature in detail for the laser fluence of 246 J cm^{-2}, which showed the maximum B2 fraction and magnetization.

3.3. Magnetocaloric Properties

FeRh ink laser sintered with a laser fluence of 246 J cm^{-2} displays considerable magnetization already below the AFM phase transition at 150 K (**Figure 8**). This is in agreement with the observation of a partial-pinned ferromagnetic state of FeRh

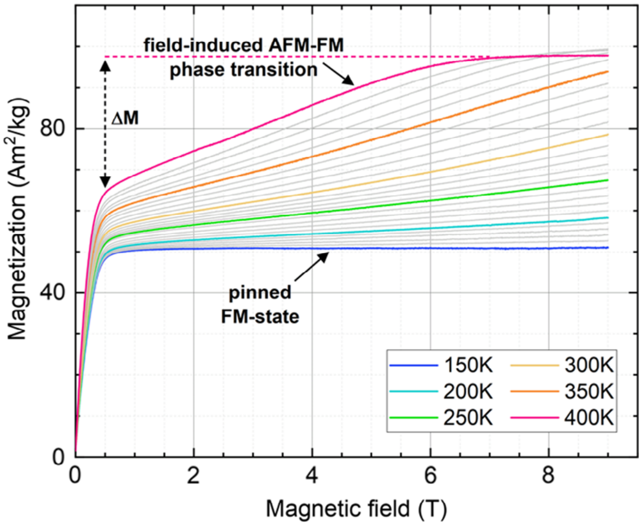

Figure 8. Magnetization of FeRh NPs deposited on glass substrate and laser sintered at a fluence of 246 J cm^{-2} measured from 0 to 9 T at 150 up to 400 K across the antiferromagnetic to ferromagnetic (AFM—FM) phase transition. The contribution of FeRh material pinned in the FM state as well as the increase in magnetization ΔM connected to the field-induced AFM–FM transition is indicated by arrows.

NPs after annealing.[65] Possible explanations for a partially pinned ferromagnetic fraction include a minor variation in stoichiometry in the NPs produced via LAL, as even miniscule variations of the Fe content in FeRh can cause considerable changes in the AFM–FM phase-transition temperature or even the permanent conservation of ferromagnetic behavior. Also, structural defects in the FeRh lattice are known to stabilize ferromagnetic order, as shown before by inducing different degrees of structural disorder via ion irradiation,[92] which could be present in the FeRh NPs after the laser-ablation process.

At higher temperatures, M(H) data shows an increase in magnetization upon rising fields, assigned to the beginning of the AFM–FM transition already at ≈150–200 K due to substantial broadening of the transition. A measurement of temperature-dependent magnetization was recorded at 0.1 T to illustrate the sample behavior across the phase transition (Figure S4, Supporting Information), which indicates that the AFM–FM phase-transition peak was achieved at ≈460 K, where all FeRh can be considered as ferromagnetic. Here, it has to be noted that minor changes in M(H) are superpositioned by a temperature-dependent decrease in the background signal of the employed glass substrate (already subtracted from the data in Figure 8). Due to the very limited net magnetic moment of the FeRh thin layer as compared to the substrate material, even minor uncertainties regarding background subtraction can result in slightly different M(H) shapes in this temperature region. Above ≈250–350 K, M(H) shows a more distinct nonlinear increase in field-dependent magnetization when approaching the bulk-phase-transition temperature where most of the FeRh NPs reach the ferromagnetic state. At 400 K, a constant magnetization value of ≈98 Am^2 kg^{-1} is reached above 7 T, as the transition to the FM state is completed, with the distinct field-driven increase in magnetization of about $\Delta M = 35$ Am^2 kg^{-1} corresponding to the field-induced phase transition. Comparing these results to previous experiments on furnace-annealed FeRh NPs ($\Delta M = 6$ Am^2 kg^{-1}),[91] a much higher field-driven increase in magnetization is observed following the laser-sintering route, being evidence of the potential of laser-written 2D structures for magnetocaloric applications. Although a more detailed analysis is hindered by the considerable para- and diamagnetic background contribution of the glass substrate, a value of ≈3–3.5 J kg^{-1} K^{-1} can be extracted from the data as a rough estimate of the change in magnetic entropy connected to the AFM–FM phase transition between 0 and 9 T, as is elucidated in more detail in the corresponding section of Supporting Information (Figure S5, Supporting Information). Further improvement in magnetocaloric performance is expected under optimization of laser-ablation and especially laser-sintering parameters by increasing attainable B2-FeRh fractions and reducing ferromagnetic pinning.

3.4. Custom FeRh Magnetocaloric Microstructures by Laser Sintering

Evaluating the magnetic properties of the FeRh structures after sintering indicated that laser sintering (at a fluence of 246 J cm^{-2}) of the FeRh NP ink leads to a higher conversion to magnetic phases and decreases the possibility of FeRh NP oxidation compared to furnace sintering, due to the rapid heating and cooling process occurring during laser sintering. The laser-sintering process provides inherent spatial resolution and scanning flexibility that enables the creation of customized magnetocaloric microstructures, as demonstrated in **Figure 9**a. After processing the desired spatial pattern, the unsintered ink can be removed by cleaning with the ink solvent (ethanol), resulting in sintered structures remaining on the substrate (as depicted in Figure 9b). The quality of the laser-sintered FeRh structures, coupled with the ability to attain accurate spatial resolution and design customized geometries, make this technique a promising method for producing micrometric cooling structures for miniaturized electronic devices in particular when compared to furnace sintering.

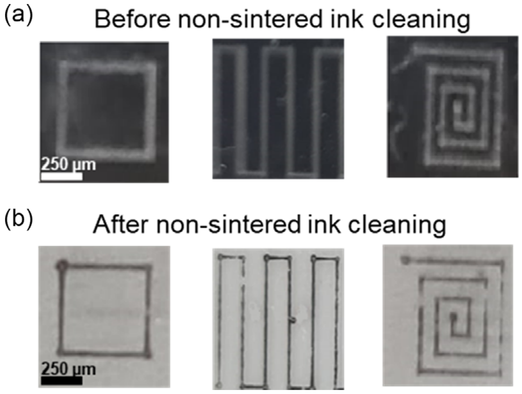

Figure 9. Depiction of the custom structures produced through laser processing at a laser fluence of 246 J cm^{-2}, with showing the structures a) before cleaning of the deposited FeRh ink and b) after cleaning with ethanol using ultrasonication for 5 min. The scale bar remains consistent across all images.

4. Conclusion

Producing micrometric magnetocaloric devices presents a promising avenue for creating compact cooling sources. In this study, we have outlined a sequential process for fabricating FeRh magnetocaloric custom structures starting with the laser-based NP synthesis employing a bulk target, followed by ink formulation, dispersion on substrate, and sintering of NP ink employing a CW laser. The CW laser sintering of the NP ink was evaluated to define the processing window. The NPs were completely sintered at $41\ \mathrm{J\,cm^{-2}}$ with further increase in the laser fluence that promotes ablation of NPs along with sintering. This results in the increase of porosity of the magnetocaloric structure, which could promote the convective heat transfer to the working fluid for magnetic regenerators.

The laser-induced heating resulted in a partial phase transformation from γ to B2 phase, with the maximum B2 fraction being 52%. This transformation caused a magnetization increase of $\approx 66\ \mathrm{Am^2\,kg^{-1}}$ and a maximum rise in magnetization of approximately $35\ \mathrm{Am^2\,kg^{-1}}$ across the field-driven AFM–FM phase transition. Compared to oven sintering, laser sintering facilitated faster processing, prevented oxidation, enabled the formation of intricate micrometric patterns, and improved the magnetocaloric phase transformation.

Supporting Information

Supporting Information is available from the Wiley Online Library or from the author.

Acknowledgements

The authors thank Tobias Bochmann for his help with the SEM imaging of sintered samples. The authors gratefully acknowledge the funding by the German Research Foundation (DFG) within the Collaborative Research Centre/Transregio (CRC/TRR) 270 (Project-ID 405 553 726, projects A11, B04, B05, and B08), as well as the CRC/TRR 247 (Project-ID 388 390 466, project B02). Bilal Gökce further thanks the DFG for funding of the project GO 2566/10-1.

Open Access funding enabled and organized by Projekt DEAL.

Conflicts of Interest

The authors declare no conflict of interest.

Data Availability Statement

The data that support the findings of this study are available from the corresponding author upon reasonable request.

Keywords

antiferromagnetic–ferromagnetic phase transition, iron–rhodium, laser ablation in liquid, laser sintering, micro cooling

Received: February 21, 2023
Revised: April 19, 2023
Published online:

[1] T. Dullweber, S. Gatz, H. Hannebauer, T. Falcon, R. Hesse, J. Schmidt, R. Brendel, *Prog. Photovoltaics* **2012**, *20*, 630.
[2] M. M. Hilali, J. M. Gee, P. Hacke, *Sol. Energy Mater. Sol. Cells* **2007**, *91*, 1228.
[3] D. C. Nguyen, S. Ito, *Int. J. Nanotechnol.* **2013**, *10*, 269.
[4] L. Z. Li, G. Tang, Z. Shi, H. Ding, C. B. Liu, D. L. Cheng, Q. Y. Zhang, L. Yin, Z. B. Yao, L. Duan, D. H. Zhang, C. G. Wang, M. X. Feng, Q. Sun, Q. Wang, Y. J. Han, L. Wang, Y. Luo, X. Sheng, *Proc. Natl. Acad. Sci. USA.* **2021**, *118*, e2023436118.
[5] Z. Bao, J. W. Luo, Y. S. Wang, T. C. Hu, S. Y. Tsai, Y. T. Tsai, H. C. Wang, F. H. Chen, Y. C. Lee, T. L. Tsai, R. J. Chung, R. S. Liu, *Chem. Eng. J.* **2021**, *426*, 130849.
[6] G. Vescio, J. L. Frieiro, A. F. Gualdron-Reyes, S. Hernandez, I. Mora-Sero, B. Garrido, A. Cirera, *Adv. Mater. Technol.* **2022**, *7*, 2101525.
[7] M. Montanino, G. Sico, A. D. Del Mauro, J. Asenbauer, J. R. Binder, D. Bresser, S. Passerini, *Energy Technol.* **2021**, *9*, 2100315.
[8] M. A. Nazri, L. M. Lim, Z. Samsudin, M. Y. T. Ali, I. Mansor, M. I. Suhaimi, S. R. Meskon, A. N. Nordin, *3D Print. Addit. Manuf.* **2021**, *8*, 176.
[9] P. H. Yang, J. Li, S. W. Lee, H. J. Fan, *Adv. Sci.* **2022**, *9*, 2103894.
[10] Y. Z. Li, Y. X. Liu, S. R. A. Bhuiyan, Y. Zhu, S. S. Yao, *Small Struct.* **2022**, *3*, 2100131.
[11] R. Rayhana, G. G. Xiao, Z. Liu, *IEEE Trans. Instrum. Meas.* **2021**, *70*, 1.
[12] E. Wawrzynek, C. Baumbauer, A. C. Arias, *Sensors* **2021**, *21*, 6557.
[13] Y. H. Xu, F. Y. Zhang, W. J. Zhai, S. J. Cheng, J. H. Li, Y. Wang, *Polymers* **2022**, *14*, 566.
[14] Y. X. Zhou, W. Grayson, *MRS Bull.* **2022**, *47*, 91.
[15] P. J. Wang, Y. Z. Sun, X. Q. Shi, H. X. Shen, H. H. Ning, H. T. Liu, *Bio Des. Manuf.* **2021**, *4*, 344.
[16] S. H. Lee, S. Lee, *Polymers* **2019**, *11*, 245.
[17] T. H. Phung, A. N. Gafurov, I. Kim, S. Y. Kim, K. M. Kim, T.-M. Lee, *Sci. Rep.* **2021**, *11* 19982.
[18] M. Smolka, S. Ruttloff, D. Nees, C. Prietl, V. Satzinger, B. Lamprecht, P. Hütter, J. Hesse, G. Kokkinis, G. Kriechhammer, D. Scheidl, B. Wilfing, *Proceedings* **2018**, *2*, 1054.
[19] S. Park, H. Kim, J.-H. Kim, W.-H. Yeo, *Materials* **2020**, *13*, 3587.
[20] P. M. Grubb, H. Subbaraman, S. Park, D. Akinwande, R. T. Chen, *Sci. Rep.* **2017**, *7*, 1202.
[21] P. Zhang, F. Wang, M. Yu, X. Zhuang, X. Feng, *Chem. Soc. Rev.* **2018**, *47*, 7426.
[22] K. Y. Mitra, A. Willert, R. Chandru, R. R. Baumann, R. Zichner, *Adv. Eng. Mater.* **2020**, *22*, 2000547.
[23] A. Jo, S. I. Chung, P. K. Kim, J.-W. Lee, H. Lee, J. H. J. Yang, T.-G. Ha, J. Kim, Y. J. Lee, H. J. Jeong, S. H. Seo, S. Y. Jeong, G.-W. Lee, K.-J. Baeg, J. T. Han, J. H. Park, *ACS Appl. Energy Mater.* **2021**, *4*, 13666.
[24] D. Ma, S. Chon, S. Cho, Y. Lee, M. Yoo, D. Kim, D. Y. Lee, J. K. Lim, *J. Electroanal. Chem.* **2020**, *876*, 114720.
[25] J. Niittynen, M. Mäntysalo, *IEEE Trans. Compon. Packag. Manuf. Technol.* **2014**, *4*, 2018.
[26] J. Jones, D. Büttner, R. Chudasama, D. Wimpenny, K. Krüger, *J. Imaging Sci. Technol.* **2012**, *56*, 40503.
[27] Y. P. Kathuria, *1997 Int. Symp. on Micromechanics and Human Science (Cat. No.97TH8311)*, October 1997, pp. 41–47.
[28] J. H. Park, J. W. Lee, Y. W. Ma, B. S. Kang, S. M. Hong, B. S. Shin, *Nanomaterials* **2022**, *12*, 387.
[29] Y. P. Yuan, Z. Liu, K. H. Zhang, W. N. Han, J. M. Chen, *Opt. Laser Technol.* **2018**, *103*, 327.
[30] A. Hurtado, D. Jevtics, B. Guilhabert, Q. Gao, H. H. Tan, C. Jagadish, M. D. Dawson, *IET Optoelectron.* **2018**, *12*, 30.
[31] N. K. Roy, D. Behera, O. G. Dibua, C. S. Foong, M. A. Cullinan, *Microsyst. Nanoeng.* **2019**, *5*, 64.
[32] A. Nazir, J.-Y. Jeng, *Proc. Inst. Mech. Eng. Part C* **2019**, *234*, 2741.

[33] M. Feinäugle, R. Eason, C. Sones, B. Mills, J. A. Grant-Jacob, I. Katis, D. J. Heath, Making Additive Manufacturing Functional - The Laser-Assisted Fabrication of Electronic and Photonic Devices, **2014**.
[34] D. Lowell, D. George, J. Lutkenhaus, C. Tian, M. Adewole, U. Philipose, H. L. Zhang, Y. K. Lin, *Micromachines* **2016**, *7*, 128.
[35] I. I. Tumkin, E. M. Khairullina, M. S. Panov, K. Yoshidomi, M. Mizoshiri, *Materials* **2021**, *14*, 2493.
[36] F. Zacharatos, M. Makrygianni, R. Geremia, E. Biver, D. Karnakis, S. Leyder, D. Puerto, P. Delaporte, I. Zergioti, *Appl. Surf. Sci.* **2015**, *374*, 117.
[37] A. F. Harper, P. J. Diemer, O. D. Jurchescu, *npj Flexible Electron.* **2019**, *3*, 11.
[38] R. K. Jayne, M. Ç. Karakan, K. Zhang, N. Pierce, C. Michas, D. J. Bishop, C. S. Chen, K. L. Ekinci, A. E. White, *Lab Chip* **2021**, *21*, 1724.
[39] Y. Nahmias, R. E. Schwartz, C. M. Verfaillie, D. J. Odde, *Biotechnol. Bioeng.* **2005**, *92*, 129.
[40] J. Xu, Y. Liao, J. Lin, Y. Zhong, X. Li, C. Jing, Y. Cheng, *Laser-based Micro- and Nanoprocessing XII* **2018**, p. 6.
[41] J. Álvarez-Martínez, O. Medina-Cázares, M. Soto-Alcaraz, R. Castaneda-Priego, G. Gutierrez-Juarez, R. Castro-Beltrán, *J. Micromech. Microeng.* **2022**, *32*, 065001.
[42] X. Zhang, H. Hu, D. Tang, C. Zhang, J. Fu, P. Zhao, *Sens. Actuators A: Phys.* **2021**, *327*, 112753.
[43] D. Zhang, H. Wei, H. Hu, S. Krishnaswamy, *APL Photonics* **2020**, *5*, 076112.
[44] Q.-Z. Zhao, J.-R. Qiu, X.-W. Jiang, E.-W. Dai, C.-H. Zhou, C.-S. Zhu, *Opt. Express* **2005**, *13*, 2089.
[45] B. AlQattan, J. Doocey, M. Ali, I. Ahmed, A. E. Salih, F. Alam, M. Bajgrowicz-Cieslak, A. K. Yetisen, M. Elsherif, H. Butt, *ACS Nano* **2021**, *15* 2340.
[46] T. Dixit, I. Ghosh, *Renewable Sustainable Energy Rev.* **2015**, *41*, 1298.
[47] H. E. Ahmed, B. H. Salman, A. S. Kherbeet, M. I. Ahmed, *Int. J. Heat Mass Transf.* **2018**, *118*, 129.
[48] T. Ikyumbur, F. Gbaorun, S. Ochi, *Curr. J. Appl. Sci. Technol.* **2019**, *32*, 1.
[49] M. Ali, A. M. El-Leathy, Z. Al-Sofyany, *Adv. Mech. Eng.* **2014**, *6*, https://doi.org/10.1155/2014/962510.
[50] Y. Joshi, Z. Wan, *Handbook of Thermal Science and Engineering* (Ed: F. A. Kulacki), Springer International Publishing, Cham **2017**, pp. 1.
[51] Z. He, Y. Yan, Z. Zhang, *Energy* **2021**, *216*, 119223.
[52] J. Lyubina, *J. Phys. D-Appl. Phys.* **2017**, *50*, 053002.
[53] A. Alahmer, M. Al-Amayreh, A. O. Mostafa, M. Al-Dabbas, H. Rezk, *Energies* **2021**, *14*, 4662.
[54] H. L. Hou, S. X. Qian, I. Takeuchi, *Nat. Rev. Mater.* **2022**, *7*, 633.
[55] A. Waske, M. Gruner, T. Gottschall, O. Gutfleisch, *MRS Bull.* **2018**, *43*, 269.
[56] S. Fähler, U. K. Rößler, O. Kastner, J. Eckert, G. Eggeler, H. Emmerich, P. Entel, S. Müller, E. Quandt, K. Albe, *Adv. Eng. Mater.* **2012**, *14*, 10.
[57] J. Y. Law, V. Franco, *J. Mater. Res.* **2022**, *38*, 37.
[58] C. B. N. Kadiyala, N. Ram, M. Prakash, N. Uppara, S. K. Nagasamudram, S. Sarmash, T. Subbarao, R. Kumar, G. Kumar, *J. Supercond. Novel Magn.* **2018**, *31*, 1971.
[59] W. H. Zhu, L. Ma, M. F. He, Z. K. Li, H. Z. Zhang, Q. R. Yao, G. H. Rao, K. P. Su, X. C. Zhong, Z. W. Liu, X. Q. Gao, *Adv. Eng. Mater.* **2023**, *2201770*, https://doi.org/10.1002/adem.202201770.
[60] X. Chen, Y. Chen, Y. Tang, D. Xiao, *J. Rare Earths* **2015**, *33*, 1293.
[61] F. Scheibel, T. Gottschall, K. Skokov, O. Gutfleisch, M. Ghorbani-Zavareh, Y. Skourski, J. Wosnitza, Ö. Çakır, M. Farle, M. Acet, *J. Appl. Phys.* **2015**, *117*, 233902.
[62] V. K. Pecharsky, J. K. A. Gschneidner, *Phys. Rev. Lett.* **1997**, *78*, 4494.
[63] M. Annaorazov, K. A. Asatryan, G. Myalikgulyev, S. A. Nikitin, A. M. Tishin, A. L. Tyurin, *Cryogenics* **1992**, *32*, 867.
[64] J. B. Staunton, R. Banerjee, M. Dias, A. Deak, L. Szunyogh, *Phys. Rev. B* **2014**, *89*, 054427.
[65] V. I. Zverev, A. M. Saletsky, R. R. Gimaev, A. M. Tishin, T. Miyanaga, J. B. Staunton, *Appl. Phys. Lett.* **2016**, *108*, 192405.
[66] V. Rodionov, A. Amirov, M. Annaorazov, E. Lähderanta, A. Granovsky, A. Aliev, V. Rodionova, *Processes* **2021**, *9*, 772.
[67] C. P. Bean, D. S. Rodbell, *Phys. Rev.* **1962**, *126*, 104.
[68] E. Valiev, R. Gimaev, V. Zverev, K. Kamilov, A. Pyatakov, B. Kovalev, A. Tishin, *Intermetallics* **2019**, *108*, 81.
[69] V. Stanković, C. Comninellis, Rhodium Recovery and Recycling from Spent Materials, **2011**.
[70] Z. Jia, J. W. Harrell, R. D. K. Misra, *Appl. Phys. Lett.* **2008**, *93*, 022504.
[71] D. Ciuculescu, C. Amiens, M. Respaud, A. Falqui, P. Lecante, R. E. Benfield, L. Jiang, K. Fauth, B. Chaudret, *Chem. Mater.* **2007**, *19*, 4624.
[72] D. Ciuculescu, C. Amiens, M. Respaud, P. Lecante, A. Falqui, B. Chaudret, *Mod. Phys. Lett. B* **2007**, *21*, 1153.
[73] Y. Cao, Y. Yuan, Y. Shang, V. I. Zverev, R. R. Gimaev, R. Barua, R. L. Hadimani, L. Mei, G. Guo, H. Fu, *J. Mater. Sci.* **2020**, *55*, 13363.
[74] R. Nadarajah, S. Tahir, J. Landers, D. Koch, A. S. Semisalova, J. Wiemeler, A. El-Zoka, S. H. Kim, D. Utzat, R. Möller, B. Gault, H. Wende, M. Farle, B. Gökce, *Nanomaterials* **2020**, *10*, 2362.
[75] K. J. Merazzo, A. C. Lima, M. Rincón-Iglesias, L. C. Fernandes, N. Pereira, S. Lanceros-Mendez, P. Martins, *Mater. Horiz.* **2021**, *8*, 2654.
[76] L. Li, B. Post, V. Kunc, A. Elliott, P. Paranthaman, *Scr. Mater.* **2017**, *135*, 100.
[77] D. Zhang, B. Gökce, S. Barcikowski, *Chem. Rev.* **2017**, *117*, 3990.
[78] E. Fazio, B. Gökce, A. De Giacomo, M. Meneghetti, G. Compagnini, M. Tommasini, F. Waag, A. Lucotti, C. G. Zanchi, P. M. Ossi, M. Dell'Aglio, L. D'Urso, M. Condorelli, V. Scardaci, F. Biscaglia, L. Litti, M. Gobbo, G. Gallo, M. Santoro, S. Trusso, F. Neri, *Nanomaterials* **2020**, *2317*, https://doi.org/10.3390/nano10112317.
[79] B. Gökce, V. Amendola, S. Barcikowski, *ChemPhysChem* **2017**, *18*, 983.
[80] T. Asahi, F. Mafuné, C. Rehbock, S. Barcikowski, *Appl. Surf. Sci.* **2015**, *348*, 1.
[81] A. Hahn, T. Stöver, G. Paasche, M. Löbler, K. Sternberg, H. Rohm, S. Barcikowski, *Adv. Eng. Mater.* **2010**, *12*, B156.
[82] S. Reichenberger, G. Marzun, M. Muhler, S. Barcikowski, *ChemCatChem* **2019**, *11* 4489.
[83] S. Dittrich, S. Kohsakowski, B. Wittek, C. Hengst, B. Gökce, S. Barcikowski, S. Reichenberger, *Nanomaterials* **2020**, *10*, 1582.
[84] T. Hupfeld, A. Wegner, M. Blanke, C. Doñate-Buendía, V. Sharov, S. Nieskens, M. Piechotta, M. Giese, S. Barcikowski, B. Gökce, *Adv. Opt. Mater.* **2020**, *8*, 2000473.
[85] M. B. Wilms, R. Streubel, F. Frömel, A. Weisheit, J. Tenkamp, F. Walther, S. Barcikowski, J. H. Schleifenbaum, B. Gökce, *Procedia CIRP* **2018**, *74*, 196.
[86] O. Ermak, M. Zenou, G. B. Toker, J. Ankri, Y. Shacham-Diamand, Z. Kotler, *Nanotechnology* **2016**, *27* 385201.
[87] J. Rodríguez-Carvajal, *Phys. B: Condens. Matter* **1993**, *192*, 55.
[88] J. H. Choi, K. Ryu, K. Park, S.-J. Moon, *Int. J. Heat Mass Transf.* **2015**, *85*, 904.
[89] A. Kitanovski, *Adv. Energy Mater.* **2020**, *10*, 1903741.
[90] E. Navarro, M. Multigner, A. R. Yavari, A. Hernando, *EuroPhysLett* **1996**, *35*, 307.
[91] R. Nadarajah, J. Landers, S. Salamon, D. Koch, S. Tahir, C. Doñate-Buendía, B. Zingsem, R. E. Dunin-Borkowski, W. Donner, M. Farle, H. Wende, B. Gökce, *Sci. Rep.* **2021**, *11*, 17581.
[92] B. Eggert, A. Schmeink, J. Lill, M. O. Liedke, U. Kentsch, M. Butterling, A. Wagner, S. Pascarelli, K. Potzger, J. Lindner, T. Thomson, J. Fassbender, K. Ollefs, W. Keune, R. Bali, H. Wende, *RSC Adv.* **2020**, *10*, 14386.

Supplementary Information (SI) to:

Development of Magnetocaloric Microstructures from Equiatomic FeRh Nanoparticles through Laser Sintering

Shabbir Tahir[1], Joachim Landers[2], Soma Salamon[2], David Koch[3], Carlos Doñate-Buendía[1], Anna R. Ziefuß[4], Heiko Wende[2], and Bilal Gökce[1]*,

[1] Chair of Materials Science and Additive Manufacturing, University of Wuppertal, Gaußstr. 20, 42119 Wuppertal, Germany

[2] Faculty of Physics and Center for Nanointegration Duisburg-Essen (CENIDE), University of Duisburg-Essen, Lotharstr. 1, 47057 Duisburg, Germany

[3] Institute of Materials Science, Technical University of Darmstadt, Darmstadt 64287, Alarich-Weiss-Str. 2, Germany

[4] Technical Chemistry I and Center for Nanointegration Duisburg-Essen (CENIDE), University of Duisburg-Essen, Universitätsstr. 7, 45141 Essen, Germany

* Corresponding author: goekce@uni-wuppertal.de; Tel.: +49-202-439-5385

1. Synthesis of FeRh nanoparticles by pulsed laser ablation of FeRh target in ethanol.

The scanning electron microscope imaging shows that the formation of spherical nanoparticles of distinct sizes (Inset Fig. S1). The size distribution gives an overview of the maximum ferret diameter of 558 nanoparticles. It has to be noted that the particles less than 2 nm were difficult to resolve, and only clearly visible, non-agglomerated particles were considered. The distribution shows higher size fraction of smaller nanoparticles (< 10 nm) with a peak maximum of 6.9 nm; and were fitted using lognormal distribution. The Polydispersity index (PDI) give an overall impression of dispersity and since the PDI is higher than 0.3, the distribution is polydisperse.

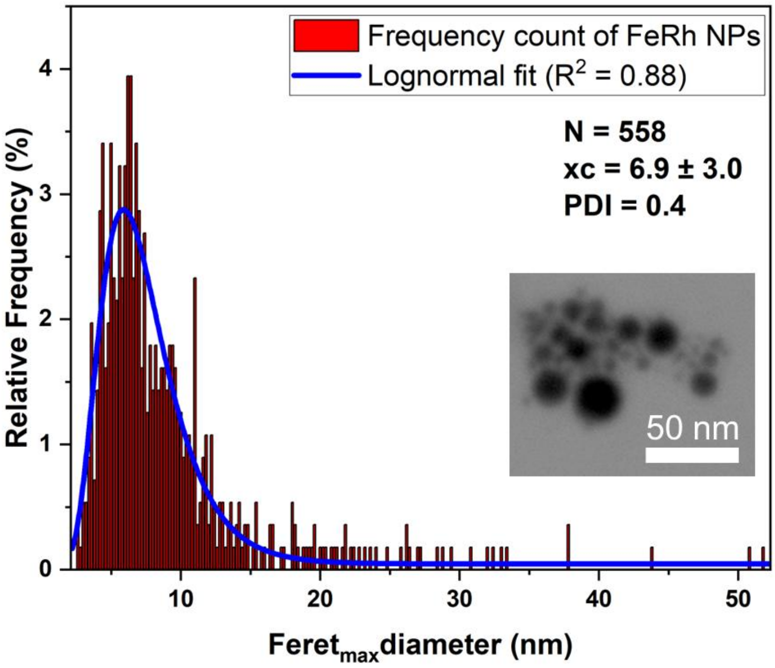

Figure S1: Particle size distribution as extracted from the SEM images of homogeneously dispersed FeRh nanoparticles (558 particles were counted).

2. Mass approximation of laser sintered FeRh ink using reflectance spectroscopy.

Reflectance spectroscopy is a technique commonly used for characterizing both powder and thin films. In this method, light from a source is transmitted through an optical fibre to a probe and directed onto the substrate of interest. The reflected light is then captured by the probe and analyzed using a spectrometer. This principle is depicted in Fig. S2. The amount of reflection depends on several factors including the coating material, thickness of the coating, and substrate. To ensure consistent background measurements, the substrate is positioned on a white holder during analysis. As a rule, the denser the coating, the lower the level of reflection observed from the film. To avoid any reflection from the glass, the ink deposition and sintering was performed on the white glass-ceramic substrate, which has similar thermal conductivity and thermal diffusivity as glass, to avoid any differences in sintering characteristics. Initially, the calibration was performed, in which ink containing FeRh NPs of different concentration (i.e., known mass) was deposited on a defined substrate area of 25 x 15 mm and sintered at the laser fluence of 41 J/cm^2. The reflectance at various laser fluence was measured between the wavelength of 200 to 1150 nm (Fig. S3a). The reflectance at various wavelengths between 600 nm and 900 nm was measured for each fluence (Fig. S3b). The results indicated a linear increase in reflectance with increasing fluence. The observed increase is attributed to the reduction in nanoparticle ink concentration caused by the ablation process. The decrease in concentration leads to a thinner coating layer, causing more reflection from the white glass-ceramic substrate. These linear relationships can be employed to determine the reflectance of sintered films at different laser fluences, provided that the experimental procedure remains consistent.

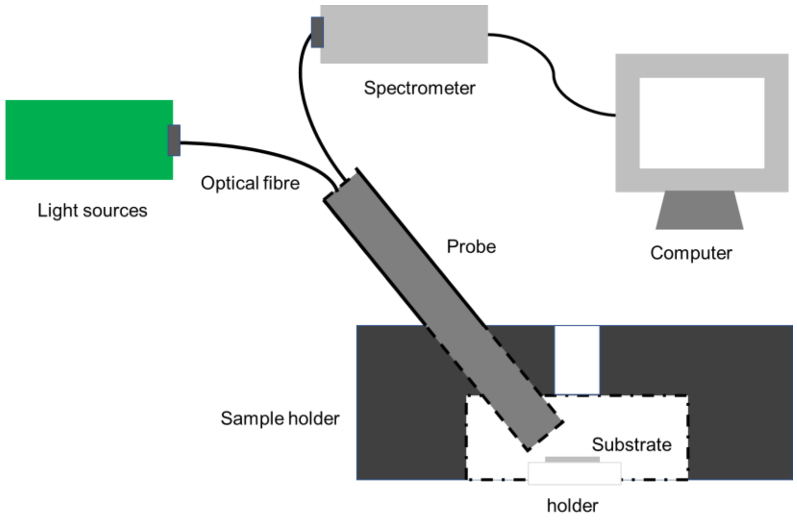

Figure S2. Schematic representation of mobile UV-VIS reflectance spectrometer used to measure the reflectance of sintered FeRh dispersed ink.

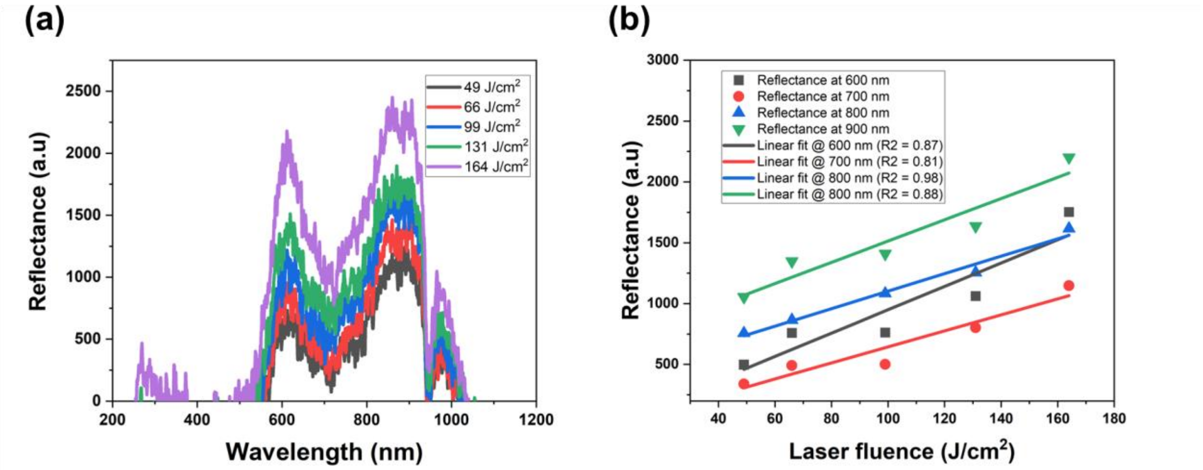

Figure S3. (a) Reflectance obtained from UV-VIS reflectometer at wavelengths between 200 to 1150 nm for the FeRh inks of different mass dispersed on the glass-ceramic substrate and sintered at fluences ranging from 49 - 164 J/cm^2 provided that the surface area of dispersion was kept constant. **(b)** The dependence of reflectance on the laser fluence for the wavelengths between 600 – 900 nm, along with the line of best fits for each fluence.

3. Temperature-dependent magnetization measurements

The distribution of phase transition temperatures of laser-sintered samples from the low temperature antiferromagnetic to the high-temperature ferromagnetic state was evaluated as follows: For the sample laser sintered at a fluence of 246 J/cm^2 we recorded the magnetization between 150 K and 700 K at 0.1 T as shown in Fig. S4. One has to keep in mind that M(T) data displayed here still contains an underlying magnetization signal originating from the glass substrate the FeRh nanoparticles were deposited on. Still, one can clearly discern the increase in magnetization slowly beginning at ca. 200 K, marking the onset of the AFM-to-FM phase transition. Possible reasons for the broadening of the phase transition as compared to bulk FeRh samples can be due to minor variation in stoichiometry and structural defects in NPs during their production by LAL. It is reasonable to assume the peak at ca. 460 K to represent the highest phase transition temperatures in our sample, above which all FeRh can be considered as ferromagnetic, with M(T) decreasing again when going to even higher temperatures, approaching T_C.

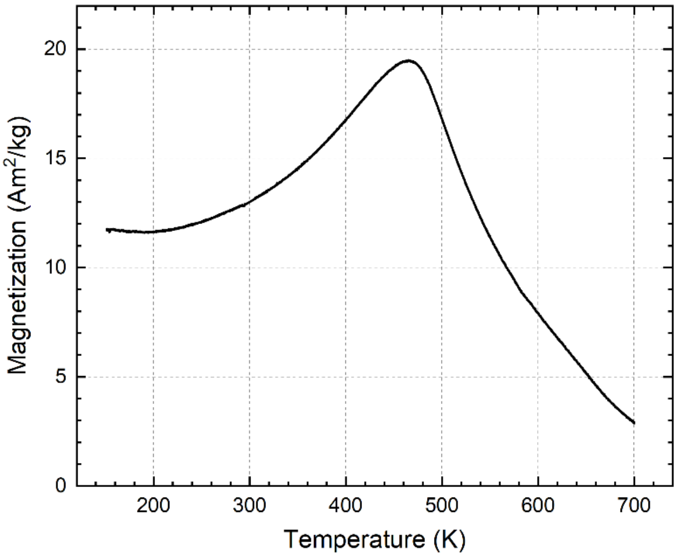

Figure S4. Temperature dependent magnetization M(T) recorded between 700 K and 150 K upon cooling in an applied magnetic field of 0.1 T.

4. Estimation of entropy change ΔS_{mag}

As already mentioned in the main text, the preparation of a thin layer of laser-sintered FeRh nanoparticles on a glass substrate results in a marginal magnetization superimposed by a considerable dia- and paramagnetic substrate contribution. It is therefore very challenging to obtain precise values for FeRh magnetization and magnetocaloric effect, especially in the low-temperature region, where the miniscule field-induced increase in magnetization is still almost linear. To enable at least a rough assessment of magnetocaloric performance of the produced laser-sintered nanostructures, the contribution of the AFM-FM phase transition to the magnetic entropy change ΔS_{mag} was estimated as shown in fig. S5 for two pieces of the sample laser sintered at a fluence of 246 J/cm^2 to 3 - 3.5 J/kg·K between 0 and 9 T. Here, we followed the method described by Pecharsky et al. to extract ΔS_{mag} from a set of M(H) curves recorded at different temperatures.[1]

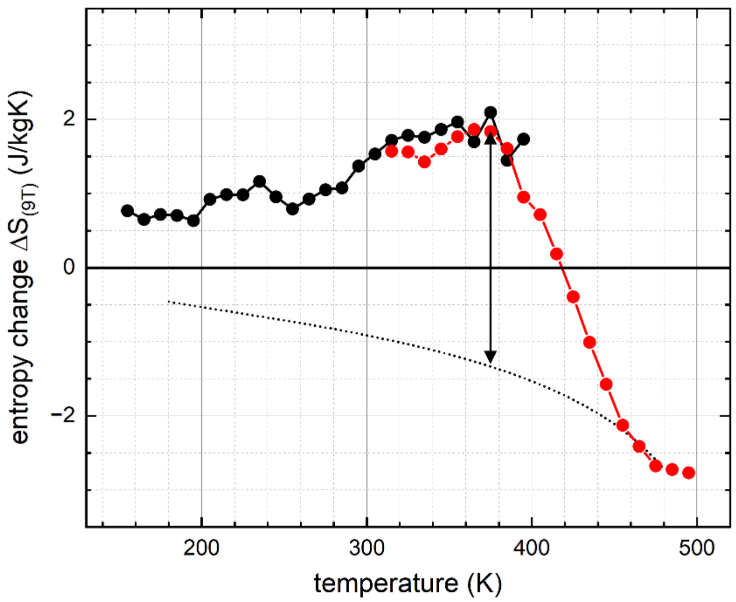

Figure S5. Entropy change determined following the method by Pecharsky et al. between 0 T and 9 T for two pieces of a sample laser sintered at a fluence of 246 J/cm^2.[1] Black data points were recorded between 150 K and 400 K using the large bore VSM option of a PPMS DynaCool, while red data points denote measurements recorded between 300 K and 500 K for a second, smaller piece of the same sample mounted on a different VSM sample holder type for high temperature measurements. The dotted line is a guide to the eye representing extrapolated values of ΔS_{mag} in the absence of the AFM-FM phase transition based on the high-temperature data. The arrow marks the maximum ΔS_{mag} at ca. 380 K originating from the phase transition, amounting to ca. 3 - 3.5 J/kg·K between 0 T and 9 T.

References

1. Pecharsky, V. K.; Gschneidner, K. A., Magnetocaloric effect from indirect measurements: Magnetization and heat capacity. J. Appl. Phys. **1999**, 86(1), 565-575

5.1.2. Study 2

Tahir, S., Shkodich, N., Eggert, B., Lill, J., Gatsa, O., Flimelová, M., . . . Gökce, B. (2024). Synthesis of High-Entropy Alloy Nanoparticles by Pulsed Laser Ablation in Liquids: Influence of Target Preparation on Stoichiometry and Productivity. ChemNanoMat, 10(5), e202400064. DOI: https://doi.org/10.1002/cnma.202400064

ACES Asian Chemical Editorial Society
doi.org/10.1002/cnma.202400064
CHEMNANOMAT
Research Article
www.chemnanomat.org

Synthesis of High Entropy Alloy Nanoparticles by Pulsed Laser Ablation in Liquids: Influence of Target Preparation on Stoichiometry and Productivity

Shabbir Tahir,[a] Natalia Shkodich,[b] Benedikt Eggert,[b] Johanna Lill,[b] Oleksandr Gatsa,[c] Miroslava Flimelová,[c] Esmaeil Adabifiroozjaei,[d] Nadezhda M. Bulgakova,[c] Leopoldo Molina-Luna,[d] Heiko Wende,[b] Michael Farle,[b] Alexander V. Bulgakov,[c] Carlos Doñate-Buendía,[a, e] and Bilal Gökce*[a]

High entropy alloys (HEAs) have a wide range of applications across various fields, including structural engineering, biomedical science, catalysis, magnetism, and nuclear technology. Nanoscale HEA particles show promising catalytic properties. Nevertheless, attaining versatile composition control in nanoparticles poses a persistent challenge. This study proposes the use of pulsed laser ablation in liquids (PLAL) for synthesizing nanoparticles using equiatomic CoCrFeMnNi targets with varied preparation methods. We evaluate the impact of target preparation method on nanoparticle yield and composition as well as the magnetic properties of the nanoparticles. The elemental powder-pressed heat-treated target (HEA-PP), identified as the most time-efficient and cost-effective, exhibits noticeable segregation and non-uniform elemental distribution compared to ball milled hot-pressed powder (HEA-BP) and face-centered cubic (FCC) single crystal (HEA-SX) alloy targets. From all targets, nanoparticles (sizes from 2 to 120 nm) can be produced in ethanol with a nearly equiatomic CoCrFeMnNi composition and a FCC structure, showing oxidation of up to 20 at.%. Nanoparticles from HEA-PP exist in a solid solution state, while those from HEA-BP and HEA-SX form core-shell structures with a Mn shell due to inhomogeneous material expulsion, confirmed by mass spectrometry. HEA-PP PLAL synthesis demonstrates 6.8% and 15.1% higher productivity compared to HEA-BP and HEA-SX, establishing PLAL of elemental powder-pressed targets as a reliable, time-efficient, and cost-effective method for generating solid solution HEA nanoparticles.

1. Introduction

For centuries, conventional alloys have been developed with the aim of enhancing specific properties such as ductility, strength, or corrosion resistance, and have become a central pillar of construction and engineering. These alloys are based on a principal element to establish the basic properties of the material, with relatively small quantities of other elements incorporated to enhance specific properties. For instance, steels are produced by the addition of carbon and chromium to iron to improve hardness and corrosion resistance. Similarly, brass incorporates zinc to enhance the strength and ductility of copper, while bronze combines tin and copper to augment its hardness. In 2004, a new class of alloys called high entropy alloys (HEAs) was introduced independently by Cantor[1] and Yeh et al.[2] These alloys consist of five or more elements with concentrations ranging from 5% to 35%. The existence of multiple elements within HEAs modifies their configurational entropy, free energy, phase, and overall stability.[3] These alloys hold significant advantages for structural applications as they possess the potential to achieve a superior combination of strength and ductility.[4,5] Industries such as aerospace employ HEAs extensively for components like compressors, combustion chambers, exhaust nozzles, and gas turbine parts, where properties such as strength-to-weight ratio, oxidation resistance, fatigue resistance, and elevated temperature strength are crucial.[6,7] Moreover, HEAs have emerged as potential replacements for conventional alloys in biomedical applications due to their exceptional corrosion resistance, low degradation in physiological environments, biocompatibility, wear resistance, and bacterial infection prevention.[8,9] Additionally, HEAs have been proposed as replacements for traditional materials in

---

[a] *S. Tahir, C. Doñate-Buendía, B. Gökce*
Chair of Materials Science and Additive Manufacturing, University of Wuppertal, Gaußstr. 20, 42119 Wuppertal, Germany
E-mail: goekce@uni-wuppertal.de

[b] *N. Shkodich, B. Eggert, J. Lill, H. Wende, M. Farle*
Faculty of Physics and Center for Nanointegration Duisburg-Essen (CENIDE), University of Duisburg-Essen, Lotharstr. 1, 47057 Duisburg, Germany

[c] *O. Gatsa, M. Flimelová, N. M. Bulgakova, A. V. Bulgakov*
HiLASE Centre, Institute of Physics of the Czech Academy of Sciences, Za Radnicí 828, 25241 Dolní Břežany, Czech Republic

[d] *E. Adabifiroozjaei, L. Molina-Luna*
Department of Materials- and Earth Sciences, Electron Microscopy Center Darmstadt (EMC-DA), Technische Universitat Darmstadt, 64287 Darmstadt, Germany

[e] *C. Doñate-Buendía*
GROC·UJI, Institute of New Imaging Technologies, Universitat Jaume I, Av. De Vicent Sos Baynat s/n, 12071 Castellón, Spain

Supporting information for this article is available on the WWW under https://doi.org/10.1002/cnma.202400064

nuclear reactors, thanks to their high resistance to irradiation damage and excellent stability at high temperatures, making them suitable for use in harsh nuclear environments.[10,11]

Downsizing HEAs to the nanoscale provides additional application possibilities resulting from the high surface-to-volume ratio and quantum confinement effect, making them suitable for catalysis[12–15] energy storage,[16,17] magnetic,[18–20] and biomedical applications.[21,22] Feng et al.[12] demonstrated that NiCoFePtRh HEA nanoparticles (NPs) outperformed commercial Pt/C catalysts by approximately a factor of 40 in hydrogen evolution reaction (HER) with excellent stability and high efficiency after 10000 cycles. Similarly, PtPdRuRhIr HEA NPs exhibit a high photothermal conversion effect, converting 808 nm near-infrared light into heat, which makes them potential candidates for cancer phototherapies.[21] Furthermore, the synthesis of ultra-mixed multi-metallic nanoparticles, comprising 21 distinct elements (Fe, Co, Ni, Cr, Y, Ti, V, Cu, Al, Nb, Mo, Ta, W, Zn, Cd, Pb, Bi, Ag, In, Mn, Sn), has been achieved through the arc-discharge plasma method.[23] These NPs have demonstrated exceptional photothermal conversion capabilities, boasting an average absorption rate exceeding 92% across the entire solar spectrum (250 to 2500 nm). This remarkable performance translates into a high photothermal conversion efficiency of nearly 99% with a water evaporation rate of 2.42 kg m^{-2} h^{-1} under simulated sunlight irradiation (1 sun), demonstrating a highly efficient photothermal conversion performance. Specifically, CoCrFeMnNi NPs have exhibited a high catalytic efficiency for the oxygen evolution reaction (OER), surpassing the current densities of multi-element perovskite catalysts.[24] Moreover, these CoCrFeMnNi NPs have shown a high performance in the degradation of methylene blue, even without the addition of any peroxide.[25]

Even though several studies demonstrate the benefits of HEA NPs, the synthesis of HEA NPs with different compositions achieving a homogeneous elemental distribution still represents a challenge. The different melting points, interatomic bonding, and miscibility of the HEA individual elements limit the generation of solid solution HEA NPs.[26,27] HEA NP production demands a versatile, robust, and scalable synthesis method. Conventional wet chemistry methods are generally not feasible due to elemental immiscibility at equilibrium conditions, leading to elemental segregation and phase separation.[28,29] Multimetallic nanoparticles consisting of various combinations of Au, Ag, Co, Cu, and Ni elements were synthesized through a polymer nanoreactor–mediated synthesis process.[30] The synthesized materials featured heterogeneous structures with phase separation due to elemental immiscibility. Products obtained through conventional near-equilibrium heating methods are typically governed by thermodynamics that are characterized by the lowest total free energy and a highly stable atomic arrangement. To surpass these thermodynamic constraints and delve into innovative materials, it becomes imperative to devise swift synthetic approaches where the preparation or processing of materials is predominantly governed by kinetics.[31] In high-temperature synthesis methods, entropy contributes to stabilizing multi-metallic phases, enabling the preparation of single-phase materials.[32] Carbothermal shock synthesis of HEA NPs using 8 elements (Pt, Pd, Ni, Co, Fe, Au, Cu, and Sn elements) resulted in the formation of single-phase homogeneously mixed solid solution NPs.[29] The synthesis process however requires electrically conductive support materials, which limits its possibilities for large-scale synthesis.[29] Pyrolysis techniques such as fixed bed pyrolysis,[33] fast moving-bed pyrolysis[33] and polymer-confined pyrolysis[34] have been explored for low-cost large-scale synthesis of HEA NPs. The process, however, either requires special experimental equipment, and additional processing to remove polymer impurities or leads to phase separation due to different starting reductive temperatures of precursors. Okejiri et al.[35] synthesized AuPdPtRhRu nanocrystals by ultrasonication of metal precursors in an alcoholic ionic liquid. Although the procedure is environmentally friendly, composition control of HEA NP is challenging due to differences in the reduction potential of the constituent metal salts. Additionally, the metal precursors are generally expensive, rendering the technique costly for mass production. Qiao et al.[36] fabricated PtPdFeCoNi NPs on carbon substrates by microwave synthesis and although the synthesis process is fast and resulted in no phase separation, the generation of NPs requires carbon-based films for efficient absorption of microwave radiation. Other techniques such as laser scanning ablation[37] and Joule heating[38] are ultra-rapid processes utilizing NP precursors to produce high entropy alloys in nanoseconds allowing a combination of dissimilar metallic elements regardless of their thermodynamic solubility. Although these methods produce high compositional diversity the process of precursors and solvent screening required for synthesis of the desired high entropy material is time-consuming.

Among non-equilibrium NP synthesis processes, pulsed laser ablation in liquid (PLAL) stands out as a simple and versatile method to produce NPs without the need of surfactants or reducing agents.[39,40] This technique involves a localized fast heating and cooling process through pulsed laser irradiation of the target surrounded by a liquid, making it a safe, versatile, and environmentally friendly approach.[41–43] PLAL has been employed for the synthesis of diverse nanomaterials, including metal, metal alloys, oxides, ceramics, and organic materials.[44] The initial efforts employing PLAL for HEA NP synthesis have shown that PLAL offers benefits such as ease of material screening, cost-effectiveness, remarkable composition and phase stability, and scalability. Jahangiri et al.[45] achieved the synthesis of HfNbTaTiZ refractory HEA NPs in water, ethanol, and hexane using femtosecond laser pulses. Their study revealed that the size, morphology, and oxidation state of the NPs primarily depend on the laser fluence, and the solvent employed. Similarly, Waag et al.[24] synthesized equiatomic CoCrFeMnNi alloy NPs (less than 5 nm) by employing pressed elemental powder targets. It was found that the size, morphology, and homogeneity of the starting elemental powder blends to produce the target significantly impacted the stoichiometry and phase control of the synthesized NPs. Here we demonstrate that the generation of alloy NPs by PLAL from pressed elemental micropowders represents a cost-effective approach to generate alloy nanoparticles with straightforward control of the composition by modifying the relative concentration of elements in the target. In order to confirm that powder-pressed targets are suitable for versatile and cost-effective HEA NP production by PLAL, the influence of the target crystallinity (single-crystal, polycrystalline or amorphous), and elemental homogeneity (alloy targets or pressed elemental powders) had to be evaluated. Previous studies confirmed that targets produced by pressing elemental powders are ideal candidates for PLAL alloy NP synthesis, since the main uncertainties of alloying the elements into alloy NPs occurs during the NP formation process after laser irradiation,[46] that is the critical need for homogenizing the elements in the target within the laser spot area. Furthermore, the synthesis of Co–Fe alloy NPs from pressed powder targets revealed that the NPs are influenced by factors such as the difference in target powder mixing, the laser pulse duration, the laser spot size, and the ablation time.[46] Schmitz et al.[47] investigated the effect of target preparation on the Yttrium Iron Garnet NP production yield using single crystal, sintered micro powder, and sintered nano-powder targets. However, the impact of target crystallinity on the PLAL synthesized HEA NP stoichiometry, phase, and properties has not been determined, yet.

In the current study, the production of equiatomic CoCrFeMnNi nanoparticles from HEA targets prepared by three different processes is studied (or compared) in terms of production rate, composition, phase, and functionality. Our research aims to control the influence of the target preparation route on the generation and functionality of HEA NPs towards a versatile and controllable stoichiometry and phase generation, while also offering advantages such as cost-effectiveness, reliability, and possibility to upscale production.

2. Materials and Methods

2.1. Preparation of CoCrFeMnNi Targets

The CoCrFeMnNi powder pressed targets (HEA-PP) were produced employing elemental Co (99.8%, 1.6 μm), Cr (99.2%, <10 μm), Fe (99.5%, 6–10 μm), Mn (99.6%, <10 μm), and Ni (99.9%, 3–7 μm) powders (Thermo Fisher Scientific, Waltham, MA USA). The HEA-PP targets preparation procedure is shown in Figure 1a. The Co, Cr, Fe, Mn, and Ni were weighted to ensure equiatomic composition and mixed. The mixed powder was homogenized by pestle mixing in a mortar for 20 minutes (Figure 1a left). The powder was pressed at 100 MPa to form 2 mm thick cylindrical pellets with a 10 mm diameter (Figure 1a middle). The samples were heat treated in a vacuum atmos-

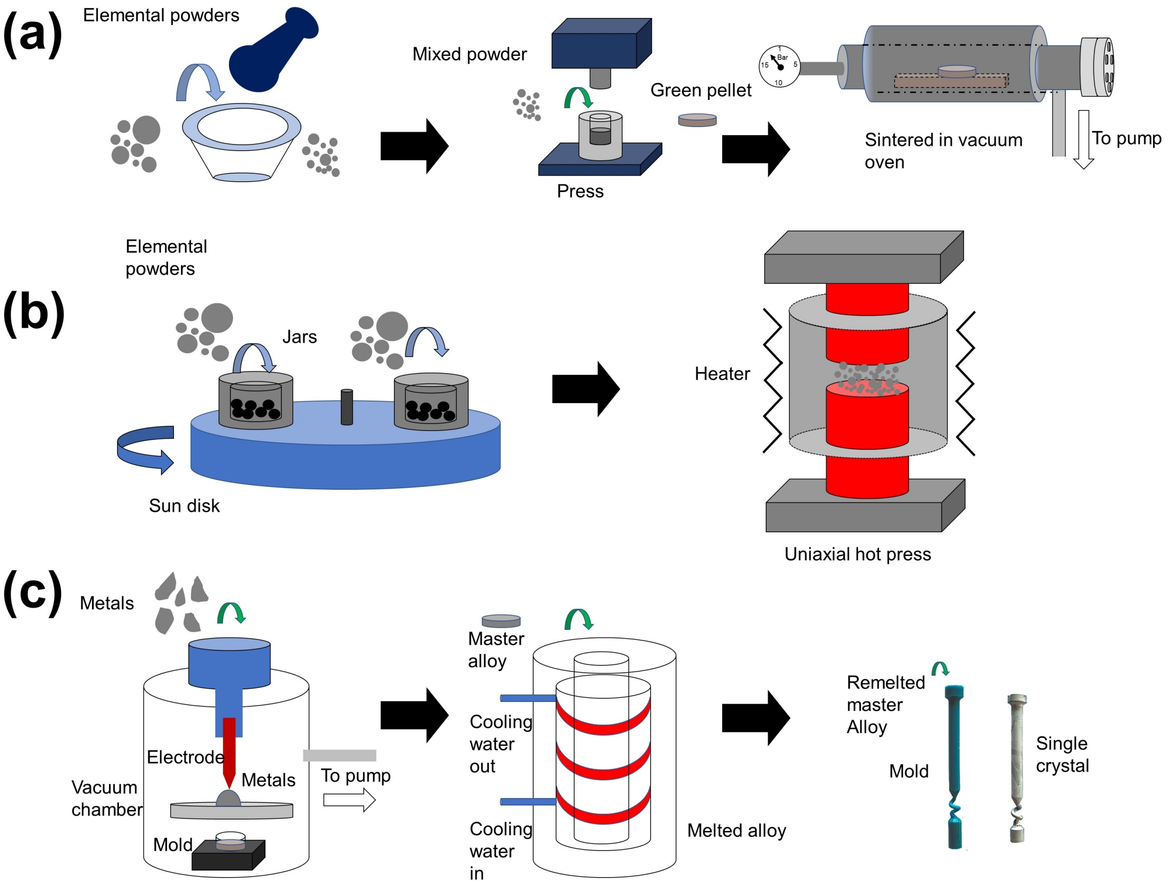

Figure 1. CoCrFeMnNi target preparation techniques for CoCrFeMnNi HEA NP synthesis. (a) HEA-PP target – by mixing of elemental powders using a pestle in a mortar, uniaxial pressing, and sintering in a vacuum oven, (b) HEA-BP target – by high energy ball milling of elemental powders with subsequent uniaxial hot pressing, (c) HEA-SX target – by melting of elemental powder blend in arc furnace followed by melting of master alloy in induction furnace and slow cooling of remelted master alloy in mold producing single crystal.

phere at 1000 ^{0}C for 20 h to achieve FCC HEA targets (Figure 1a right), as proposed by Waag et al.[24]

The CoCrFeMnNi ball-milled powder pressed (HEA-BP) targets were prepared into two steps. As a first step the elemental powders of Co (99.7 %, mean particle size 3 μm), Cr (99.35 %, $>$71 μm), Fe (99.96 %, 10–20 μm), Ni (99.5 %, 45–60 μm), and Mn (99.2 %, 3 μm) in equiatomic concentrations (20 at.% of each element) were processed by high energy ball milling (HEBM) in argon for 60 min to get nanocrystalline single FCC HEA micropowders. The ball/powder weight ratio was 20:1. The HEBM was carried out at rotation speeds of the sun disk/jars: 700 rpm/1400 rpm. As a second step, the obtained HEA powder was consolidated by hot pressing (Direct Hot Pressing – DSP-515 SA) at 800°C for 60 min in argon. The HEA powder was placed into a cylindrical graphite die (Ø 50 mm) and uniaxially compressed at 50 MPa. The thickness of produced target was ~3 mm. The procedure for the preparation of HEA-BP is shown in Figure 1b.

To prepare CoCrFeMnNi single crystal (HEA-SX) targets, master alloys were prepared via melting high-purity bulk elements ($>$99.9 % purity) in an arc furnace under argon atmosphere of 5×10^{-4} Pa (Figure 1c). Single crystal casting was then performed in a Bridgman investment casting furnace by melting several arc-melted buttons together at approximately 1600 °C. The shell molded material (produced by investment casting) was heated to 1450 °C using a second furnace located in a vacuum chamber. The liquid metal was poured into the mold cavity and the mold was lowered through a baffle with a gradient of 6 K/mm at a rate of 3 mm/min. The resulting cylindrical rod solidified in the [001] direction was FCC single-crystalline with a diameter of 15 mm and a length of 130 mm. These rods were then cut via wire-EDM into 2 mm thick pellets. To confirm the absence of grain boundaries, the samples were etched after casting.

Non-ablated and ablated regions of the targets were visualized by scanning electron microscopy (SEM) (Apreo S LoVac, Thermo Fisher Scientific) in a secondary electron (SE) mode. The non-ablated region denotes the surface of the target before the ablation, while the ablated regions show a crater after the ablation as shown in the supplementary (Figure S1). The elemental composition was determined by energy dispersive X-ray spectroscopy (EDX).

2.2. Synthesis of Colloidal CoCrFeMnNi HEA NPs

The CoCrFeMnNi colloidal NPs were synthesized by PLAL of HEA-PP, HEA-BP, and HEA-SX targets in ethanol using a near-infrared picosecond pulsed Nd:YAG laser source (Coherent, HyperRapid NX, Kaiserslautern, Germany, 10 ps, 1064 nm). The HEA targets were ablated by focusing the laser beam with an f = 167 mm f-theta lens coupled to a galvanometric scanner (Raylase, SS-IV-15 [1070], Wessling, Germany) generating a 6 mm-diameter hollow spiral pattern on the target surface at 10 m/s (Figure 2). The distance of the target is fixed from the f-theta lens and the laser fluence was varied by changing the repetition rate, ranging from 1.9 J/cm^2 to 11.2 J/cm^2. It is important to highlight that the fluences considered here are

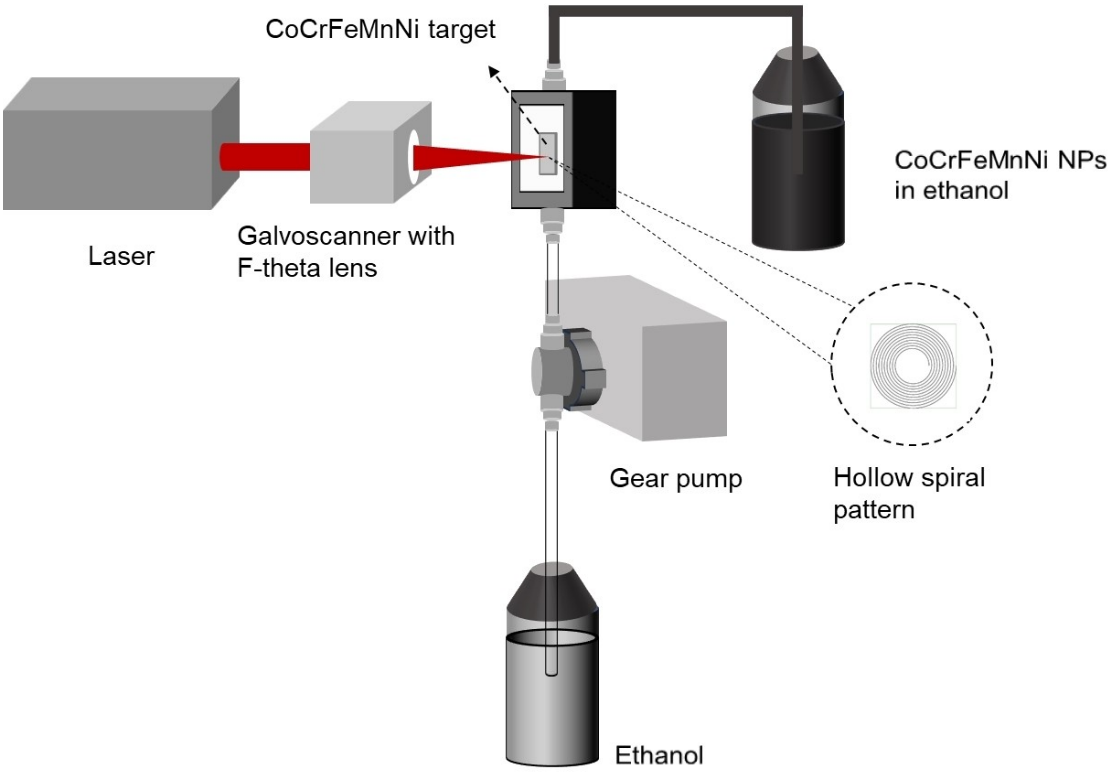

Figure 2. Schematic representation of the ps-pulsed laser ablation of CoCrFeMnNi HEA targets in ethanol employing a liquid flow chamber.

the values before the interaction with the liquid. Given the consistent thickness of the liquid layer and the narrow fluence range, it's assumed that losses remain uniform across all experiments. Consequently, this uniformity does not impact the comparison between targets but solely influences the absolute values obtained. To prevent shielding of the laser beam by the produced NPs and reduce energy losses, a gear pump was used to pump the liquid at a flow rate of 100 ml/min.

2.3. CoCrFeMnNi HEA NPs Characterization

The NP production rate (measured in mg/h) was determined by gravimetric measurements of the mass of the targets before and after ablation and taking into account the ablation time. The NP size distribution, morphology, and elemental composition were characterized by transmission electron microscopy (TEM) and EDX using a JEOL JEM-2200FS microscope equipped with a ZrO_2/W emitter and JEOL JEM-2100 microscope with LaB6 gun. For the TEM sample preparation, the colloids were dispersed on a copper grid and dried at ambient conditions. For particle size distribution, the ferret diameter of individual particles from TEM images was measured using ImageJ.[48] The crystal structure of the NPs produced from each target was analyzed by X-ray diffraction performed on a Huber G670-360 Gunier-Camera using Mo–K alpha1 radiation. The oxidation of the CoCrFeMnNi NPs and their structural and magnetic properties were investigated by ^{57}Fe-Mössbauer spectroscopy on dried powder samples under zero-field conditions. ^{57}Fe-Mössbauer spectra were collected in transmission geometry and constant acceleration mode at 4.3 K using a closed-cycle He cryostat (SHI-850-5, Lake Shore Cryotronics).

2.4. Mass Spectrometric Characterization of HEA Laser-Ablation Plumes

To get insight into the dynamics of laser-induced particle ejection for different HEA targets, a mass spectrometric (MS) analysis of the plumes produced by laser ablation in vacuum was performed. The three targets (HEA-PP, HEA-BP, and HEA-SX) were placed simultaneously in a vacuum chamber (base pressure 10^{-6} mbar) and irradiated at a 45° incidence angle under conditions similar to those in the PLAL experiments using a Yb:KGW laser PHAROS (Light Conversion, Vilnius, Lithuania) operating at 1030 nm, 2 kHz repetition rate, 7 ps pulse duration. The laser beam was focused by a glass lens ($f = 400$ mm) into a circular spot with an effective radius $w_0 = 150\ \mu m$ ($1/e^2$ criterion). The laser fluence at the spot was varied in the range of 0.2–3 J/cm^2. The laser beam was scanned over the target surface at a speed of 2 mm/s to generate a zig-zag pattern over the area of 10×8 mm^2.

The abundance and velocity distributions of the laser-produced particles were analyzed using a customized time-of-flight (TOF) mass spectrometer (Kore Technology, Ely, UK). At 46 cm from the target, the positive ions of the ablation plume were sampled parallel to the plume axis by a 760-V repeller pulse and directed to the mass spectrometer drift tube. The ions in the mass-to-charge range of 6–600 u/e were detected in the analog mode by a dual microchannel-plate detector using a digital oscilloscope DSOS054A (Keysight, USA). The time delay between the repeller pulse and laser pulse was varied to investigate the ion velocity distributions. All mass spectra were averaged over 200 laser pulses.

3. Results and Discussion

3.1. Composition Analysis of Bulk CoCrFeMnNi Targets

Figure 3a shows the non-uniform distribution of elements ofthe non-ablated region of the HEA-PP target, with substantial deviations in the elemental concentrations. The white arrowheads denote areas of elevated elemental concentration, whereas the yellow arrowheads highlight regions with an elemental content deficiency. This inhomogeneous elemental distribution could be attributed to their limited diffusion during the mixing and sintering process and due to the large fluctuation in the lattice potential energy between the crystal sites.[49] In contrast, the uniform elemental distribution of the non-ablated region was observed in HEA-BP (Figure 3b) and HEA-SX (Figure 3c) targets due to the use of prealloyed powders before the remelting or heat treating process. Figure 3d shows the elemental composition (at.%) measured at three different sites on the non-ablated regions. The non-ablated region of HEA-PP possesses higher Mn (28 ± 9 at.%) and Cr (32 ± 12 at.%) contents than other elements, with relatively large deviations, while the compositions of HEA-BP and HEA-SX were relatively more homogeneous and near to equimolar, with the maximum deviation observed for Cr, 22 ± 2 at.% and 20 ± 2 at.%, respectively. In Figure 3e, the elemental distribution (at.%) is presented, revealing measurements from three distinct sites within the ablated regions. Notably, a higher concentration of Mn is evident on the target's surface (i.e., the non-ablated region), consequently, the Mn content within the ablated region is comparatively lower, measuring at 12 ± 4 at%. Additionally, the deviation in compositions for all elements is lower in the non-ablated region when compared to the ablated region. For HEA-BP and HEA-SX, the maximum compositional deviation in the ablated region was found for Mn (ca. 22 ± 1 at.% and 23 ± 1 at.% respectively). It is worth noting that the largest difference in composition was observed for Cr and Mn, which could be due to the difference in melting points : Mn (1246 °C), Cr (1907 °C), Co (1495 °C), Fe (1538 °C), and Ni (1455 °C). This could give rise to the difference in the mobility of each metal during the alloying process, leading to compositional heterogeneity in the overall bulk structure. In addition, different melting and boiling points of the elements imply different volatilities during the ablation process resulting in non-stoichiometric laser vaporization (see Section 3.6).

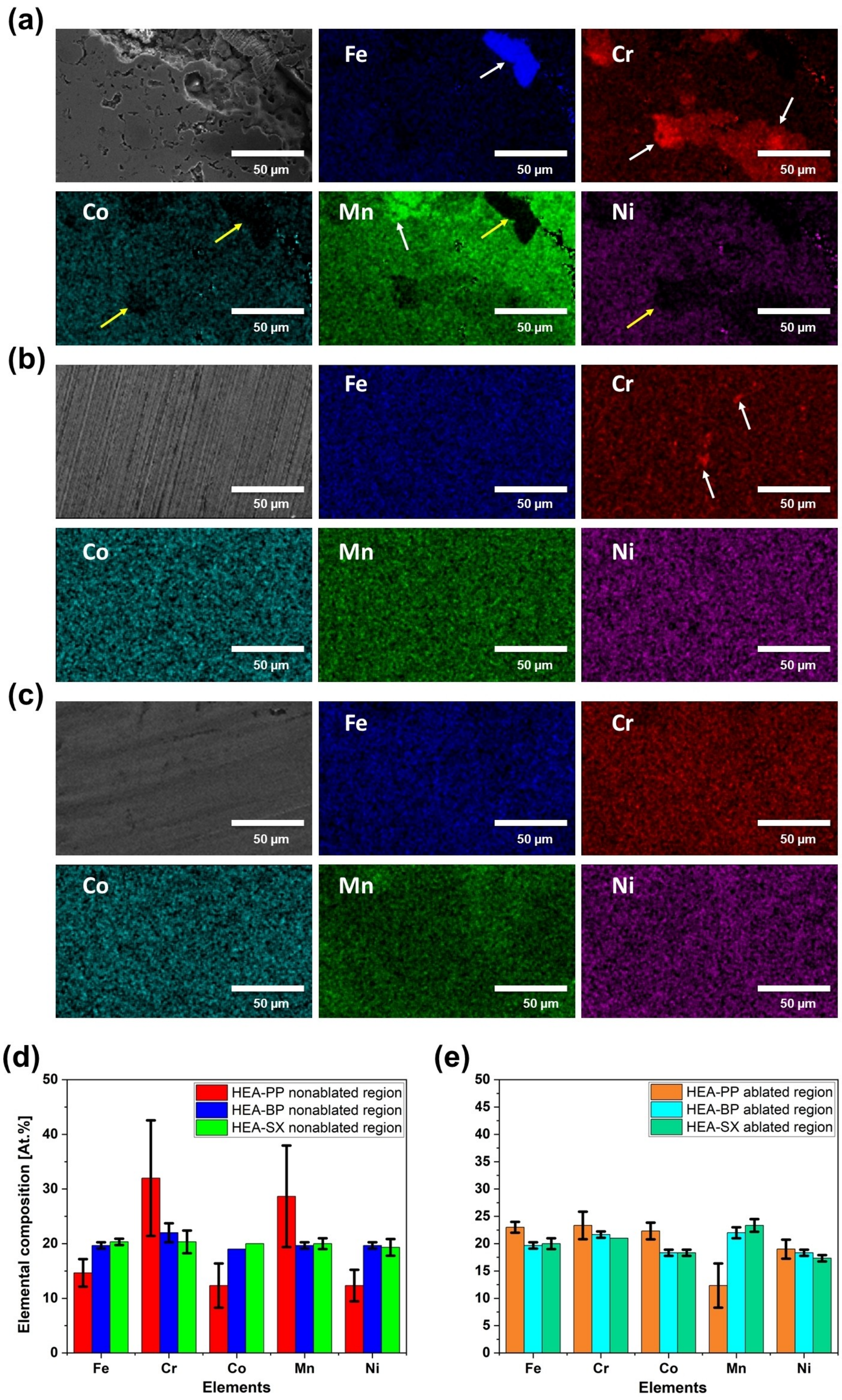

Figure 3. SEM (SE) and elemental maps of Co, Cr, Fe, Mn, and Ni obtained by EDX of (a) HEA-PP, (b) HEA-BP, (c) HEA-SX, (d) Elemental composition obtained from three non-ablated regions of each target, (e) Elemental composition obtained from three ablated regions of each target area. The ablated region corresponds to the area following a 10-minute target ablation. Error bars denote statistical error. Yellow and white arrows in the SEM images highlight regions with deficient and elevated concentrations of elements, respectively.

3.2. PLAL Productivity of CoCrFeMnNi NPs

The production of NPs was carried out through pulsed laser ablation of an HEA-PP target in ethanol for different repetition rates at maximum laser power (110 W) to maximize the productivity. Figure 4a show the productivity as a function of the repetition rate and laser fluence. The maximum ablation efficiency with an average productivity of 311 mg/h was achieved at 2000 kHz and a laser fluence of 2.8 J/cm^2. The differences in reproducibility could be due to small differences of laser focal position or variations of the surface roughness of the target.

The ablation threshold fluence of the material was calculated according to the equation $\Phi_{th} = \frac{\Phi_{op}}{e^2}$[50] (where Φ_{op} is the optimum fluence), which is 0.38 J/cm^2. This value is higher compared to the threshold fluence reported for CoCrFeMnNi laser ablation in air (0.24 J/cm^2).[51] However, the experiments in [47] were performed with a crystalline HEA target which had a considerable lower ablation threshold than that for the HEA-PP target (see below Section 3.6). The decrease in ablation rate by increasing fluence can be attributed to the formation of laser-induced periodic surface structures (LIPSS) after ablation of the targets as observed by SEM (Figure S2).[52] At a fluence of 11.2 J/cm^2, the removal of larger cluster of the sintered elemental micropowders target can lead to an increased ablated mass, as also observed by Schmitz et al.[47] for yttrium iron garnet pressed powders.

In figure 4b we compare the influence of the CoCrFeMnNi targets preparation method on the NP productivity. Remarkably, the average productivity for the HEA-PP target was 6.5 % and 15.1 % higher compared to HEA-BP and HEA-SX targets, respectively. However, considering the uncertainties, the difference is not statistically significant. The variations in productivity could be attributed to variations in the focal position adjustment and materials properties due to disparities in the mixing of elements in the target as shown in Figure 1.

The laser processing at low intensities follows the two-temperature diffusion model, where heating of the electron gas is followed by relaxation of the electron, transferring heat to the lattice.[53] Additionally, the ablation rate is also strongly influenced by material properties. The total energy needed to evaporate a unit volume at room temperature in an adiabatic, isobaric process depends on the material solid and liquid specific heat capacities, melting and boiling temperatures, enthalpy of vaporization, and enthalpy of fusion.[54] For alloys with a similar composition and perfect mixing, all the parameters can be interpreted using the rule of mixing.[51] However, the elemental mixing depends on the alloy preparation method, and therefore the ablation rate may be affected. For the HEA-PP target, elemental diffusion occurs during the heat treatment process leading to heterogenous elemental mixing (as shown in figure 3a). In the HEA-BP target, alloying occurs mechanically during high-energy ball milling and later during hot pressing. Finally, for the HEA-SX target, alloying occurs during the melting of the elemental components while preparing the master alloy and during remelting and casting into a single crystal. Consequently, during the ablation process, the stoichiometries are not uniform locally, which results in differences in the energy needed for vaporization resulting in variations in productivity.

3.3. Particle Size Distribution of the CoCrFeMnNi NPs

The particle size distributions of the CoCrFeMnNi NPs produced by laser ablation of the HEA-PP, HEA-BP, and HEA-SX targets were analyzed by TEM. Figure 5a shows that ablation of each target results in the formation of spherical particles with a wide particle size distribution. Each distribution consisted of distinct size fractions, with a dominant fraction of small NPs (< 10 nm) (Figure 5a). The coexistence of small and large NPs can be explained by two mechanisms of NP synthesis through picosecond pulse laser ablation in liquid, as computationally predicted by Zhigilei et al.[55] for a fairly high laser fluence, about three times above the ablation threshold. They revealed that small NPs were synthesized due to the phase explosion process,

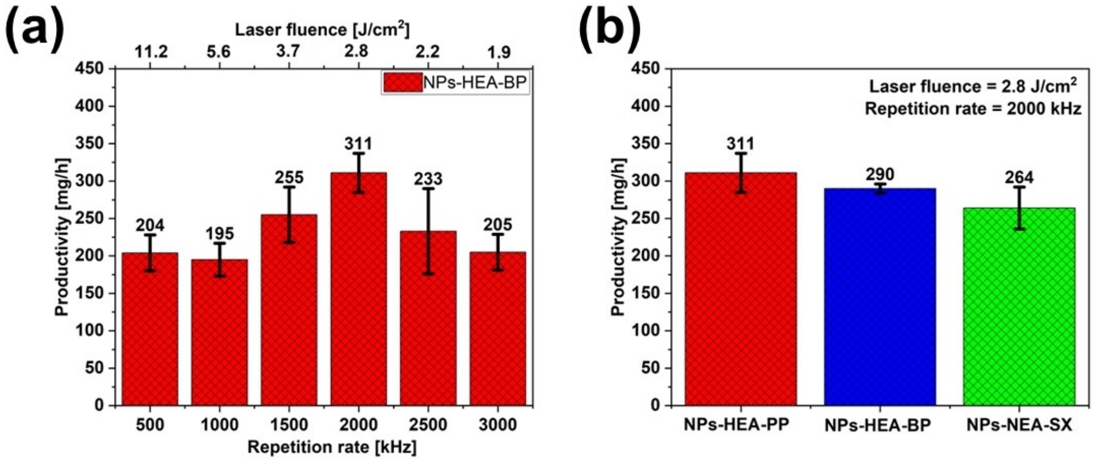

Figure 4. (a) Effect of repetition rate and laser fluence on productivity of NPs generated from HEA-PP target in ethanol. (b) Productivity of NPs generated from PLAL of HEA-PP, HEA-BP and HEA-SX using the same laser parameters.

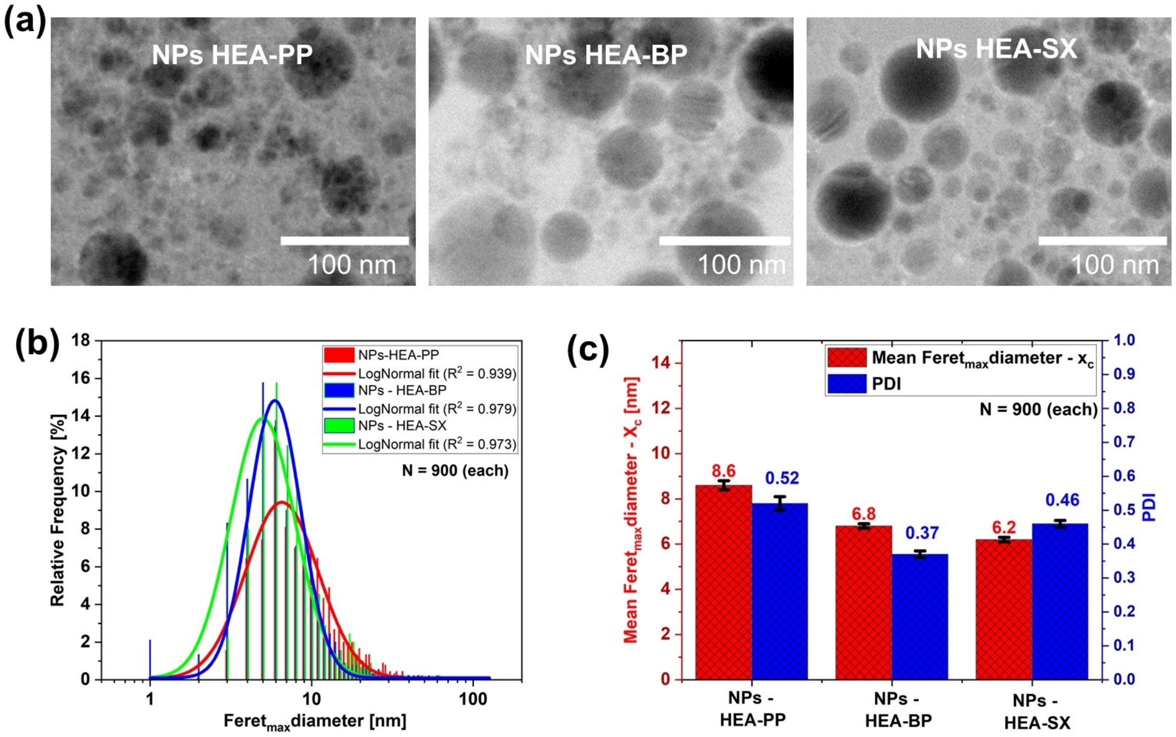

Figure 5. (a) TEM images of the produced CoCrFeMnNi NPs from the HEA-PP, HEA-BP, and HEA-SX targets. (b) Particle size distributions as extracted from the TEM images. (c) Mean Feret diameter and polydispersity index (PDI) of the NPs generated from HEA-PP, HEA-BP and HEA-SX targets by PLAL. 900 particles were analyzed for statistics.

where the rapid release of vapor leads to the decomposition of superheated regions of the target into vapors, atomic clusters, and small droplets, which nucleate and grow to form small NPs in the metal-ethanol mixed region. The larger particles were formed by photomechanical spallation of the target from the deeper regions, thereby breaking up the superheated molten metal layer generated at the plume-liquid interface.

The analysis of the produced CoCrFeMnNi NPs from the different targets revealed the presence of NP size distributions with a peak value of 8.6, 6.8, and 6.2 nm for HEA-PP, HEA-BP, and HEA-SX, respectively (Figures 5b and 5c). The polydispersity index was larger than 0.3, revealing that the particle size distributions were polydisperse.

The shape of the size distribution curves (Figure 5b) shows that the NPs from HEA-BP and HEA-SX were relatively similar, with almost the same fraction of smaller particles (less than 10 nm), while NPs from HEA-PP targets consisted of a relatively larger fraction of bigger particles. The difference could be due to compositional inhomogeneity in the target material, which can affect NP formation, as described above. Although the overall composition within the ablated region is similar, the composition at the sub-micron scale varied significantly for HEA-PP, as shown in Figure 3a. This caused local variation in electron and lattice heating, thereby affecting the dynamics of NP formation. The local composition was more homogeneous for HEA-BP and HEA-SX targets, and this may lead to a lower variation in particle size distribution.

3.4. Composition of the CoCrFeMnNi NPs

TEM and EDX analysis were used to identify the elemental composition of NPs generated via PLAL of HEA-PP, HEA-BP, and HEA-SX. The findings unveiled the generation of spherical nanoalloys comprising all five elements within the NPs, regardless of the target preparation method, as depicted in Figure 6.

The average composition is near to equiatomic like the bulk target however with large deviations between the particles (Figure S3). Interestingly, the large NPs (above 20 nm) synthesized from the HEA-PP target were mostly solid solution alloys consisting of all constituent elements, while NPs generated from HEA-BP and HEA-SX were mainly core-shell structures as visible in TEM images in Figure 6, with a Mn-rich shell as shown in the supplementary (Figure S4). The average thickness of the shell within NPsvaries between 5.7 ± 1.3 nm and 6.7 ± 3.6 nm for HEA-BP and HEA-SX, respectively, as averaged at 10 different positions. Jacob et al.[56] proposed four general rules for the formation of core-shell NPs. Firstly, there should be a distinct miscibility gap in the phase diagram which could lead to the formation of distinct phases. Dreimow et al.[57] demonstrated thermodynamically that the HEAs could undergo phase separation, which occurs when the positive enthalpy of mixing is higher than the entropy of mixing, and suggested that elements such as Co and Ni promote miscibility, while Cr increases the miscibility gap temperature. Zhang et al.[58] hypothesized that secondary phase formation is related to the immiscibility of binary mixtures in the alloy system. Although

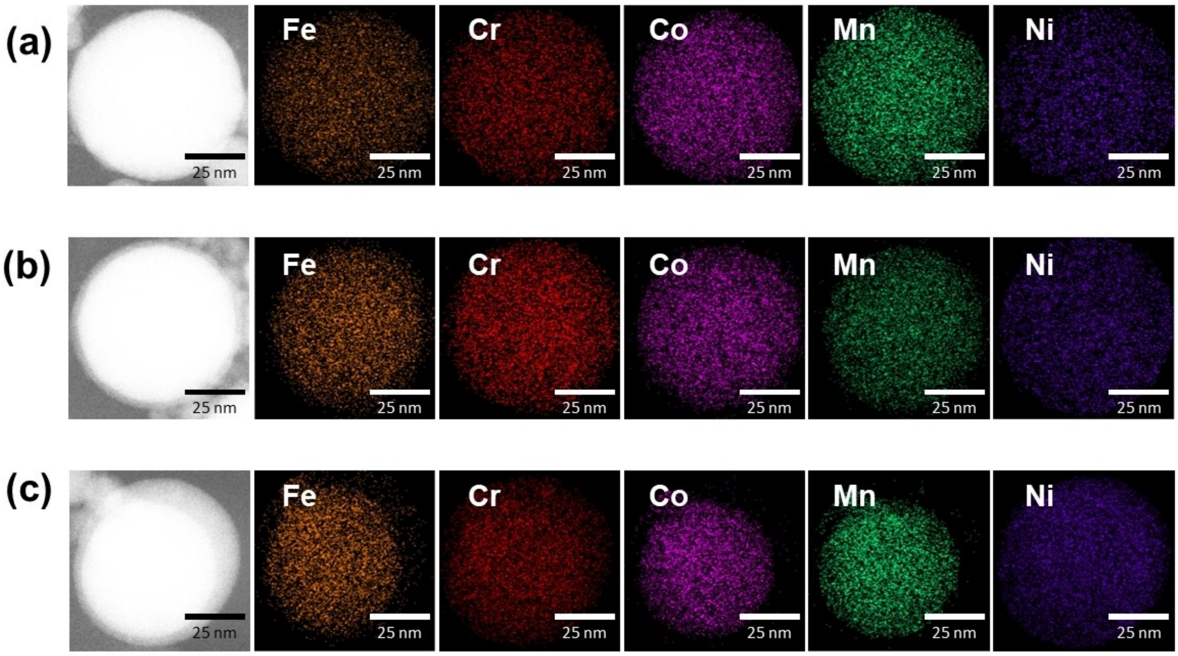

Figure 6. High resolution STEM images and elemental maps of Co, Cr, Fe, Mn, and Ni obtained by EDX of NPs generated by PLAL of (a) HEA-PP (b), HEA-BP and (c) HEA-SX.

calculations of phase diagrams (CALPHAD) for CoCrFeMnNi suggest that binary solubility in FCC is maintained, it only considers equilibrium phases, and thus the effects from material synthesis and processing are not taken into account.[59] Secondly, core-shell is thermodynamically more stable for a solid solution when the diameter of the generated NPs is larger than a certain size. This was previously investigated by Tymoczko et al.[60] for the Fe–Au system, indicating that elemental segregation occurs due to the lower free energy of the large particles. Also, in HEA-BP and HEA-SX NPs, a core-shell structure is primarily observed in large particles, but not in small particles (Figure S4), which can be due to the difference in free energy of core-shell and solid solution structures. Thirdly, the formation mechanism in PLAL indicates that elements in the core need to have a higher melting point than in the shell. In our case, for HEA-BP and HEA-SX, the NP shell is rich in Mn, while the core is rich in the other elements. The melting point of Mn is ca.17 %, 35 %, 19 %, and 15 % lower than Co, Cr, Fe, and Ni, respectively. Thus, Mn is expected on the NP surface, verifying the prediction. Lastly, the difference in the surface energies of the NPs leads to particle coarsening and the evolution to an inhomogeneous structure, also known as Ostwald ripening.[61] It is evident from EDX mapping that sub-nanometric Mn-rich particles are observed in the HEA-BP and HEA-SX colloids (Figure S4). Due to their high surface-to-volume ratio, they are unstable, and thus, most of them form a shell around a larger particle, lowering the overall surface energies. In HEA-PP, core-shell formation was not observed as in HEA-SX and HEA-BP. This is associated with the composition of the target material in the ablated region where a lower Mn content was observed. Hence, the generated NPs exhibit a lower amount of Mn-rich clusters, leading to solid solution formation. In addition, laser ablation of the HEA targets proceeds incongruently with predominant vaporization of the most volatile component (manganese) as demonstrated in the mass spectrometric studies (Section 3.6). The incongruent ablation is found to be more pronounced for HEA-SX and HEA-BP further favoring the formation of core-shell NPs for these targets.

The small particles (less than 20 nm) in all cases were solid solution particles as shown in Figure S5. This variation may be attributed to the disparity in the formation mechanism of small and large NPs via ultrashort pulses, as previously discussed.

3.5. Mössbauer Analysis

Mössbauer spectroscopy was performed on the nano powders extracted from the generated colloids produced by PLAL of HEA-PP, HEA-BP, and HEA-SX targets in ethanol (Figure 7). All the spectra show a similar trend and therefore there are no significant differences in the Fe environment, which can be associated to the preparation method. By a least square fitting, we have determined three spectral contributions that occur in all samples.

For all samples, a major contribution (~50 % of the spectral area) is evident at small velocities and can be associated with the magnetically ordered HEA in a low spin state with similar hyperfine splitting that has been discussed previously in the work of Schneeweiß et al.[62] for bulk Cantor alloys and for FCC–Fe(100) films grown on Cu(100).[63] Besides, we observe two additional spectral contributions. There is a magnetically ordered spectral contribution (~30 % of the spectral area) with a broad hyperfine field distribution $p(B_{hf})$ between 15 to 35 T with an average isomer shift $<\delta_{iso}>$ of 0.34 mm/s. Similar hyperfine

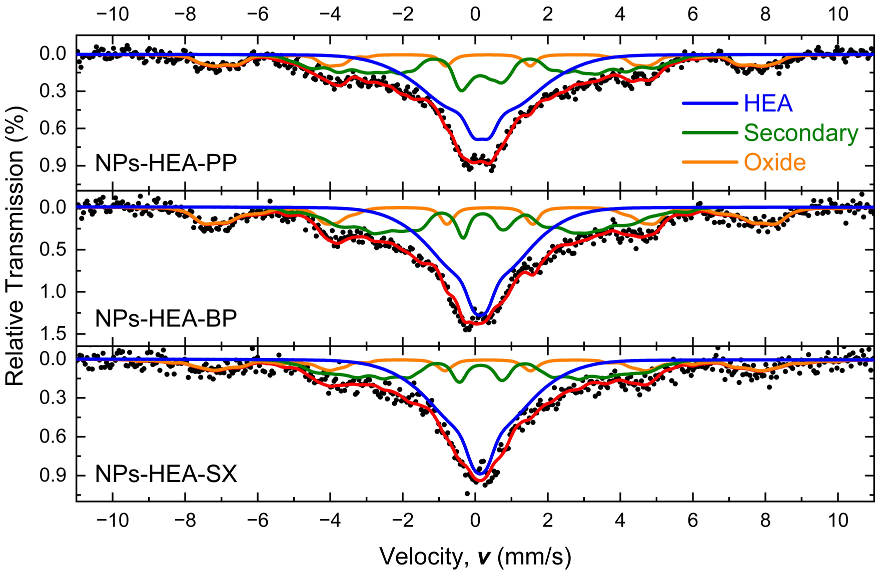

Figure 7. Low temperature Mössbauer spectra of PLAL-generated NPs from HEA-PP, HEA-BP, and HEA-SX targets (dots and red lines). Subspectra are assigned to NPs from FCC-like Fe (blue), a secondary bcc-phase (green), and a Fe^{3+} oxide phase (orange).

field distributions p(B_{hf}) are known for different TM-alloys, such as short-range ordered Fe–Cr[64] or α-Fe–Mn.[65] The observation of this broad distribution might indicate the presence of Mn-rich or disordered Cr-containing parasitic phases. Such an Fe environment is in agreement with the EDX results revealing that Fe is mainly found in the core of the NPs and could be surrounded by four other elements, causing differences in the local Fe environment. Besides, all samples have a ~20% oxide phase. The absence of any oxide contribution in the XRD pattern (Figure S6) indicates the formation of amorphous oxides or to a small oxide volume in different orientations. The obtained hyperfine field distribution p(B_{hf}) and isomer shift δ_{iso} correspond typically to Fe^{3+} oxides. Due to the relatively broad absorption lines, it is not possible to further determine the kind of formed oxide. From the literature, we can exclude the formation of ordered $(CoCrFeMnNi)_3O_4$[66,67] oxide indicating a partial oxidation of different NPs. Due to the similarity of the oxide contribution in the different prepared alloys, it can be assumed that the partial oxidation of NPs is independent of the target preparation method.

3.6. Mass Spectrometric Studies of the HEA Ablation Plumes

Figure 8 shows a typical mass spectrum of the ablation products produced by laser ablation in vacuum of the HEA-PP sample at a fluence of 1.7 J/cm^2. The ablation plume is found to consist mainly of atomic species of the alloy components (Cr,

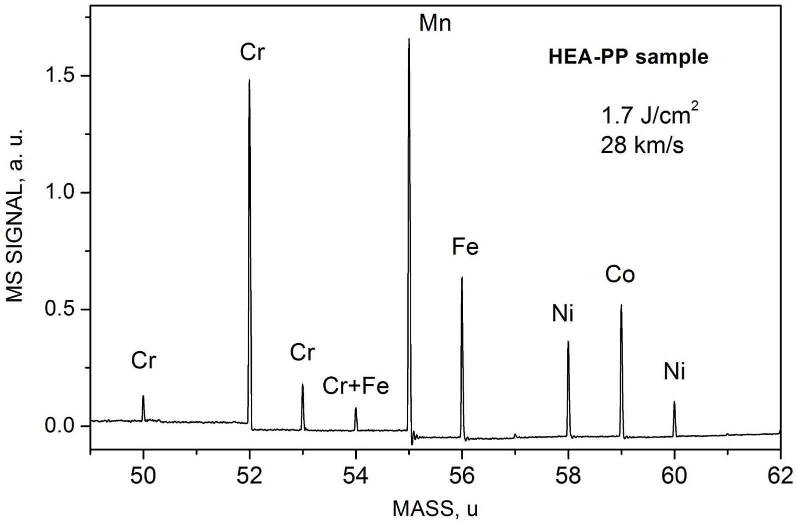

Figure 8. Mass spectrum of the plasma plume ions produced by laser ablation of the HEA-PP target in vacuum at a fluence of 1.7 J/cm^2. The spectrum is taken at a TOF delay of 16 μs corresponding to the particle velocity of 28 km/s.

Fe, Co, Ni, and Mn), and the plume compositions are similar for the 3 different targets. At fluences above ~1 J/cm^2, doubly-charged ions of all elements are observed in the plume. No mixed species or clusters were detected. Similar spectra were obtained for the HEA-BP and HEA-SX targets in the studied fluence range. However, the thresholds for ion emission (which can be considered similar to or slightly below the conventional ablation threshold[68]) are different for the studied targets. For the HEA-BP and HEA-SX targets, the ion emission threshold is found to be 0.22 J/cm^2, i.e., very close to the ablation threshold value of 0.24 J/cm^2 measured by Redka et al.[51] for a crystalline CoCrFeMnNi target. However, for the HEA-PP sample, the ion emission threshold is found to be 0.36 J/cm^2, which is in good agreement with the threshold value of 0.38 J/cm^2 evaluated here based on the NP productivity measurements (section 3.2). The observed difference in the ablation thresholds for alloyed HEA-BP and HEA-SX targets and the mixed elemental HEA-PP sample is likely due to different optical and thermophysical properties of the targets.

The relative abundance of the atomic ablation products in the plume does not correspond to the equiatomic composition of the target. In particular, Cr^+ and Mn^+ ions are significantly more abundant than other plume species. This can be partially explained by the lower ionization potentials (IPs) of these elements (IP = 6.76 eV for Cr and 7.43 eV for Mn) compared to the other elements (7.88 eV, 7.90 eV, and 7.64 eV for Co, Fe, and Ni, respectively). Indeed, the lower the IP, the easier the corresponding particle can be ionized and thus the stronger is the signal in the mass spectrum. However, a closer inspection shows that the observed abundance distributions and plume expansion dynamics cannot be explained solely based on the IPs as demonstrated by using the measured TOF distributions.

Figure 9 shows the TOF distributions $I(t)$ of the main plume particles produced by laser ablation of the HEA-PP, HEA-BP, and HEA-SX targets at a laser fluence of 1.7 J/cm^2. For elements with several isotopes (Cr, Fe, and Ni), the peak intensities of the most abundant isotopes ^{52}Cr (abundance 83.8 %), ^{56}Fe (91.7 %), and ^{58}Ni (68.3 %), were used for the plots. By integrating the distributions of individual elements over the delay time t, one can evaluate the total number of the emitted particles Y and their mean kinetic energy $\bar{E}_k$ using the following equations:[69]

$$Y = \int_0^{\infty} I(t)dt \qquad \text{(Eq.1)}$$

$$\bar{E}_k = \frac{1}{2Y}\int_0^{\infty} m[u(t)]^2 I(t)dt = \frac{mL^2}{2Y}\int_0^{\infty} t^{-2} I(t)dt \qquad \text{(Eq.2)}$$

where m is the mass of an atom, $u = \frac{L}{t}$ is the velocity, and $L =$ 46 cm is the flight distance. The obtained values for all the plume particles and all three studied HEA targets are summarized in Table 1. The ion yields Y of different components are corrected for their isotope abundancies and normalized to the yield of Mn atoms. In addition, the particle mean velocity $\bar{u} = \sqrt{\frac{2\bar{E}_k}{m}}$ and the maximal velocity u_{max} (corresponding to the peak of the TOF distributions) are presented in Table 1.

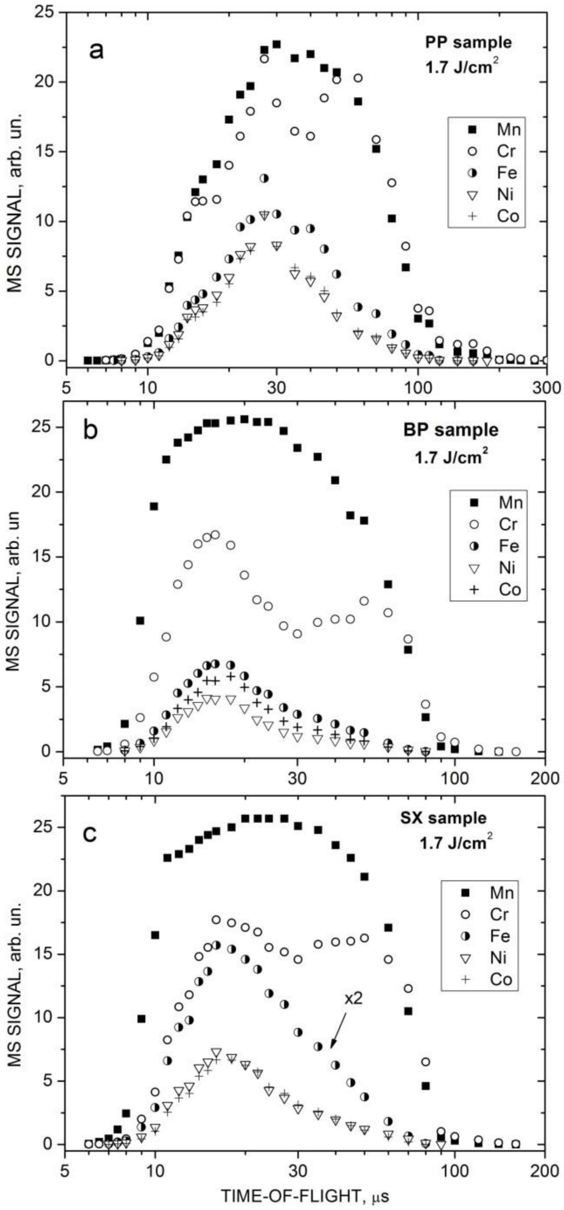

Figure 9. TOF distributions of the plasma plume particles produced by laser ablation of (a) HEA-PP, (b) HEA-BP and (c) HEA-SX samples at a laser fluence of 1.7 J/cm^2.

Three remarkable results emerge from Figure 9 and Table 1. First, the total yield of Mn ions is considerably higher than that of Cr ions for the HEA-BP and HEA-SX targets, despite that the IP of the Cr is lower. Also, Fe and Co atoms have virtually identical IPs while iron is always more abundant in the plume than cobalt. Second, for all the samples, the heavier components of the plume (Fe, Ni, and Co) have higher mean velocities than those of the lighter components (Cr and Mn) that is rather atypical for laser-ablation plumes. Third, the TOF distributions of chromium exhibit a bi-modal shape with two distinct peaks (especially pronounced for the HEA-BP and HEA-SX targets)

Table 1. Normalized yield *Y*, mean kinetic energy $\bar{E}_{kin}$, mean velocity $\bar{u}$, and maximal velocity u_{max} of the main plume particles under laser ablation of the HEA-PP, HEA BP, and HEA-SX samples at a fluence of 1.7 J/cm^2.

Parameter	HEA sample	^{55}Mn	^{52}Cr	^{56}Fe	^{58}Ni	^{59}Co
Y	PP	1	1.1	0.35	0.30	0.26
	BP	1	0.73	0.14	0.10	0.10
	SX	1	0.73	0.16	0.11	0.11
$\bar{E}_k$, eV	PP	50	42	64	76	75
	BP	108	83	147	167	165
	SX	96	68	132	150	150
$\bar{u}$, km/s	PP	13.2	12.5	14.9	15.9	15.7
	BP	19.5	17.5	22.5	23.6	23.2
	SX	18.4	15.9	21.3	22.3	22.2
u_{max}, km/s	PP	15.3	17.0/8.4	17.0	17.0	17.0
	BP	23.0	28.7/8.8	28.7	28.7	28.7
	SX	19.2	28.7/8.8	28.7	28.7	28.7

where the second peak corresponds to relatively low particle velocities of around 8 km/s.

All the above observations cannot be explained by the difference in IPs of the elements and indicate that another factor governs primarily the particle yields and velocities under these ablation conditions. We believe that this factor is the component volatility. Due to different component volatilities, the laser ablation of multicomponent targets affects the target stoichiometry, since the more volatile components are released (evaporated) more efficiently than the less volatile ones.[70–72] Furthermore, this can strongly affect the expansion dynamics of the ablation plume.[72–74]

The relative volatility of the CoCrFeMnNi HEA components can be estimated based on the vapor pressure and boiling point of the corresponding materials (Table. ST1 in the supplementary). Based on these data, the following hierarchy of the HEA elements in terms of their volatility can be deduced: Mn > Cr > Fe > Ni~Co with Mn being the most volatile metal. Then, if we assume incongruent vaporization during HEA laser ablation, all our mass spectrometry observations can be consistently explained. The most volatile Mn is the most abundant species in the plume despite its relatively high IP. Fe is more volatile than Co and thus is more abundant, although their IPs are identical. Moreover, this approach explains the observed particle velocity behavior with higher mean velocities for heavier particles. This is due to a delayed evaporation of the morevolatile components.[72] The incongruent vaporization process in the multi-shot irradiation regime proceeds as follows.[72] After a sufficiently large number of laser pulses, the target surface is enriched by low-volatile components (Fe, Ni, and Co in the considered case). The following pulses induce predominantly emission of these components with high kinetic energies. However, the laser heating of the near-surface target layer induces the diffusion of the high-volatile components (Mn) from the bulk to compensate for their deficiency at the surface.[66,67] As a result, they can be released from the target for a fairly long time, when the surface temperature is still sufficient for them to evaporate. Such delayed particles have much lower velocities. This explains also the low-velocity tail in the Cr distribution. For Mn, the delayed vaporization is even more significant, but it is not manifested as a separate peak in the TOF distribution since the delayed peak is likely broad and overlaps with the peak of directly emitted Mn atoms (Figure 9).

If we compare the mass spectrometry results for different HEA targets (Figure 9 and Table 1), we can see that ablation of the alloyed HEA-BP and HEA-SX targets results in similar particle abundance and TOF distributions which are, however, quite different from those obtained with the HEA-PP sample. For the latter, all the plume particles are considerably slower, which can be explained by the higher ablation threshold of this sample. Furthermore, although the relative particle abundancies in the plume deviate from the initial equiatomic target composition for all the targets, the deviation is much larger for the alloyed targets where Mn ions are the dominant species in the plume (Figure 9b and 9c). This indicates that the incongruent ablation is more pronounced for the HEA-BP and HEA-SX samples and thus the delayed evaporation of the high-volatile components is more efficient in this case. This can be therefore a plausible explanation of the PLAL formation of core-shell NPs from the HEA-BP and HEA-SX targets with a Mn-rich shell (Figure S4) since the shell is formed mainly by Mn atoms released from the target at a significant delay after the main ablation. For the HEA-PP target, the delayed evaporation contributes to the ablation process to a lesser extent and thus the PLAL-produced NPs are mostly uniform in composition. Note that the total ion yields are almost identical for all the targets (MS signals in Figures 9a-c are given in comparable units) which confirms the similar PLAL productivity of HEA NPs from the three targets (Figure 4b).

We should underline here that laser ablation processes in vacuum, especially the plume expansion, are different from those in the liquid environment. However, the initial ablation stages, including target heating, melting, and material ejection, before the plume expansion starts, can be considered quite similar. Therefore, mass spectrometry investigations of the ablation products in vacuum provide valuable information on the initial ablation stage in liquids and reveal differences in ablation dynamics for the evaluated targets.

4. Conclusions

The influence of the morphology, composition, and crystallinity of the target on the generation of HEA nanoparticles by PLAL has been evaluated. The elemental distribution within the targets shows a higher segregation and inhomogeneity in the HEA-PP (powder mixing-pressing-heat treatment) target compared to HEA-BP (ball milling-hot pressing) and HEA-SX (single crystal via Bridgeman method) targets.

Despite this difference, laser ablation of all the targets resulted in the formation of similar CoCrFeMnNi alloy nanoparticles of 6–8 nm diameter on average. Interestingly, the nanoparticles of the large fraction (>20 nm) generated from the HEA-PP target were found to be in a solid solution state, whereas the nanoparticles produced using HEA-BP and HEA-SX targets exhibited the formation of core-shell structures with a Mn-rich shell. Remarkably, the HEA-PP target yielded a 6.8% and 15.1% higher productivity compared to the HEA-BP and HEA-SX targets, respectively. Furthermore, the nanoparticles from all targets exhibit an FCC structure with partially amorphous phases, predominantly oxides. Mössbauer spectroscopy indicates a consistent 20 at.% oxide content in the nanoparticles, irrespective of the target composition.

The summary of the NPs properties obtained from the HEA-PP, HEA-BP, and HEA-SX targets is shown in Table 2. These findings underscore the feasibility of producing HEA nanoparticles from targets prepared via the HEA-PP process offering a fast, reliable, and economically favourable in comparison to HEA-BP and HEA-SX targets.

The authors gratefully acknowledge the funding by the German Research Foundation (DFG) within the Collaborative Research Centre/Transregio (CRC/TRR) 270 (Project-ID 405553726, projects (B04, B05, B08, A04 and Z01). The authors also acknowledge funding by the DFG grant numbers GO 2566/14-1, GO 2566/7-2. The authors further thank the DFG and NRW for funding in the frame of the major equipment program (INST 218/87-1, 503865051). Bilal Gökce further thanks DFG for funding of the project GO 2566/10-1. Carlos Doñate Buendia thanks Generalitat Valenciana for funding of the project CIDEIG/2023/08 within Gen-T programme. Oleksandr Gatsa, Miroslava Flimelová, and Alexander V. Bulgakov acknowledge financial support from the Czech Science Foundation (GACR), project 22-38449L. We thank Dr. Markus Heidelmann for his help with the TEM EDX-mapping of HEA nanoparticles for composition analysis. We thank Dr.-Ing. Christian Gadelmeier and Prof. Dr. Ing. Uwe Glatzel, University of Bayreuth for the preparation of HEA single crystals. We also thank David Koch for his help with XRD analysis.

Conflict of Interests

The authors declare no conflicts of interest.

Data Availability Statement

The data that support the findings of this study are available from the corresponding author upon request.

[1] B. Cantor, I. T. H. Chang, P. Knight, A. J. B. Vincent, *Mater. Sci. Eng. A* **2004**, *375–377*, 213.
[2] J.-W. Yeh, S. K. Chen, S.-J. Lin, J.-Y. Gan, T.-S. Chin, T. Shun, C. H. Tsau, S. Y. Chang, *Adv. Eng. Mater.* **2004**, *6*, 299.
[3] X. Chang, M. Zeng, K. Liu, L. Fu, *Adv. Mater.* **2020**, *32(14)*, 1907226.
[4] D. Miracle, J. Miller, O. Senkov, C. Woodward, M. Uchic, J. Tiley, *Entropy* **2013**, *16*.
[5] T. Yang, Y. Zhao, W. Liu, J. Kai, C. Liu, *J. Mater. Res.* **2018**, *33(19)*, 2983.
[6] M. Dada, P. Popoola, S. Adeosun, N. Mathe, *High Entropy Alloys for Aerospace Applications*, IntechOpen, Rijeka, **2019**.
[7] M. Dada, P. Popoola, N. Mathe, *World J. Eng.* **2021**, *20*, 43.

Table 2. Overview of the HEA NPs properties produced via PLAL employing different target preparation methods.

	HEA-PP NPs	HEA-BP NPs	HEA-SX NPs
Maximum productivity (mg/h)	311 ± 26	290 ± 6	264 ± 8
Mean particle diameter (x_c) (nm)	8.6 ± 5.2	6.8 ± 0.4	6.2 ± 0.5
Composition analysis by EDX	Near to equiatomic composition, mostly solid solution	Near to equiatomic composition, small particles (<10 nm) solid solution, large particles (>20 nm) core Mn-rich shell particles	Near to equiatomic composition, small particles (<10 nm) solid solution, large particles (>20 nm) core Mn-rich shell particles
Phase analysis by Mossbauer spectroscopy and XRD	FCC crystal structure + ~20% amorphous oxide phase	FCC crystal structure + ~20% amorphous oxide phase	FCC crystal structure + ~20% amorphous oxide phase
Ablation threshold fluence for ion emission (J/cm^2)	0.36	0.22	0.22
Mass spectrometric analysis	High abundance of Mn and Cr ions Lower maximum velocity of Mn ions than other elements	High abundance of Mn ions Lower maximum velocity of Mn ions than other elements	High abundance of Mn ions Lower maximum velocity of Mn ions than other elements

[8] J. Feng, Y. Tang, J. Liu, P. Zhang, C. Liu, L. Wang, *Front. Bioeng. Biotechnol.* **2022**, *10*, 1091752.

[9] T. G. De Oliveira, D. Fagundes, P. Capellato, D. Sachs, A. a a P Da Silva, *Metals* **2022**.

[10] E. J. Pickering, A. W. Carruthers, P. J. Barron, S. C. Middleburgh, D. E. J. Armstrong, A. S. Gandy, *Entropy* **2021**, *23*, 98.

[11] M. Moschetti, P. A. Burr, E. Obbard, J. J. Kruzic, P. Hosemann, B. Gludovatz, *J. Nucl. Mater.* **2022**, *567*, 153814.

[12] G. Feng, F. Ning, J. Song, H. Shang, K. Zhang, Z. Ding, P. Gao, W. Chu, D. Xia, *J. Am. Chem. Soc.* **2021**, *143(41)*, 17117.

[13] K. Li, W. Chen, *Mater. Today* **2021**, *20*, 100638.

[14] B. Wang, X. Zhu, X. Pei, W. Liu, Y. Leng, X. Yu, C. Wang, L. Hu, Q. Su, C. Wu, Y. Yao, Z. Lin, Z. Zou, *J. Am. Chem. Soc.* **2023**, *145(25)*, 13788.

[15] T. Löffler, F. Waag, B. Gökce, A. Ludwig, S. Barcikowski, W. Schuhmann, *ACS Catal.* **2021**, *11(3)*, 1014.

[16] D. Modupeola, P. Popoola, *Front. Energy Res.* **2023**, *11*, 1149446.

[17] H. Shen, J. Zhang, J. Hu, J. Zhang, Y. Mao, H. Xiao, X. Zhou, X. Zu, *Nanomaterials* **2019**, *9(2)*, 248.

[18] A. Poulia, A. S. Azar, P. Švec, C. Bazioti, B. D. Belle, A. E. Gunnæs, S. Diplas, P. Mikheenko, *IEEE NAP* **2020**, *01*, nmm02.

[19] A. Quintana-Nedelcos, Z. Leong, N. A. Morley, *Mater. Today* **2021**, *20*, 100621.

[20] C. L. P. Pavithra, R. Janardhana, K. M. Reddy, C. Murapaka, U. Klement, S. R. Dey, *J. Electrochem. Soc.* **2022**, *169(2)*, 022501.

[21] Y. J. Ai, M. Q. He, H. Sun, X. M. Jia, L. Wu, X. Y. Zhang, H. B. Sun, Q. L. Liang, *Adv. Mater.* **2023**, *35*, 2302335.

[22] A. A. Alamdari, U. Unal, A. Motallebzadeh, *Surf. Interfaces* **2022**, *28*, 101617.

[23] Y. Liao, Y. Li, R. Zhao, J. Zhang, L. Zhao, L. Ji, Z. Zhang, X. Liu, G. Qin, X. Zhang, *Natl. Sci. Rev.* **2022**, *9(6)*, nwac041.

[24] F. Waag, Y. Li, A. R. Ziefuß, E. Bertin, M. Kamp, V. Duppel, G. Marzun, L. Kienle, S. Barcikowski, B. Gökce, *RSC Adv.* **2019**, *9(32)*, 18547.

[25] Y. Liu, Z. Chen, X. Yang, J. Zhang, Z. Sun, Y. Chen, F. Liu, *RSC Adv.* **2021**, *11(40)*, 24636.

[26] Q. F. He, Z. Y. Ding, Y. F. Ye, Y. Yang, *JOM* **2017**, *69(11)*, 2092.

[27] S. Moniri, Y. Yang, J. Ding, Y. Yuan, J. Zhou, L. Yang, F. Zhu, Y. Liao, Y. Yao, L. Hu, P. Ercius, J. Miao, *Nature* **2023**, *624(7992)*, 564.

[28] X. Zhang, S. Cranford, *Matter* **2020**, *3(5)*, 1391.

[29] Y. Yao, Z. Huang, P. Xie, S. D. Lacey, R. J. Jacob, H. Xie, F. Chen, A. Nie, T. Pu, M. Rehwoldt, D. Yu, M. R. Zachariah, C. Wang, R. Shahbazian-Yassar, J. Li, L. Hu, *Science* **2018**, *359(6383)*, 1489.

[30] P.-C. Chen, X. Liu, J. L. Hedrick, Z. Xie, S. Wang, Q.-Y. Lin, M. C. Hersam, V. P. Dravid, C. A. Mirkin, *Science* **2016**, *352(6293)*, 1565.

[31] Y. Liu, X. Tian, Y.-C. Han, Y. Chen, W. Hu, *Chin. J. Catal.* **2023**, *48*, 66.

[32] R. K. Pittkowski, C. M. Clausen, Q. Chen, D. Stoian, W. Van Beek, J. Bucher, R. L. Welten, N. Schlegel, J. K. Mathiesen, T. M. Nielsen, J. Du, A. W. Rosenkranz, E. D. Bøjesen, J. Rossmeisl, K. M. Ø Jensen, M. Arenz, *EES Catal.* **2023**, *1(6)*, 950.

[33] S. Gao, S. Hao, Z. Huang, Y. Yuan, S. Han, L. Lei, X. Zhang, R. Shahbazian-Yassar, J. Lu, *Nat. Commun.* **2020**, *11(1)*, 2016.

[34] H. Guo, Z. Guo, K. Chu, W. Zong, H. Zhu, L. Zhang, C. Liu, T. Liu, J. Hofkens, F. Lai, *Adv. Funct. Mater.* **2023**, 2308229.

[35] F. Okejiri, Z. Yang, H. Chen, C.-L. Do-Thanh, T. Wang, S. Yang, S. Dai, *Nano. Res.* **2022**, *15(6)*, 4792–4798.

[36] H. Qiao, M. Saray, X. Wang, S. Xu, G. Chen, Z. Huang, C. Chaoji, G. Zhong, Q. Dong, M. Hong, H. Xie, R. Shahbazian-Yassar, L. Hu, *ACS Nano* **2021**, *15*, 14928.

[37] B. Wang, C. Wang, X. Yu, Y. Cao, L. Gao, C. Wu, Y. Yao, Z. Lin, Z. Zou, *Nat. Synth.* **2022**, *1(2)*, 138.

[38] M. Cui, C. Yang, S. Hwang, M. Yang, S. Overa, Q. Dong, Y. Yao, A. H. Brozena, D. A. Cullen, M. Chi, T. F. Blum, D. Morris, Z. Finfrock, X. Wang, P. Zhang, V. G. Goncharov, X. Guo, J. Luo, Y. Mo, F. Jiao, L. Hu, *Sci. Adv.* **2022**, *8(4)*, eabm4322.

[39] D. Zhang, B. Gökce, S. Barcikowski, *Chem. Rev.* **2017**, *117(5)*, 3990.

[40] S. Barcikowski, V. Amendola, G. Marzun, C. Rehbock, S. Reichenberger, D. Zhang, B. Gökce, *Handbook of Laser Synthesis of Colloids*, DuEPublico, Duisburg-Essen, **2016**.

[41] D. Zhang, B. Gökce, S. Barcikowski, *Chem. Rev.* **2017**, *117(5)*, 3990.

[42] E. Fazio, B. Gökce, A. De Giacomo, M. Meneghetti, G. Compagnini, M. Tommasini, F. Waag, A. Lucotti, C. G. Zanchi, P. M. Ossi, M. Dell'aglio, L. D'urso, M. Condorelli, V. Scardaci, F. Biscaglia, L. Litti, M. Gobbo, G. Gallo, M. Santoro, S. Trusso, F. Neri, *Nanomaterials (Basel)* **2020**, *10(11)*, 2317.

[43] R. Streubel, S. Barcikowski, B. Gökce, *Opt. Lett.* **2016**, *41(7)*, 1486.

[44] D. Zhang, Z. Li, K. Sugioka, *JPhys Photonics* **2021**, *3*, 042002.

[45] H. Jahangiri, Y. Morova, A. Asghari Alamdari, Z. Eroğlu, A. Sennaroğlu, S. Guo, O. Metin, A. Motallebzadeh, *Intermetallics* **2023**, *156*, 107834.

[46] F. Waag, W. I. M. A. Fares, Y. Li, C. Andronescu, B. Gökce, S. Barcikowski, *J. Mater. Sci.* **2022**, *57(4)*, 3041.

[47] T. Schmitz, U. Wiedwald, C. Dubs, B. Gökce, *ChemPhysChem* **2017**, *18(9)*, 1125.

[48] R. Kaegi, M. Fierz, B. Hattendorf, *Microsc. Microanal.* **2021**, *27(3)*, 557.

[49] K. Y. Tsai, M. H. Tsai, J. W. Yeh, *Acta Mater.* **2013**, *61(13)*, 4887.

[50] B. Neuenschwander, B. Jaeggi, M. Schmid, G. Hennig, *Phys. Procedia* **2014**, *56*, 1047.

[51] D. Redka, C. Gadelmeier, J. Winter, M. Spellauge, C. Eulenkamp, P. Calta, U. Glatzel, J. Minár, H. P. Huber, *Appl. Surf. Sci.* **2021**, *544*, 148839.

[52] R. Nadarajah, S. Barcikowski, B. Gökce, *Opt. Express* **2020**, *28(3)*, 2909.

[53] Y. Afanasiev, N. Demchenko, V. Isakov, I. Zavestovskaya, B. Chichkov, *Proc. SPIE - Int. Soc. Opt. Eng.* **2002**, *4760*, 424.

[54] J. Lopez, G. Mincuzzi, R. Devillard, Y. Zaouter, C. Hönninger, E. Mottay, R. Kling, *J. Laser Appl.* **2015**, *27*, S28008.

[55] C.-Y. Shih, R. Streubel, J. Heberle, A. Letzel, M. V. Shugaev, C. Wu, M. Schmidt, B. Gökce, S. Barcikowski, L. V. Zhigilei, *Nanoscale* **2018**, *10(15)*, 6900.

[56] J. Johny, M. Kamp, O. Prymak, A. Tymoczko, U. Wiedwald, C. Rehbock, U. Schürmann, R. Popescu, D. Gerthsen, L. Kienle, S. Shaji, S. Barcikowski, *J. Phys. Chem. C* **2021**, *125*, 9534.

[57] N. Derimow, R. Abbaschian, *Entropy (Basel)* **2018**, *20(11)*, 890.

[58] F. Zhang, C. Zhang, S. L. Chen, J. Zhu, W. S. Cao, U. R. Kattner, *Calphad* **2014**, *45*, 1.

[59] B. Ruiz-Yi, J. K. Bunn, D. Stasak, A. Mehta, M. Besser, M. J. Kramer, I. Takeuchi, J. Hattrick-Simpers, *ACS Comb. Sci.* **2016**, *18(9)*, 596.

[60] A. Tymoczko, M. Kamp, O. Prymak, C. Rehbock, J. Jakobi, U. Schürmann, L. Kienle, S. Barcikowski, *Nanoscale* **2018**, *10(35)*, 16434.

[61] P. W. Voorhees, *J. Stat. Phys.* **1985**, *38(1)*, 231.

[62] O. Schneeweiss, M. Friák, M. Dudová, D. Holec, M. Šob, D. Kriegner, V. Holý, P. Beran, E. P. George, J. Neugebauer, A. Dlouhý, *Phys. Rev. B* **2017**, *96(1)*, 014437.

[63] W. A. Macedo, W. Keune, *Phys. Rev. Lett.* **1988**, *61(4)*, 475.

[64] S. M. Dubiel, J. Cieslak, *Phys. Rev. B* **2011**, *83(18)*, 180202.

[65] C. Paduani, E. Galvão Da Silva, G. A. Perez-Alcazar, M. Mcelfresh, *J. Appl. Phys.* **1991**, *70(12)*, 7524.

[66] A. Sarkar, B. Eggert, R. Witte, J. Lill, L. Velasco, Q. Wang, J. Sonar, K. Ollefs, S. S. Bhattacharya, R. A. Brand, H. Wende, F. M. F. De Groot, O. Clemens, H. Hahn, R. Kruk, *Acta Mater.* **2022**, *226*, 117581.

[67] J. Cieslak, M. Reissner, K. Berent, J. Dabrowa, M. Stygar, M. Mozdzierz, M. Zajusz, *Acta Mater.* **2021**, *206*, 116600.

[68] A. V. Bulgakov, I. Ozerov, W. Marine, *Thin Solid Films* **2004**, *453–454*, 557.

[69] N. M. Bulgakova, A. V. Bulgakov, O. F. Bobrenok, *Phys. Rev. E* **2000**, *62(4)*, 5624.

[70] K. Abe, O. Eryu, S. Nakashima, M. Terai, M. Kubo, M. Niraula, K. Yasuda, *J. Electron. Mater.* **2005**, *34(11)*, 1428.

[71] O. A. Bulgakova, N. M. Bulgakova, V. P. Zhukov, *Appl. Phys. A* **2010**, *101(1)*, 53.

[72] A. V. Bulgakov, A. B. Evtushenko, Y. G. Shukhov, I. Ozerov, W. Marine, *Quantum Electron.* **2010**, *40(11)*, 1021.

[73] A. A. Morozov, S. V. Starinskiy, A. V. Bulgakov, *J. Phys. D* **2021**, *54(17)*, 175203.

[74] X. Yao, C. W. Schneider, N. M. Bulgakova, A. V. Bulgakov, T. Lippert, *Appl. Phys. A* **2023**, *129(8)*, 590.

Manuscript received: January 24, 2024
Revised manuscript received: February 23, 2024
Version of record online: March 26, 2024

Supplementary Information (SI):

Synthesis of High Entropy Alloy Nanoparticles by Pulsed Laser Ablation in Liquids: Influence of Target Preparation on Stoichiometry and Productivity

Shabbir Tahir[1], Natalia Shkodich[2], Benedikt Eggert[2], Johanna Lill[2], Oleksandr Gatsa[3], Miroslava Flimelová[3], Esmaeil Adabifiroozjaei[4], Nadezhda M. Bulgakova[3], Leopoldo Molina-Luna[4], Heiko Wende[2], Michael Farle[2], Alexander V. Bulgakov[3], Carlos Doñate-Buendía[1,5], and Bilal Gökce[1]*

[1] Chair of Materials Science and Additive Manufacturing, University of Wuppertal, Gaußstr. 20, 42119 Wuppertal, Germany

[2] Faculty of Physics and Center for Nanointegration Duisburg-Essen (CENIDE), University of Duisburg-Essen, Lotharstr. 1, 47057 Duisburg, Germany

[3] HiLASE Centre, Institute of Physics of the Czech Academy of Sciences, Za Radnicí 828, 25241 Dolní Břežany, Czech Republic

[4] Department of Materials- and Earth Sciences, Electron Microscopy Center Darmstadt (EMC-DA), Technische Universitat Darmstadt, 64287 Darmstadt, Germany

[5] GROC·UJI, Institute of New Imaging Technologies, Universitat Jaume I, Av. De Vicent Sos Baynat s/n, 12071 Castellón, Spain

*Corresponding author: goekce@uni-wuppertal.de.

1. Ablated and non-ablated target regions.

The region on the target where the laser irradiates and forms a crater is designated as an ablated region, while the non-radiated region or the surface of the targets is identified as a non-ablated region.

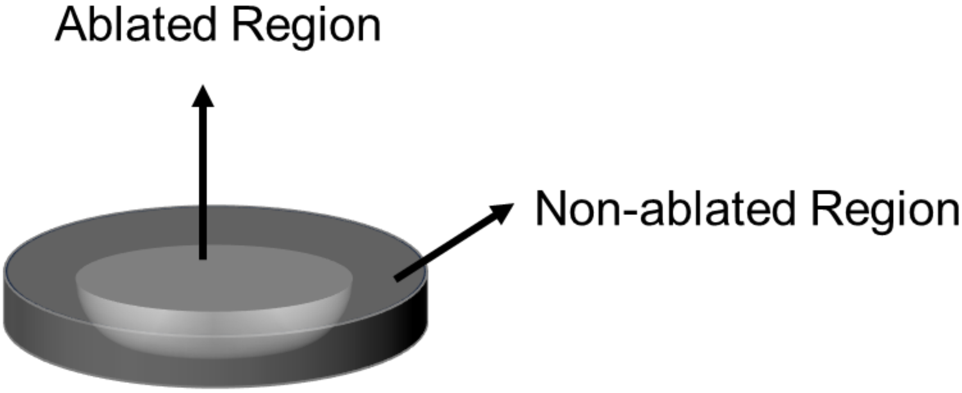

Figure S1: Ablated and non-ablated regions of the target.

2. Formation of laser-induced periodic surface structures (LIPSS)

Figure S2 presents scanning electron microscopy images illustrating the formation of LIPSS on the ablated region marked with arrows. On the surface of HEA-PP (Fig. S2a), the pattern is less distinct due to higher porosity, making challenging to detect the size of the periodic structure. The surface of the ball-milled powder-pressed target appears more compact, resulting in continuous periodic structures with an average period of ~840 nm. The surface of HEA-SX exhibits higher porosity than HEA-BP with the detected LIPSS periodicity of ~ 2 µm.

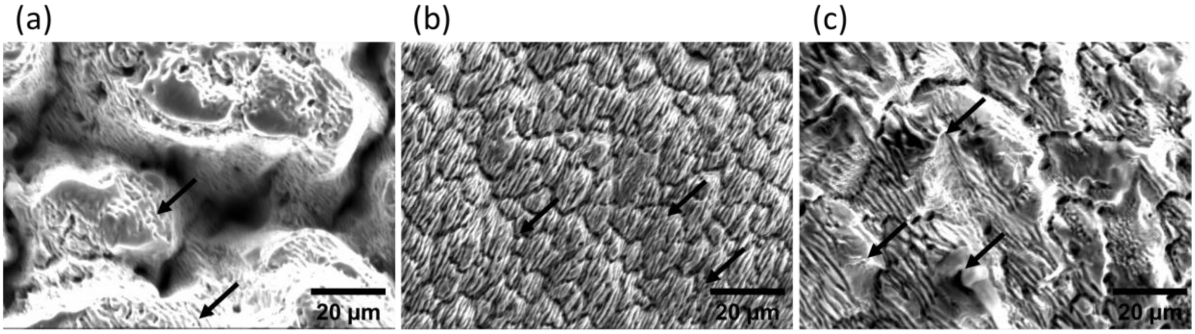

Figure S2: LIPPS formation on the (a) surface of HEA-PP ablated region, (b) surface of HEA-BP ablated region and (c) surface of HEA-SX ablated region after PLAL.

3. HEA NPs composition

Figure S3 displays the average compositions of nanoparticles derived from three different targets using TEM-EDX. The average composition of all elements is close to equiatomic with significant deviations regardless of the target preparation method.

Figure S4 shows the TEM-EDX mapping of particles showing the formation of Mn-rich shell particles mainly in NPs derived from HEA-BP and HEA-SX. The arrows show the formation of isolated Mn nanoclusters which are not the part of NPs.

The nanoparticle composition of less than 20 nm was analyzed by EDX-TEM as shown in Fig. S5. Unlike large particles, small ones are solid solutions with non-homogeneous distribution of elements throughout, independent of the target preparation method.

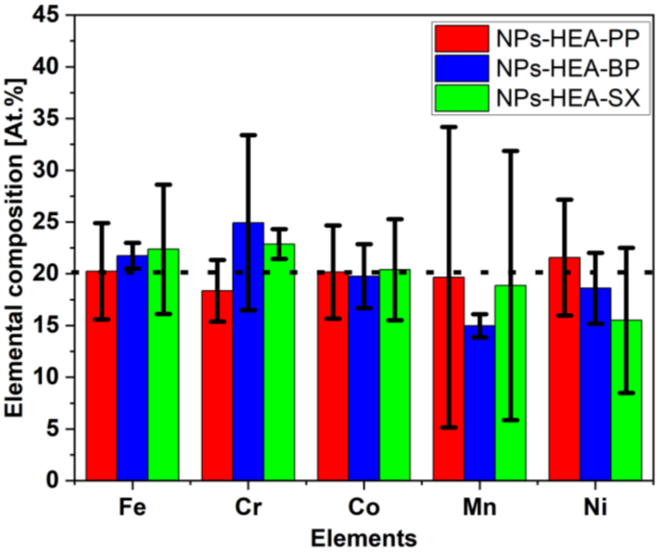

Figure S3. The average composition of all constituent elements of nanoparticles achieved by PLAL of HEA-PP, HEA-BP, and HEA-SX.

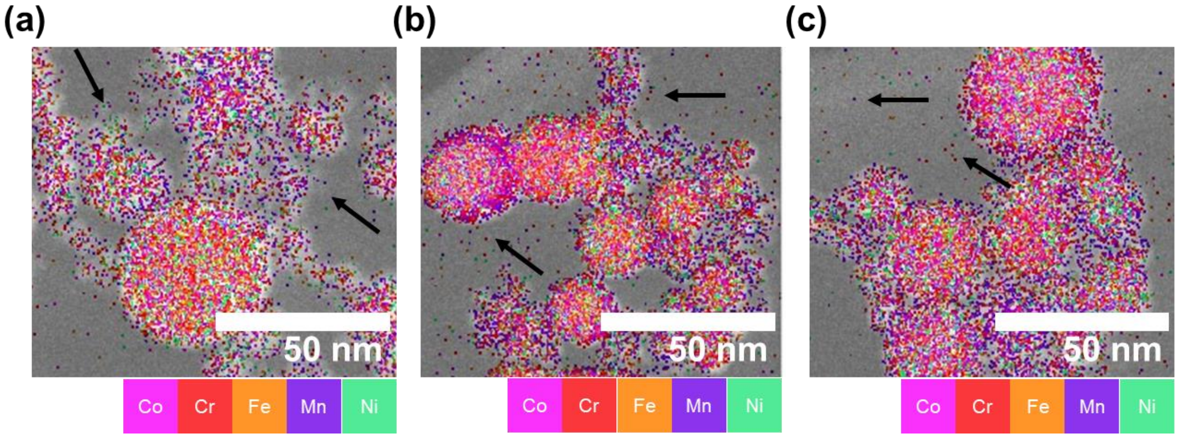

Figure S4. The overall average composition of nanoparticles obtained by PLAL of HEA-PP (a), HEA-BP (b), and HEA-SX (c), showing Mn-rich nano clusters.

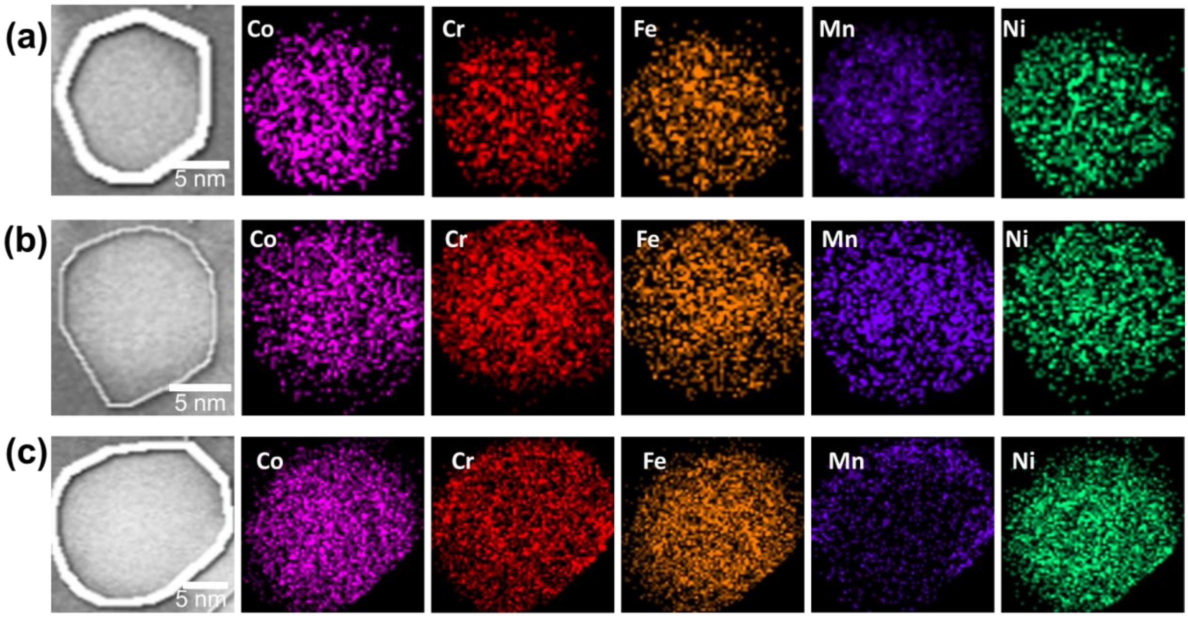

Figure S5. The elemental mapping of small nanoparticles (less than 20 nm) produced by PLAL of HEA-PP (a), HEA-BP (b), and HEA-SX (c), showing HEA NP's solid solution.

4. Crystal structure studies of HEA NPs

Figure S6 shows XRD patterns of NPs generated from HEA-PP, HEA-BP, and HEA-SX. The crystalline sample fraction consists of FCC crystal structure for all samples, irrespective of the target preparation method. The five major peaks (111), (200), (220), (311) and (222) correspond to standard Bragg reflections. Some reflection features also shows the presence of secondary phases. The broad features come from partially amorphous HEA or their oxides. The crystalline to amorphous phase transition in Cantor alloy was previously witnessed by Wang et al.[1] who proposed that amorphization comes from the increase of dislocation densities which promotes the development of stresses favoring crystalline to amorphous transformation. Since the formation of NPs by PLAL involves ultrafast heating and cooling, the residual stresses can promote such transformation.

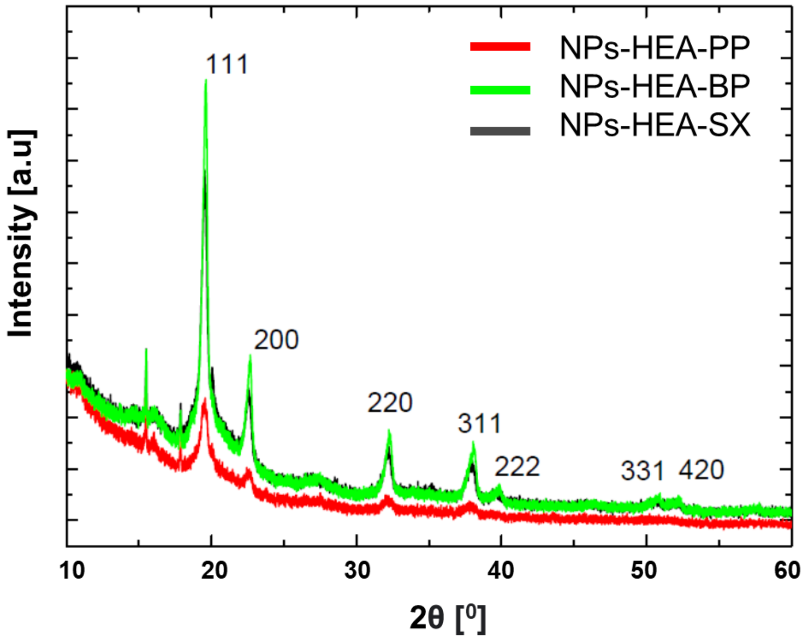

Figure S6. XRD patterns for NPs generated by PLAL of HEA-PP, HEA-BP, and HEA-SX. Crystalline NPs represented by five peaks corresponding to standard Bragg reflections (111), (200), (220), (311), and (222) of face-centered cubic lattice.

5. Volatility-related parameters of the CoCrFeMnNi HEA components

Table ST1. Volatility-related parameters of the CoCrFeMnNi HEA components. [2,3]

Parameter	Mn	Cr	Fe	Ni	Co
Vapor pressure at 1500 K, Torr	0.9	4.5×10^{-4}	1.4×10^{-4}	7×10^{-5}	5×10^{-5}
Boiling temperature, K	2334	2944	3134	3186	3200

References

1. Wang, H.; Chen, D.; An, X.; Zhang, Y.; Sun, S.; Tian, Y.; Zhang, Z.; Wang, A.; Liu, J.; Song, M.; Ringer, S. P.; Zhu, T.; Liao, X., Deformation-induced crystalline-to-amorphous phase transformation in a CrMnFeCoNi high-entropy alloy. *Sci Adv* **2021,** *7* (14).

2. Honig, R. E.; Kramer, D. A. Vapor pressure data for the solid and liquid elements. *RCA Review* **1969**, *30 (2)*, 285-288.

3. https://www.webelements.com

5.1.3. Study 3

Tahir, S., Smoliarova, T., Doñate-Buendía, C., Farle, M., Shkodich, M., and Gökce,B. (2025) Synthesis and magnetic transitions of rare-earth-free Fe–Mn–Ni–Si-based compositionally complex alloys at bulk and nanoscale. Beilstein J. Nanotechnol, 16, 823–836. DOI: https://doi.org/10.3762/bjnano.16.62

BEILSTEIN JOURNAL OF NANOTECHNOLOGY

Synthesis and magnetic transitions of rare-earth-free Fe–Mn–Ni–Si-based compositionally complex alloys at bulk and nanoscale

Shabbir Tahir[1], Tatiana Smoliarova[2], Carlos Doñate-Buendía[1,3], Michael Farle[2], Natalia Shkodich*[2] and Bilal Gökce*[1]

Full Research Paper

Open Access

Address:
[1]Chair of Materials Science and Additive Manufacturing, University of Wuppertal, Gaußstr. 20, 42119 Wuppertal, Germany, [2]Faculty of Physics and Center for Nanointegration Duisburg-Essen (CENIDE), University of Duisburg-Essen, Lotharstr. 1, 47057 Duisburg, Germany and [3]GROC·UJI, Institute of New Imaging Technologies, Universitat Jaume I, Av. De Vicent Sos Baynat s/n, 12071 Castellón, Spain

Email:
Natalia Shkodich* - natalia.shkodich@uni-due.de; Bilal Gökce* - goekce@uni-wuppertal.de

* Corresponding author

Keywords:
compositionally complex alloys; magnetic phase transition; nanoparticles; pulsed laser ablation in liquid; rare-earth free

Beilstein J. Nanotechnol. **2025,** *16,* 823–836.
https://doi.org/10.3762/bjnano.16.62

Received: 18 February 2025
Accepted: 07 May 2025
Published: 05 June 2025

This article is part of the thematic issue "Laser–material interactions in liquids applied to nanoparticles and nanocomposites".

Associate Editor: X. Song

Abstract

Magnetic phase transitions at the Curie temperature are essential for applications like magnetocaloric refrigeration, magnetic sensors, and actuators, but the reliance on costly, scarce rare-earth materials limits sustainability. Developing affordable, rare-earth-free materials with tunable magnetic properties and scalable miniaturization methods is vital for advancing technology. We present a comprehensive synthesis approach for rare-earth-free compositionally complex alloys (CCAs) with magnetic phase transitions, spanning from bulk materials to nanoparticles. Specifically, we investigate $Mn_{22.3}Fe_{22.2}Ni_{22.2}Ge_{16.65}Si_{16.65}$ (Ge-based CCA) and $Mn_{0.5}Fe_{0.5}NiSi_{0.93}Al_{0.07}$ (Al-based CCA). The bulk materials are prepared by ball milling and spark plasma sintering or powder pressing and sintering. Nanoparticles (NPs) from the bulk materials are synthesized by pulsed laser ablation in liquid. Magnetization measurements confirm a ferromagnetic-to-paramagnetic phase transition in bulk alloys, with T_c = 179 K for Ge-based CCA and T_c = 263 K for Al-based CCA. At the nanoscale, both Ge- and Al-based NPs exhibit superparamagnetic behaviour, with blocking temperatures of $T_B \approx 120$ K for Ge-based NPs (x_c = 13.4 ± 15.5 nm, average particle size) and $T_B \approx 100$ K for Al-based NPs (x_c = 18.4 ± 9.1 nm, average particle size), demonstrating the intrinsic superparamagnetic nature of NPs. While the Ge-based CCA demonstrates almost twice the saturation magnetization (M_s) and ≈20% lower hysteresis (H_c) in bulk form, the Al-based CCA exhibits comparable M_s and ≈45% lower H_c at the nanoscale at 5 K. These results indicate that the Al-based CCA is a promising, cost-effective alternative to Ge-based CCA at nanoscale, providing an economically viable and cost-effective alternative for nanoscale-based applications.

Introduction

Magnetic phase transitions are characterized by changes in the material's magnetic properties in response to varying conditions such as applied magnetic or electric fields, temperature, and/or pressure. In particular, the magnetic phase transition at the Curie temperature (T_c) is a type of magnetic phase transition characterized by the loss of spontaneous magnetization in ferromagnetic materials [1]. One key application of such transitions is in magnetocaloric cooling systems where magnetocaloric materials, when cycled near T_c in an external magnetic field, exhibit an adiabatic temperature change, enabling energy-efficient and environmentally friendly refrigeration [2]. These solid-state cooling systems are being developed as alternatives to conventional gas-based refrigeration and are especially advantageous for applications requiring tailored temperature ranges, such as room-temperature cooling and cryogenic systems [3,4]. The magnetic transition also plays a critical role in the development of temperature-sensitive magnetic sensors and actuators [5,6]. These devices harness the abrupt change in magnetic properties at T_c to detect temperature fluctuations or trigger mechanical responses, making them essential in automation, industrial processes, and healthcare monitoring technologies.

Considerable research has been dedicated to tailoring the Curie temperature and associated magnetic properties through material design. Advances in composition modification, doping strategies, and material synthesis have been shown to effectively tune the phase transition characteristics, such as the temperature, coercivity (H_c), magnetization, and Curie or Néel temperatures [7-9]. For instance Zhou et al. [10] reported that adjusting the composition of NiMnGa to $Ni_{55.2}Mn_{18.6}Ga_{26.2}$, a giant magnetocaloric response with a ΔS of −20.4 $J{\cdot}kg^{-1}{\cdot}K^{-1}$ at 317 K in a 5 T field can be achieved compared to $Ni_{57.2}Mn_{15.9}Ga_{27.0}$ where a ΔS of just −2 $J{\cdot}kg^{-1}{\cdot}K^{-1}$ at 310 K was witnessed.

Within the myriad of material systems exhibiting magnetic transitions, compositionally complex alloys (CCAs) have garnered considerable attention because of their compositional flexibility and exceptional thermomechanical [11,12], magnetic [13,14], and electrical insulation properties [15,16]. CCAs are composed of five or more elements, offering design freedom. This flexibility allows for elemental combinations that control the configurational entropy of mixing, phase, and free energy of the material. Consequently, the magnetic phase transition of CCAs can be tuned by altering their chemical composition because of the different elemental interactions [17]. A significant advantage of using CCAs is their potential to replace rare earth elements in magnetic materials [18]. The development of rare-earth-free or rare-earth-lean magnets is critical because of the economic, environmental, and supply chain challenges associated with rare earth elements [19,20]. For instance, mining and processing of rare earths are linked to significant environmental risks, while geopolitical factors pose supply chain vulnerabilities [21]. By avoiding the use of rare earth elements, CCAs present a sustainable alternative for functional magnetic materials [14]. Specifically, MnTX-based CCA alloys (where T is the transition metal and X can be Si, Ge or Al) have gained attention because of their magneto-structural phase transition at low temperatures. As ternary alloys, these materials undergo a magnetic and structural transition from a low-temperature orthorhombic TiNiSi-type structure to a high-temperature hexagonal Ni_2In-type structure [22]. For instance, a ternary MnNiSi alloy transitions from the hexagonal Ni_2In structure to the orthorhombic TiNiSi structure at 1200 K [23], which is far from ideal for magnetocaloric, electronic, and spintronic-based applications. When these alloys are doped with elements such as Fe (which partly substitutes Mn atoms) and Ge or Al (which partially replaces Si atoms) [24] (forming CCAs), it effectively lowers the structural and magnetic phase transition temperatures while maintaining the overall magnetization. Previous studies on bulk MnFeNiGeSi [25] (i.e., doping MnNiSi with Fe and Ge) and MnFeNiSiAl [24] (i.e., doping NiMnSi with Fe and Al) alloys, synthesized by arc melting of pure elements show a second-order magnetostructural phase transition between 170 and 220 K with an isothermal entropy change of −7.3 $J{\cdot}kg^{-1}{\cdot}K^{-1}$ at 2.5 T and a first-order magnetostructural phase transition near 200 K with an isothermal entropy change of −23 $J{\cdot}kg^{-1}{\cdot}K^{-1}$ at 2 T, respectively.

Bulk CCAs are explored thanks to the metallurgy approaches that allow for material composition control and alloying. However, it is desirable to achieve controlled methodologies to downsize CCAs to the nanoscale because they exhibit remarkable properties due to the interplay between their compositional complexity and nanoscale effects, such as a high surface-to-volume ratio and quantum confinement. These unique characteristics make CCA nanoparticles (NPs) highly suitable for catalysis [26,27], energy storage [28], wear resistant coatings [29], environmental [30], biomedical [31], magnetic [32] and electronic [33] technologies. In magnetic NPs, a key feature is the superparamagnetic blocked-to-superparamagnetic fluctuating transition, which occurs at a characteristic blocking temperature (T_B). Below T_B, NPs exhibit superparamagnetic behavior, where magnetic moments of particles fluctuate due to thermal energy but can be aligned under an external field. Above T_B, thermal fluctuations dominate, causing a transition to a superparamagnetic fluctuating state. This transition is particularly relevant for applications such as magnetic hyperthermia, where NPs are used in cancer therapy to induce localized heating when exposed to an alternating magnetic field [34].

However, producing CCAs at the nanoscale presents significant challenges. Traditional wet chemistry approaches often fail because of elemental immiscibility under equilibrium conditions, which leads to elemental segregation and phase separation [35]. Additionally, standard near-equilibrium heating methods are not suitable for synthesizing CCA NPs because of inherent thermodynamic limitations [36]. While high-temperature synthesis techniques have been successful in producing CCA NPs, they come with certain drawbacks. For instance, carbothermal synthesis requires an electrically conductive substrate, making it unsuitable for large-scale production [37]. Pyrolysis requires purification steps to eliminate polymer impurities and also result in phase segregation due to differences in precursor reduction temperatures [38]. Other techniques such as laser scanning ablation [39] and Joule heating [40] have also been employed to generate CCAs, but they often involve costly precursors and lengthy solvent screening processes.

Among the various techniques available for producing CCA NPs, pulsed laser ablation in liquids (PLAL) stands out as a particularly promising method [41-43]. PLAL is a straightforward and versatile method that does not require expensive precursors, reducing agents, or surfactants [44,45]. The process is based on the laser irradiation of the target material submerged in a liquid environment. This makes PLAL a safe, scalable and environmentally friendly approach [46-48]. Research on the synthesis of CoCrFeMnNi Cantor alloy NPs by PLAL demonstrated that this method consistently produces NPs with near-equiatomic compositions, regardless of the target preparation technique. Additionally Gatsa et al. [49] provide a realistic perspective that the CCA NPs production using a multibeam PLAL approach can be scaled up to ca. 3 $g \cdot h^{-1}$. The CCA NPs produced by PLAL have shown a promising response as catalysts for oxygen reduction reactions [50].

In the current work, we aim to develop NPs of bulk rare-earth-free MnTX-based CCAs via PLAL. We start with bulk Ge-based CCA synthesized by high energy ball milling (HEBM) followed by spark plasma sintering (SPS), and an Al-based CCA obtained by powder pressing and sintering. Our goal is not only to replace rare earth elements but also to substitute other expensive elements, such as Ge, with more cost-effective alternatives such as Al. Notably, Ge is nearly a thousand times more expensive than Al, making this substitution economically advantageous [51]. By employing a more efficient and reliable alloy production method, we aim to create sustainable magnetic materials. Additionally, we compare the composition and magnetic transitions of the CCAs at the nanoscale to assess how these factors influence material magnetic performance. This research addresses the economic challenges associated with costly elements and rare earth materials, providing a pathway for developing bulk and nanometric functional magnetic materials that meet the demands of modern technological applications.

Materials and Methods

Preparation of bulk Ge-based CCAs

The bulk Ge-based CCA was synthesized by a two-step process. Initially, elemental Mn (99.2%, 3 µm), Fe (99.96%, 10–20 µm), Ni (99.5%, 45–60 µm), Si (99.999%, 45–60 µm), and Ge (99.99%, <250 µm) powders were mixed in the desired stoichiometric proportions and underwent HEBM in a planetary ball mill for 90 min under argon atmosphere and a ball-to-powder weight ratio of 20:1 with a rotation speed of sun disk/jars 700 rpm/1400 rpm. In the second step, the HEBM powders were consolidated using SPS (Dr. Sinter Lab – Fuji Electronic Industrial Co. Ltd.) in a vacuum environment. The powder mixture was loaded into a cylindrical graphite die with an inner diameter = 10 mm and uniaxially compressed at 50 MPa. SPS was carried out at 1073 K with a dwelling time of 10 min and a heating rate of 100 $K \cdot min^{-1}$. The temperature was measured by a K-type thermocouple placed in a radial hole inside the die. The SPS-processed disks had a thickness of d = 3–4 mm and a diameter of ∅ = 10 mm. The preparation procedure for the bulk Ge-based CCA is illustrated in Figure 1a.

Preparation of bulk Al-based CCAs

The bulk Al-based CCA was produced from elemental Mn (99.6%, <10 µm), Fe (99.5%, 6–10 µm), Ni (99.9%, 3–7 µm), Al (99.5%, 44 µm), and Si (99%, 44 µm) powders. The bulk targets preparation process is illustrated in Figure 1b. To achieve the desired composition, each elemental powder was weighed and mixed in the correct proportions by mass. The powders were thoroughly blended for 20 min using a mortar and pestle, as shown in the left panel of Figure 1b. After mixing, the powder was compressed at 100 MPa to produce cylindrical pellets of 10 mm in diameter and 2 mm in thickness (middle panel, Figure 1b). Finally, the samples underwent heat treatment in a near-vacuum environment (down to 10 mbar) at 600 °C for seven days, followed by rapid quenching in water. This procedure helps achieving a homogeneous alloy and is a cost-effective and time-efficient alternative to conventional target preparation methods, such as arc melting or HEBM followed by SPS, and suitable for CCA NP generation because of the inherent alloying produced during PLAL processing.

The bulk CCAs were ground, polished, and analyzed by SEM (JEOL JSM-7600 F, Japan). The chemical composition was determined using energy-dispersive X-ray spectroscopy (EDX) with an Oxford Inca spectrometer.

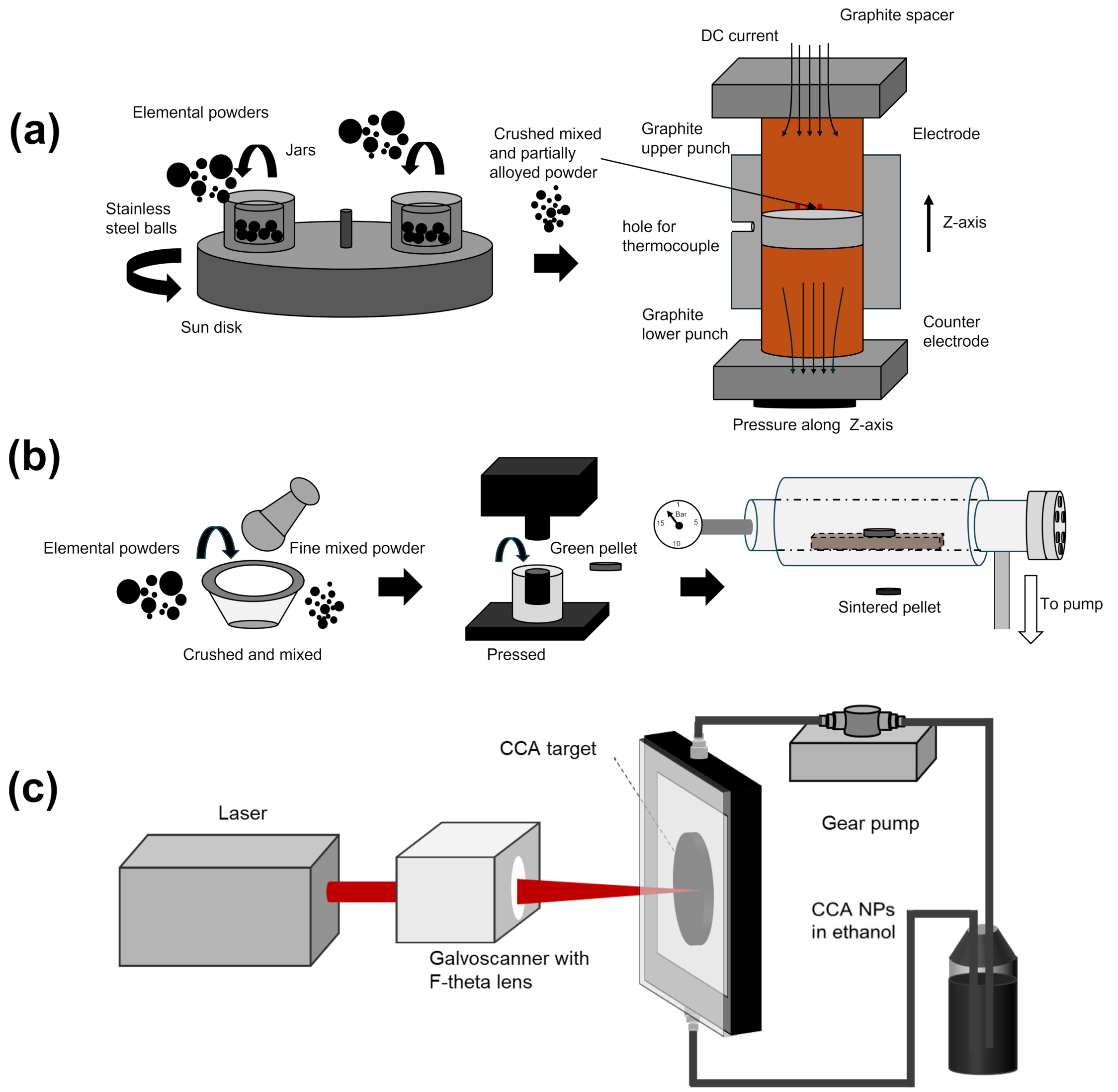

Figure 1: Synthesis route of the Ge- and Al-based CCAs. (a) Bulk Ge-based CCA produced via HEBM of elemental powders followed by SPS. (b) Bulk Al-based CCA synthesized through a process of mixing elemental powders using mortar and pestle, followed by uniaxial pressing and vacuum oven sintering. (c) CCA NPs produced by picosecond-pulsed laser ablation of the CCA alloy targets in ethanol employing a closed loop liquid flow chamber.

The crystal structure of bulk CCAs was characterized by X-ray diffraction (XRD) using a DRON-4–07 diffractometer with Co Kα radiation over a 2θ range of 20–110°. The magnetic properties of the samples were measured using a Quantum Design DynaCool physical property measurement system at temperatures ranging from 5 to 390 K under external magnetic fields up to 9 T.

Synthesis of CCA NPs by PLAL

The CCA colloidal NPs were synthesized by PLAL using the bulk Ge-based and Al-based CCA targets submerged in ethanol (Figure 1c). A near-infrared picosecond-pulsed Nd:YAG laser source (Coherent, HyperRapid NX, Kaiserslautern, Germany, 10 ps, 1064 nm) was employed to irradiate the targets within ethanol at a laser fluence of 2.8 J·cm^{-2} [41]. Additionally, to increase the NP concentration and reduce the organic solvent use, a closed loop liquid flow system was employed.

Size distribution, morphology, elemental composition, and crystal structure of the NPs from both CCA targets were examined using transmission electron microscopy (TEM) and EDX with a Jeol 2200FS microscope (Japan) equipped with an Oxford X-MaxN TLE 80 EDX detector (UK). The microscope was operated at an acceleration voltage of 200 kV and utilized a 2k × 2k GATAN UltraScan 1000XP CCD camera. For TEM analysis, the colloidal particles were dispersed onto a carbon-supported TEM copper grid and dried under ambient conditions. The particle size distribution was determined by measuring the Feret diameter of individual particles from TEM images using ImageJ software [52]. The NP crystal structure was evaluated using CrysTBox software [53] using digital diffractograms. EDX data was processed using AZtec software.

Results and Discussion

Microstructural characterization of bulk CCAs

The SEM images and EDX elemental maps of the polished surface of the Ge-based CCA (Figure 2a) revealed a homogeneous microstructure, with no significant elemental segregation on the micrometer scale, indicating a successful mixing and compaction. This uniformity results from the HEBM, which facilitates pre-alloying of elemental powders, followed by SPS. The controlled heating during SPS helps to prevent the grain growth and retains the nanoscale structure from HEBM powders. Table 1 presents the average composition of the Ge-based and Al-based CCAs measured at different spatial positions of the target's surface, showing that the measured values nearly align with the expected alloy composition. Notably, the percentage variance in Table 1 highlights that Ge exhibits the highest variance (14.1%) compared to other elements. This may be attributed to higher diffusion rates due to its lower latent heat of fusion (31.8 kJ·mol^{-1}) and its relatively low melting point (1211 K) compared to other constituents, as observed by Tiwari and colleagues [54]. Additionally, the target composition was re-evaluated from both the surface and cross-section, confirming that the composition remains consistent throughout the surface and bulk of the CCA within the limits of experimental error (Figure S1 and Table S1, Supporting Information File 1). Figure 2b provides an overview of the alloy's crystallographic information, indicating the coexistence of BCC and FCC phases. This differs from the work by Law et al. [25] where the alloy synthesized by arc melting resulted in a single-phase HCP structure at room temperature. The BCC phase, predominant in the current work, may not appear in alloys processed by arc melting due to the higher cooling rates (≈2000 K·s^{-1}) [55], which can stabilize HCP structures through a quenching effect [56] that does not occur for the SPS cooling rates (1.6 to 6.9 K·s^{-1}) [57]. The appearance of the FCC phase is consistent with Mn segregation and possible MnO formation, as evidenced by XRD peaks. The microsegregation of Mn can

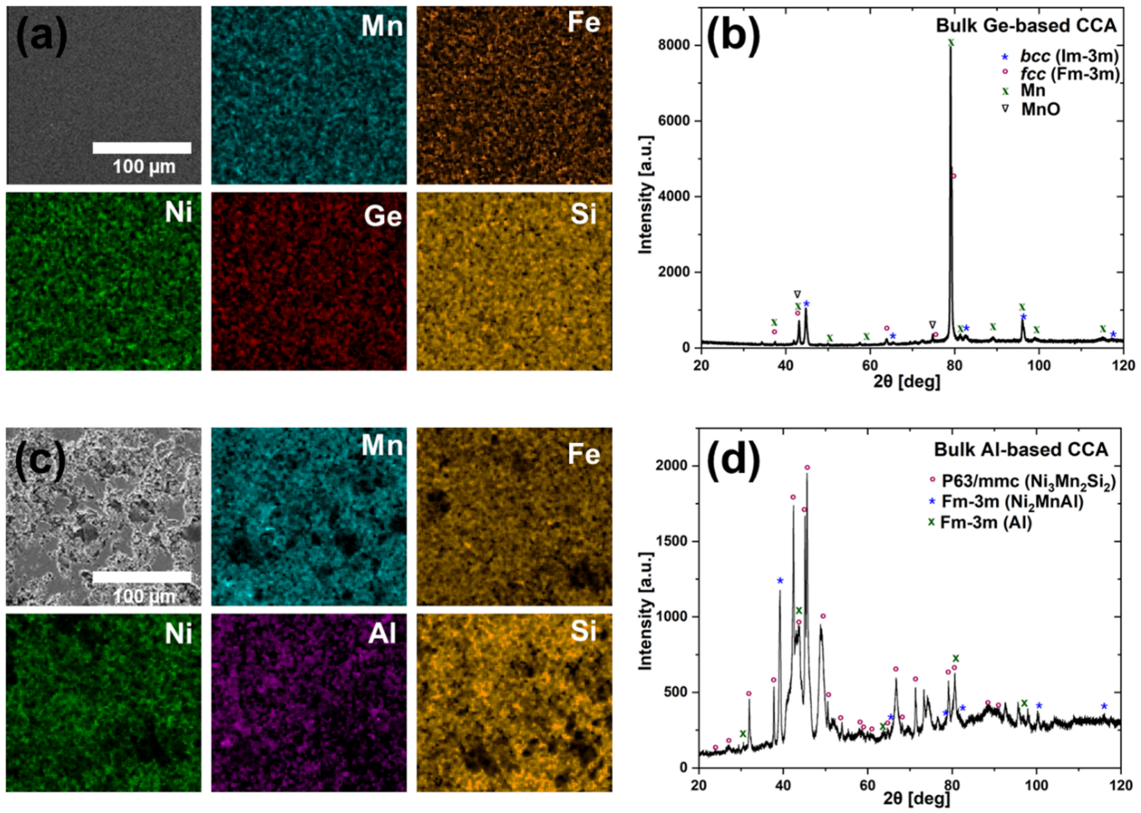

Figure 2: (a, c) SEM (SE) and EDX elemental maps of Mn, Fe, Ni, Ge, and Si obtained for bulk the Ge-based CCA and Mn, Fe, Ni, Al, and Si, obtained for bulk Ge-based CCA. (b, d) X-ray diffraction (XRD) patterns of the bulk Ge-based CCA and the bulk Al-based CCA, showing the presence of side phases.

Table 1: Comparison of the surface composition with the expected bulk composition, along with the percentage variance for both bulk Ge-based and Al-based CCAs.

Bulk Ge-based CCA				Bulk Al-based CCA			
	expected bulk composition (E) [atom %]	surface composition (S) [atom %]	percent variance = $\frac{\lvert E-S \rvert}{E} \times 100$ [%]		expected bulk composition [atom %]	surface composition [atom %]	percent variance = $\frac{\lvert E-S \rvert}{E} \times 100$ [%]
Mn	22.3	22.7 ± 0.9	1.8	Mn	16.67	20.8 ± 8.1	24.8
Fe	22.2	24.3 ± 0.7	9.5	Fe	16.67	17.5 ± 2.9	5.0
Ni	22.2	20.8 ± 0.8	6.3	Ni	33.3	31.2 ± 2.8	6.3
Ge	16.65	14.3 ± 0.5	14.1	Al	2.3	5.10 ± 0.6	121.7
Si	16.65	17.9 ± 1.8	7.5	Si	31.0	25.4 ± 2.3	18.1

be due to a phenomenon consistent with observations in other CCAs, often attributed to the elastic strain energy [58] or due to the presence of oxygen on the surface forming MnO [59].

As expected, the SEM images and EDX elemental mapping of the polished Al-based CCA surface (Figure 2b) show a more porous structure and inhomogeneous elemental distribution, with noticeable segregation. This results from a less effective mixing during the powder mixing process in the mortar, compared to the Ge-based CCA prepared by HEBM with subsequent consolidation by SPS. The lower sintering temperature and absence of pre-alloying limits the diffusion of the elements, leading to incomplete alloying. The composition exhibits a much larger percentage variance from the expected bulk composition compared to the Ge-based CCA. Al with its much lower latent heat of fusion (10.7 kJ·mol^{-1}) and melting point (933.5 K) compared to Ge, segregates easier, resulting in a significantly higher percentage variance (121.7%) for Al compared to other elements. However, it is important to note that the percentage variance is strongly influenced by the absolute elemental concentration; thus, even small absolute deviations at low concentrations can result in disproportionately high percentage variance. XRD analysis revealed the formation of multiphase alloys, with identifiable peaks corresponding to Al-deficient and Al-rich phases. The Al-deficient phase, Ni_2Mn_2Si, was found to have a hexagonal ($P6_3/mmc$) structure, while a cubic ($Fm{-}3m$) structure was observed in Ni_2MnAl and elemental Al. The hexagonal structure was also found in the Al-based CCA produced by Biswas and colleagues [24]. The elemental characterization by SEM/EDX from different surface positions (see Figure S2 and Table S2, Supporting Information File 1), further supports the formation of multielement phases. Nevertheless, the purpose of the produced target through this procedure is not to directly generate a bulk CCA, but to prepare in a fast, up-scalable, and economically feasible manner intermixed targets with the CCA components that can be later in-situ alloyed during PLAL to generate compositionally controlled CCA NPs.

CCA NP synthesis and characterization

Particle size distribution

The NPs synthesized by pulsed laser ablation in ethanol exhibit a log–normal particle size distribution ranging from 2 to 130 nm for both Ge- and Al-based CCAs (Figure 3). The polydispersity index (PDI) exceeds 0.3, indicating a polydisperse size distribution. This polydispersity is further supported by simulation studies by Shih et al. [60], where small NPs are formed following the phase explosion process, in which a superheated region of the target decomposes into vapor, small clusters, and droplets, and large particles result from photomechanical spallation, leading to the ejection of larger droplets. The average particle size of the Al alloy NPs ($x_c = 18.4 \pm 15.5$ nm) is larger than that of Ge-based CCA NPs ($x_c = 13.4 \pm 9.1$ nm). This difference can be attributed to variations in alloy composition and material properties, which influence the ablation plume dynamics and particle formation kinetics during PLAL. Specifically, the thermal properties, such as melting point and heat conductivity, and the volatility of the alloy components affect the balance between phase explosion and spallation mechanisms, ultimately leading to differences in particle size distribution.

Composition analysis

The EDX mapping of Ge-based CCA NPs shows that the particles contain all constituent elements of the target (Figure 4a). As shown in Table 2, the percentage variation of each element in the CCA NPs is higher than in the bulk alloy when compared to the expected composition, and the standard deviation between NPs is also greater than that of the bulk alloys.

This discrepancy is due to the different synthesis mechanisms of NPs and bulk alloys and the intrinsic difficulties associated

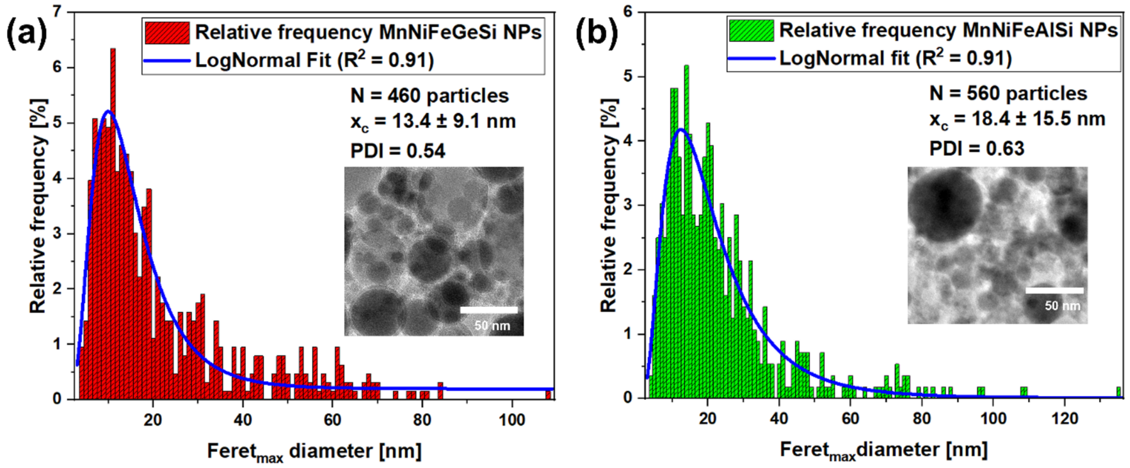

Figure 3: Particle size distribution extracted from TEM images (inset) from (a) bulk Ge-based CCA and (b) bulk Al-based CCA target.

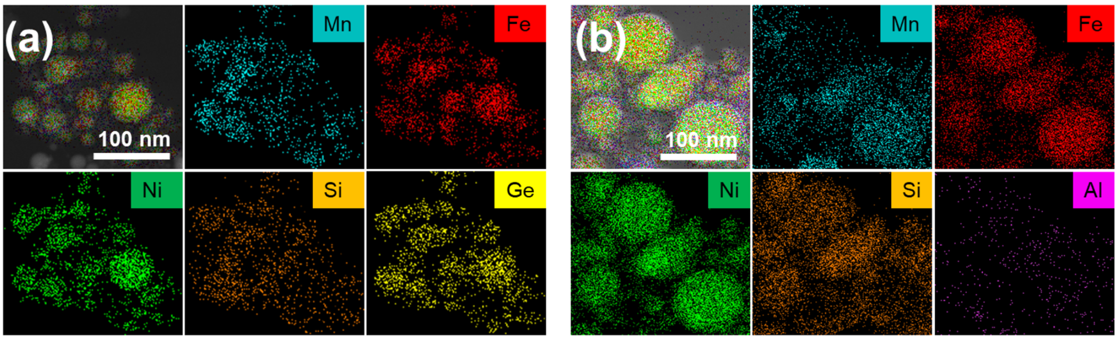

Figure 4: (a) Mn, Fe, Ni, Ge, and Si EDX elemental maps of the PLAL-generated CCA NPs from the bulk Ge-based CCA target. (b) Mn, Fe, Ni, Al, and Si EDX elemental maps of the PLAL generated CCA NPs from the Al-based CCA target.

Table 2: Comparison of the NP composition with the expected bulk composition, along with the percentage variance for both Ge-based and Al-based CCAs.

Ge-based CCA NPs				Al-based CCA NPs			
	expected NP composition (*E*) [atom %]	average NP composition (*N*) [atom %]	percent variance = $\frac{\lvert E-N \rvert}{E} \times 100$ [%]		expected NP composition (*E*) [atom %]	average NP composition (*N*) [atom %]	percent variance = $\frac{\lvert E-N \rvert}{E} \times 100$ [%]
Mn	22.3	15.3 ± 4.6	31.4	Mn	16.67	12.0 ± 1.8	28.0
Fe	22.2	21.6 ± 3.9	2.7	Fe	16.67	18.3 ± 0.3	9.8
Ni	22.2	25.4 ± 4.1	14.4	Ni	33.3	35.3 ± 4.1	6.0
Ge	16.65	19.8 ± 1.9	18.9	Al	2.3	1.30 ± 0.4	43.5
Si	16.65	17.8 ± 2.1	6.9	Si	31	33.0 ± 5.0	6.5

with the synthesis of CCA NPs. Beyond the elemental composition of the bulk target, the PLAL NP composition depends on the volatility and ionization potential of each element. Hence, the laser ablation of multicomponent targets has an impact on NP stoichiometry, since the more volatile components evaporate more efficiently. The greatest deviation was observed for Mn, with a variance of 31.4% below the expected composition, compared to just 1.8% variance in the bulk Ge-based CCA. This was also observed in our previous work [41] on Cantor alloy NPs synthesized via PLAL, where separate Mn-rich clusters formed due to elemental evaporation during synthesis. Additionally, the ionization potential influences the ablation plume dynamics. Notably, the Ge variation from the expected composition is lower than for Mn, contrasting with the bulk alloy's surface composition. This can be attributed to Mn's lower ionization potential (7.34 eV) compared to Ge (7.90 eV). Furthermore, HRTEM imaging (Figure S3a, Supporting Information File 1) reveals the formation of a ≈2.5 nm thick oxide shell surrounding the NPs. A line scan analysis (Figure S3b, Supporting Information File 1) confirms an elevated oxygen concentration at the NP surface, indicating surface oxidation effects. Most oxide shells, such as MnO, NiO, or FeO are antiferromagnetic [61] and exhibit higher anisotropy than the NP core, leading to an exchange bias effect in the hysteresis loop and an increase in coercivity [62].

EDX mapping of the Al-based CCA NPs (Figure 4b) confirms that all constituent elements from the target material are present within the particles. Table 2 shows the NP composition deviation from the bulk target. The largest percentage variation in composition was found to be in Al content, which is 43.5% lower than the expected composition. This can also be due to the lower melting point of Al and lower ionization potential of 5.99 eV compared to the other elements of the alloy. Mn content in the CCA NP is lower by 28.0% than the expected value, as described earlier for the Ge-based CCA. However, unlike the Ge-based CCA NPs, no visible core–shell structure was detected around the Al-based NPs, and oxygen intensity was significantly lower in line scan analyses (Figure S4, Supporting Information File 1). This suggests that surface oxidation effects were less pronounced, potentially because of differences in particle formation dynamics or the protective role of other alloying elements.

Structural characterization of the CCA NPs

Figure 5a and Figure 5b show HRTEM bright-field images of the Ge-based CCA NPs and Al-based CCA NPs. The insets reveal the crystallographic structure of the NPs and their corresponding diffractograms. The observed contrast variations (with light and dark areas marked in red and green, respectively) indicate differences in elemental distribution, suggesting the presence of distinct phases and crystalline defects, such as twin boundaries and inhomogeneous stacking of multiple elements (marked with blue and purple arrows, respectively). The line scan of one of the NPs further illustrates deviations in elemental concentration as shown in Figure S3b and Figure S4, Supporting Information File 1. This phenomenon is attributed to the nonequilibrium nature of PLAL, where each laser pulse, occurring on a picosecond timescale, rapidly quenches non-equilibrium phases or highly defective structures [63].

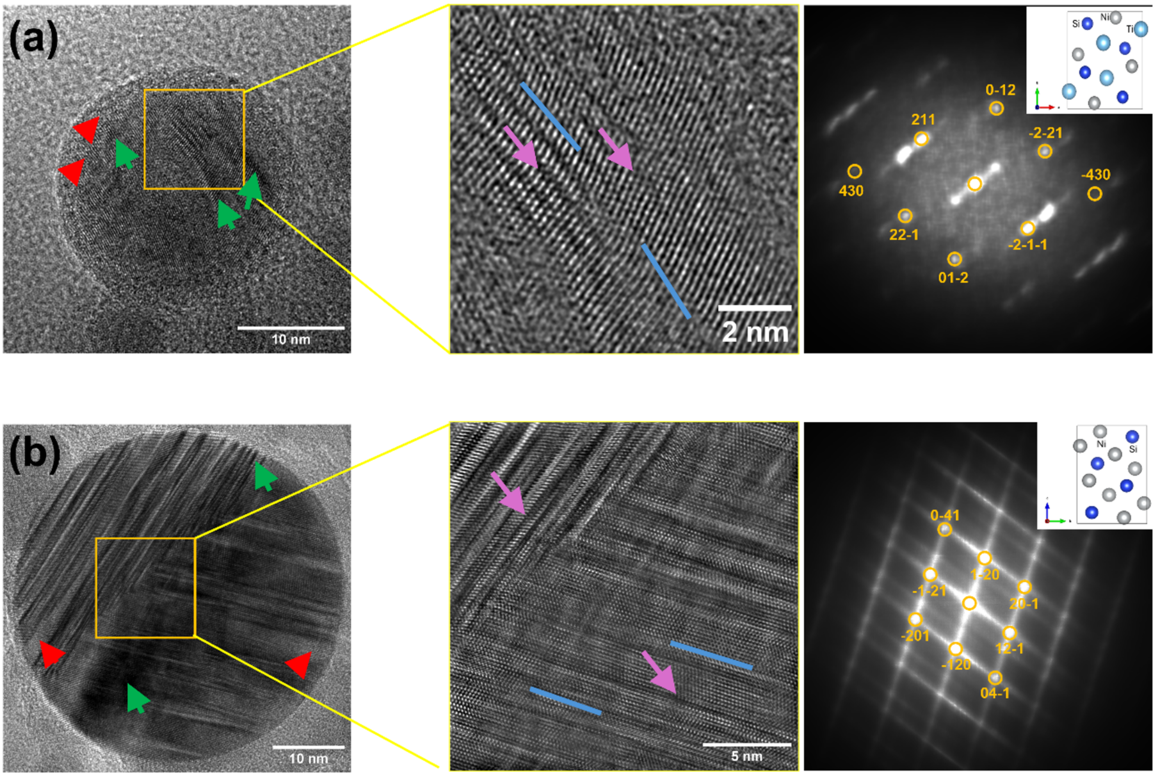

Figure 5: High-resolution TEM images and diffractograms of PLAL-generated CCA NPs. (a) Ge-based CCA NP and (b) Al-based CCA NP.

The Ge-based CCA NP diffractogram shows a distribution of diffraction peaks corresponding to an orthorhombic NiSiTi-type crystal structure, with lattice parameters a = 0.58492 nm, b = 0.70136 nm, and c = 0.40149 nm. A previous work by Law et al. using a bulk Ge-based CCA [25] suggested that the orthorhombic crystal structure transforms fully to a hexagonal structure below 190 K. However, the PLAL-synthesized Ge-based CCA NPs do not show a hexagonal structure but remain orthorhombic at room temperature. Additionally, the FCC crystal structure observed in the bulk Ge-based CCA target is not observed.

For the Al-based CCA NPs, the diffractogram reveals numerous bright spots corresponding to an orthorhombic NiSi-type crystal structure with lattice parameters a = 0.36062 nm, b = 0.51256 nm, and c = 0.73241 nm. This aligns with the findings of Biswas et al. [24], where the orthorhombic phase predominates at room temperature for lower Al contents. However, in our XRD analysis of the synthesized bulk Al-based CCA, the orthorhombic crystal structure was not observed. This discrepancy suggests that PLAL influences the resulting crystal structure, paving the way to control the material phase by modifying the laser synthesis conditions such as pulse duration, intensity, or solvent, which would drastically affect temperature, pressure, and cooling rate conditions during NP synthesis [64].

Magnetic properties of the bulk and nanoscale CCAs

Bulk CCAs

The Ge-based bulk CCA shows an abrupt magnetic phase transition, with the zero-field cooled (ZFC) and field cooled (FC) curves starting to diverge around 179 K (Figure 6a), indicating a shift from a paramagnetic to a ferromagnetic state. This transition temperature differs from previous reports that suggested a

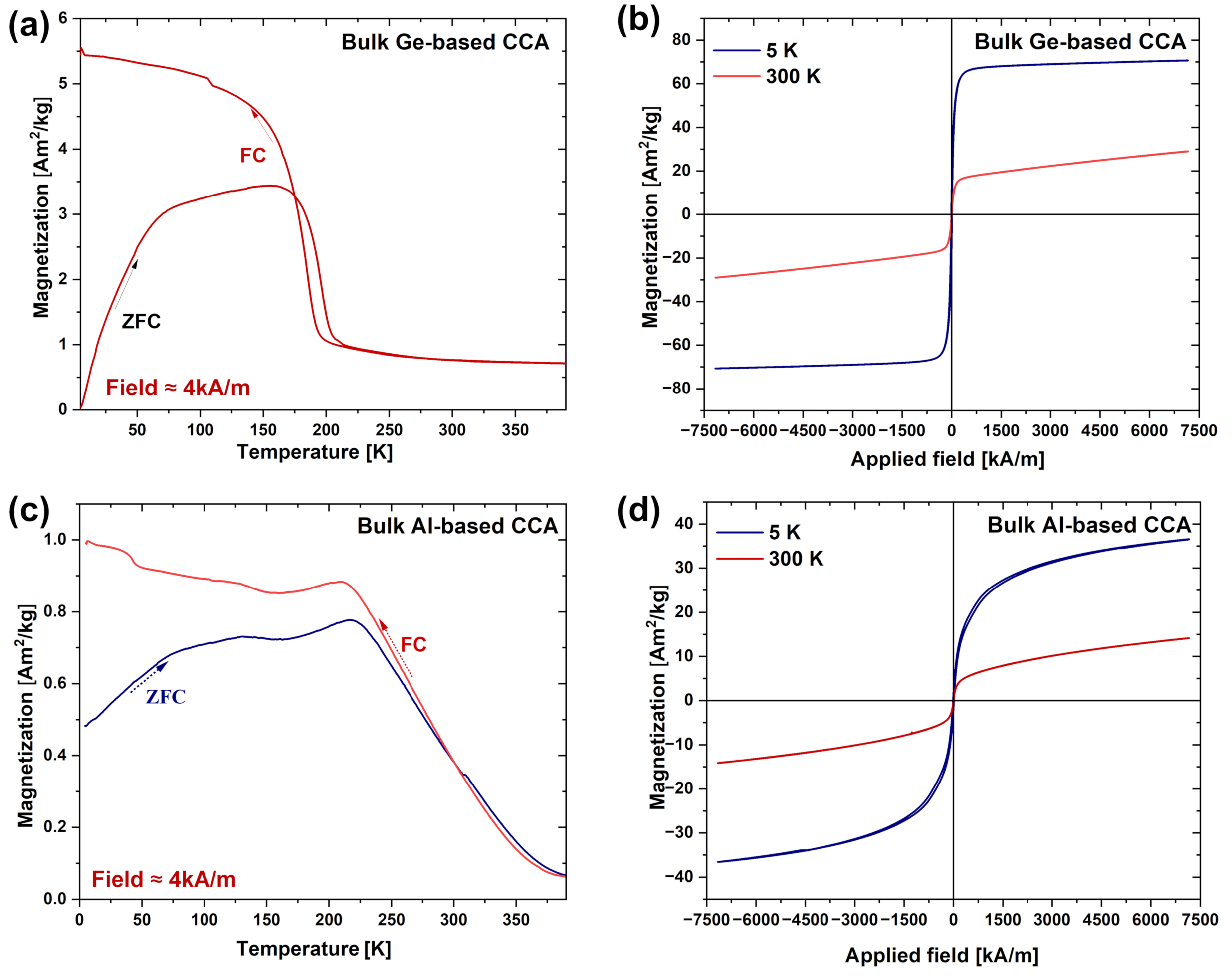

Figure 6: (a) ZFC-FC temperature-dependent magnetization (*M*–*T* curve) of the bulk Ge-based CCA. (b) Field-dependent magnetization curve at 5 and 300 K for the Ge-based CCA. (c) ZFC-FC temperature-dependent magnetization (*M*–*T* curve) of the bulk Al-based CCA. (d) Field-dependent magnetization curve at 5 and 300 K for the Al-based CCA.

transition above 170 K. Unlike earlier studies, no metamagnetic transition occurs between 125 and 170 K; instead, the magnetization decreases gradually even under a low field (4kA/m). It is noteworthy that varying the target preparation technique alters the magnetic properties of the material significantly. This is probably related to the low cooling rates employed during SPS (compared to arc melting in a previous study [25]), which result in a different crystal structure and modify the magnetic properties. At temperatures below 179 K, the FC curve shows higher magnetization than the ZFC curve, indicating that spin alignment occurs faster when cooled in the presence of a magnetic field because of the pre-alignment that the magnetic field produces. Above 179 K, the ZFC and FC curves converge, suggesting that thermal energy disrupts magnetic ordering, leading to the appearance of a peak at around 179 K in the dM/dT–T curve (Figure S5a, Supporting Information File 1), which corresponds to the phase transition temperature, accompanied by a sharp drop in the derivative, indicating a second-order phase transition. This type of transition suggests that the magnetization changes smoothly across the transition point, consistent with ferromagnetic or ferrimagnetic ordering.

The M–H curve at 5 K (Figure 6b and Figure S5b, Supporting Information File 1) exhibits a pronounced hysteresis loop with a H_c of 8.4 kA·m^{-1} and a high saturation magnetization M_s (5 K, 9 T) of 68.2 A·m^2·kg^{-1}, indicating strong ferromagnetic properties (Table 3). At 300 K, the loop becomes narrower, and H_c drops significantly to 1.2 kA·m^{-1}, while M_s decreases to 18 A·m^2·kg^{-1}. This behavior suggests that the material becomes easier to demagnetize, which is generally good for magnetocaloric cycles. However, the demagnetization comes with a weakened ferromagnetic interaction, likely due to increased thermal agitation at higher temperatures.

The Al-based CCA ZFC and FC curves diverge significantly near 263 K (Figure 6c and Figure S5c, Supporting Information File 1). The higher transition temperature compared to the Ge-based CCA implies stronger magnetic interactions in the Al-based CCA, which are able to persist even at higher temperatures. The broader dip in the dM/dT–T curve, compared to the sharper drop seen in the Ge-based CCA, suggests that the magnetic ordering in the Al-based CCA is more gradual, possibly because of different multiple phases and microstructures. However, the low-temperature magnetization of the Al-based CCA (≈1 A·m^2·kg^{-1}) is much lower than that of the Ge-based CCA (≈5 A·m^2·kg^{-1}), indicating that antiferromagnetic correlations may become important in the Al-based alloy at low temperatures.

The M–H curves for the Al-based CCA (Figure 6d and Figure S5d, Supporting Information File 1) shows a higher H_c at 5 K (11 kA·m^{-1}) than that observed for the Ge-based CCA (8.4 kA·m^{-1}). The M_s (5 K, 9 T) reaches 32.7 A·m^2·kg^{-1}, which, although significant, is still lower than the 68.2 A·m^2·kg^{-1} observed for the Ge-based CCA. As the temperature increases to 300 K, the Al-based CCA exhibits a marked decrease in both H_c (down to 1 kA·m^{-1}) and M_s (9.5 A·m^2·kg^{-1}).

CCA NPs

The M–T curve (Figure 7a) for the Ge-based CCA NPs exhibits a distinct ZFC-FC behavior differing from that of the bulk material. The magnetization increases with temperature, reaching a peak at 100 K, corresponding to the superparamagnetic blocking temperature (T_B). Unlike the bulk CCA, which undergoes an apparent magnetic phase transition at T_c = 179 K, the NPs experience a superparamagnetic-to-paramagnetic transition at 204 K (Figure S6a, Supporting Information File 1).

The magnetization M (5 K, 50 mT) for the NPs (≈1.2 A·m^2·kg^{-1}) is lower than that of the bulk (≈5 A·m^2·kg^{-1}) mainly because of the blocking temperature effect. Below T_B, the thermal energy is sufficient to cause flipping of magnetic moments, reducing the measured magnetization at low fields compared to the bulk, where the moments remain fully aligned. Additionally, the formation of an oxide shell (≈2.5 nm thick) on Ge-based NPs further contributes to a decrease in M_s by reducing the magnetically active volume.

At 5 K, the M–H curve displays a significant hysteresis loop with a H_c of 26.2 kA·m^{-1}, which is higher than that of the bulk Ge-based CCA (8.4 kA·m^{-1}) (Figure 7b, Table 4, and Figure S6b, Supporting Information File 1). At 300 K, H_c drops to 0.7 kA·m^{-1}, and M_s (300 K, 9 T) decreases to 6.6 A·m^2·kg^{-1}, indicating that the thermal energy at room temperature is suffi-

Table 3: Comparison of magnetic phase transition temperature (T_c), saturation magnetization (M_s), and coercivity (H_c) at 5 and 300 K for bulk Ge-based and Al-based CCAs.

	T_c [K]	M_s (5 K) [A·m^2·kg^{-1}]	M_s (300 K) [A·m^2·kg^{-1}]	H_c (5 K) [kA·m^{-1}]	H_c (300 K) [kA·m^{-1}]
bulk Ge-based CCA	179	68.2	18	8.4	1.2
bulk Al-based CCA	263	32.7	9.5	11	1

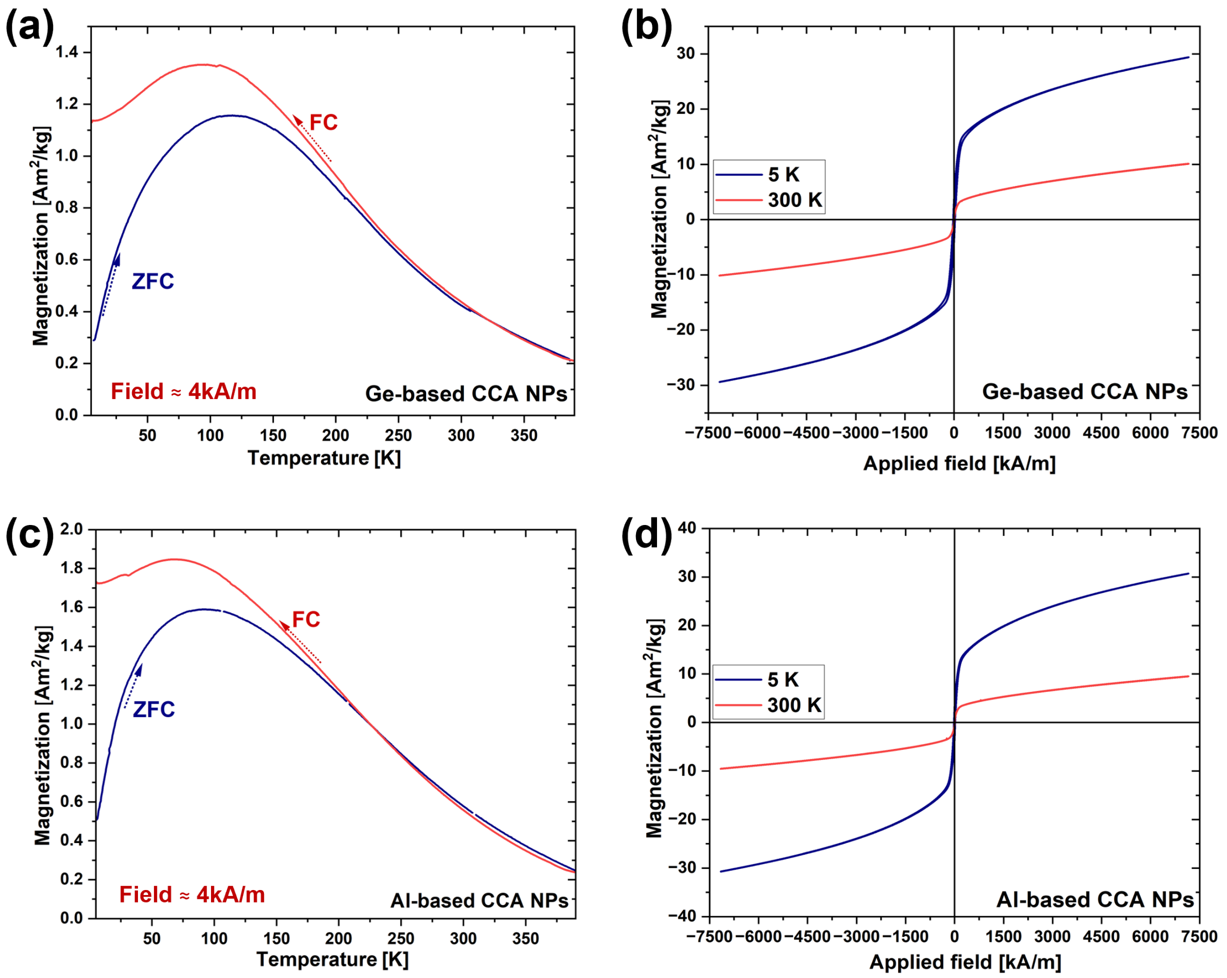

Figure 7: (a) ZFC-FC temperature-dependent magnetization (*M–T*) curves of NPs generated from PLAL of the Ge-based CCA target. (b) Field-dependent magnetization curves (*M–H*) curves of NPs generated from PLAL of the Ge-based CCA target at 5 and 300 K. (c) ZFC-FC temperature-dependent magnetization (*M–T* curve) for NPs generated from PLAL of the Al-based CCA target. (d) Field-dependent magnetization curves (*M–H*) curves of NPs generated from PLAL of the Al-based CCA target at 5 and 300 K.

cient to overcome the magnetic anisotropy. The value of M_s (5 K, 9 T) for the bulk material (68.2 A·m^2·kg^{-1}) is much higher than that of the NPs (25.1 A·m^2·kg^{-1}). This reduction in M_s in the NPs can be attributed to the inhomogeneity of the NPs and the formation of oxide shells. At 300 K, H_c drops to 0.7 kA·m^{-1}, and M_s decreases to 6.6 A·m^2·kg^{-1}, indicating that the thermal energy at room temperature is sufficient to overcome the magnetic anisotropy, leading to a weaker magnetic response. The larger drop in M_s and H_c in the NPs with increasing temperature reflects the greater impact of thermal fluctuations on nanoscale materials.

The magnetic response of the Al-based CCA NPs exhibited a behavior (Figure 7c,d) similar to that of the Ge-based CCA NPs. The magnetization increases with temperature, reaching a peak at superparamagnetic blocking temperature of around 100 K and then decreases, indicating a superparamagnetic-to-paramagnetic transition. A divergence between ZFC and FC curves is observed below 202 K (Figure S6c, Supporting Information File 1), suggesting spin freezing or magnetic domain alignment when the material is cooled in the presence of a magnetic field.

The *M–H* curve (Figure 7d and Figure S6d, Supporting Information File 1) of the Al-based CCA at 5 K shows significant hysteresis, with a H_c of 16.6 kA·m^{-1}, which is higher than that of the bulk Al-based CCA (11 kA·m^{-1}). The increase in H_c in the NPs is likely due to enhanced surface anisotropy effects that arise from the smaller particle size. However, M_s (300 K, 9 T) and M_s (5 K, 9 T) of the Al-based CCA NPs are comparable, while a lower H_c is exhibited at low temperature (5 K) compared to Ge-based CCA NPs (Table 4). This decrease in H_c can be attributed to absence of oxide shell formation and the difference in composition and crystal structure.

Table 4: Comparison of saturation magnetization (M_s) and coercivity (H_c) at 5 and 300 K for Ge-based and Al-based CCAs NPs.

	M_s (5 K) [A·m^2·kg^{-1}]	M_s (300 K) [A·m^2·kg^{-1}]	H_c (5 K) [kA·m^{-1}]	H_c (300 K) [kA·m^{-1}]
Ge-based CCA NPs	25.1	6.6	26.2	0.7
Al-based CCA NPs	25.9	6.8	16.6	1.1

Conclusion

We present rare-earth-free Ge-based and Al-based CCAs as promising candidates for low-temperature magnetic applications. In the bulk state, the Ge-based CCA exhibits a T_c of 179 K, while the Al-based CCA has a higher T_c of 263 K. The Ge-based CCA exhibits almost twice the M_s and a ≈20% lower H_c than the Al-based CCA at 5 and 300 K.

At the nanoscale, both CCAs exhibit superparamagnetic behavior with T_B of 120 K for Ge-based NPs (x_c = 13.4 ± 9.1 nm) and 100 K for Al-based NPs (x_c = 18.4 ± 15.1 nm). While the Ge-based NPs maintain a higher M_s, the Al-based NPs exhibit a comparable M_s and an approximately 45% lower H_c at low temperature (5 K). This reduction in coercivity makes the Al-based CCA NPs particularly attractive for applications requiring soft magnetic materials with enhanced magnetocaloric performance and lower hysteretic losses at low temperatures.

Beyond their magnetic properties, Al-based CCAs offer notable economic and material availability advantages. As Al is significantly more cost-effective and abundant than Ge, Al-based CCAs present a scalable and sustainable alternative for rare-earth-free magnetic materials. This substitution is particularly relevant for future advancements in magnetocaloric refrigeration, sensors, and other energy-efficient technologies.

Supporting Information

Supporting Information File 1

Additional experimental data.
[https://www.beilstein-journals.org/bjnano/content/supplementary/2190-4286-16-62-S1.pdf]

Acknowledgements

We thank Tobias Bochmann for his help with the SEM imaging and EDX mapping of the Ge- and Al-based CCA targets. We also thank Dr. Alex Aubert for his help performing SPS at Functional Materials in TU Darmstadt.

Funding

The authors gratefully acknowledge the funding by the German Research Foundation (DFG) within the Collaborative Research Centre/Transregio (CRC/TRR) 270 (Project-ID 405553726, projects (B08, A04 and Z02). We further thank the DFG for funding of the projects GO 2566/10-1 and GO 2566/14-1. Carlos Doñate Buendia thanks Generalitat Valenciana for funding of the project CIDEIG/2023/08 within Gen-T programme.

Conflict of Interest

The authors declare no conflicts of interest.

Author Contributions

Shabbir Tahir: formal analysis; investigation; methodology; writing – original draft. Tatiana Smoliarova: investigation; visualization; writing – review & editing. Carlos Doñate-Buendía: conceptualization; supervision; validation; writing – review & editing. Michael Farle: formal analysis; resources; writing – review & editing. Natalia Shkodich: formal analysis; investigation; resources; software; visualization; writing – review & editing. Bilal Gökce: conceptualization; funding acquisition; supervision; writing – review & editing.

ORCID® iDs

Shabbir Tahir - https://orcid.org/0000-0001-6757-7785
Tatiana Smoliarova - https://orcid.org/0000-0002-0123-1965
Carlos Doñate-Buendía - https://orcid.org/0000-0002-7022-0960
Michael Farle - https://orcid.org/0000-0002-1864-3261
Natalia Shkodich - https://orcid.org/0000-0001-8883-340X
Bilal Gökce - https://orcid.org/0000-0001-6368-9659

Data Availability Statement

Data generated and analyzed during this study is available from the corresponding author upon reasonable request.

References

1. Rajaram, M. Depth To Curie Temperature. In *Encyclopedia of Geomagnetism and Paleomagnetism;* Gubbins, D.; Herrero-Bervera, E., Eds.; Springer: Dordrecht, Netherlands, 2007; pp 157–159. doi:10.1007/978-1-4020-4423-6_66
2. Fortunato, N. M.; Taubel, A.; Marmodoro, A.; Pfeuffer, L.; Ophale, I.; Ebert, H.; Gutfleisch, O.; Zhang, H. *Adv. Sci.* **2023,** *10,* 2206772. doi:10.1002/advs.202206772
3. Liu, W.; Gottschall, T.; Scheibel, F.; Bykov, E.; Fortunato, N.; Aubert, A.; Zhang, H.; Skokov, K.; Gutfleisch, O. *JPhys Energy* **2023,** *5,* 034001. doi:10.1088/2515-7655/accb0b

4. Jiang, J.; Xie, H.; Yu, K.; Li, Z.; Shen, J.; Mo, Z. *Ceram. Int.* **2024,** *50,* 19749–19756. doi:10.1016/j.ceramint.2024.03.098
5. Skokov, K. P.; Karpenkov, A. Y.; Karpenkov, D. Y.; Radulov, I. A.; Günzing, D.; Eggert, B.; Rogalev, A.; Wilhelm, F.; Liu, J.; Shao, Y.; Ollefs, K.; Gruner, M. E.; Wende, H.; Gutfleisch, O. *Appl. Phys. Rev.* **2023,** *10,* 031408. doi:10.1063/5.0133411
6. Tang, Y.; Li, M.; Wang, T.; Dong, X.; Hu, W.; Sitti, M. *Adv. Mater. (Weinheim, Ger.)* **2022,** *34,* 2204185. doi:10.1002/adma.202204185
7. Yan, J.; Shi, K.; Deng, S.; Zhao, W.; Lu, H.; Sun, Y.; Chen, Y.; Wang, C. *Solid State Commun.* **2018,** *282,* 33–37. doi:10.1016/j.ssc.2018.07.012
8. Liang, Y.; Deng, Q.; Tan, X. H.; Li, H.; Xu, H. *Sci. Rep.* **2019,** *9,* 1758. doi:10.1038/s41598-018-36583-x
9. Mandziak, A.; Soria, G. D.; Prieto, J. E.; Prieto, P.; Granados-Miralles, C.; Quesada, A.; Foerster, M.; Aballe, L.; de la Figuera, J. *Sci. Rep.* **2019,** *9,* 13584. doi:10.1038/s41598-019-49642-8
10. Zhou, X.; Li, W.; Kunkel, H. P.; Williams, G. *J. Magn. Magn. Mater.* **2005,** *293,* 854–862. doi:10.1016/j.jmmm.2004.12.004
11. Sun, Z.; Shi, C.; Gao, L.; Lin, S.; Li, W. *J. Alloys Compd.* **2022,** *901,* 163554. doi:10.1016/j.jallcom.2021.163554
12. Martins, R.; Gonçalves, A. P.; Correia, J. B.; Galatanu, A.; Alves, E.; Tejado, E.; Pastor, J. Y.; Dias, M. *Metals (Basel, Switz.)* **2024,** *14,* 436. doi:10.3390/met14040436
13. Kumari, P.; Gupta, A. K.; Mishra, R. K.; Ahmad, M. S.; Shahi, R. R. *J. Magn. Magn. Mater.* **2022,** *554,* 169142. doi:10.1016/j.jmmm.2022.169142
14. Huang, E.-W.; Hung, G.-Y.; Lee, S. Y.; Jain, J.; Chang, K.-P.; Chou, J. J.; Yang, W.-C.; Liaw, P. K. *Crystals* **2020,** *10,* 200. doi:10.3390/cryst10030200
15. Chou, H.-P.; Chang, Y.-S.; Chen, S.-K.; Yeh, J.-W. *Mater. Sci. Eng., B* **2009,** *163,* 184–189. doi:10.1016/j.mseb.2009.05.024
16. Kim, H.; Nam, S.; Roh, A.; Son, M.; Ham, M.-H.; Kim, J.-H.; Choi, H. *Int. J. Refract. Met. Hard Mater.* **2019,** *80,* 286–291. doi:10.1016/j.ijrmhm.2019.02.005
17. Tang, N.; Quigley, L.; Boldman, W. L.; Jorgensen, C. S.; Koch, R.; O'Leary, D.; Medal, H. R.; Rack, P. D.; Gilbert, D. A. *Phys. Rev. Mater.* **2021,** *5,* 114405. doi:10.1103/physrevmaterials.5.114405
18. Sarlar, K.; Tekgül, A.; Kucuk, I. *IEEE Magn. Lett.* **2019,** *10,* 2109905. doi:10.1109/lmag.2019.2955667
19. Gutfleisch, O.; Willard, M. A.; Brück, E.; Chen, C. H.; Sankar, S. G.; Liu, J. P. *Adv. Mater. (Weinheim, Ger.)* **2011,** *23,* 821–842. doi:10.1002/adma.201002180
20. Cui, J.; Kramer, M.; Zhou, L.; Liu, F.; Gabay, A.; Hadjipanayis, G.; Balasubramanian, B.; Sellmyer, D. *Acta Mater.* **2018,** *158,* 118–137. doi:10.1016/j.actamat.2018.07.049
21. Zapp, P.; Schreiber, A.; Marx, J.; Kuckshinrichs, W. *MRS Bull.* **2022,** *47,* 267–275. doi:10.1557/s43577-022-00286-6
22. Kanomata, T.; Ishigaki, H.; Suzuki, T.; Yoshida, H.; Abe, S.; Kaneko, T. *J. Magn. Magn. Mater.* **1995,** *140–144,* 131–132. doi:10.1016/0304-8853(94)00833-7
23. Liu, J.; Gong, Y.; Xu, G.; Peng, G.; Shah, I. A.; ul Hassan, N.; Xu, F. *Sci. Rep.* **2016,** *6,* 23386. doi:10.1038/srep23386
24. Biswas, A.; Pathak, A. K.; Zarkevich, N. A.; Liu, X.; Mudryk, Y.; Balema, V.; Johnson, D. D.; Pecharsky, V. K. *Acta Mater.* **2019,** *180,* 341–348. doi:10.1016/j.actamat.2019.09.023
25. Law, J. Y.; Moreno-Ramírez, L. M.; Díaz-García, Á.; Martín-Cid, A.; Kobayashi, S.; Kawaguchi, S.; Nakamura, T.; Franco, V. *J. Alloys Compd.* **2021,** *855,* 157424. doi:10.1016/j.jallcom.2020.157424
26. Shah, S.; Xu, M.; Pan, X.; Gilliard-AbdulAziz, K. L. *ACS Appl. Nano Mater.* **2022,** *5,* 17476–17481. doi:10.1021/acsanm.2c03857
27. Zhang, Q.; Lian, K.; Liu, Q.; Qi, G.; Zhang, S.; Luo, J.; Liu, X. *J. Colloid Interface Sci.* **2023,** *646,* 844–854. doi:10.1016/j.jcis.2023.05.074
28. Modupeola, D.; Popoola, P. *Front. Energy Res.* **2023,** *11,* 1149446. doi:10.3389/fenrg.2023.1149446
29. Mu, Y. K.; Jia, Y. D.; Xu, L.; Jia, Y. F.; Tan, X. H.; Yi, J.; Wang, G.; Liaw, P. K. *Mater. Res. Lett.* **2019,** *7,* 312–319. doi:10.1080/21663831.2019.1604443
30. Miao, L.-Z.; Guo, Y.-X.; Liu, Z.-Y.; Li, Y.; Zhu, J.; Wu, L. *Chem. Eng. J.* **2023,** *467,* 143451. doi:10.1016/j.cej.2023.143451
31. Wang, F.; Feng, X.; Gao, Y.; Ding, X.; Wang, W.; Zhang, J. *ACS Omega* **2023,** *8,* 47773–47780. doi:10.1021/acsomega.3c06122
32. Jiang, D.; Yuan, Z.; Zhu, Z.; Yao, M. *Materials* **2024,** *17,* 534. doi:10.3390/ma17020534
33. Kumar, S.; Kumar, M. *Trans. Indian Natl. Acad. Eng.* **2024,** *9,* 679–687. doi:10.1007/s41403-023-00447-2
34. Pucci, C.; Degl'Innocenti, A.; Belenli Gümüş, M.; Ciofani, G. *Biomater. Sci.* **2022,** *10,* 2103–2121. doi:10.1039/d1bm01963e
35. Zhang, X.; Cranford, S. *Matter* **2020,** *3,* 1391–1393. doi:10.1016/j.matt.2020.10.013
36. Liu, Y.; Tian, X.; Han, Y.-C.; Chen, Y.; Hu, W. *Chin. J. Catal.* **2023,** *48,* 66–89. doi:10.1016/s1872-2067(23)64428-6
37. Yao, Y.; Huang, Z.; Xie, P.; Lacey, S. D.; Jacob, R. J.; Xie, H.; Chen, F.; Nie, A.; Pu, T.; Rehwoldt, M.; Yu, D.; Zachariah, M. R.; Wang, C.; Shahbazian-Yassar, R.; Li, J.; Hu, L. *Science* **2018,** *359,* 1489–1494. doi:10.1126/science.aan5412
38. Guo, H.; Guo, Z.; Chu, K.; Zong, W.; Zhu, H.; Zhang, L.; Liu, C.; Liu, T.; Hofkens, J.; Lai, F. *Adv. Funct. Mater.* **2023,** *33,* 2308229. doi:10.1002/adfm.202308229
39. Wang, B.; Wang, C.; Yu, X.; Cao, Y.; Gao, L.; Wu, C.; Yao, Y.; Lin, Z.; Zou, Z. *Nat. Synth.* **2022,** *1,* 138–146. doi:10.1038/s44160-021-00004-1
40. Cui, M.; Yang, C.; Hwang, S.; Yang, M.; Overa, S.; Dong, Q.; Yao, Y.; Brozena, A. H.; Cullen, D. A.; Chi, M.; Blum, T. F.; Morris, D.; Finfrock, Z.; Wang, X.; Zhang, P.; Goncharov, V. G.; Guo, X.; Luo, J.; Mo, Y.; Jiao, F.; Hu, L. *Sci. Adv.* **2022,** *8,* eabm4322. doi:10.1126/sciadv.abm4322
41. Tahir, S.; Shkodich, N.; Eggert, B.; Lill, J.; Gatsa, O.; Flimelová, M.; Adabifiroozjaei, E.; Bulgakova, N. M.; Molina-Luna, L.; Wende, H.; Farle, M.; Bulgakov, A. V.; Doñate-Buendía, C.; Gökce, B. *ChemNanoMat* **2024,** *10,* e202400064. doi:10.1002/cnma.202400064
42. Waag, F.; Li, Y.; Ziefuß, A. R.; Bertin, E.; Kamp, M.; Duppel, V.; Marzun, G.; Kienle, L.; Barcikowski, S.; Gökce, B. *RSC Adv.* **2019,** *9,* 18547–18558. doi:10.1039/c9ra03254a
43. Johny, J.; Li, Y.; Kamp, M.; Prymak, O.; Liang, S.-X.; Krekeler, T.; Ritter, M.; Kienle, L.; Rehbock, C.; Barcikowski, S.; Reichenberger, S. *Nano Res.* **2022,** *15,* 4807–4819. doi:10.1007/s12274-021-3804-2
44. Fazio, E.; Gökce, B.; De Giacomo, A.; Meneghetti, M.; Compagnini, G.; Tommasini, M.; Waag, F.; Lucotti, A.; Zanchi, C. G.; Ossi, P. M.; Dell'Aglio, M.; D'Urso, L.; Condorelli, M.; Scardaci, V.; Biscaglia, F.; Litti, L.; Gobbo, M.; Gallo, G.; Santoro, M.; Trusso, S.; Neri, F. *Nanomaterials* **2020,** *10,* 2317. doi:10.3390/nano10112317

45. Zhang, D.; Gökce, B.; Barcikowski, S. *Chem. Rev.* **2017,** *117,* 3990–4103. doi:10.1021/acs.chemrev.6b00468
46. Khairani, I. Y.; Spellauge, M.; Riahi, F.; Huber, H. P.; Gökce, B.; Doñate-Buendía, C. *Adv. Photonics Res.* **2024,** *5,* 2300290. doi:10.1002/adpr.202300290
47. Gökce, B.; Amendola, V.; Barcikowski, S. *ChemPhysChem* **2017,** *18,* 983–985. doi:10.1002/cphc.201700310
48. Khairani, I. Y.; Mínguez-Vega, G.; Doñate-Buendía, C.; Gökce, B. *Phys. Chem. Chem. Phys.* **2023,** *25,* 19380–19408. doi:10.1039/d3cp01214j
49. Gatsa, O.; Tahir, S.; Flimelová, M.; Riahi, F.; Doñate-Buendia, C.; Gökce, B.; Bulgakov, A. V. *Nanomaterials* **2024,** *14,* 365. doi:10.3390/nano14040365
50. Löffler, T.; Waag, F.; Gökce, B.; Ludwig, A.; Barcikowski, S.; Schuhmann, W. *ACS Catal.* **2021,** *11,* 1014–1023. doi:10.1021/acscatal.0c03313
51. Ramasamy, R. P.; Hurd, A. J. *MRS Energy Sustainability* **2021,** *8,* 16–32. doi:10.1557/s43581-020-00001-5
52. Kaegi, R.; Fierz, M.; Hattendorf, B. *Microsc. Microanal.* **2021,** *27,* 557–565. doi:10.1017/s1431927621000398
53. Klinger, M. *J. Appl. Crystallogr.* **2017,** *50,* 1226–1234. doi:10.1107/s1600576717006793
54. Tiwari, G. P.; Mehrotra, R. S. *Defect Diffus. Forum* **2008,** *279,* 23–37. doi:10.4028/www.scientific.net/ddf.279.23
55. Nagase, T.; Mizuuchi, K.; Nakano, T. *Entropy* **2019,** *21,* 483. doi:10.3390/e21050483
56. Saxena, A.; Sanati, M.; Albers, R. C. *Mater. Sci. Eng., A* **1999,** *273–275,* 226–230. doi:10.1016/s0921-5093(99)00376-7
57. Zhang, F.; Reich, M.; Kessler, O.; Burkel, E. *Mater. Today* **2013,** *16,* 192–197. doi:10.1016/j.mattod.2013.05.005
58. Maldonado, A. J.; Misra, K. P.; Misra, R. D. K. *Mater. Technol. (Abingdon, U. K.)* **2023,** *38,* 2221959. doi:10.1080/10667857.2023.2221959
59. Ferrari, A.; Körmann, F. *Appl. Surf. Sci.* **2020,** *533,* 147471. doi:10.1016/j.apsusc.2020.147471
60. Shih, C.-Y.; Streubel, R.; Heberle, J.; Letzel, A.; Shugaev, M. V.; Wu, C.; Schmidt, M.; Gökce, B.; Barcikowski, S.; Zhigilei, L. V. *Nanoscale* **2018,** *10,* 6900–6910. doi:10.1039/c7nr08614h
61. Roth, W. L. *Phys. Rev.* **1958,** *110,* 1333–1341. doi:10.1103/physrev.110.1333
62. Majetich, S. A. Magnetic Nanoparticles. In *Handbook of Magnetism and Magnetic Materials;* Coey, M.; Parkin, S., Eds.; Springer International Publishing: Cham, Switzerland, 2020; pp 1–36. doi:10.1007/978-3-030-63101-7_20-1
63. Amendola, V.; Amans, D.; Ishikawa, Y.; Koshizaki, N.; Scirè, S.; Compagnini, G.; Reichenberger, S.; Barcikowski, S. *Chem. – Eur. J.* **2020,** *26,* 9206–9242. doi:10.1002/chem.202000686
64. Yan, Z.; Chrisey, D. B. *J. Photochem. Photobiol., C* **2012,** *13,* 204–223. doi:10.1016/j.jphotochemrev.2012.04.004

License and Terms

BEILSTEIN JOURNAL OF NANOTECHNOLOGY

Supporting Information

for

Synthesis and magnetic transitions of rare-earth-free Fe–Mn–Ni–Si-based compositionally complex alloys at bulk and nanoscale

Shabbir Tahir, Tatiana Smoliarova, Carlos Doñate-Buendía, Michael Farle,
Natalia Shkodich and Bilal Gökce

Beilstein J. Nanotechnol. **2025,** *16,* 823–836. doi:10.3762/bjnano.16.62

Additional experimental data

1. Elemental composition of Bulk Ge-based CCAs

The ground and polished surface were re-examined, along with the cross-section of the bulk Ge-based CCA sample using SEM/EDX. Figures S1a and S1b present the elemental distribution maps obtained from the surface and cross-section, respectively. The results indicate a highly homogeneous distribution of Mn, Fe, Ni, Ge, and Si across both the surface and the interior of the alloy. The quantitative EDX data (Table S1) further confirm that the average elemental composition closely matches the intended bulk composition, with only minor variations observed between different regions. These findings, in agreement with the results shown in the main manuscript, demonstrate that the surface and the internal volume of the alloy are compositionally consistent within experimental error.

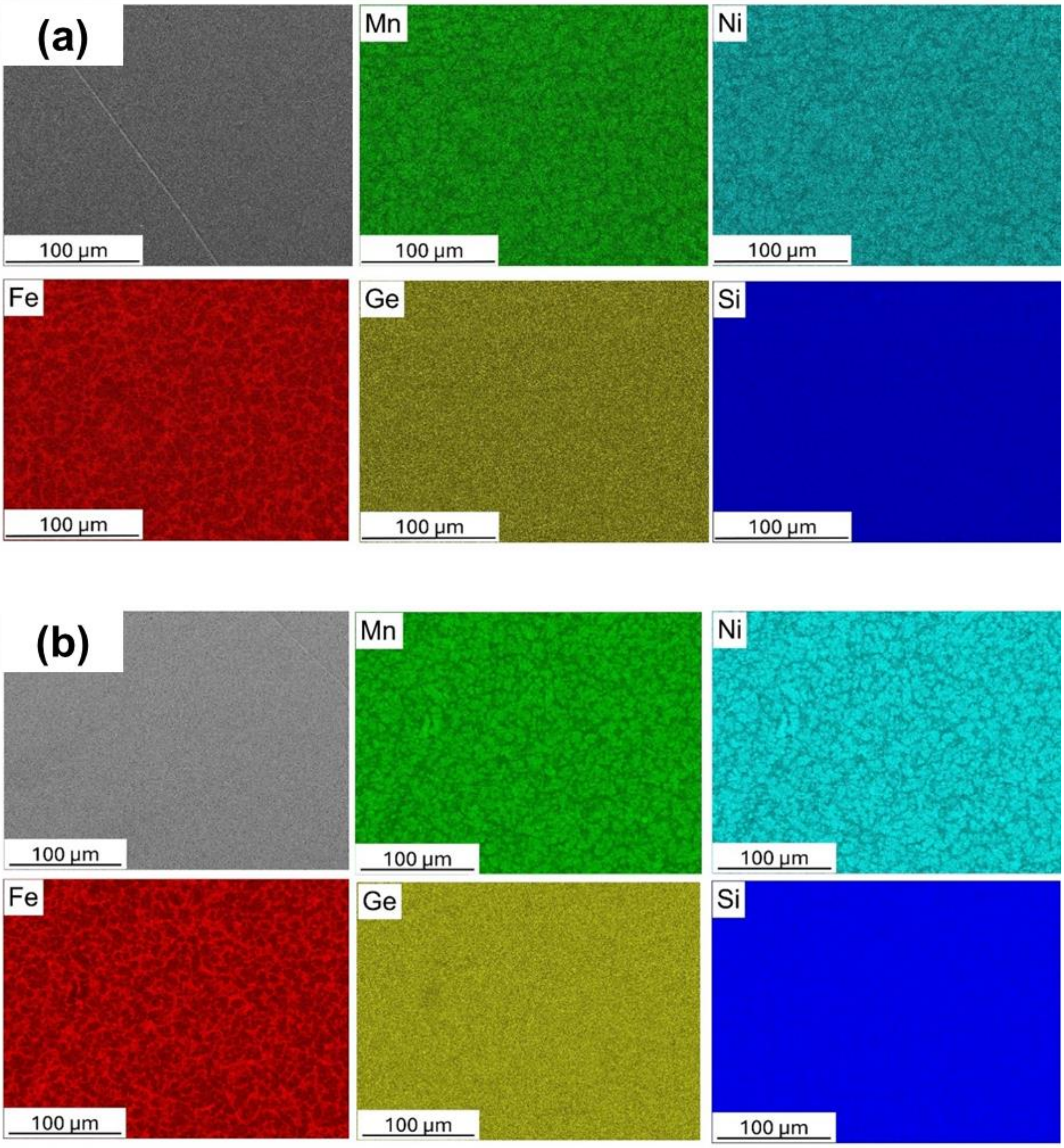

Figure S1: (a): SEM (SE) and EDX elemental maps of Mn, Fe, Ni, Ge and Si obtained from the surface of the bulk Ge-based CCA. (b): SEM (SE) and EDX elemental maps of Mn, Fe, Ni, Ge and Si obtained from the cross-section of the bulk Ge-based CCA.

Table S1: EDX results performed from the fine-polished surface, and the cross-section of the Bulk-Ge based CCA sample.

Bulk Ge-based CCA	Mn [atom %]	Ni [atom %]	Fe [atom %]	Ge [atom %]	Si [atom %]
Surface	21.66 ± 0.06	20.95 ± 0.04	23.91 ± 0.08	15.76 ± 0.06	17.71 ± 0.05
Cross-section	21.57 ± 0.08	20.91 ± 0.06	23.98 ± 0.08	15.92 ± 0.04	17.63 ± 0.07

2. Local elemental composition of Bulk Al-based CCAs.

Figure S2 and Table S2 below present the local compositions of the bulk Al-based CCA, measured at various positions. The table highlights the formation of multiphase alloying or possible alloying inconsistencies, with noticeable segregation of Al and Mn in most cases.

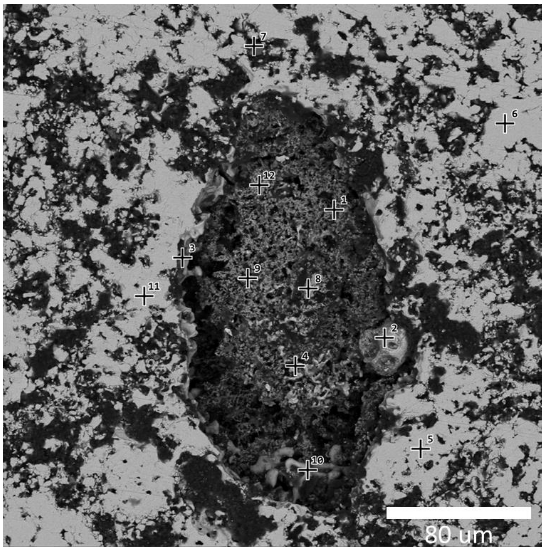

Figure S2: SEM image of bulk Al-based CCA, with marked positions indicating where EDX mapping was performed.

Table S2: Elemental composition by SEM EDX-mapping at local position of bulk Al-based CCA.

	Ni (atom %)	Mn (atom %)	Fe (atom %)	Si (atom %)	Al (atom %)
1	31.94	11.42	20.54	36.09	-
2	32.56	11.36	20.55	35.52	-
3	34.72	30.62	-	18.23	16.43
4	34.72	30.62	-	18.23	16.43
6	11.61	58.79	12.12	17.49	-
7	28.49	23.49	46.74	1.25	-
8	38.32	15.07	38.91	4.23	2.97
9	-	89.01	-	10.99	-
10	-	78.19	-	21.81	-
11	12.6	29.74	50.11	4.84	2.69
12	35.09	30.40	8.08	26.41	-

3. Formation of core–shell structure for Ge-based CCA NPs

Figure S3 presents the HRTEM image and EDX line scan of a Ge-based CCA NP. The HRTEM image clearly shows the formation of an amorphous shell around the NP, indicating surface oxidation. The EDX line scan confirms the presence of all constituent elements within the NP, while a higher oxygen intensity at the edges suggests the formation of an oxide layer on the surface. Since oxidation is predominantly observed at the surface, it likely occurred after the PLAL process, possibly during nanoparticle colloid deposition and drying on the TEM grid or due to interactions with the solvent.

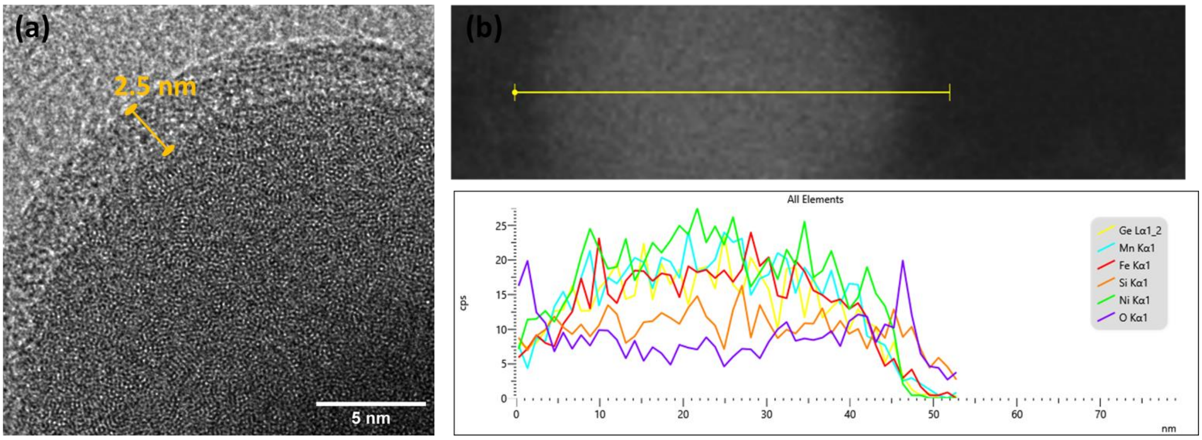

Figure S3: (a) HRTEM image and (b) EDX line scan of a Ge-based CCA NP, showing the elemental distribution of Ni, Mn, Fe, Si, Ge, and O. The higher oxygen intensity at the NP's surface indicates the formation of an oxide layer.

4. EDX line scan of Al-based CCA NP

The TEM image of Al-based CCA confirm that no shell formation was observed in Al-based NPs and the EDX line scan reveals that all constituent elements (Ni, Mn, Fe, Al and Si) were present. The O peak was same throughout, showing that some oxide phases could be formed within the particle.

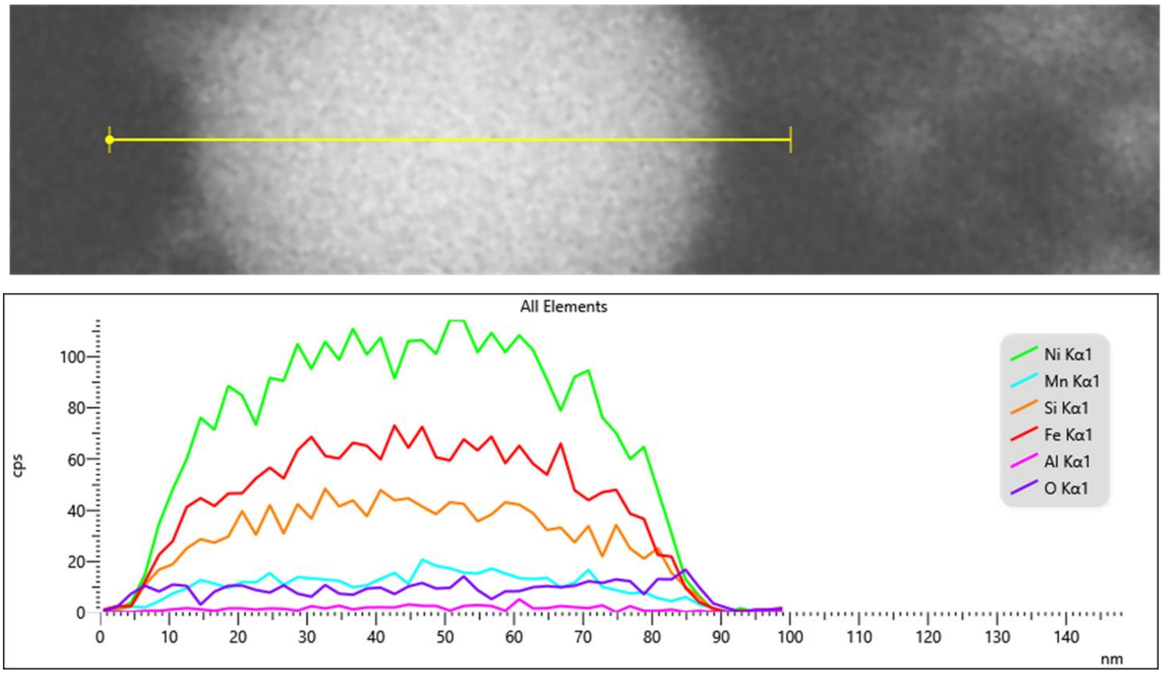

Figure S4: TEM image and EDX line scan of an Al-based CCA NP, showing the elemental distribution of Ni, Mn, Fe, Si, Al, and O.

5. Magnetic properties of bulk CCA (Additional information)

Figure S5a shows the temperature derivative of magnetization (d*M*/d*T*) obtained from ZFC-FC *M*–*T* curves of the bulk Ge-based CCA measured at an applied field of ≈4kA/m. A sharp minimum is observed at 179 K, indicating a well-defined second-order ferromagnetic-to-paramagnetic phase transition. The field-dependent magnetization (*M*–*H*) curves of the bulk Ge-based CCA are shown near zero field for 5 K (blue) and 300 K (red) in Figure S5b. At 5 K, the loop exhibits clear hysteresis, with coercivity of H_c = 8.4 kA/m while at 300 K the coercivity decreases to H_c = 1.2 kA/m). The d*M*/d*T* curve (Figure S5c) for the bulk Al-based CCA displays a broader and shallower minimum at around 263 K, corresponding to its Curie temperature. The broader transition suggests either multiphase behaviour or more gradual magnetic ordering compared to the Ge-based alloy. The *M*–*H* curves of the Al-based CCA (Figure S5c) show H_c = 11.0 kA/m at 5 K and 1.0 kA/m at 300 K.

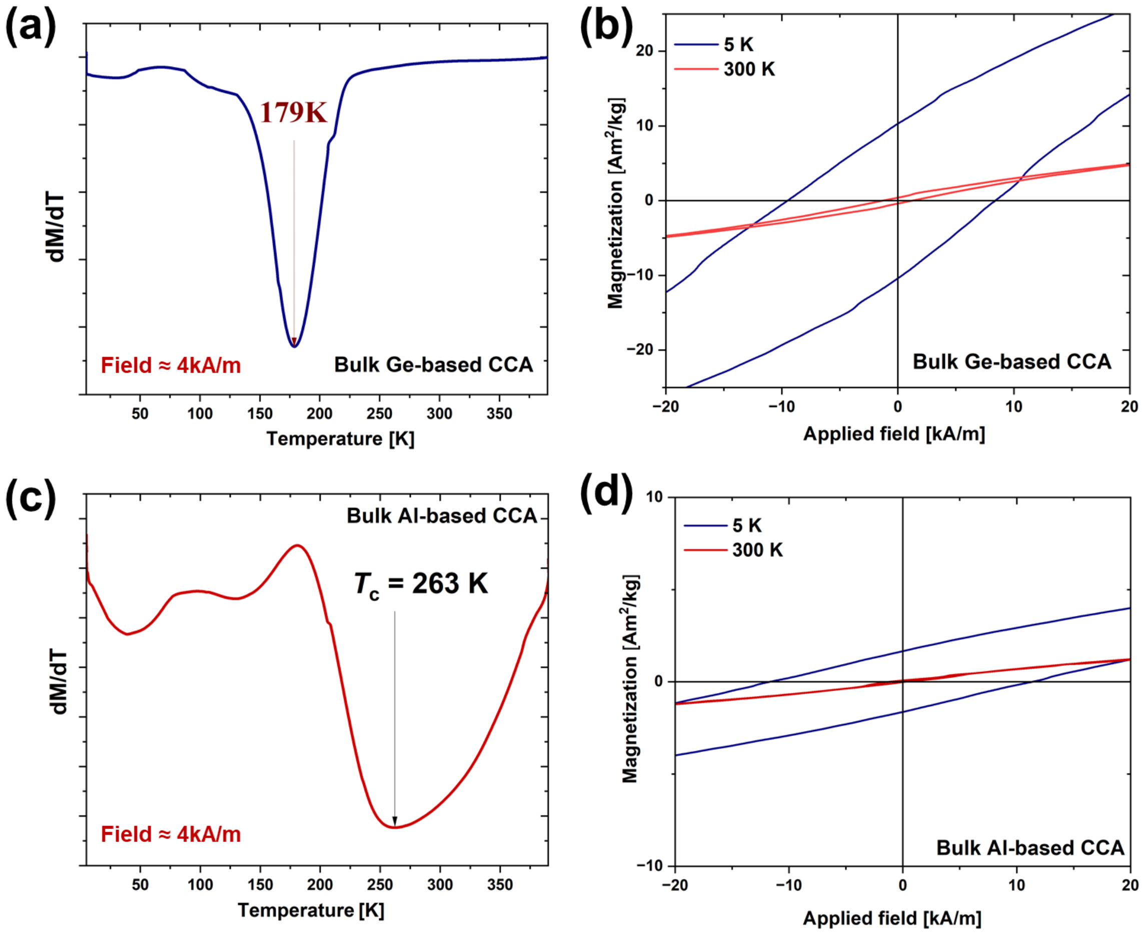

Figure S5: (a) the magnetization derivative with the temperature of ZFC-FC M-T curve of bulk Ge-based CCA. (b) Field-dependent magnetization near 0 T at 5 K (blue) and 300 K (red) for bulk Ge-based CCA. (c) The magnetization derivative with the temperature of ZFC-FC *M*–*T* curve of bulk Al-based CCA. (d) Field-dependent magnetization near 0 T at 5 K (blue) and 300 K (red) for bulk Al-based CCA.

6. Magnetic properties of CCA NPs (Additional information)

The d*M*/d*T* for Ge-based CCA nanoparticles, measured at ≈4kA/m (Figure S6a), shows a magnetic transition at 204 K, indicating a shift from superparamagnetic to paramagnetic behavior. The *M*–*H* curves of Ge-based CCA NPs at 5 K (blue) and 300 K (red) show significant hysteresis at low temperature, with H_c = 26.2 kA/m, and a nearly linear response at 300 K, with H_c = 0.7 kA/m. The d*M*/d*T* curve for Al-based CCA NPs shows a magnetic transition at 202 K (Figure S6c), similar to the Ge-based system. The *M*–*H* curves of Al-based CCA NPs show H_c = 16.6 kA/m at 5 K and 1.1 kA/m at 300 K. These results show that both nanoparticle systems exhibit superparamagnetic-to-paramagnetic transitions and Al-based NPs show lower coercivity at low temperatures.

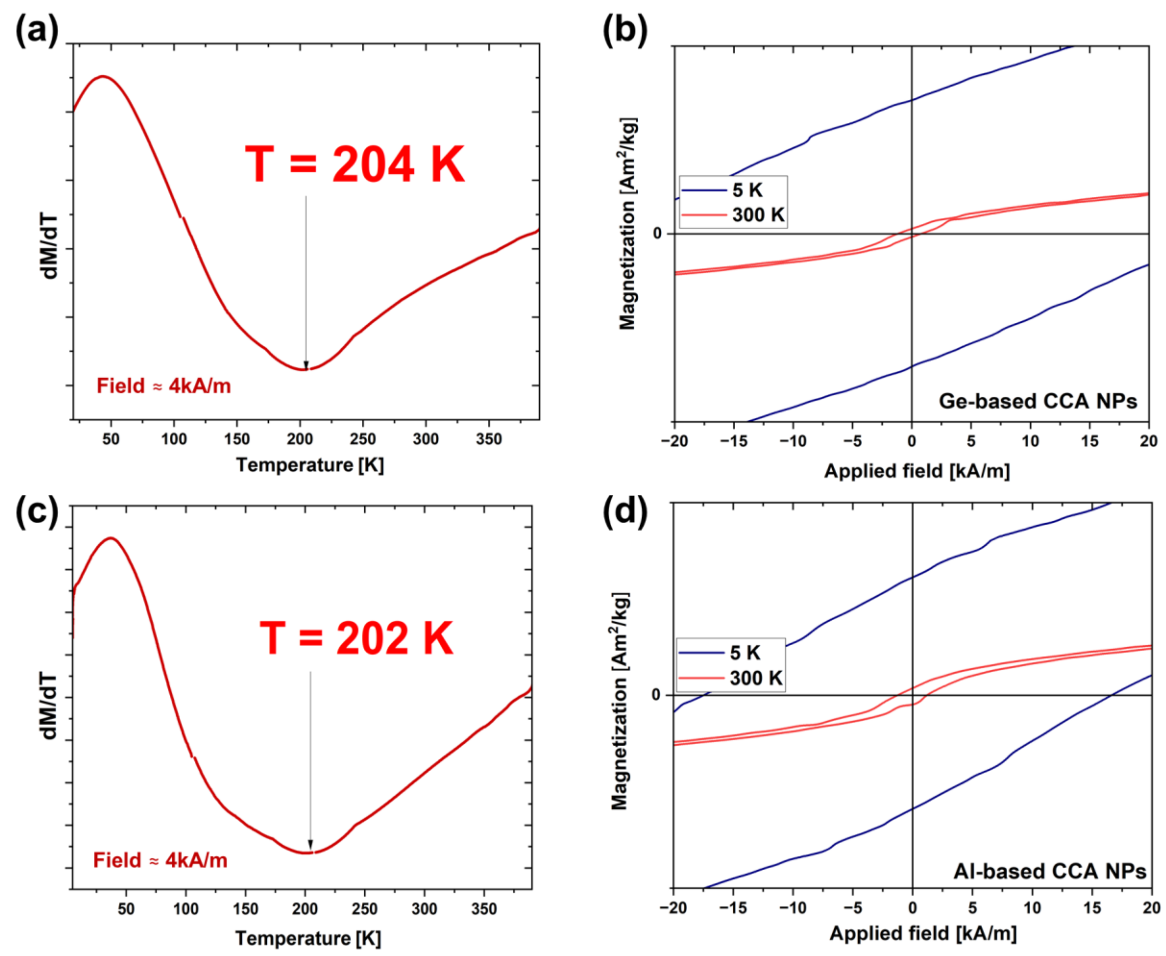

Figure S6: (a) The magnetization derivative with the temperature of ZFC-FC *M*–*T* curve of Ge-based CCA NPs. (b) Field-dependent magnetization near 0 T at 5 K (blue) and 300 K (red) and of Ge-based CCA NPs. (c) The magnetization derivative with the temperature of ZFC-FC *M*–*T* curve of Al-based CCA NPs. (d) Field-dependent magnetization near 0 T at 5 K (blue) and 300 K (red) for Al-based CCA NPs.

5.1.4. Study 4

Tahir, S., Scheibel, F., Doñate-Buendía, C Fu, Z., Koch, D., Heidelmann, M., Donner, W., Gutfleish, O., Gökce, B. "Compositionally Controlled Synthesis and Magnetic Properties of NiMnSn Heusler Alloy Nanoparticles"

(To be submitted)

Article

Compositionally Controlled Synthesis and 2D Laser Printing of Magnetocaloric NiMnSn Nanoparticles

Shabbir Tahir[1], Franziska Scheibel[2], Carlos Doñate-Buendía[1,3] Zongwen Fu[1], David Koch[4], Markus Heidelmann[5], Wolfgang Donner[4], Oliver Gutfleish[2], and Bilal Gökce[1]*

[1]Chair of Materials Science and Additive Manufacturing, University of Wuppertal, Gaußstr. 20, 42119 Wuppertal, Germany

[2]Functional Materials, Institute of Materials Science, Technical University of Darmstadt, Peter-Grünberg-Str. 16, Darmstadt 64287, Germany

[3]GROC·UJI, Institute of New Imaging Technologies, Universitat Jaume I, Av. De Vicent Sos Baynat s/n, 12071 Castellón, Spain

[4]Institute of Materials Science, Technical University of Darmstadt, Darmstadt 64287, Alarich-Weiss-Strasse 2, Germany

[5]Interdisciplinary Center for Analytics on the Nanoscale (ICAN) and Center for Nanointegration Duisburg-Essen (CENIDE), University of Duisburg-Essen, Carl-Benz-Straße 199, 47057 Duisburg, Germany

*Corresponding authors: goekce@uni-wuppertal.de

Abstract

Ni-Mn-Sn-based Heusler alloys exhibit a strong inverse magnetocaloric effect (IMCE) near room temperature, making them ideal for solid-state cooling applications. High-resolution 2D printing of such materials enables the precise structuring of magnetocaloric materials, facilitating their seamless integration into microcoolers, MEMS, and flexible electronics.

This study explores the utilization of fine NiMnSn microparticles through ink formulation for 2D laser printing and compositionally controlled nanoparticle (NP) synthesis via pulsed laser ablation in liquid (PLAL). Different PLAL target fabrication strategies are investigated to optimize NP composition,

Among the investigated methods, PLAL using pressed NiMnSn microparticles (MPs) mixed with additional Mn MPs results in a NP composition that more closely matches the desired $Ni_{50}Mn_{50-x}Sn_x$ (at. %; for 13 at. % < x < 15 at. %), minimizing overall deviations. The synthesized NPs exhibit significant size reduction compared to MPs and distinct magnetic behavior with broad phase transitions. Laser sintering of both MP and NP inks successfully produces structured magnetocaloric materials. The sintered MP ink shows an increase in overall magnetization compared to the sintered NP ink, while the NP ink demonstrates improved uniformity and higher resolution during 2D laser printing.

This study establishes a compositionally controlled approach for synthesizing NiMnSn NPs from MPs and demonstrates precise laser structuring of magnetocaloric materials. These findings provide critical insights into the scalability of NiMnSn materials for next-generation solid-state refrigeration, MEMS, and miniaturized magnetic devices.

Keywords: Magnetic phase transition, Heusler alloys, Rare-earth free, Pulse laser ablation in liquid, Nanoparticles.

1. Introduction

Heusler alloys are a class of intermetallic compounds with the general formula X_2YZ or XYZ, where X and Y are typically transition metals and Z is a main-group element. These materials exhibit a wide range of functional properties, including ferromagnetism[1, 2], half-metallicity[3, 4], and shape memory effects[5, 6], making them highly attractive for applications in spintronics[7, 8], magnetocaloric refrigeration[9, 10], and energy conversion[11, 12]. In magnetocaloric refrigeration, Heusler alloys are particularly promising due to their ability to undergo a martensitic transformation near room temperature, which is accompanied by a large change in magnetization. This phenomenon leads to the inverse magnetocaloric effect (IMCE), where the application of a magnetic field induces a negative entropy change, resulting in heat absorption from the surroundings. Conversely, removing the field releases heat, making these materials excellent candidates for solid-state refrigeration as an alternative to conventional gas-compression cooling, which relies on environmentally harmful refrigerants. The Heusler-type alloys composed of $Ni_{50}Mn_{50-x}Sn_x$ (at.%; for 13 at.% < x < 15 at.%) have attracted significant attention due to their highly reversible magneto-structural phase transition, which produces an inverse magnetocaloric effect nearly three times larger than that of Ni-Mn-Ga-based alloys[13]. These alloys exhibit ferromagnetic behavior in the high-temperature austenite phase (below their Curie temperature T_c) which transforms into a low-magnetization martensitic phase upon cooling, leading to a strong IMCE. Additionally, being rare-earth-free, and their ability to maintain a balance between thermal stability and transformation temperatures near room temperature further enhance their suitability for next-generation energy-efficient, cost-effective solid-state refrigeration technologies[14].

High-resolution 2D printing of magnetocaloric materials presents a promising approach for integrating these materials into miniaturized cooling devices, offering precise control over structural geometry while maximizing heat exchange efficiency.[15] Unlike bulk fabrication methods, which often require extensive post-processing to achieve the desired shapes, 2D printing can enable direct deposition of finely structured magnetocaloric layers onto substrates, facilitating their incorporation into microelectronic cooling systems, MEMS, and flexible electronics.[16] The resolution of printed structures is critically dependent on the size and morphology of the feedstock material, where fine microparticles (MPs) or nanoparticles (NPs) play a key role. Smaller particle sizes enable smoother, more uniform ink formulations with enhanced printability, reducing defects and ensuring consistent material distribution.[17, 18] This, in turn, leads to improved thermal and magnetic properties, as well as greater precision in fabricating patterned structures with optimized surface-to-volume ratios. Furthermore, the use of fine powders minimizes material waste[19] which can allow development of thinner, flexible magnetocaloric films that can be tailored to specific device architectures.

Transitioning from fine MPs to the nanoscale is particularly desirable due to the distinct properties of NPs compared to their bulk counterparts. This transition from fine MPs to the nanoscale will be particularly desirable due to further improvement in print resolution and due to the distinct properties of NPs compared to their bulk counterparts. At the nanoscale, materials exhibit size-dependent phenomena such as an enhanced surface-to-volume ratio, reduced hysteresis losses[20], tunability of phase transitions[21, 22], and a significant magnetocaloric effect due to superparamagnetic behavior[23, 24]. Additionally, magnetocaloric NPs demonstrate a broader entropy change over a wider temperature span, which can enhance relative cooling power (RCP), making them highly promising for next-generation cooling technologies.[25]

While bulk and thin film Heusler compounds have been extensively studied, achieving magnetic Heusler NPs remains a challenge due to the positional disorder of intermetallic atoms.[26] The synthesis of Heusler alloy NPs has been explored through both top-down and bottom-up approaches.[27-30] High-energy ball milling, a common top-down method, has been employed to reduce particle sizes from the micron to nanometer scale. However, this approach often leads to the formation of disordered intermediate phases due to lattice strain, as observed in Ni-Mn-Ga[28, 31] or results in core-shell structures, as seen in $(Mn,Fe)_2(P,Si)$-based NPs[32]. In contrast, wet chemical techniques have been successfully used to synthesize Heusler alloys of various compositions, including Co_2FeSn[26], Ni_2FeGa[33] Fe_3Ga[34], Co_2FeAl[35], Co_2FeGa[36] and Co_2NiGa[37] with high purity and well-defined size distributions. These methods enable the formation of $L2_1$-ordered structures with minimal secondary phases. However, the presence of residual surfactants, ligands, or precursors in wet chemical synthesis can alter the surface chemistry and influence the overall properties of the NPs, necessitating additional purification steps.[38]

Pulsed laser ablation in liquid (PLAL) can offer a rapid, surfactant-free, and versatile alternative for synthesizing high-purity Mn-based Heusler alloy NPs.[39-42] In this method, a target material is ablated in an immersed solvent, and the resulting NP composition is primarily dictated by the target composition. Unlike conventional chemical synthesis routes, PLAL eliminates the need for precursors or stabilizing agents, reducing contamination risks. Additionally, the rapid quenching from the surrounding liquid stabilizes metastable phases and facilitates the formation of nanostructures with tailored compositions, which are often unattainable through solid-state or gas-phase synthesis. This technique also offers high flexibility, as NP composition and properties can be tuned by modifying the target material or adjusting laser parameters such as wavelength, fluence, and pulse duration.[43, 44] Additionally, PLAL allows the use of targets made by pressed and sintered elemental or pre-alloyed powders, offering a simpler and more scalable route to achieving the desired compositions.[45, 46]

In this work, gas atomized fine Ni-Mn-Sn MPs were used as feedstock. First, these fine MPs were dispersed in an ink and their potential to create functional 2D structures by laser printing was investigated. Second, PLAL was used to synthesize compositionally controlled NPs by pressing and sintering powders into targets and compare the composition of NPs obtained from different target fabrication techniques (see Section 2.2). By integrating these strategies, this work seeks to provide new pathways for tailoring the properties of Ni-Mn-Sn-based magnetocaloric materials. Ultimately, our findings will contribute to the development of advanced solid-state cooling technologies that leverage nanoscale enhancements to optimize performance and efficiency.

2. Materials and methods

2.1. Preparation of NiMnSn finer MPs

Pre-alloyed NiMnSn MPs were custom-produced by means of gas atomization and analyzed by VTT (Technical Research Centre of Finland). Its composition was determined by X-ray fluorescence (XRF) as $Ni_{47.2}Mn_{39.2}Sn_{13.0}$ (at. %). The elemental composition and elemental mapping were visualized by energy dispersive X-ray spectroscopy (EDX) in scanning electron microscopy (SEM, Apreo S LoVac, Thermo Fisher Scientific). The process of target preparation, NP synthesis via PLAL, ink formulation, and laser sintering is illustrated in Figure 1.

2.2. Preparation of NiMnSn targets

To enable compositionally controlled synthesis of NiMnSn NPs, different target materials were prepared for PLAL.

- Type 1 target: For the preparation of polycrystalline NiMnSn alloy targets, arc melting was performed under an argon atmosphere using a water-cooled Cu crucible. The resulting ingot was annealed for 2 hours in a quartz glass tube at 1000°C under an argon atmosphere to ensure compositional homogeneity resulted in the formation of $Ni_{50}Mn_{36}Sn_{14}$ (at. %) alloy. The solidified ingot was cut into thin slices using a low-speed diamond saw and immersed in distilled water for subsequent PLAL.
- Type 2 targets: Elemental Ni (purity: 99.5%, particle size: 45-60 µm), Mn (purity: 99.2%, average particle size: ~3 µm), and Sn (99%, ~10 µm) MPs at different ratios were mixed with 10 wt.% polyvinylpyrrolidone (PVP, Molecular weight = 40 k) for the preparation of powder-pressed targets.
- Type 3 targets: Pre-alloyed MP composed of $Ni_{47.2}Mn_{39.2}Sn_{13.0}$ (at. %) fabricated by means of gas atomization was mixed with elemental Mn (99.2%, ~3 µm) with different ratios and 10 wt.%

PVP. The powders were manually ground using a pestle and mortar for 30 minutes to ensure uniform mixing. Afterward, the mixtures were compressed at 100 MPa to form cylindrical pellets of 10 mm in diameter and 2 mm in thickness. The pellets were then heat-treated in a nitrogen atmosphere at 500°C for 2 hours, followed by slow cooling inside the furnace.

2.3. Synthesis of NiMnSn NPs

NiMnSn NPs were synthesized via PLAL of Type 1, 2 or 3 targets in molecular sieve treated ethanol using a near-infrared picosecond pulsed Nd:YAG laser (Coherent, HyperRapid NX, Kaiserslautern, Germany, 10 ps, 1064 nm). The laser beam was focused with an f-theta lens (f = 167 mm) and guided using a galvanometric scanner (Raylase, SS-IV-15 [1070], Wessling, Germany) to generate a 6 mm-diameter hollow spiral ablation pattern on the target surface at a scanning speed of 10 m/s. The distance between the target and the lens was kept constant, and the laser fluence was set at 2.8 J/cm^2. The NPs were collected in 2 L of ethanol, which was continuously circulated in a closed-loop system to ensure efficient collection while minimizing solvent usage.

The size distribution and morphology of the NPs were characterized using scanning electron microscopy (SEM) in scanning transmission electron microscopy (STEM) mode. Their elemental composition and mapping were analyzed by EDX in STEM mode using an aberration-corrected JEOL JEM-ARM200F NEOARM, equipped with two 100 mm^2 EDX detectors. For both techniques, NP colloids were dispersed onto a copper grid and allowed to dry before imaging. The crystal structure of NPs synthesized from each target was examined using X-ray diffraction (XRD) with Mo Kα radiation in transmission geometry. Measurements were conducted on a custom-built setup featuring a Mythen2 R 1K detector (Dectris Ltd., Baden, Switzerland). To correct for geometric errors, the dried NP powder was mixed with NIST 640d standard silicon powder and adhered to a graphite foil. Magnetic properties were assessed using vibrating sample magnetometry (VSM). The NP powder was pressed into small pellets (~3 × 2 mm, ~10 mg) and mounted on the heater stick of the VSM. Temperature-dependent magnetization M-T curves were recorded during both heating and cooling under applied magnetic fields of 1 mT and 1 T across a temperature range of 0–400 K.

2.4. Ink Formulation, Dispersion, and Sintering of NP/MP Ink

The synthesized colloidal NiMnSn NPs were used to formulate a 1 wt.% ink by partial evaporation of ethanol, followed by polymer addition to stabilize the dispersion. The NiMnSn MP ink was prepared by dispersing 10 wt.% commercial NiMnSn MP and 20 wt.% PVP in ethanol. The mixture was ultrasonicated using an ultrasonic tip operating at 2000 kHz for 5 minutes. A volume of 200 µL of the ink was then dispersed onto a glass substrate, covering an area of approximately 25 × 15 mm^2.

The dispersed NP and MP inks were sintered using a continuous-wave (CW) laser (Laser Quantum, 532 nm) and a programmable 2-axis linear stage (Thorlabs DDSM100/M). Laser parameters were optimized to achieve uniform sintering while preventing excessive ablation, and additional details on the sintering process can be found in previous studies.[48]

The morphology of the sintered MPs and NPs was analyzed using SEM. Further structural characterization of the sintered NPs was performed using an aberration-corrected JEOL JEM-2200FS transmission electron microscope (TEM) operating at 200 kV. The magnetic properties were determined using a vibrating sample magnetometer (VSM), as described earlier.

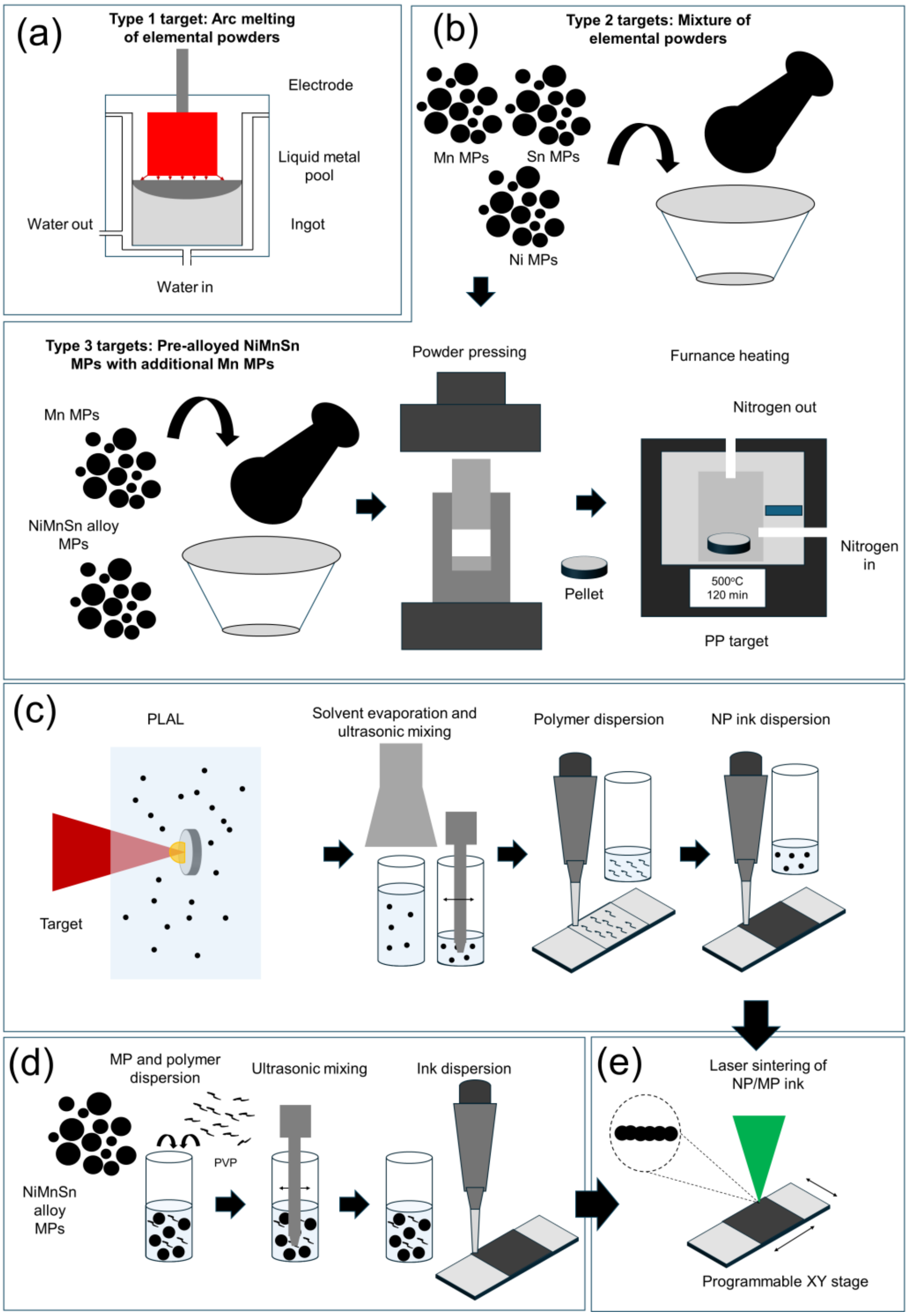

Figure 1. Schematic representation of the synthesis, NP generation, ink formulation, and laser sintering processes for NiMnSn alloy. (a) Preparation of Type 1 target by arc melting elemental Ni, Mn, and Sn in appropriate ratio to obtain $Ni_{50}Mn_{36}Sn_{14}$ bulk alloy. (b) Preparation of Type 2 and 3 targets: Type 2 targets are synthesized by mixing elemental Ni, Mn, and Sn MPs with varying ratios, while Type 3 targets are prepared by mixing commercial NiMnSn MPs and Mn MPs with varying ratios. Both mixtures are pressed into pellets and sintered in a nitrogen environment. (c) PLAL of Type 1, 2, or 3 targets in ethanol to generate NiMnSn NPs, followed by ink formulation through solvent evaporation, ultrasonic mixing, and polymer dispersion before deposition on a glass substrate. (d) Ink formulation using commercial NiMnSn MPs, involving polymer dispersion and ultrasonic mixing before deposition on a glass substrate. (e) Laser sintering of NP/MP ink using a continuous-wave laser on a programmable XY stage to fabricate 2D structures.

3. Results and discussion

3.1 Composition analysis and particle size distribution

Fig. 2a presents the elemental composition analysis of commercial NiMnSn MPs and NPs synthesized using PLAL of Type 1, 2 or 3 targets. The composition of the commercial NiMnSn MP closely aligns with the desired composition $Ni_{50}Mn_{50-x}Sn_x$ (at.%; for 13 at.% < x < 15 at.%) as indicated by the dashed lines. A slightly higher Mn content was used to compensate for the loss during evaporation during laser printing.

NPs from **Type 1** target: NPs synthesized via PLAL of the arc-melted $Ni_{50}Mn_{36}Sn_{14}$ (at.%) bulk target show a significant depletion of Mn (about 14 at.% lower) compared to the initial target composition suggesting that Mn is selectively lost during laser ablation. This Mn loss is commonly observed in PLAL[46] due to differences in volatility, as Mn has a lower boiling point (2095°C) compared to Ni (2913°C) and Sn (2602°C), making it more prone to vaporization during ablation. Additionally, the difference in ionization potential among the elements contributes to this selective loss.

NPs from **Type 2** targets: To achieve NPs with a composition closer to the desired NiMnSn ratio, powder-pressed targets using elemental Ni, Mn and Sn were used with an increased Mn content. The composition with 37 at.% Ni, 53 at.% Mn, and 10 at.% Sn were the closest composition to achieve the average desired ratio after PLAL, but substantial deviations (maximum 30 at.% in Ni) were still observed between individual NPs. The composition of individual alloy NPs remained inconsistent, and the trend seemed independent of stoichiometric ratio (Fig. S1). This variation can again be attributed to differences in the latent heat of fusion and vaporization of Ni, Mn, and Sn, which affect alloy formation. Ni has approximately 1.4 times higher latent heat of fusion and vaporization compared to Mn and about 2.5 and 1.25 times higher latent heat of fusion and vaporization than Sn, respectively. This disparity in thermal properties leads to uneven element distribution during the rapid quenching process in PLAL. Interestingly, apart from lower Mn content, such compositionally random NPs were not observed in Cantor alloy NPs composed of NiCoFePtRh which was also produced by PLAL of elemental powder pressed targets[46], likely because the latent vaporization of its constituent elements (Co, Cr, Fe, and Ni) except Mn are quiet close to each other.

NPs from **Type 3** targets: The synthesis of NPs by PLAL using a mixture of NiMnSn MPs and additional Mn MPs in a pressed target showed that increasing Mn content in the target effectively increases the Mn content in the resulting NPs, bringing the composition closer to the desired stoichiometry $Ni_{50}Mn_{50-x}Sn_x$ (at.%; for 13 at.% < x < 15 at.%) when 20 at.% additional Mn was added to the pre-alloyed $Ni_{47.2}Mn_{39.2}Sn_{13.0}$ (at.%) MP. The Fig.2a also indicates that the deviations in composition are significantly lower compared to NPs synthesized from PLAL of Type 2 targets. Fig. S2 further confirms that increasing Mn content in the target leads to a corresponding increase in Mn within the NPs. This improvement could be due to the smaller difference in latent heat of fusion and vaporization between NiMnSn alloy and Mn, which enhances the probability of forming particles with the desired composition. Despite this, some agglomerated smaller NPs appear Mn-rich (Fig. S3), contributing to compositional deviation, whereas most NPs exhibit a composition close to the desired ratio. The EDX mapping shows that both MPs and NPs display well-defined distributions of Mn, Ni, and Sn (Fig. 2b).

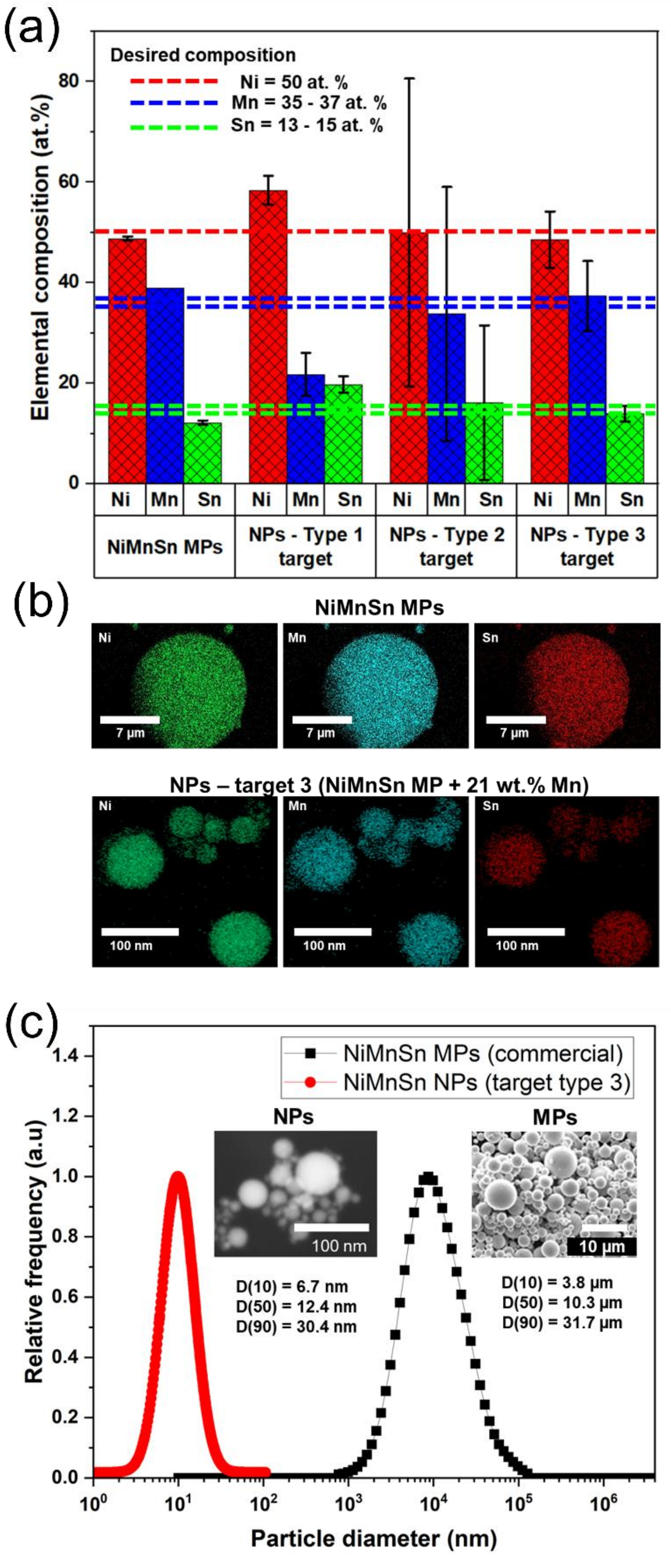

Figure 2. (a) Average elemental composition of commercial NiMnSn MPs and PLAL-synthesized NiMnSn NPs from Type 1, 2, and 3 targets, determined via EDX mapping. The dashed lines indicate the desired composition. (b) Elemental distribution maps of Ni, Mn, and Sn for commercial NiMnSn MPs (top row) and PLAL-synthesized NPs from Type 3 target (bottom row), showing homogeneous elemental dispersion. (c) Particle size distribution of commercial NiMnSn MPs and PLAL-synthesized NPs from Type 3 target. Insets show representative SEM images of NPs and MPs.

From this point onward (in the following sections), all characterizations related to NPs will refer specifically to those synthesized via PLAL of Type 3 target (NiMnSn MP + 20 at. % Mn MP), unless stated otherwise. Fig. 2c presents the particle size distribution of NiMnSn MPs and NPs synthesized via PLAL. The two insets show SEM images of the NPs (left) and MPs (right). The average particle size (x_c) for the NPs is 12.4 nm, whereas the MPs have a significantly larger average size of 10.0 µm. The size distribution curve for the PLAL-synthesized NPs (red) is narrow and monomodal, indicating a relatively uniform NP size. Both the NPs and MPs exhibit a spherical morphology with a similar composition and phase structure (Fig. S4), making them a suitable basis for comparative analysis of their properties and potential applications.

3.2. Magnetic response of MP and NPs

The temperature-dependent magnetization (M-T) curves of NiMnSn MPs were measured under two different applied magnetic fields (10 mT and 1 T) to study the phase transitions and magnetic properties of the material (Fig. 3a). In the low-field measurement (10 mT, red curve), two distinct transitions are observed. The first transition at ~300 K and second at ~200 K. Both transitions are associated with the transformation from the high-temperature austenite phase (crystal structure shown in Fig. S4) to the martensite phase. The presence of two transitions is likely due to compositional inhomogeneity within the powder, causing different regions to undergo phase transformations at slightly varying temperatures. This suggests that the segregation commonly observed in gas atomized powders leads to compositional heterogeneity among the MPs, resulting in multiple Curie temperatures. The Curie temperature of the austenite phase T_C (austenite) ≈ 315 K and the martensitic phase T_C (martensite) ≈ 230 K indicate a mixed-phase system, which is common in NiMn-based Heusler alloys due to the complexity of phase coexistence and atomic ordering effects.[14] Under higher applied field (1 T, blue curve), the transition temperature of the first transformation shifts downward by ≈ 5 K to 295 K, due to the influence of the external magnetic field stabilizing one of the phases. The second transition is no longer visible, because the magnetization values of the martensite and austenite phases become comparable, leading to $dM/dT \approx 0$, which makes the transition indistinguishable.

The M-T curve for the NPs exhibits a gradual decrease in magnetization with increasing temperature, measured under two different applied fields (10 mT and 1 T) (Fig. 3b). Unlike the MPs, which show two distinct magnetic transitions at approximately 200 K and 300 K, the NPs display broad and weak features around these temperatures. These diffuse transitions could be attributed to oxidation effects in some NPs, superparamagnetic behavior in smaller particles, or antiferromagnetic interactions, typically originating from oxides. Additionally, compositional inhomogeneity in the NPs may result in a lower overall fraction of austenite-martensite phase conversion. Interestingly, these broad transitions are absent in NPs synthesized via PLAL of Type 1 target (Fig. S5), suggesting that compositionally controlled synthesis is crucial for achieving a distinct austenite-martensite transition near room temperature. At 1 T, the transition is further suppressed due to the comparable magnetization values of the austenite and martensite phases, leading to a reduced magnetic contrast between phases, similar to what is observed in MPs.

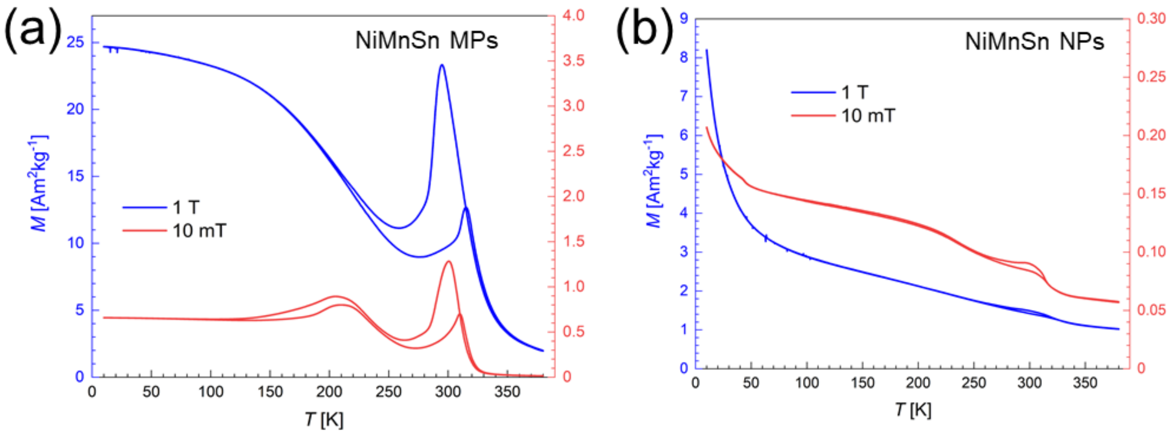

Figure 3. (a) Temperature-dependent magnetization (M-T) curves of NiMnSn MPs measured under applied fields of 10 mT and 1 T, showing distinct magnetic transitions associated with the austenite-martensite phase transformation. (b) M-T curves of NiMnSn NPs measured under 10 mT and 1 T, displaying a more gradual magnetization change with broad transition features.

3.3. Laser printing of MP and NPs

Laser irradiation of MP- and NP-dispersed inks resulted in the successful sintering of both particle types (Fig 4). For the MP ink, sintering began at a fluence of 0.76 J/cm^2, although some regions remained unsintered due to difference in the homogeneity of dispersed ink, leading to difference optical absorption. Complete and uniform sintering occurred at 0.89 J/cm^2, where the entire irradiated region fused effectively (Fig 4a), resulting in an average sintered line width of 254 ± 17 µm (at 325 mW). At fluences above this threshold, partial ablation of the particles was observed. The sintering and ablation mechanisms have been discussed in our previous work, where it was noted that ablation occurs once a critical fluence is exceeded.[47] The ablation initiates at the center of the laser-exposed region, where the intensity is highest due to the Gaussian intensity profile of the laser beam.

For NP ink, sintering initiated at a lower fluence of 0.66 J/cm² and was fully achieved at 0.87 J/cm², which is comparable to the sintering threshold of the MP ink. This indicates that the sintering temperature for NPs and MPs is quite similar. Above this fluence, the NPs were ablated similar to what was observed for MPs. The average sintered line thickness of NPs was measured at 65 ± 4 µm (at 90 mW), significantly narrower than the 254 ± 17 µm obtained for MP sintering. This difference can be attributed to objective focusing adjustments affecting the beam spot size, which influences the sintered line thickness. As a result, lower laser power was used for NP sintering, while maintaining a similar fluence.

The standard deviation for the width of the sintered line was found to be about 4 times smaller for NPs compared to MPs, which could be due to the size variation in MPs affecting the uniformity of the sintering process. This distinction is particularly important for precision printing of miniaturized devices, where NPs offer higher resolution and consistency. Furthermore, the ratio of the ablation regime to the total sintered regime was higher for NPs than for MPs. This could be due to differences in their specific surface areas, which profoundly affect their sintering activity, or the higher particle concentration in MP inks, which increases the film thickness, enhances heat distribution, and therefore reduces ablation effects (Fig. 4b). The SEM images confirm the sintering behavior, showing clusters of NPs fused together, forming larger aggregates. Additionally, HRTEM analysis of sintered NPs reveals the merging of a large single-crystal NP with a smaller polycrystalline NP. The sintered surface appears to retain its crystallinity, although the lattice spacing within the sintered region is difficult to compute, likely due to localized lattice distortions and partial disorder induced by laser sintering.

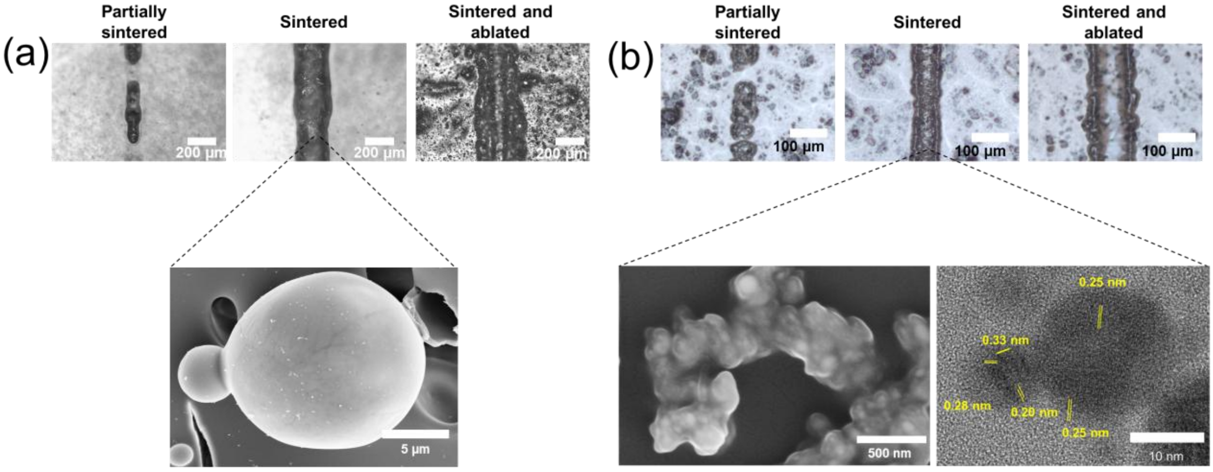

Figure 4. (a) Optical microscopy images of laser-sintered NiMnSn MP ink, highlighting the partially sintered, fully sintered, and ablated regions. The SEM image shows the sintering behavior of two adjacent particles, demonstrating partial fusion. (b) Optical microscopy images of laser-sintered NiMnSn NP ink, illustrating the transition from partially sintered to fully sintered and ablated regions. The SEM image reveals sintered NP clusters, while the high-resolution TEM image provides insight into the atomic-scale bonding between sintered NPs.

3.4. Magnetic response of laser printed structures

The M-T curves for sintered NiMnSn MPs were measured at low fluence (sintered regime) and high fluence (sintered + ablation regime) under two different applied fields (1 mT and 1 T). At low fluence (Fig. 5a) the M-T curve at 1 mT (red) is very similar to the MP, showing characteristic magnetic phase transitions around 200 K and 300 K, which are associated with the martensitic transformation and Curie temperature transitions of the NiMnSn Heusler phase. Higher magnetization values are observed in the sintered sample compared to raw MPs, which can be attributed to improved particle connectivity and enhanced ferromagnetic coupling due to sintering, or the differences in the estimated and actual mass, since the dispersion could have resulted in different concentration of MPs on the surface. For T < 50 K, the M-T curve shows an increasing trend, likely due to contributions from paramagnetic impurities in the glass substrate.

At high fluence (Fig. 5b), the overall magnetization is lower compared to the low-fluence sample due to the loss of material caused by ablation at high laser power. The M-T curve at 1 mT still shows a similar trend to the powder, but the peak at 300 K is reduced, indicating that some fraction of the material no longer undergoes a complete austenite-martensite transition. At 1 T, the M-T curve is again comparable to the powder, but magnetization is lower than in the low-fluence case. This is either due to higher ablation-induced mass loss, potential oxidation effects, compositional inhomogeneity, or structural disruptions due to excessive heating, which may lead to partial decomposition of the Heusler phase. The M-T trend for T < 50 K remains similar, again attributed to the glass substrate contribution.

The M-T curves for sintered NiMnSn NPs at low fluence (Fig. 5c) and high fluence (Fig. 5d) provide insight into the effect of laser printing on the magnetic properties of the deposited ink. Since the mass of these dispersions cannot be accurately measured, the magnetization values are normalized with respect to the NPs, and the discussion will focus on the differences in curve shape rather than absolute magnetization values. For low-fluence (sintered structures) the overall shape of the M-T curve closely resembles that of unsintered NPs, with a gradual decrease in magnetization with increasing temperature. No sharp magnetic transitions are observed, further confirming that austenite-martensite transformation is either highly suppressed or absent in the NPs. A broad feature near 200–300 K can still be noticed, similar to unsintered NPs, suggesting austenitic-martensitic transformation. At T < 50 K, the magnetization shows a slight increase as for MP sintering, which can be attributed to paramagnetic contributions from the substrate. For high-fluence NP laser printing, The M-T curve shape is similar to the low-fluence NP laser printing, but the broad feature around 200–300 K is further suppressed. This suggests that at higher fluences, increased thermal energy and ablation effects disrupt the structural transitions, leading to a more uniform paramagnetic-like response. The increased laser fluence may enhance diffusion and disorder, further suppressing the characteristic transitions seen in the low-fluence sample.

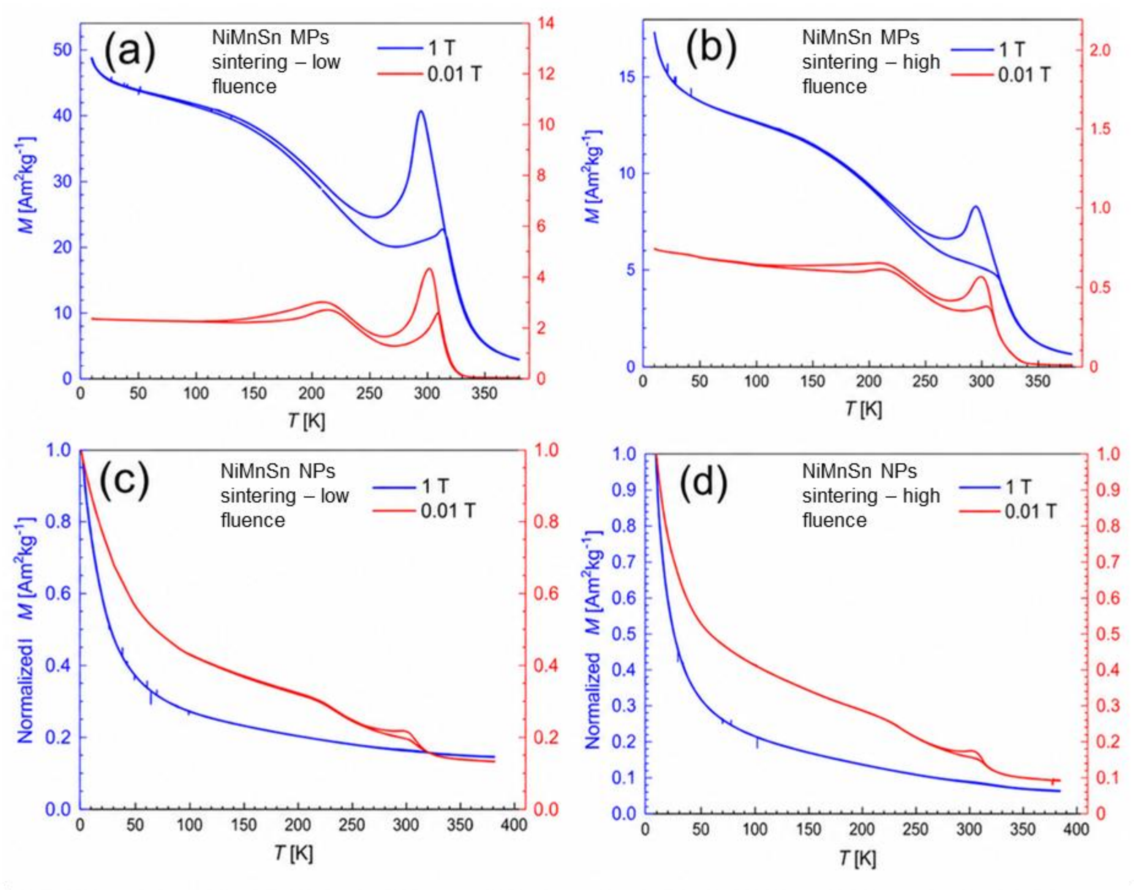

Figure 5. Temperature-dependent magnetization (M-T) curves measured under applied fields of 1 mT and 1 T for laser-sintered NiMnSn inks. (a) M-T curves of NiMnSn MP ink sintered at low fluence, showing preserved magnetic phase transitions similar to the raw powder. (b) M-T curves of NiMnSn MP ink sintered at high fluence, exhibiting reduced magnetization due to ablation effects and possible structural modifications. (c) M-T curves of NiMnSn NP ink sintered at low fluence, displaying a gradual magnetization decrease with broad transition features. (d) M-T curves of NiMnSn NP ink sintered at high fluence, where further suppression of transition features suggests increased thermal and ablation-induced structural disruption.

Conclusion

In this study, we explored the utilization of fine NiMnSn MPs through high-resolution 2D laser printing and investigated their role in achieving compositionally controlled NP synthesis via PLAL. These approaches provide cost-effective strategies for device miniaturization, particularly in applications such as microcoolers, actuators, and microsensors, where precise material structuring is essential. The successful development of structured magnetocaloric materials through 2D printing and the controlled synthesis of Heusler alloy NPs highlight the potential of fine MPs and NPs in enhancing the performance and integration of magnetocaloric materials into micro-scale devices.

PLAL successfully synthesized NiMnSn NPs with tailored compositions using different target types. Among all targets, ablation of Type 3 target, fabricated from powder pressing and sintering of NiMnSn alloy MP and an additional 20 at.% elemental Mn MP, achieved compositional homogeneity closer to closer to desired $Ni_{50}Mn_{50-x}Sn_x$ (at. %; for 13 at. % < x < 15 at. %) composition, with deviations limited to ~7 at. % Mn. The synthesized NPs had a monodisperse size distribution (12 ± 6 nm), a significant reduction from the starting MPs ($x_c \approx 10$ µm). Their magnetization behavior differed notably from MPs, exhibiting a 4× lower magnetization with a gradual M-T decrease and no sharp transitions at 200 K or 300 K, unlike MPs, which showed distinct magnetic phase transitions.

Laser printing of MP and NP inks successfully produced 2D structures with distinct sintering behaviors. NP-sintered structures exhibited 4× better uniformity than MP-based ones, highlighting their advantage for high-resolution structuring. MP laser printing at low fluence resulted in twice the overall magnetization of MPs at 1 T, but high fluence reduced magnetization by 20–30%, likely due to ablation-induced material loss. NP laser printing followed a similar trend, showing broad transitions at 200 K and 300 K at low fluence as NPs, which were further suppressed at high fluence.

This study demonstrates a compositionally controlled method for synthesizing NiMnSn NPs using fine MPs. Laser sintering offers a precise approach for structuring functional magnetic materials, though suppression of magnetization and phase transitions at high fluence emphasizes the need for optimized processing conditions. Future work will focus on minimizing oxidation effects, refining laser sintering parameters, and exploring further flexibility in PLAL NP synthesis technique to enhance the magnetic performance of structured NiMnSn materials.

Funding: The authors gratefully acknowledge the funding by the German Research Foundation (DFG) within the Collaborative Research Centre/Transregio (CRC/TRR) 270 (Project-ID 405553726, projects (B08, B01, B05, and B11). Bilal Gökce further thanks DFG for funding of the project GO 2566/10-1. Carlos Doñate Buendia thanks Generalitat Valenciana for funding of the project CIDEIG/2023/08 within Gen-T programme.

Acknowledgments: We thank Tobias Bochmann for his help with the SEM imaging of NiMnSn NPs and their sintered structures

Conflicts of Interest: The authors declare no conflicts of interest.

References

[1] R. R. Heikes, *Physical Review **1951,** 84 (2), 376.*

[2] H. Luo; F. Meng; Z. Feng; Y. Li; W. Zhu; G. Wu; X. Zhu; C. Jiang; H. Xu, *Journal of Applied Physics **2009,** 105 (10).*

[3] R. Paudel; G. C. Kaphle; M. Batouche; J. Zhu, *International Journal of Quantum Chemistry **2020,** 120 (24), e26417.*

[4] K. Özdoğan; E. Sasioglu; I. Galanakis, *Nova Publisher **2008**.*

[5] R. Kainuma; K. Oikawa; W. Ito; Y. Sutou; T. Kanomata; K. Ishida, *Journal of Materials Chemistry **2008,** 18 (16), 1837.*

[6] S. K. Sarkar; P. D. Babu; V. K. Sharma; S. D. Kaushik; S. Goswami; M. A. Manekar, *Acta Materialia **2024,** 276, 120126.*

[7] A. Hirohata; D. C. Lloyd, *MRS Bulletin **2022,** 47 (6), 593.*

[8] K. Elphick; W. Frost; M. Samiepour; T. Kubota; K. Takanashi; H. Sukegawa; S. Mitani; A. Hirohata, *Sci Technol Adv Mater **2021,** 22 (1), 235.*

[9] J. Sharma; A. A. Coelho; K. G. Suresh; A. Alam, *Physical Review B **2024,** 109 (6), 064418.*

[10] N. M. Fortunato; X. Li; S. Schönecker; R. Xie; A. Taubel; F. Scheibel; I. Opahle; O. Gutfleisch; H. Zhang, *Chemistry of Materials **2024,** 36 (14), 6765.*

[11] L. Chen; X. Zeng; T. M. Tritt; S. J. Poon, *Journal of Electronic Materials **2016,** 45 (11), 5554.*

[12] J. Joseph; M. Ohtsuka; H. Miki; M. Kohl, *Joule **2020,** 4 (12), 2718.*

[13] T. Krenke; E. Duman; M. Acet; E. Wassermann; X. Moya; L. Mañosa; A. Planes, *Nature materials **2005,** 4, 450.*

[14] Q. Tao; Z. Han; J. Wang; B. Qian; P. Zhang; X. Jiang; D. Wang; Y. Du, *AIP Advances **2012,** 2.*

[15] L. Patra; Y. Quan; B. Liao, *Journal of Applied Physics **2024,** 136 (2).*

[16] R. Nadarajah; J. Landers; S. Salamon; D. Koch; S. Tahir; C. Doñate-Buendía; B. Zingsem; R. E. Dunin-Borkowski; W. Donner; M. Farle; H. Wende; B. Gökce, *Scientific Reports **2021,** 11 (1), 13719.*

[17] Y. Li; A. Flynn; C. Masternick; B. Kolanovic; B. Li; B. Li, *Advanced Materials Technologies n/a (n/a), 2401443.*

[18] A. Jana; M. Das; S. Tiwari; S. S. Basha; A. R. S. Gautam; S. K. Panda; R. Mitra; S. Kumar; R. Devasia; C. S. Tiwary, *Ceramics International **2023,** 49 (11, Part A), 17396.*

[19] A. Lanzutti; E. Marin. The Challenges and Advances in Recycling/Re-Using Powder for Metal 3D Printing: A Comprehensive Review *Metals* [Online], 2024.

[20] M. Ghahremani; A. Aslani; M. Hosseinnia; L. H. Bennett; E. Della Torre, *AIP Advances **2018,** 8 (5).*

[21] S. Gubin; Y. Koksharov; G. Khomutov; G. Yurkov, *Russian Chemical Reviews **2005,** 74, 539.*

[22] A. Aslani; M. Ghahremani; M. Zhang; L. Bennett; E. Della Torre, *IEEE Transactions on Magnetics **2018,** PP, 1.*

[23] P. Roy; S. M. Hoque; S. Akter; S. I. Liba; S. Choudhury, *Heliyon **2024,** 10 (14), e34413.*

[24] R. D. Mcmichael; R. D. Shull; L. J. Swartzendruber; L. H. Bennett; R. E. Watson, *Journal of magnetism and magnetic materials **1992,** 111 (1), 29.*

[25] P. Gorria; J. L. Sánchez Llamazares; P. Álvarez; M. J. Pérez; J. Sánchez Marcos; J. A. Blanco, *Journal of Physics D: Applied Physics **2008,** 41 (19), 192003.*

[26] M. R. Karim; S. Naryan Panda; A. Barman; I. Sarkar, *Nanotechnology **2022,** 33 (23), 235701.*

[27] A. Ahmad; S. Mitra; S. K. Srivastava; A. K. Das, *Journal of Magnetism and Magnetic Materials **2019,** 474, 599.*

[28] G. Cavazzini; F. Cugini; D. Delmonte; G. Trevisi; L. Nasi; S. Ener; D. Koch; L. Righi; M. Solzi; O. Gutfleisch; F. Albertini, *Journal of Alloys and Compounds **2021,** 872, 159747.*

[29] S. Govindan; A. Venkatesan; R. K. Kalaiezhily; K. Ravichandran, *Structural and magnetic studies of half-metallic Heusler alloy Cr2CoSi nanoparticle synthesized by mechanical-alloying method*. 2018; Vol. 1953, p 120052.

[30] D. A. Kumar, *MATERIALS SCIENCE-POLAND **2013,** 31.*

[31] Y. D. Wang; Y. Ren; Z. H. Nie; D. M. Liu; L. Zuo; H. Choo; H. Li; P. K. Liaw; J. Q. Yan; R. J. Mcqueeney; J. W. Richardson; A. Huq, *Journal of Applied Physics **2007,** 101 (6).*

[32] F. Zhang; C. Taake; B. Huang; X. You; H. Ojiyed; Q. Shen; I. Dugulan; L. Caron; N. Van Dijk; E. Brück, *Acta Materialia **2022,** 224, 117532.*

[33] Y. Xu; L. Liu; G. Lu; L. Yi; M. Liu; H.-G. Piao; L. Pan, *Journal of Nanoparticle Research **2021,** 23 (6), 123.*

[34] R. Ghunaim; V. Eckert; M. Scholz; M. Gellesch; S. Wurmehl; C. Damm; B. Büchner; M. Mertig; S. Hampel, *Journal of Materials Chemistry C **2018,** 6 (5), 1255.*

[35] A. Ahmad; S. Mitra; S. K. Srivastava; A. K. Das, *Journal of Physics D: Applied Physics **2021,** 54 (38), 385001.*

[36] C. Wang; L. Basit; Y. Khalavka; Y. Guo; F. Casper; T. Gasi; V. Ksenofontov; B. Balke; G. H. Fecher; C. Sönnichsen; Y.-K. Hwu; J.-J. Lee; C. Felser, *Chemistry of Materials **2010,** 22 (24), 6575.*

[37] C. Wang; A. A. Levin; L. Nasi; S. Fabbrici; J. Qian; C. E. V. Barbosa; S. Ouardi; J. Karel; F. Albertini; H. Borrmann; G. H. Fecher; C. Felser, *Chemistry of Materials **2015,** 27 (20), 6994.*

[38] M. Modan; A.-G. Schiopu, ***2020,** 43.*

[39] E. Fazio; B. Gökce; A. De Giacomo; M. Meneghetti; G. Compagnini; M. Tommasini; F. Waag; A. Lucotti; C. Zanchi; P. Ossi; M. Dell'aglio; L. D'urso; M. Condorelli; V. Scardaci; F. Biscaglia; L. Litti; M. Gobbo; G. Gallo; M. Santoro; F. Neri, *Nanomaterials **2020,** 10, 2317.*

[40] I. Y. Khairani; G. Mínguez-Vega; C. Doñate-Buendía; B. Gökce, *Physical Chemistry Chemical Physics **2023,** 25 (29), 19380.*

[41] B. Gökce; V. Amendola; S. Barcikowski, *ChemPhysChem **2017,** 18 (9), 983.*

[42] D. Zhang; B. Gökce; S. Barcikowski, *Chemical Reviews **2017,** 117 (5), 3990.*

[43] M. Ratti; J. J. Naddeo; J. C. Griepenburg; S. M. O'malley; D. M. Bubb; E. A. Klein, *J Vis Exp **2017,** (124).*

[44] A. Subhan; A.-H. I. Mourad; Y. Al-Douri. Influence of Laser Process Parameters, Liquid Medium, and External Field on the Synthesis of Colloidal Metal Nanoparticles Using Pulsed Laser Ablation in Liquid: A Review *Nanomaterials* [Online], 2022.

[45] F. Waag; Y. Li; A. R. Ziefuß; E. Bertin; M. Kamp; V. Duppel; G. Marzun; L. Kienle; S. Barcikowski; B. Gökce, *RSC Advances **2019,** 9 (32), 18547.*

[46] S. Tahir; N. Shkodich; B. Eggert; J. Lill; O. Gatsa; M. Flimelová; E. Adabifiroozjaei; N. M. Bulgakova; L. Molina-Luna; H. Wende; M. Farle; A. V. Bulgakov; C. Doñate-Buendía; B. Gökce, *ChemNanoMat* ***2024,*** *10 (5), e202400064.*

[47] S. Tahir; J. Landers; S. Salamon; D. Koch; C. Doñate-Buendía; A. R. Ziefuß; H. Wende; B. Gökce, *Advanced Engineering Materials* ***2023,*** *25 (20), 2300245.*

[48] A. Riskin. Study of the CSD process for the ordered deposition of metallic nanocrystals. 2012.

Supplementary Information (SI):

Compositionally Controlled Synthesis and 2D Laser Printing of Magnetocaloric NiMnSn Nanoparticles

Shabbir Tahir[1], Franziska Scheibel[2], Carlos Doñate-Buendía[1,3] Zongwen Fu[1], David Koch[4], Markus Heidelmann[5], Wolfgang Donner[4], Oliver Gutfleish[2], and Bilal Gökce[1]*

[1]Chair of Materials Science and Additive Manufacturing, University of Wuppertal, Gaußstr. 20, 42119 Wuppertal, Germany

[2]Functional Materials, Institute of Materials Science, Technical University of Darmstadt, Peter-Grünberg-Str. 16, Darmstadt 64287, Germany

[3]GROC·UJI, Institute of New Imaging Technologies, Universitat Jaume I, Av. De Vicent Sos Baynat s/n, 12071 Castellón, Spain

[4]Institute of Materials Science, Technical University of Darmstadt, Darmstadt 64287, Alarich-Weiss-Strasse 2, Germany

[5]Interdisciplinary Center for Analytics on the Nanoscale (ICAN) and Center for Nanointegration Duisburg-Essen (CENIDE), University of Duisburg-Essen, Carl-Benz-Straße 199, 47057 Duisburg, Germany

*Corresponding authors: goekce@uni-wuppertal.de

1. Elemental composition of NPs by PLAL of NiMnSn elemental pressed powders

Figure S1 shows the elemental composition of synthesized NPs obtained from pressed powder targets with varying Ni-Mn-Sn ratios. Despite systematically altering the target composition, the resulting NPs exhibit significant variations, with no clear correlation to the intended composition. The large standard deviations indicate substantial heterogeneity in elemental distribution, suggesting that the ablation and synthesis process does not lead to uniform incorporation of elements into the nanoparticles.

These discrepancies can be attributed to the differences in the volatilities and ionization potentials of Ni, Mn, and Sn during PLAL. Mn, being more volatile, tends to be lost more easily, leading to Mn depletion and an enrichment of Ni or Sn in certain cases. The laser-material interaction further contributes to selective vaporization and recondensation, making precise composition control challenging. This suggests that using alternative synthesis strategies, such as pre-alloyed bulk targets or optimized laser parameters, may be necessary to achieve more consistent nanoparticle compositions.

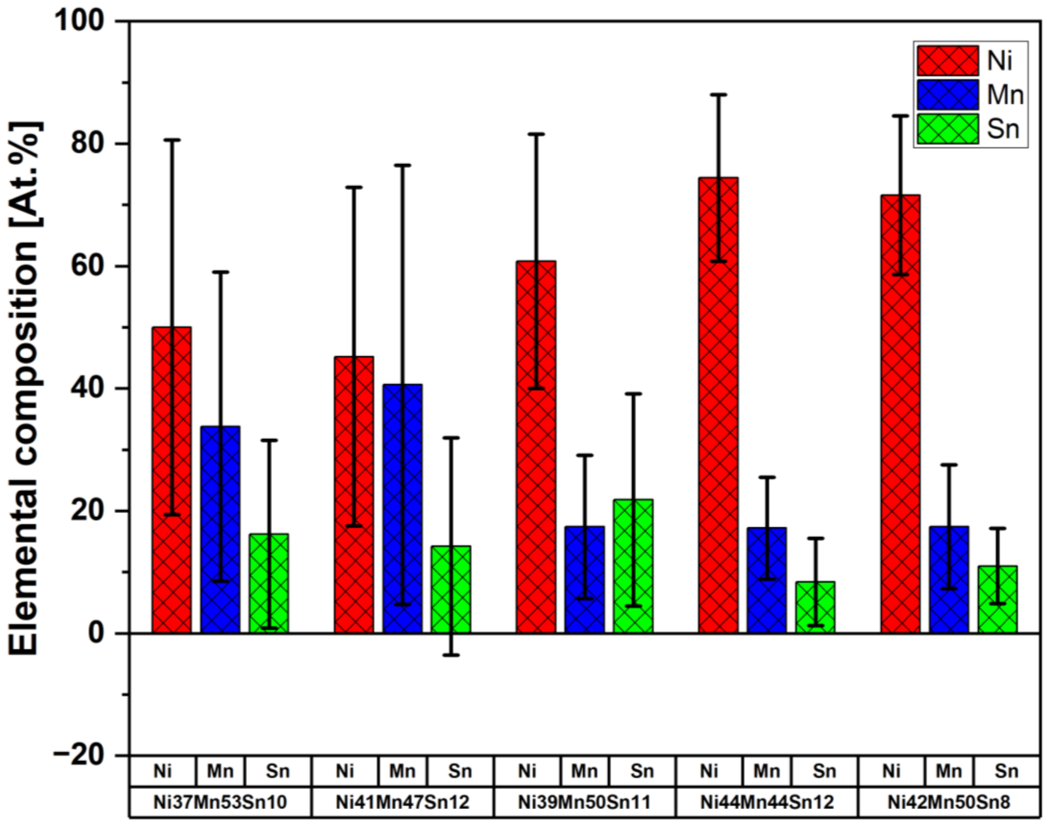

Figure S1. Average elemental composition of NiMnSn NPs produced using PLAL of elemental-pressed and sintered targets with varying elemental ratio.

2. Elemental composition of NPs by PLAL of powder pressed and sintered NiMnSn alloy MPs with Mn MPs

Fig S2 illustrates the elemental composition of NP synthesized via PLAL using NiMnSn MP mixed with additional Mn powder, which was pressed and sintered into targets. Unlike the previous results where nanoparticle composition showed little correlation with the target, here a clear trend emerges: as the Mn content in the pressed target increases, the Mn content in the resulting NPs also increases. This suggests that compensating for Mn loss by preloading the target with excess Mn is an effective strategy for achieving the desired composition in the synthesized NPs.

The observed linear trend is likely due to the similar volatility of the NiMnSn alloy and Mn during the PLAL process. Since the alloy and the added Mn have comparable ablation and ionization characteristics, their relative evaporation rates remain balanced, preventing the disproportionate loss of Mn. This minimizes compositional drift and ensures better retention of the intended Ni-Mn-Sn ratios. These results highlight that adjusting the target composition by compensating for elemental losses—rather than relying solely on bulk alloy targets—offers a more reliable method for tailoring the final NP composition.

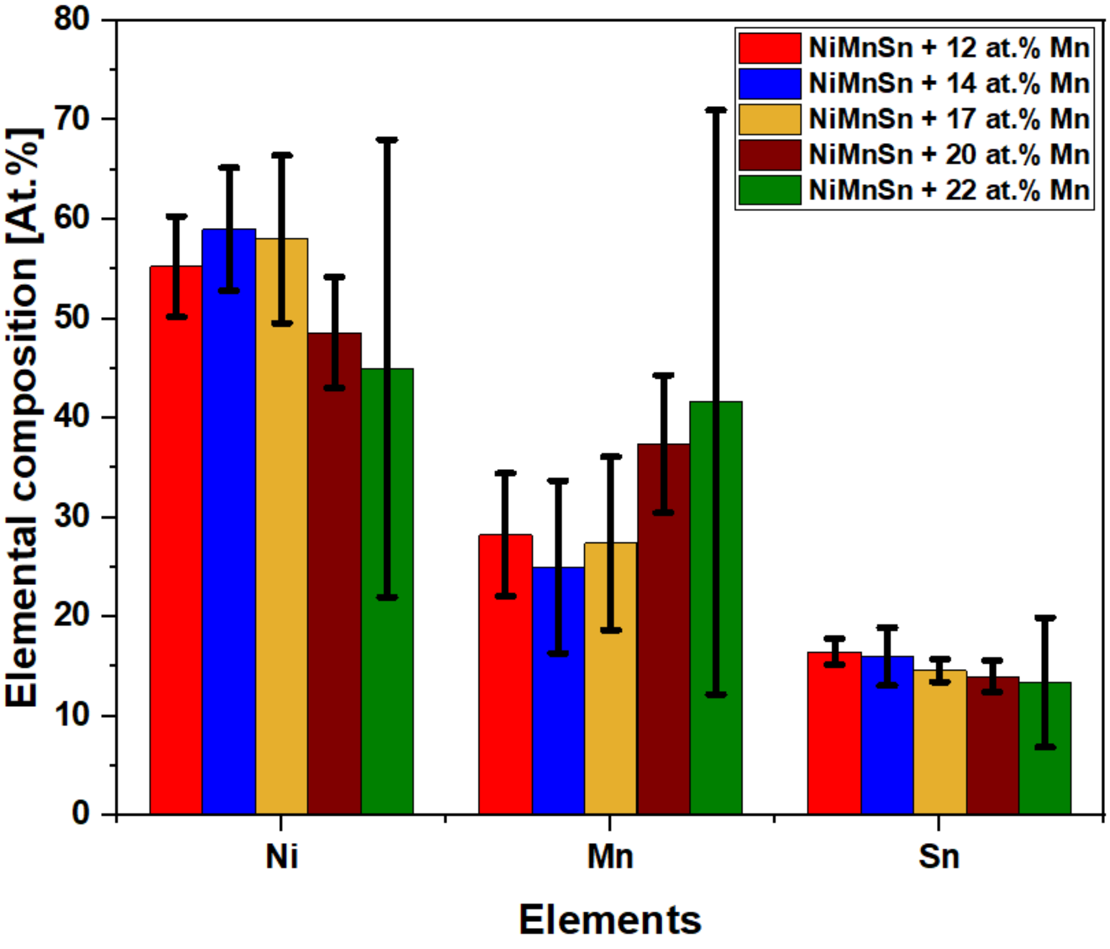

Figure S2. Average elemental composition of NiMnSn NPs produced using PLAL of powder pressed and sintered NiMnSn alloy MP and varying Mn MPs.

3. Mn-rich NPs produced during PLAL of powder-pressed and sintered NiMnSn and Mn MPs

The image presents a scanning transmission electron microscopy (STEM) image (top) and an energy-dispersive X-ray spectroscopy (EDX) line scan (bottom) of NPs synthesized via PLAL of powder-pressed and sintered NiMnSn and Mn MPs. The EDX line scan shows the spatial distribution of Ni (green), Mn (purple), and Sn (red) across the selected NP. The intensity of Mn (purple) is significantly higher than that of Ni and Sn, indicating preferential incorporation or segregation of Mn during the ablation process. This Mn enrichment likely results from differences in the volatility and ionization potential of the constituent elements. During PLAL, Mn atoms may ablate more efficiently due to their higher vapor pressure and lower bonding strength in the target material, leading to the preferential formation of Mn-rich nanoparticles. The Ni and Sn signals are weaker and more dispersed, suggesting that these elements either coalesce into separate particles or are less efficiently incorporated into the Mn-rich phase.

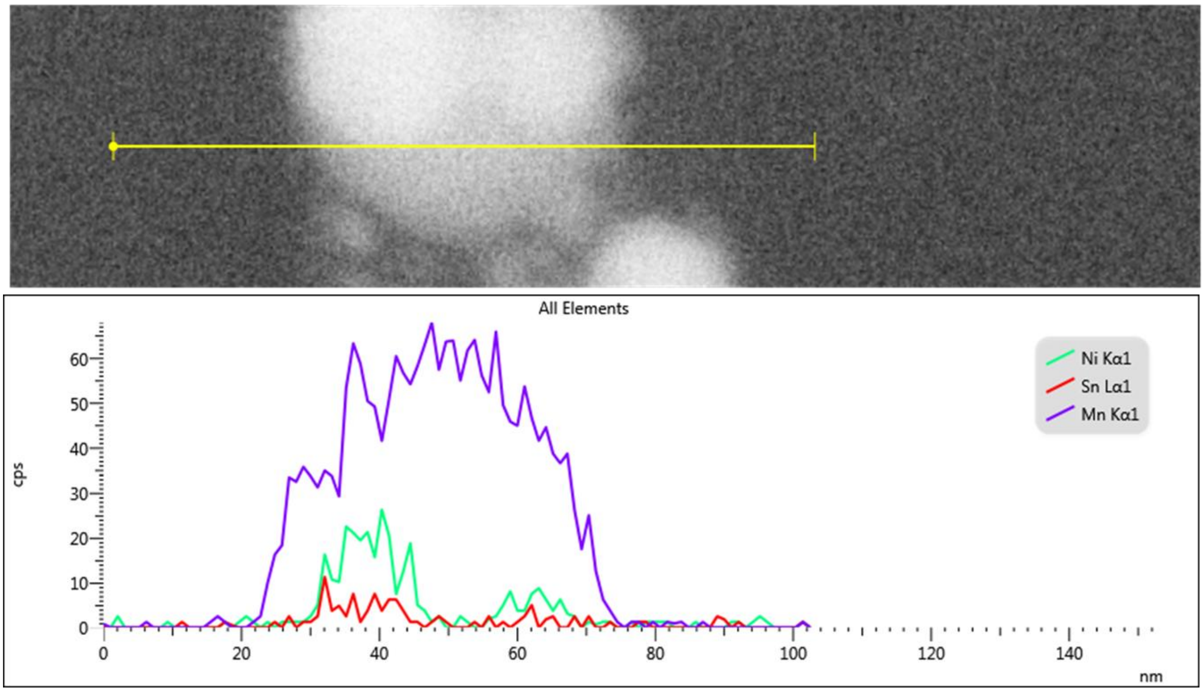

Figure S3. STEM image and EDX elemental line scan of NiMnSn NPs produced using PLAL of powder pressed and sintered NiMnSn alloy MP and varying Mn MPs, showing rich Mn phases.

4. Crystal structure of NiMnSn NPs

The X-ray diffraction (XRD) pattern in the figure S4 represents the structural analysis of a cubic Heusler alloy, specifically in the austenite phase, recorded at room temperature (RT). The diffraction data consists of measured intensities (red circles) and a calculated fit (black line) obtained from Rietveld refinement, showing an excellent match between the experimental and theoretical patterns. The difference curve (blue line) at the bottom highlights the minimal deviation between the measured and calculated data, confirming a good fit.

The identified phase corresponds to a cubic Pm-3m (space group 221) Heusler structure, with a refined lattice parameter of a = 5.987 Å, indicative of the austenitic (high-temperature) phase of the alloy. The presence of well-defined Bragg peaks (green markers) at expected positions confirms the phase purity and crystallinity of the sample. The absence of additional peaks suggests that no significant secondary phases are present, reinforcing that the synthesized material predominantly adopts the cubic Heusler structure.

The austenite phase is characteristic of Ni-Mn-Sn-based Heusler alloys at higher temperatures, where the structure is cubic before undergoing a martensitic transformation at lower temperatures. The fact that the diffraction pattern corresponds to the cubic phase at room temperature suggests that either the material has a high martensitic transformation temperature or Mn depletion during synthesis has suppressed the transformation, stabilizing the austenite phase. This is consistent with previous findings where deviations in stoichiometry, especially Mn content, influence the phase stability and transformation behavior of Heusler alloys.

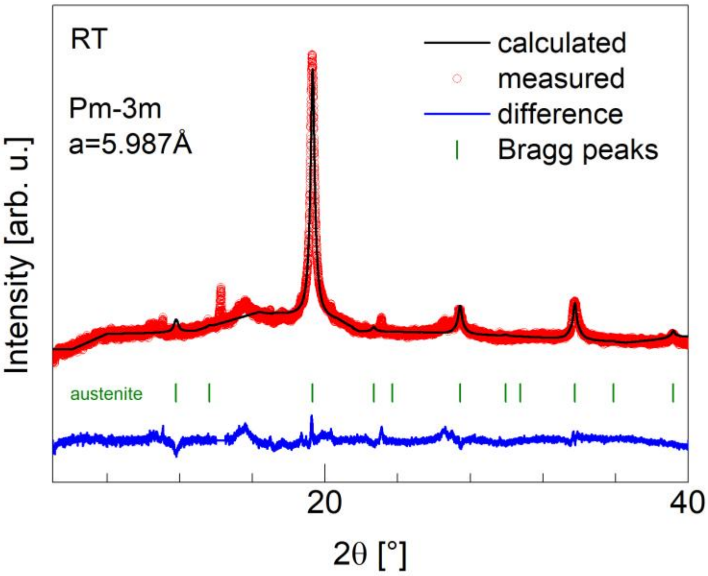

Figure S4. XRD pattern of NiMnSn nanoparticles synthesized via PLAL, showing a cubic Heusler structure in the austenite phase at room temperature. The measured data (red circles) and calculated fit (black line) exhibit a good match, with the difference curve (blue) confirming minimal deviation.

4. Magnetic response of NiMnSn NPs produced by PLAL of bulk NiMnSn target (target type 1).

The figure S5 shows the M-T curves for nanoparticles synthesized via PLAL of bulk NiMnSn alloy (target type 1) under different applied fields. In the low-field measurement (10 mT), the ZFC curve exhibits a small peak at low temperatures, likely due to blocked nanoparticles or weak interactions, while the FC and FW curves show a smooth and gradual decrease in magnetization with increasing temperature. At a higher field (1 T), the magnetization follows a continuous decay without any abrupt changes, indicating the absence of a magnetostructural phase transition. This behavior contrasts with the results from PLAL using target type 3 (NiMnSn MP + Mn MP), where a clear phase transition was observed.

The lack of a distinct transition in these nanoparticles suggests that Mn depletion during PLAL of bulk NiMnSn alloy significantly alters the composition, suppressing the expected magnetocaloric transformation. Instead, the magnetization decreases in a smooth manner, resembling a disordered ferromagnetic or superparamagnetic system. This highlights the impact of elemental loss on the final magnetic properties and reinforces the effectiveness of compensating for Mn loss in the target preparation process, as seen with target type 3, to retain the desired phase transformation behavior.

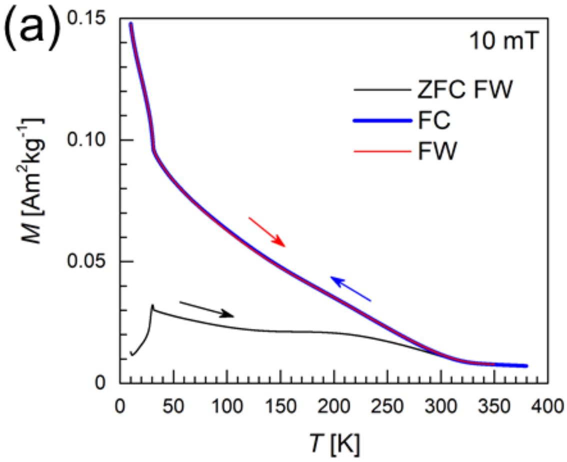

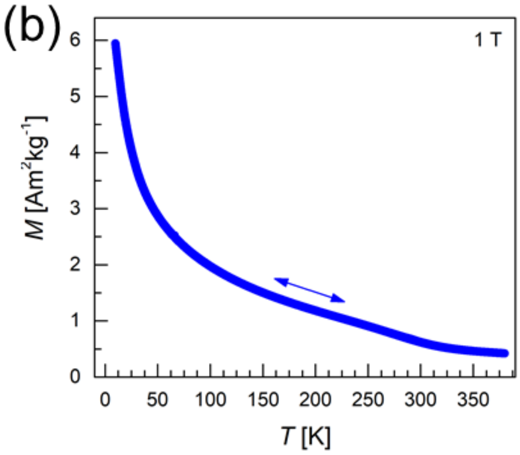

Figure S5. Temperature-dependent magnetization M-T and magnetization vs. field M(H) curves of NiMnSn NPs synthesized via PLAL from target type 1 (bulk NiMnSn alloy).

These pages of the Dissertation are not included in the electronic version

These pages of the Dissertation are not included in the electronic version